Studies on Higher Order Modes in Accelerating Structures for Linear Colliders

DISSERTATION
zur Erlangung des Doktorgrades
des Fachbereichs Physik
der Universität Hamburg

vorgelegt von

Nicoleta-Ionela Baboi
aus Ploieşti, Rumänien

Hamburg
2001

Gutachter der Dissertation:	Prof. Dr. P. Schmüser Dr. R. Brinkmann
Gutachter der Disputation:	Prof. Dr. P. Schmüser Dr. J. Rossbach
Datum der Disputation:	18. Mai 2001
Dekan des Fachbereichs Physik und Vorsitzender des Promotionsausschusses:	Prof. Dr. F.-W. Büßer

Abstract

An electron-positron linear collider with a center-of-mass energy of 500 GeV is considered to be an essential instrument for future experiments in particle physics. An important parameter of a collider is the luminosity, the collision rate of the particles. In order to obtain a high luminosity, the emittance of the beam, a measure of the distribution of transverse positions and angles of the particles, has to be very small. Wake fields are the main source of emittance increase for ultra-relativistic bunches. They are electromagnetic fields generated by the beam itself interacting with the environment, for example with the accelerating structures, and act back on the following particles. The consequence is usually an enlargement of the energy distribution and an increase in the transverse emittance.

Wake fields can be decomposed in the so-called higher order modes (HOM), resonant electromagnetic fields. This thesis covers studies of HOMs in the proposed accelerating structures for two linear colliders: the SBLC (S-Band Linear Collider) and TESLA (TeV Energy Superconducting Linear Accelerator). Experimental investigations and simulations have been made.

In the normal conducting accelerating structure for the SBLC, working at 3 GHz, modes have been excited using particle beams. HOMs have been studied both directly at special pick-ups and indirectly through their effect on the beam. The measurements made with single bunches and with bunch trains are discussed.

The HOMs of superconducting 9-cell TESLA cavities working at 1.3 GHz have been studied both using a beam of charged particles and on a test bench. Through experiments with beam, some modes have been found to be unexpectedly poorly damped in several cavities. Detailed studies made in the laboratory of one such mode have indicated the boundary conditions of the fields imposed by the neighboring cavities to be a possible cause. Simulations of the multi-bunch beam dynamics in the TESLA main linac show that the emittance growth due to wake field effects is within tolerable limits both for the TESLA base line design, using 9-cell cavities, and for the design based on so-called superstructures, groups of multi-cell cavities.

Zusammenfassung

Ein Elektron-Positron Linear Collider mit einer Schwerpunktsenergie von 500 GeV gilt als Option für zukünftige Experimente in der Elementarteilchenphysik. Ein wichtiger Parameter eines Colliders ist die Luminosität, d.h. die Kollisionsrate der beschleunigten Teilchen am Wechselwirkungspunkt. Um eine hohe Luminosität zu erzielen, ist eine möglichst geringe Emittanz beider Strahlen erforderlich, wobei die Emittanz ein Mass für die Verteilung der Teilchen im Phasenraum darstellt. Störwellenfelder (engl. Wake Fields), vom Strahl im Zusammenwirken mit seiner Umgebung erzeugte elektromagnetische Felder, wirken auf nachfolgende Teilchen und führen somit zu einer Emittanzaufweitung. Dies geschieht sowohl transversal als auch longitudinal.

Diese Störwellenfelder können als Überlagerung von Moden höherer Ordnung (engl. Higher Order Modes, HOMs) dargestellt werden. Diese Arbeit beschreibt theoretische und experimentelle HOM-Studien an den Beschleunigungsstrukturen zweier Linear Collider Konzepte, SBLC (S-Band Linear Collider) und TESLA (TeV Energy Superconducting Linear Accelerator).

In den normalleitenden 3 GHz-Beschleunigungsstrukturen des S-Band Linear Colliders wurden gezielt Moden höherer Ordnung durch den Strahl angeregt und sowohl durch spezielle Sensoren als auch durch ihren Effekt auf den Strahl untersucht. In dieser Arbeit werden Messungen mit Einzelbunchen und mit Bunchzügen diskutiert.

Im Falle der supraleitenden 9-zelligen TESLA-Strukturen wurden die Untersuchungen mit Hilfe des Strahls und auf einem speziellen Teststand durchgeführt. Bei den Experimenten am Strahl stellte sich heraus, dass einige Moden in einzelnen Kavitäten unerwartet schlecht gedämpft sind. Detaillierte Studien einer einzelnen solchen Mode auf dem Teststand deuten darauf hin, dass die durch die benachbarten Kavitäten erzeugten Randbedingungen dies hervorrufen könnten. Simulationen der Multi-Bunch Strahldynamik in TESLA zeigen, dass das Emittanzwachstum durch Störwellenfelder sowohl für das TESLA Basisdesign mit 9-zelligen Kavitäten als auch für sogenannte Superstrukturen tolerabel ist.

Contents

1 Introduction **1**

2 Linear Collider Project Studies at DESY **5**
2.1 The S-Band Linear Collider 5
2.2 The TeV Energy Superconducting Linear Accelerator 6
2.3 A Qualitative Comparison 8
2.3.1 General considerations 8
2.3.2 The accelerating gradient 8
2.3.3 The luminosity 9

3 Wake Fields and their Influence on Particle Beams **11**
3.1 Linear Beam Dynamics 11
3.2 Particle Acceleration 14
3.3 Wake Fields and Wake Potentials 18
3.3.1 Short range wake fields 18
3.3.2 Long range wake fields. Higher Order Modes 20
3.4 Wake Field Influence on the Beam Properties 22
3.4.1 Short range effects 22
3.4.2 Long range effects 25
3.4.3 Wake field measurements 29

4 Higher Order Modes in the S-Band Accelerating Structure **33**
4.1 The S-Band Test Facility 33
4.2 Accelerating Structure Design 33
4.2.1 The S-band structure 33
4.2.2 The HOM couplers 40
4.3 Single Bunch Frequency Spectrum 41
4.3.1 Experimental setup 41
4.3.2 Measurements and results 42
4.4 Bunch Trains. Amplification of Modes 45
4.4.1 Theory 45
4.4.2 Measurements and results 46
4.5 Kicker Experiment 46
4.5.1 Principle of the experiment 46
4.5.2 Measurements and results 49

5 Higher Order Modes in the TESLA Cavities **53**
5.1 The TESLA Test Facility 53
5.2 The TESLA Cavity 56
5.3 HOM Excitation with an Intensity Modulated Beam 59
5.3.1 Principle of the experiment 59
5.3.2 First experimental results 61
5.3.3 Simulations 64
5.3.4 Measurements and results 74
5.4 Investigations on Cavities of Module 1 83
5.4.1 Last mode of the third dipole passband 83
5.4.2 Measurements on individual cavities from module 1 89
5.4.3 Experimental study of boundary conditions 100

6 Emittance Growth in the TESLA Main Linac **105**
6.1 Alternative Design of the Accelerating Structure 105
6.1.1 General considerations 105
6.1.2 Higher Order Modes 107
6.2 Beam Dynamics with the TESLA Alternative Design 114
6.2.1 Required HOM damping in the superstructure 114
6.2.2 Multi-bunch emittance growth 117
6.2.3 Pulse-to-pulse orbit jitter 118
6.3 Comparison to the CDR Design 122
6.3.1 Beam dynamics with the TESLA CDR design 122
6.3.2 Comparison 126
6.4 Beam Dynamics in the Presence of an Insufficiently Damped Mode . . . 128

7 Summary **131**

A Auxiliary Functions **133**

B TTF Module 1 **135**

Bibliography **137**

List of Symbols

$\beta_{x,y}(s)$	horizontal and vertical beta function (Twiss parameter)
$\beta^*_{x,y}$	horizontal and vertical beta function at IP
δ_E	energy loss due to beamstrahlung
δx	maximum bunch offset along train with modulated transverse position
δx_n	offset of bunch index n
$\delta x'_n$	kick of bunch index n
Δx	offset amplitude (difference between maximum and minimum bunch offset along a train with modulated current)
$\varepsilon_{x,y}$	horizontal and vertical emittance
ε_n	normalized transverse emittance
$\gamma = E/m_0c^2$	relativistic energy factor
$\lambda(\zeta)$	longitudinal charge distribution
$\omega_l = 2\pi f_l$	angular frequency of mode with index l
$\omega_b = 2\pi f_b$	bunch angular frequency
$\omega_K = 2\pi f_K$	angular frequency of modulation in transverse offset (applied by help of kicker)
ω_{Kl}	angular frequency of modulation in transverse offset on resonance (for which $\mathcal{A}_- = \max$)
ω^+_{Kl}	angular frequency of modulation in transverse offset for which $\mathcal{A}_+ = \max$)
$\omega_{mod\,l} = 2\pi f_{mod\,l}$	angular frequency of modulation of bunch charges
ψ_l	phase advance per cell for mode with index l
φ	initial phase of modulation in transverse offset
$\sigma_{x,y}$	horizontal and vertical beam size (rms)
$\sigma^*_{x,y}$	horizontal and vertical beam size at IP (rms)
σ_z	rms bunch length
τ_l	decay time of mode with index l
ζ	longitudinal coordinate with respect to the beginning of the bunch (or with respect to the first bunch in a train)
$\mathcal{A}_{+,-}(\omega t, Q, \Omega t)$	auxiliary functions (see Appendix A)
c	velocity of light
e	electron charge
E	bunch energy
E_{cm}	center-of-mass energy
E_z	longitudinal component of the electric field

f_{rep}	pulse repetition frequency
k_l	loss factor of mode with index l
$k_{\|\|l}$	longitudinal loss factor of mode with index l
$k^n_{\perp l}$	transverse loss factor of mode with index l (normalized to the transverse position)
L	luminosity
m_0	electron mass
$\mathbf{M}_{12}$	transfer matrix
n_b	number of bunches
N	number of bunches in a train
N_e	number of electrons (positrons) per bunch
P_b	average beam power
P_l	power dissipated into the walls for mode l
$p_r(\omega t, Q)$	auxiliary function (see Appendix A)
q	bunch charge
Q_l	quality factor of mode with index l
$(R/Q)_l$	$= 4 \cdot k_l/\omega_l$
s	longitudinal coordinate along the design trajectory
$t_b = 1/f_b$	bunch spacing
V_l	voltage corresponding to mode with index l
v_{gr_l}	group velocity for mode with index l
v_{ph_l}	phase velocity for mode with index l
W_l	energy stored in mode with index l
$W^{\delta}_{\|\|}(s)$	longitudinal delta-function wake potential
$W_{\|\|}(s)$	longitudinal wake potential of a charge distribution
$W^{n\delta}_{\perp}(s)$	transverse delta-function wake potential
$x(s)$, $x'(s)$	horizontal particle offset and angle
$y(s)$	vertical particle offset
z	longitudinal coordinate along the linac
$Z_{\perp}(\omega)$	transverse coupling impedance

List of Abbreviations

ASSET	Accelerator Structure Setup
BBU	beam break-up
BPM	bunch position monitor
CDR	Conceptual Design Report (for TESLA) [11]
CERN	European Organization for Nuclear Research (Organisation Européenne pour la Recherche Nucléaire)
CLIC	Compact Linear Collider
c.m.	center-of-mass
DDS	damped detuned structure
DESY	Deutsches Elektronen Synchrotron
EM	electromagnetic
FEL	free electron laser
FNAL	Fermi National Accelerator Laboratory
FWHM	full width at half maximum
HERA	Hadron Electron Circular Facility (Hadron Elektron Ring-Anlage)
HOM	higher order mode
IP	interaction point
JLC	Japanese Linear Collider
KEK	High Energy Accelerator Research Organization
LEP	Large Electron Positron Collider
LHC	Large Hadron Collider
NLC	Next Linear Collider
R&D	Research and Development
SBLC	S-Band Linear Collider
SBTF	S-Band Test Facility
SLAC	Stanford Linear Accelerator Center
SLC	SLAC Linear Collider
TESLA	TeV Energy Superconducting Linear Accelerator
TTF	TESLA Test Facility

List of Figures

2.1 The SBLC layout 5
2.2 The TESLA layout 7

3.1 Transverse phase space of a bunch. 13
3.2 Pill box cavity. 14
3.3 Cross-section through a multi-cell accelerating cavity. 15
3.4 Electric and magnetic field distribution 16
3.5 Dispersion diagram 17
3.6 Wake field generation 19
3.7 Gaussian bunch 20
3.8 The short range wake potential for the SBLC structure 21
3.9 Undamped long range wake of the SBLC structure 23
3.10 Slice offsets at the end of the SBLC main linac 24
3.11 The single bunch vertical emittance along the main linac 25
3.12 Bunch offsets at the end of the SBLC main linac 26
3.13 The multi-bunch emittance along the SBLC main linac 27
3.14 Trajectory of the first bunch in the train 28
3.15 Trajectory of the 321st bunch in the train 28
3.16 Transverse bunch positions at the end of the SBLC main linac for damped and detuned structures 30
3.17 The multi-bunch emittance along the SBLC main linac for damped and detuned structures 30

4.1 The SBTF layout. 34
4.2 The SBLC dispersion diagram 35
4.3 The field distribution of several trapped modes 37
4.4 Loss factors of the modes of the first, third and sixth dipole passbands. . 38
4.5 Loss factors of the modes of the first dipole passband. 38
4.6 The HOM waveguide coupler 40
4.7 The experimental setup for the HOM measurements. 41
4.8 The time domain HOM signal 43
4.9 Spectrum from upstream horizontal pick-ups 44
4.10 Spectrum from downstream horizontal pick-ups 44
4.11 The field amplitude as a function of the bunch offset 45
4.12 The function $(\exp(-iN\omega t_b)-1)/(\exp(-i\omega t_b)-1)$ 47
4.13 The spectrum with 20 bunches from upstream horizontal pick-ups . . . 47

4.14 Experimental setup for the kicker experiment. 49
4.15 BPM difference and sum signals 50
4.16 Fourier transform of BPM difference signal 51
4.17 Current monitor signals 51

5.1 TTF layout 54
5.2 TTF cryo-module 55
5.3 TESLA cavity 56
5.4 TESLA HOM couplers 57
5.5 Dispersion diagram for the dipole modes of the TESLA cavity 58
5.6 Dispersion diagram for the first monopole passband of the TESLA cavity 59
5.7 Bunch offsets at the BPM location ($\omega_b/(2\pi) = 216$ MHz) 61
5.8 Setup of experiment with intensity modulated beam 62
5.9 BPM signal measured with and without HOM resonance 63
5.10 Δx around resonances of two modes ($\omega_b/(2\pi) = 54$ MHz and 27 MHz) . . 65
5.11 Trajectory for $\omega_b/(2\pi) = 54$ MHz 66
5.12 Trajectory for $\omega_b/(2\pi) = 27$ MHz 66
5.13 Bunch offsets at the BPM location on resonance ($\omega_b/(2\pi) = 54$ MHz) . . . 67
5.14 Bunch offsets at the BPM location off-resonance 68
5.15 Scans around a resonance for various R/Q values 69
5.16 Scans around a resonance for various Q values 69
5.17 Δx as a function of $(R/Q)Q$ 72
5.18 Scan of modulation frequency ($\omega_b/(2\pi) = 54$ MHz) 73
5.19 Setup of experiment with intensity modulated beam 74
5.20 BPM difference signal 75
5.21 Spectrum of the BPM difference signal 76
5.22 Setup for filtering of BPM signal 76
5.23 Filtered BPM difference signal 77
5.24 Filtered BPM difference signal for $\omega_{mod}/(2\pi)$ around 23.776 MHz 78
5.25 Modulation frequency scan 79
5.26 Time domain filtered signal from a HOM coupler 80
5.27 Sketch of mode polarization 81
5.28 Signal of HOM coupler as a function of beam offset 81
5.29 S_{21} for cavity 2 of module 1; 3rd passband 84
5.30 S_{21} for cavity 3 of module 1; 3rd passband 84
5.31 S_{21} for cavity 3 of module 1; last mode of passband 87
5.32 S_{21} across cavity 3 plus tube; last mode of passband 87
5.33 TM_{011} modes in the cavities of the TTF modules 1-3 88
5.34 Frequency of last TM_{011} mode as function of cavity length 88
5.35 S_{21} at room temperature for cavity 3 of module 1; 3rd passband 89
5.36 S_{21} for cavity 3 at room temperature; last mode of the 3rd passband . . . 90
5.37 S_{21} across cavity 3 plus tube at room temperature; last mode of passband 90
5.38 S_{21} of cavity S10; 3rd passband; open tubes 91
5.39 S_{21} of cavity S10; 3rd passband; closed tubes 92
5.40 S_{21} of cavity S10; last mode of the 3rd passband; closed tubes 92

5.41 S_{21} of cavity D4; 3rd passband; open tubes 93
5.42 S_{21} of cavity D4; 3rd passband; closed tubes 93
5.43 Measurement setup of cavity 94
5.44 Frequencies of last modes of 3rd passband of cavity S10 as function of tube length 96
5.45 Frequencies of last modes of 3rd passband of cavity D4 as function of tube length 96
5.46 Field distribution for cavities S10 and D4 with symmetrical boundaries . 97
5.47 Field distribution for cavity S10 with asymmetrical boundaries 99
5.48 Definition of the coupling efficiency 100
5.49 Experimental setup for study of coupling efficiency 101
5.50 Transmission from adaptor to couplers for $\varphi = 20^\circ$ 102
5.51 Transmission from adaptor to couplers for $\varphi = 158^\circ$ 102
5.52 Angles of polarizations with low transmission 103

6.1 Superstructure made of 4×7-cell cavities. 106
6.2 Main linac layout 106
6.3 Beta function along the TESLA main linac 107
6.4 R/Q for the dipole modes of the 9-cell cavity and the superstructure . . 113
6.5 R/Q for the monopole modes of the 9-cell cavity and the superstructure 113
6.6 Bunch offsets at the end of linac 116
6.7 Multi-bunch emittance along the main linac 116
6.8 Measured Q_{ext} in the copper superstructure model 117
6.9 Multi-bunch emittance along the main linac for the alternative design . . 118
6.10 The rms offset of the quadrupoles versus time, due to ground motion. . 120
6.11 The average offset of the bunch train at the linac end versus time, caused by ground motion. 120
6.12 Bunch offsets of two pulses: at the initial time moment and after 1 min . 121
6.13 Bunch offsets for two pulses: with no initial offset and an offset of 1 σ_y . 121
6.14 Bunch offset for two pulses: with constant charge and with 1 % charge fluctuation 122
6.15 Bunch train offsets at linac end for CDR design 124
6.16 Multi-bunch emittance along the main linac for CDR design 124
6.17 Average mode frequencies measured at the TTF modules 1-3 125
6.18 Histogram with measured Q-values 126
6.19 Multi-bunch emittance in the main linac for CDR design with TTF modes 127
6.20 $(R/Q)Q$ for the 9-cell cavity and the superstructure 127
6.21 Bunch offsets at linac end with high impedance mode 128
6.22 Multi-bunch emittance along the main linac with high impedance mode 129

A.1 $p_r(\omega t, Q_l)$ 133
A.2 $\mathcal{A}_+(\omega_l t, Q_l, \Omega t)$ 134
A.3 $\mathcal{A}_-(\omega_l t, Q_l, \Omega t)$ 134

List of Tables

1.1 Worldwide linear collider studies 2

2.1 Main parameters of the SBLC and TESLA. 9

3.1 Parameters used in simulations 24

4.1 Main characteristics of the SBLC accelerating structures. 36

5.1 Beam parameters for the HOM experiments 55
5.2 HOMs excited by an intensity modulated beam generated by injector 1. 63
5.3 Properties of two example modes 64
5.4 Beam parameters used for simulation of HOM experiments with injector 2. 68
5.5 Dipole modes measured in the cavities of module 3 71
5.6 Two dipole modes in cavities of module 3 75
5.7 Dipole modes excited in the HOM experiment. 82
5.8 High-Q mode measured with a network analyzer 85
5.9 Estimated Q_{ext} for the HOM couplers of cavities D4 and S10 95
5.10 Measured cell lengths for cavity S10 98

6.1 Main characteristics of the main linac and of the beam 108
6.2 Monopole modes in the superstructure 110
6.3 Monopole modes in the 9-cell cavities 110
6.4 Dipole modes in the superstructure 111
6.5 Dipole modes in the 9-cell cavities 112
6.6 Comparison of loss factor sums for the 9-cell cavity and the superstructure 112
6.7 Multi-bunch emittance for various Q-values 115
6.8 Dipole modes used for simulations 123
6.9 Summary of the simulations for the alternative and CDR designs. 126

B.1 TTF cryo-modules 1, 2 and 3 135

Chapter 1

Introduction

An electron-positron linear collider with an energy of 500 GeV center-of-mass (c.m.) is nowadays considered to be the next step for experimental studies in particle physics. Accelerators have played an important role in the successful Standard Model that offers a picture of nature at the level of its smallest constituents. According to this model, matter is composed of few elementary particles, leptons and quarks. The interactions between these are mediated by force-carrying particles. The electromagnetic force is unified at high energies with the weak force into the electroweak interaction. The strong interaction is described by Quantum Chromodynamics. Some predictions of the Standard Model remain to be proven experimentally. Among these is the so-called Higgs mechanism that could explain the masses of all particles. Other questions arise beyond the model. Based on the successful unification of the electric and magnetic forces, and of these with the weak interaction, it is believed that at higher energies the electroweak force is unified with the strong force. The favored theory implies the existence of a supersymmetric partner of each matter and force-carrying particle.

In order to further check the theories, colliders that accelerate particles to very high energies are required. The highest energies achieved so far are: about 200 GeV c.m. for e^+e^- collisions in LEP (Large Electron Positron Collider), close to 2 TeV c.m.[1] for $p\overline{p}$ in the Tevatron and 300 GeV c.m. for ep in HERA (Hadron Electron Circular Facility). Currently under construction is the LHC (Large Hadron Collider) that will accelerate protons up to 7 TeV. Although many discoveries are expected to come from hadron collisions, precise measurements can be made only with lepton machines. Therefore the need exists to build an e^+e^- collider at energies of 500 GeV and above.

Circular e^+e^- colliders become inefficient at energies higher than that of LEP due to synchrotron radiation, which is emitted by charged particles traveling on a curved trajectory. The amount of radiated power is much higher for electrons than for heavier particles. The energy loss per revolution is proportional to the fourth power of the energy and inversely proportional to the trajectory radius. The solution is to build linear colliders, but the advantage of circular accelerators of using an injected beam many times is lost. Therefore one has to use pulses with many particle bunches in

[1] Note that the effective collision energy at constituent (quark) level is about an order of magnitude lower than the c.m. energy of the proton-proton collision.

order to increase the efficiency. In addition, the beam size at the interaction point (IP) must be extremely small (in the nm range) to achieve the required high collision rate of the particles.

The SLC (SLAC Linear Collider), the only existing linear collider, proved the feasibility of such a machine [1]. It accelerates electrons and positrons to 50 GeV. Several projects of second generation linear colliders are now under study. Three concepts can be distinguished [2, 3, 4, 5, 6, 7]:

1. The SBLC (S-Band Linear Collider[2]) and the JLC/NLC (Japanese Linear Collider/Next Linear Collider) are based on normal conducting accelerating structures, driven by pulsed high power klystrons;

2. TESLA (TeV Energy Superconducting Linear Accelerator) uses superconducting accelerating structure technology;

3. CLIC (Compact Linear Collider) is also based on normal conducting technology, but makes use of the two-beam concept. Here, instead of using klystrons, the beam is accelerated by a drive beam, which is decelerated. Very high power levels can be achieved.

A few main characteristics of these projects are summarized in Table 1.1. The frequency given is the one used in the accelerating structures. The loaded gradient takes into account the decrease in the electric field in the accelerating sections due to the energy extracted by the beam. The gradient and the luminosity (defined below) are indicated in all cases for the 500 GeV c.m. design.

		TESLA	**SBLC***	**JLC/NLC**	**CLIC**
Frequency	[GHz]	1.3	3	11.4	30
c.m. energy	[GeV]	500-800	500-1000	500-1000	500-5000
Gradient (loaded) (for 500 GeV)	[MV/m]	23	17	55	150
Luminosity (for 500 GeV)	[10^{33} cm^{-2}s^{-1}]	34	5	7	14

* this study was terminated at the end of 1998

Table 1.1: Worldwide linear collider studies

Besides the c.m. energy, an important parameter of a collider is the luminosity:

$$L = \frac{P_b}{E_{cm}} \frac{N_e}{4\pi\sigma_x^*\sigma_y^*} H_D, \tag{1.1}$$

where P_b is the average beam power, E_{cm} is the center-of-mass energy, N_e the number of particles per bunch, $\sigma_{x,y}^*$ is the horizontal/vertical beam size at the IP and H_D is the

[2]The accelerating frequency (3 GHz) lays in the S-band in the microwave spectrum

disruption enhancement factor [2]. The higher is L, the higher is the probability that an event occurs. The luminosity is limited by beamstrahlung, the emission of synchrotron radiation in the strong space-charge field of the opposing bunch. The beam energy loss due to beamstrahlung δ_E is inversely proportional to $\sigma_z(\sigma_x^* + \sigma_y^*)^2$, where σ_z is the bunch length. By using a vertically flat beam, with $\sigma_y^* \ll \sigma_x^*$, δ_E becomes independent of the vertical beam size. Therefore one can increase the luminosity by decreasing σ_y^*, while keeping δ_E within acceptable limits [8]. Such flat beams can be achieved with damping rings[3]. The beam size is given by the beta function at the IP and the emittance. Since the lower limit of the vertical beta function β_y^* is given by the bunch length, one can write the luminosity as:

$$L \propto \frac{P_b}{E_{cm}} \sqrt{\frac{\delta_E}{\varepsilon_{y,n}}}\, H_D, \tag{1.2}$$

where $\varepsilon_{y,n}$ is the normalized vertical emittance, which is a measure of the beam size and divergence.

This equation implies that the small vertical emittance provided by the damping ring should be preserved during acceleration in the main linac. The main source of emittance increase are the so-called wake fields that are excited by charged particles in the interaction with their environment, typically the accelerating structures, and act on the following particles. Therefore the study of the wake fields is essential when designing a collider. There are short range wake fields with effects within a bunch, and long range ones acting on following bunches. One can distinguish longitudinal effects, mainly an increase in the energy spread, from transverse ones, specifically an increase in the transverse emittance.

Longitudinal wake fields vary approximately with the second power of the accelerator frequency, while the transverse ones scale with the third power. For this reason, lower frequency accelerators are preferable in order to preserve small emittances, leading to a higher luminosity. For TESLA, this advantage of the lower frequency combines with the higher efficiency, due to the superconducting technology used, to give the highest luminosity. On the other hand, the SBLC and the JLC/NLC have the potential of using a higher gradient leading to a shorter facility or a higher energy for a given length. CLIC aims at much higher energies, but considerable R&D is needed to establish the viability of the two-beam accelerator concept. It may be considered a third generation linear collider.

This thesis deals with studies of the wake fields in the accelerating structures for the two linear collider projects centered at DESY: SBLC and TESLA. Chapter 2 gives an overview of the two projects. The two concepts are qualitatively compared. The basic concepts related to wake fields are introduced in chapter 3. Both short range and long range effects are discussed. Possible remedies of their negative impact on the beam quality are pointed out.

In chapter 4 the experimental studies made at the S-Band Test Facility are presented. A 6 m long accelerating structure was designed for the SBLC, aiming to minimize the

[3]It now seems possible to build a gun for low-emittance flat beams that could eliminate the electron damping ring [9].

effects of long range wake fields. The experimental results are discussed and compared with the theoretical expectations.

The following two chapters are dedicated to the wake field studies for TESLA. Experimental studies are presented in chapter 5. Investigations of 9-cell TESLA cavities were made both in the cryo-modules installed in the TESLA Test Facility and in individual cavities on a test bench. Chapter 6 deals with beam dynamics issues in the main linac of TESLA. A comparison is made between various design options. The last chapter gives a summary of the studies presented in this thesis.

Chapter 2

Linear Collider Project Studies at DESY

Two linear collider projects have been initially proposed at DESY:

- The S-Band Linear Collider (SBLC);
- The TeV Energy Superconducting Linear Accelerator (TESLA).

They are based on two different types of accelerating structures: For the SBLC, normal conducting technology is used, as for most of the other linear collider studies. TESLA is the only study based on superconducting cavities. In the following section, the two linear collider concepts are shortly presented and a qualitative comparison is made.

2.1 The S-Band Linear Collider

The name of the collider refers to the frequency used for acceleration, 3 GHz, which is in the S-band of the microwave spectrum. The layout of the SBLC is shown in Fig. 2.1 [3]. Polarized electrons are produced with a pulsed DC-gun operating at 90 kV (bottom right in the figure). The length of the bunches is shortened by two standing wave sub-harmonic bunchers operating at 166 MHz and 500 MHz and two S-band traveling wave structures. These four structures also increase the beam energy to a few MeV. Together with the gun they constitute the injector. The electron bunches are then accelerated by the pre-accelerator up to 3.15 GeV. The damping ring decreases the normalized

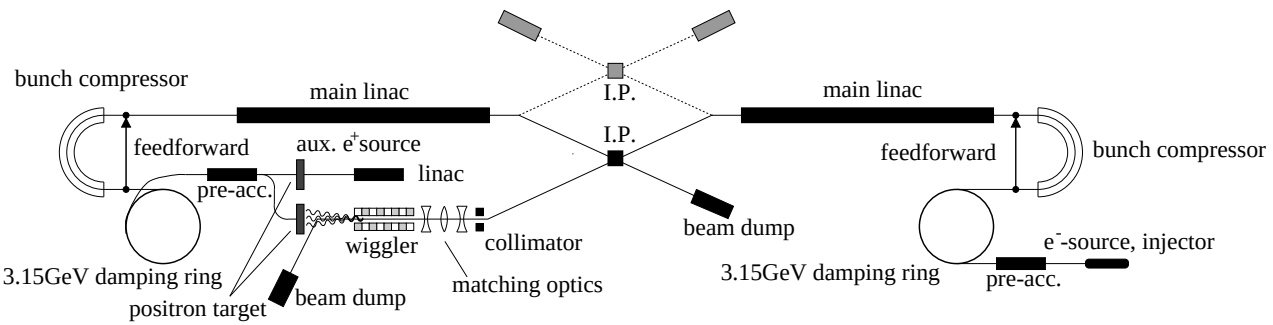

Figure 2.1: The SBLC layout [3].

transverse emittance from 10^{-4} m·rad to $4 \cdot 10^{-6}$ m·rad horizontally and $2 \cdot 10^{-7}$ m·rad vertically, providing a flat beam. Then the bunches go through the bunch compressor that further reduces their rms length from 4 mm to 0.3 mm. The compression is made by introducing an energy-position correlation within an RF section. When passing a series of bending magnets, the less energetic head of the bunch travels on a longer path than the tail, so that they come closer to each other.

After compression, the main linac increases the energy to 250 GeV (for the 500 GeV c.m. design). A special accelerating structure has been designed, in order to minimize the effects of the wake fields on the beam. This structure is normal conducting, working with 3 GHz traveling waves. Its design is described in detail in chapter 4. The beam delivery system and the final focus region decrease the transverse beam size down to 335 nm $\times$ 15 nm, suitable for the interaction point (IP).

The positron accelerator (left in the figure) is similar to that for electrons, except for the injector part [10]. The positrons are produced using the electron beam after collision. An auxiliary electron linac for positron production is foreseen as well. The electrons passing through a wiggler generate photons that produce electron-positron pairs in a thin target. The positrons are separated and then sent to a pre-accelerator. Apart from the e^+e^- IP, a second IP is intended for $\gamma\gamma$ interactions.

The main parameters of the SBLC are given in Table 2.1, found in section 2.3.

2.2 The TeV Energy Superconducting Linear Accelerator

The layout of TESLA is shown in Fig. 2.2 [2]. The electron accelerator is similar to that of the SBLC: electron source, pre-accelerator, damping ring, main linac and beam delivery section. A polarized laser-driven gun is used here to generate short electron bunches. Their energy is increased by a pre-accelerator to 5 GeV. The damping ring reduces the transverse emittance of the beam from 10^{-5} m·rad to $8 \cdot 10^{-6}$ m·rad horizontally and $2 \cdot 10^{-8}$ m·rad vertically.

For acceleration, the main linac uses 9-cell niobium cavities operating at 1.3 GHz. Twelve such cavities are grouped together in a cryo-module, where they are cooled to 2 K and become superconducting. This is a slightly different cryo-module design compared to the one initially proposed in [11] containing 8 cavities and now in use in the TESLA Test Facility [12]. The fill-factor and the length of the module were optimized in the newer design.

Instead of the 9-cell cavities, an option is to use so-called superstructures for acceleration, groups of cavities fed by one input coupler. At present the preferred version of superstructure consists of two 9-cell cavities, as compared to the older one with four 7-cell cavities. The accelerating structure will be described in chapter 6.

The positrons are produced with the help of an undulator through which the electrons pass, before going to the IP [10]. Using an undulator leads to a higher positron beam intensity than a wiggler. The emittance of the positron beam has to be reduced by the damping ring from 0.01 m·rad to the same values as for the electrons. Due to the long pulse train used in TESLA, the circumference of the damping ring is very large

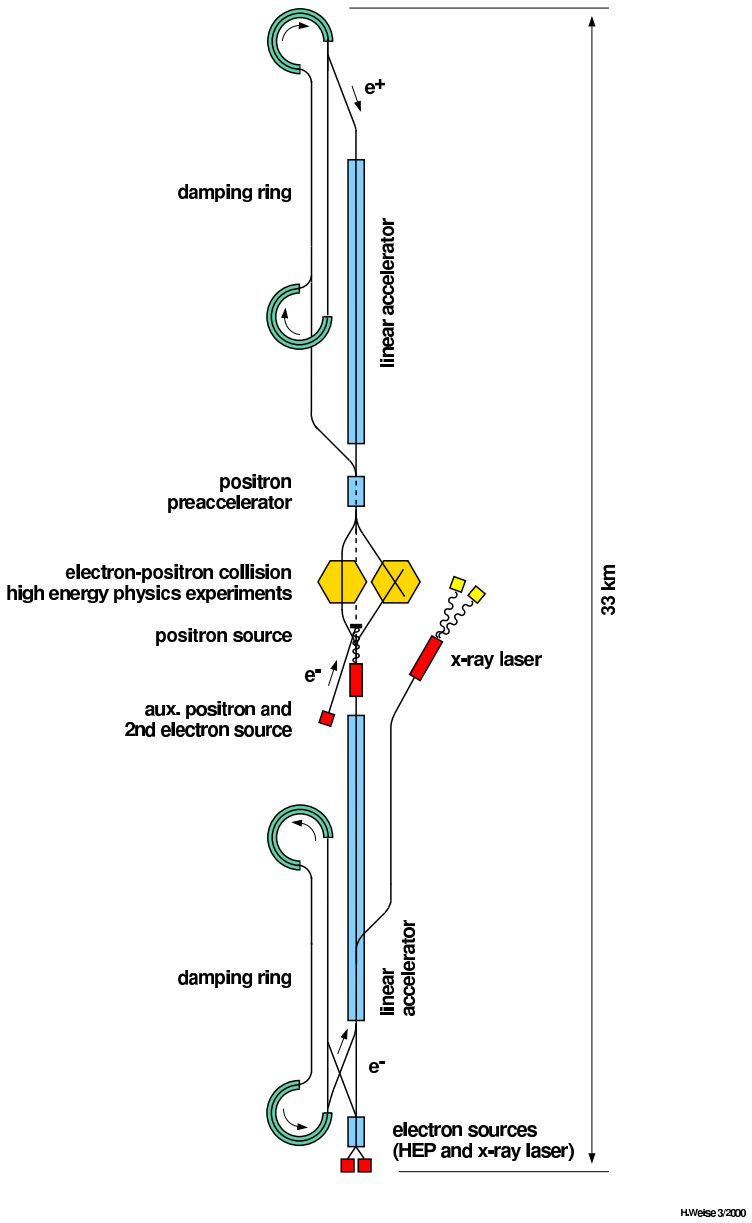

Figure 2.2: The TESLA layout [2].

even with a reduced bunch spacing. Therefore a special geometry of the ring has been chosen with two long straight sections placed in the main tunnel. In this way only two smaller additional tunnels are needed for the arcs at the ends, reducing the costs.

A special feature of TESLA is the integrated X-ray FEL facility [13]. This uses a beam accelerated in the first 3 km of the electron main linac which is operated at twice the nominal repetition rate. The FEL mode alternates pulse for pulse with the collider mode. A separate low emittance gun and a pre-accelerator, as well as a bunch compressor system are required.

The main parameters of TESLA are listed in Table 2.1 and compared to those of the SBLC.

2.3 A Qualitative Comparison

2.3.1 General considerations

The main difference between the two linear collider concepts[1] is the *technology* chosen for acceleration. The SBLC uses a relatively conventional technology, based on normal conducting structures. Advantage is taken of the experience gained with the SLC, that works at the same frequency, 3 GHz. Nevertheless to build 250 GeV linacs that preserve a low emittance beam is not easy. This requires the use of high power klystrons (150 MW) and careful wake field suppression in the accelerating structures.

For TESLA, superconducting technology was chosen. A frequency below 3 GHz was chosen, because in superconducting structures the power losses in the resonator walls increase approximately with the square of the frequency. Frequencies well above 350 and 500 MHz as used in LEP or HERA, were preferred in order to reduce the size of the cavities and the costs. A frequency of 1.3 GHz was chosen due to the availability of klystrons. The rather low frequency, compared to the other linear collider concepts, relaxes the wake field issue. The low losses in the accelerating cavity walls imply that a longer bunch train can be accelerated and the necessary RF-peak power is low. On the other hand, extended research on superconducting cavities is needed in order to reliably achieve gradients high enough to keep the length and cost of a linear collider within reasonable limits.

The main parameters of the two linear collider studies are given in Table 2.1[2] [2, 3].

The technology used is the most important aspect for two main parameters of a collider: the c.m. energy and the luminosity. The accelerating gradient determines the length of the machine for a given energy and therefore is an important ingredient in the total cost. The gradient and the luminosity issues will be discussed separately in the following sections.

2.3.2 The accelerating gradient

The gradient for superconducting niobium cavities working at 1.3 GHz is limited to about 50 MV/m where superconductivity breaks down. The RF breakdown limit for the SBLC is much higher[3], approaching 100 MV/m. In order to come close to this limit in practice, klystrons with a high peak power have to be developed. The higher achievable gradient for the SBLC together with the higher fill factor enable an upgrade at a later date to a higher c.m. energy than possible for TESLA.

[1] Many of the comments on the SBLC are valid also for the JLC/NLC and CLIC, due to the common normal conducting technology.

[2] For the SBLC data from 1997 is given, while for TESLA up-to-date parameters are listed.

[3] An unexpected limitation for normal conducting structures appears to be the breakdown that has been recently observed at quite low gradients: In NLC structures (11.4 GHz) breakdown occurred above 50 MV/m unloaded gradient (as compared to the designed 72 MV/m) [14]. In CLIC 30 GHz structures surface damage was observed at gradients of only 125 MV/m (design 170 MV/m) [15]. This effect is being extensively studied at present.

		SBLC	TESLA
Accelerating gradient	[MV/m]	17	23.4
RF frequency	[GHz]	3	1.3
Fill factor		0.95	0.75
Site length	[km]	33	33
# of accel. structures		5032	21024
# of klystrons		2516	584
Klystron peak power	[MW]	150	9.5
Repetition rate	[Hz]	50	5
Beam pulse length	[μs]	2	950
RF pulse length	[μs]	2.8	1370
# of bunches per pulse		333	2820
Bunch spacing	[ns]	6	337
Bunch charge	[10^{10}]	1.1	2
Emittance at IP (x,y)	[mm·mrad]	5, 0.25	10, 0.03
Beta at IP (x,y)	[mm]	11, 0.45	15, 0.4
Beam size at IP (x,y)	[nm]	335, 16	553, 5
Bunch length at IP	[mm]	0.3	0.3
Beamstrahlung	[%]	2.8	3.2
Luminosity	[10^{33} cm^{-2}s^{-1}]	5	34
Power per beam	[MW]	7	11.3
AC power (two linacs)	[MW]	140	97

Table 2.1: Main parameters of the SBLC and TESLA.

For a given gradient, the klystron power needed for normal conducting structures is much higher than that for superconducting structures due to the higher power loss in the walls. The SBLC loaded gradient of 17 MV/m is made with a 150 MW klystron feeding two S-band structures (approx. 12 m); $\sqrt{2}$ times more can be achieved by feeding each structure with one klystron. A klystron peak power of 9.5 MW is sufficient to achieve a gradient of 23 MV/m for three TESLA cryo-modules (approx. 36 m of accelerating structure)[4]. For the energy upgrade a gradient of 35 MV/m is assumed, by using twice as many klystrons.

2.3.3 The luminosity

The luminosity L is described by equation 1.2. As mentioned in chapter 1, the beamstrahlung parameter δ_E is kept small for both project studies by making the horizontal beam size σ_x^* rather large. For a given center-of-mass energy, L is then given by the vertical normalized emittance and by the beam power.

The single bunch *vertical emittance* is smaller for TESLA than for the SBLC due to

[4]Only at such high gradients is a superconducting linear collider competitive to the normal conducting ones. In the past few years gradients beyond this value have been achieved in TESLA cavities.

the lower wake fields related to the lower RF frequency. The multi-bunch emittance, that gives a measure of the distribution of the bunch transverse positions and angles, should be negligible with respect to the single bunch one. This goal is easier to realize with TESLA: Due to the low losses in the cavity walls, the RF pulse is longer for TESLA enabling a larger bunch spacing. Under this condition a bunch-to-bunch feedback can be used in the beam delivery system. This corrects for the effects of quadrupole misalignment and wake fields.

The lower repetition frequency in TESLA is compensated by the higher number of bunches per pulse, leading to a design *beam power* twice as high as for the SBLC. In addition to the emittance, this is a deciding parameter leading to a much higher luminosity for TESLA.

Test facilities were built for both projects, where various components are tested. An overview of the S-Band Test Facility is given in chapter 4. Chapter 5 contains a brief description of the TESLA Test Facility. In these chapters more considerations about the two project studies regarding the accelerating structures are given.

Chapter 3

Wake Fields and their Influence on Particle Beams

In the linear optics of charged particle beams, the normalized emittance is conserved along an accelerator. In real accelerators one has to take into account various effects, such as space charge and wake fields, that can lead to an increase of the emittance. In this chapter, after a brief review of the main notions related to charged particle optics, wake fields are introduced and their influence on accelerated beams is discussed.

3.1 Linear Beam Dynamics

In high energy linear accelerators, the particles grouped in bunches gain energy in accelerating structures and are transversely focused by magnetic quadrupoles. In addition, one needs steering magnets to correct for the misalignments of various components and diagnostic elements such as screens, current and position monitors in order to measure the properties of the beam.

The motion of a charged particle in the transverse planes, $x(s)$ and $y(s)$, can to a good approximation be considered as decoupled, so that one can write separate equations for each plane. The motion in the horizontal plane is described by the equation [16, 17, 18]:

$$\frac{1}{\gamma(s)}\frac{d}{ds}\left(\gamma(s)\frac{dx}{ds}\right) + K_x(s)x(s) = \frac{1}{\rho(s)}\frac{\Delta p(s)}{p(s)}, \tag{3.1}$$

where x is the horizontal offset of the particle from the design trajectory at the longitudinal position s, $\gamma = E/m_0c^2$ is the relativistic factor, $\rho(s)$ the bending radius at the location s. p is the particle design momentum and Δp is the momentum deviation. $K_x(s)$ is a function describing the focusing strength of the magnets at the position s. A similar equation can be written for the vertical offset, y. In the following we will denote by x the transverse particle offset, which can be either horizontal or vertical, unless otherwise specified. In the absence of acceleration, the γ factors cancel. In a linear accelerator, when not taking into account alignment errors and steering magnets, $\rho = \infty$ and the right-hand part of the equation vanishes.

From equation 3.1 the particle position and slope, x and x', can be obtained as a linear transformation from the initial values, x_0 and x'_0. *Transfer matrices* can be used to track the motion through various sections of the accelerator:

$$\begin{pmatrix} x \\ x' \end{pmatrix}_{s_2} = \mathbf{M}_{12} \begin{pmatrix} x \\ x' \end{pmatrix}_{s_1}, \tag{3.2}$$

where $\mathbf{M}_{12}$ is the *transfer matrix* in the x plane from position s_1 to position s_2 in the accelerator. A matrix can be written for each component of the accelerator, so that $\mathbf{M}_{12}$ is itself a product of matrices. The transfer matrices for common accelerator components can be found, for example, in [18].

The solution of the equation of motion 3.1 can be written in terms of the *Twiss parameters*, α, β and a phase function μ:

$$x(s) = \sqrt{a^2 \beta(s)}\, \cos(\mu(s) - \mu_0), \tag{3.3}$$

$$x'(s) = \sqrt{\frac{a^2}{\beta(s)}}\, (-\alpha(s)\, \cos(\mu(s) - \mu_0) - \sin(\mu(s) - \mu_0)). \tag{3.4}$$

$\beta(s)$ is called the *beta function* and the other Twiss parameters can be derived from it. $\alpha(s) = -1/2\ d\beta(s)/ds$ describes the convergence or divergence of the trajectory at the position s. $\mu(s) = \int_0^s ds/\beta(s)$ is the betatron phase advance and $\mu_0 = \mu(0)$. a is a constant describing the amplitude of the particle oscillations. From these equations it can be seen that particles execute "*betatron oscillations*" around the ideal trajectory. From the trigonometric relation $\sin^2(\xi) + \cos^2(\xi) = 1$ for any argument ξ, one finds from eqs. 3.3 and 3.4 an invariant of motion, the so-called *Courant-Snyder invariant*:

$$\frac{1 + \alpha^2(s)}{\beta(s)}\, x^2(s) + 2\,\alpha(s)\, x(s)\, x'(s) + \beta(s)\, x'^2(s) = a^2 = \text{constant}. \tag{3.5}$$

This equation defines the trajectory of one particle in the phase space (x, x') as being an ellipse. The area of this ellipse is πa^2.

For a bunch having many particles one can define an *emittance* with the help of the second-order moments of the particle distribution [19]:

$$\overline{x^2} = \frac{1}{q} \sum_i q_i (x_i - \overline{x})^2, \quad \overline{x'^2} = \frac{1}{q} \sum_i q_i (x'_i - \overline{x'})^2 \quad \text{and} \quad \overline{xx'} = \frac{1}{q} \sum_i q_i (x_i - \overline{x})(x'_i - \overline{x'}). \tag{3.6}$$

In this equation $\overline{x}$ and $\overline{x'}$ are the average position and angle of the bunch, q_i is the charge of particle i and $q = \sum_i q_i$. Of course, a bunch is normally made of identical particles. But to calculate the position and trajectory slopes of, for example, 10^{10} particles along a long accelerator would be impossible. Therefore it is practical to group many particles together in macro-particles or slices, often with different charges. For generalization we give the above definition.

The *r.m.s. emittance* is defined as:

$$\varepsilon_x = \sqrt{\overline{x^2}\,\overline{x'^2} - \overline{xx'}^2}. \tag{3.7}$$

If one replaces in this definition the explicit forms of x and x' of each particle from eqs. 3.3 and 3.4, one finds that the emittance is equal to the average of the Courant-Snyder invariants divided by two:

$$\varepsilon_x = \frac{\overline{a^2}}{2}. \tag{3.8}$$

Therefore the emittance can be defined as being $1/\pi$ of the area of the ellipse in the phase space that contains one standard deviation of the statistical distribution of the particles in the bunch, $\sigma_x = \sqrt{\beta_x \varepsilon_x}$.

The position and angles of the particles of a bunch can be represented in the transverse *phase space* (x, x') (see Fig. 3.1). The ellipse defining the emittance can be seen. The beam transverse dimension and divergence can then be derived from the parameters of the ellipse, using the emittance and beta function.

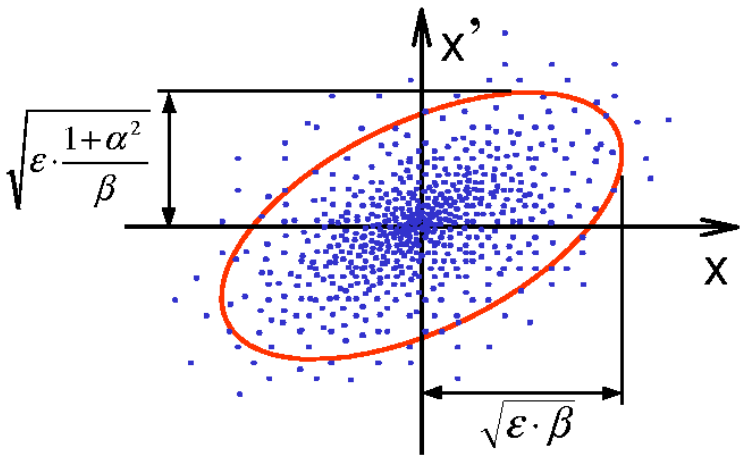

Figure 3.1: Transverse phase space of a bunch.

The beta function at a certain point depends on the initial Twiss parameters and emittance. A particular case is that of circular accelerators or periodic lattices, for which the beta function is also periodic. A lattice often used in high energy accelerators is the FODO cell. This consists of a focusing quadrupole (F), a drift space (O), a defocusing quadrupole (D) and another drift space (O).

When the beam energy stays constant and one neglects effects such as coupling between the degrees of freedom, space charge effects, wake fields etc., the emittance remains constant in time, although the distribution of the particles in the phase space may change [16, 19]. During acceleration, the so-called *adiabatic damping* occurs, that is the angle of the particle decreases due to the increasing longitudinal momentum while the transverse momentum stays constant. The emittance thus decreases as $1/\beta\gamma$, where β is here the relative velocity of the bunch. Therefore one defines a *normalized emittance*:

$$\varepsilon_n = \beta\gamma\varepsilon, \tag{3.9}$$

that is preserved also during acceleration.

If in eq. 3.6 x_i and x_i' represent the offsets and angles of the bunch centers (the phase space coordinates of the bunches), then with the help of eq. 3.7 one defines a *multi-bunch emittance*. Similarly to eq. 3.9, a normalized multi-bunch emittance can be defined.

For the longitudinal phase space, one can similarly define an emittance, by considering the energy and time differences with respect to the reference particle.

3.2 Particle Acceleration

The accelerating structures used nowadays are RF structures. A single metallic cylindrical cavity, called pill box, can be used to accelerate a charged beam (see Fig. 3.2). For such a cavity one can calculate analytically the resonant electromagnetic (EM) fields, called *modes*. The various modes differ in frequency and field distribution inside the cavity. They can be classified into *transverse magnetic* (TM) and *transverse electric* (TE) modes. TM modes have no longitudinal magnetic field on the axis, TE modes no longitudinal electric field, therefore not being appropriate for acceleration.

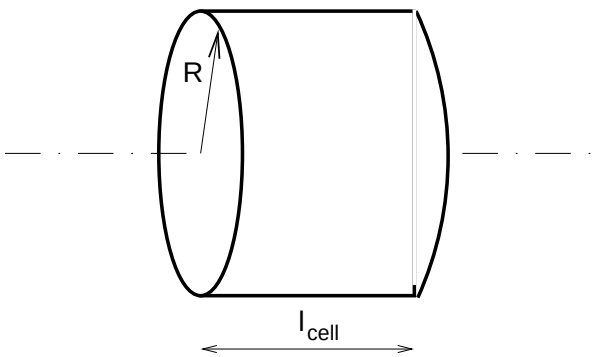

Figure 3.2: Pill box cavity.

Usually accelerating structures are composed of many such cavities built together, with an iris in between to ensure both coupling between them and space for the beam to go through (see Fig. 3.3). We will use the term *cell* for a single cavity of the chain and *accelerating structure*, *cavity* or *resonator* for the whole chain. The whole accelerating structure is fed through a power coupler, usually with a klystron or magnetron, with an EM wave at one of the resonance frequencies. Inside the cavity, the wave can be *traveling*, when it is coupled out at the other end of the structure and sent to a load, or it may be *standing*. The SBLC is based on normal conducting S-band structures working with traveling waves, while TESLA uses superconducting L-band cavities working with standing waves (see Chapter 2).

If all cells of a structures are identical, one has a *constant impedance* structure. The gradient decreases along the structure. A *constant gradient* structure can be realized by varying the iris holes to smaller apertures along the section.

When many pill boxes are coupled together, each mode degenerates into as many coupled modes as the number of cells. The field lines are distorted, the modes are no

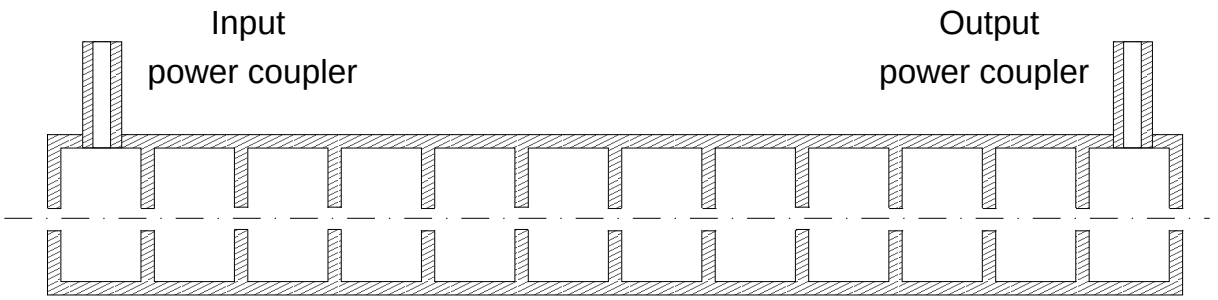

Figure 3.3: Cross-section through a multi-cell accelerating cavity.

longer purely TE or TM. Nevertheless one keeps the classification of *TM-like* and *TE-like* modes. By stronger degeneration hybrid modes appear as well. According to the azimuthal field distribution of the modes, there are monopole modes, with azimuthal symmetry, dipole modes, when there are two nodes of the field amplitude azimuthally, as well as quadrupole, sextupole etc. modes. Monopole modes are dominant among the modes with longitudinal electric field, while dipole modes dominate the modes with transverse field. In Fig. 3.4 the distribution of the electric and magnetic fields for several dipole modes (TM_{110}-like) in 3 cells of a long structure with identical cells are shown. The various modes differ by the phase advance per cell, $\psi = m \cdot \pi / N$, with m an integer and N the number of cells.

The frequencies of the coupled modes (for example TM_{110}-like) as a function of the phase advance per cell give a *dispersion curve*. A *dispersion diagram* consisting of several curves is plotted in Fig. 3.5 for a periodic structure. The curves for the modes with the lowest frequencies are represented. The curves are symmetrical with respect to phase advance per cell of 0 and π, therefore one draws only the region between these values. The frequency range given by the extreme values of each dispersion curve is referred to as a *passband*. The frequency range between two passbands is called a *stop-band*[1]. The three modes whose field distributions were shown in Fig. 3.4, are marked on the curve for the TM_{110} passband.

Two important parameters can be defined for periodic structures with the help of this diagram: the *phase velocity*, v_{ph}, and the *group velocity*, v_{gr} [21, 22]. For a mode with index l they are defined by:

$$v_{ph_l} = l_{cell} \, \frac{\omega_l}{\psi_l}, \qquad v_{gr_l} = l_{cell} \left(\frac{d\omega}{d\psi} \right)_l , \tag{3.10}$$

where l_{cell} is the cell length, ω_l the angular frequency and ψ_l the phase advance per cell of mode l. The phase velocity represents the velocity with which the wave propagates. In order to use a wave for acceleration, v_{ph} should be equal to the particle velocity. This means that the wave should be slowed down with respect to the case of a smooth waveguide, where the phase velocity is bigger than c, for example by means of irises.

[1]These terms were introduced for traveling wave structures, but are used also for standing wave structures since one can consider a standing wave as being composed of two traveling waves of opposite directions.

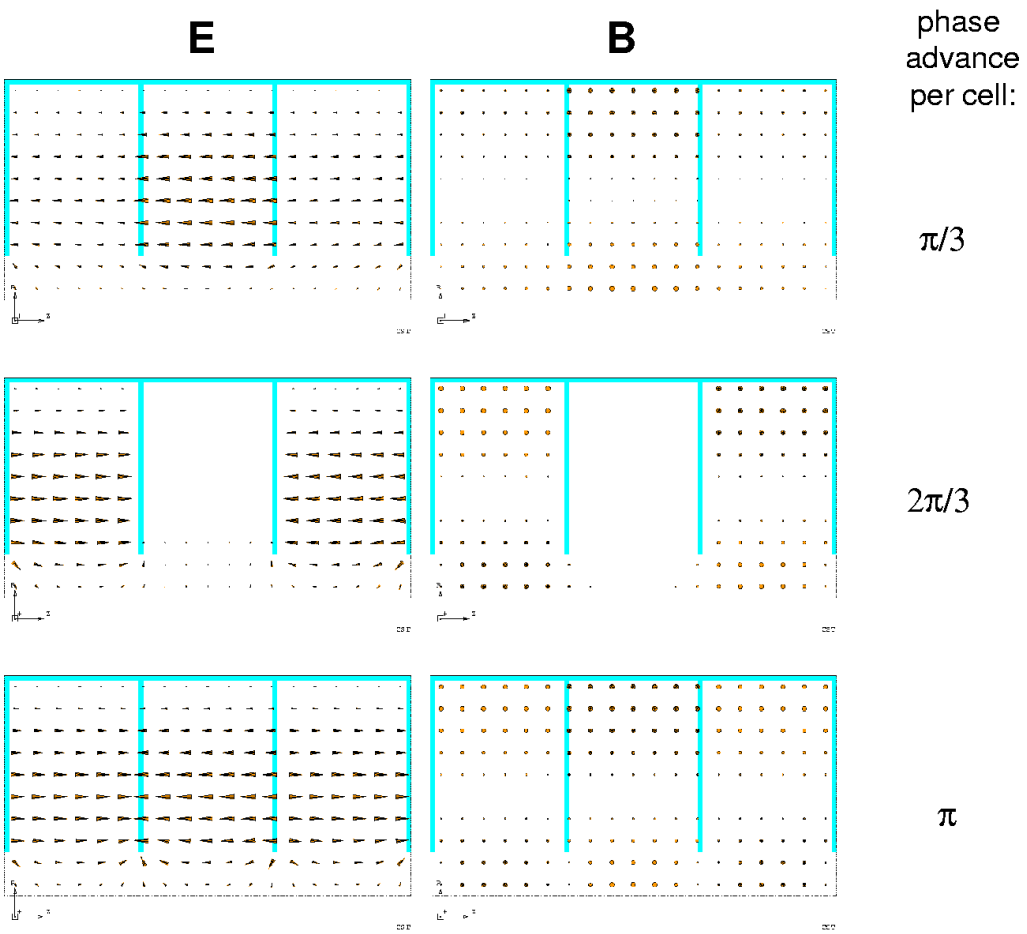

Figure 3.4: Distribution of electric and magnetic field for three TM_{110}-like modes. The modes were obtained by taking 3 cells with periodic boundary conditions, using the MAFIA code [20]. Only the upper half of the transverse section of the cells is shown. (the cell length is 30 mm, the radius is 50 mm)

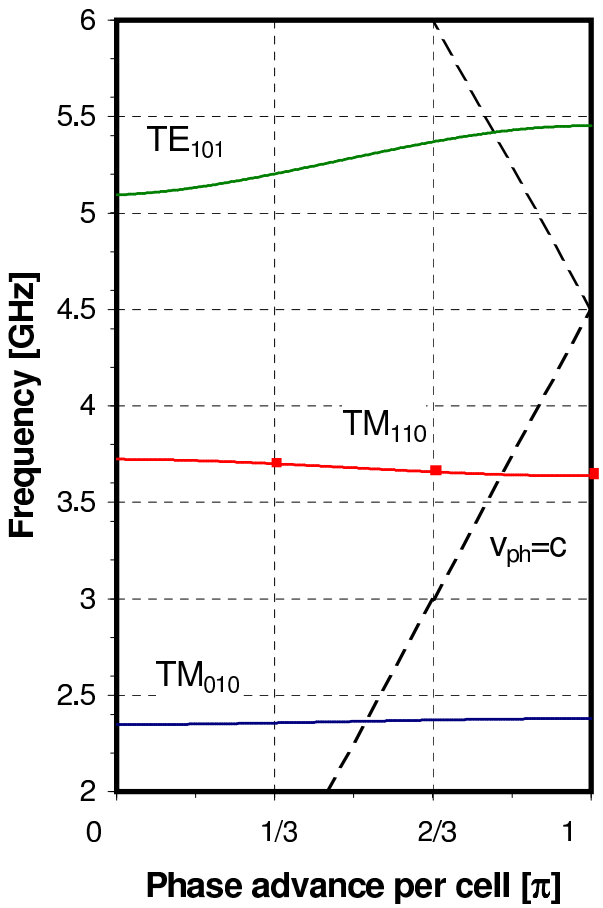

Figure 3.5: Dispersion diagram for a periodic structure. The three dipole passbands with the lowest frequencies are given. On the TM_{110} curve, the symbols correspond to the modes for which the field distribution is shown in Fig. 3.4. The dashed lines represent the velocity of light.

The group velocity gives the velocity of the energy flow in the structure. For a non-periodic structure, instead of the group velocity, one can define an analogue function which depends on the position along the resonator.

The beam excites mainly modes which are synchronous to the beam, i.e. modes with the phase velocity equal to the light velocity. The curve corresponding to the light velocity is represented in Fig. 3.5, folded to the phase range between 0 and π.

The coupling between the wave and the charged beam is controlled by an appropriate design of the cavity shape. This coupling is described by the *loss factor*, k_l, which is characteristic for each mode l. The *quality factor* Q_l, describes the energy losses of mode l in the cavity walls. These parameters are defined analytically in the following way:

$$k_l = \frac{|V_l|^2}{4W_l}, \qquad Q_l = \frac{\omega_l W_l}{P_l}, \tag{3.11}$$

where V_l is the voltage corresponding to mode l, W_l is the energy stored in the electromagnetic field of the mode and P_l the power dissipated in the walls. Low losses imply a high Q. These losses may be reduced by choosing a material with high conductivity, for example a superconducting one, like in the case of the TESLA cavities.

The parameter R/Q is often used, which is related to the loss factor through the equation:

$$\left(\frac{R}{Q}\right)_l = \frac{4k_l}{\omega_l}, \tag{3.12}$$

where R is the shunt impedance.

3.3 Wake Fields and Wake Potentials

When a charged particle travels through a perfectly conducting cylindrical pipe, as is approximately the case in an accelerator, the electromagnetic field lines move together with the particle [23, 24]. This is illustrated in Fig. 3.6 (left) for the case of a bunch with Gaussian charge distribution. When the geometry of the walls changes, the wall currents can not keep up with the bunch (middle in the figure). A part of the electromagnetic field generated by the charge remains behind. When the beam tube narrows again (right), reflections of the field may occur. This constitutes the so-called *wake fields* [24, 25]. Another charge following the first one interacts with these fields, leading to a change in its energy or an orbit deflection. Wake fields occur also without geometrical change, when the walls have a finite resistivity.

3.3.1 Short range wake fields

In this section, we concentrate on single bunches. The dynamics of a bunch train will be discussed in the next section.

A point-like charge q at the longitudinal position s along the design trajectory and at the transverse position $\vec{r}_1$ generates at the distance ζ behind it and at the transverse

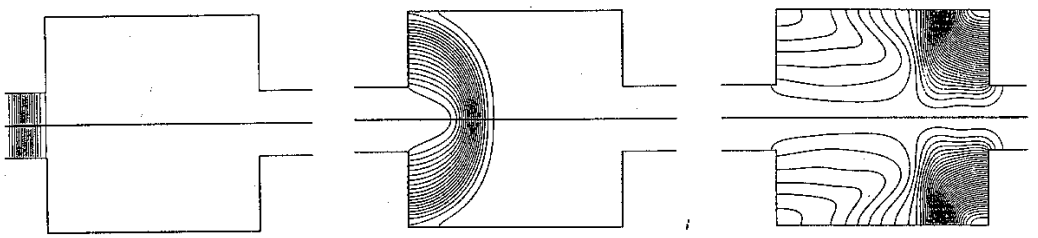

Figure 3.6: Wake field generation when a Gaussian bunch passes a change in geometry in the vacuum pipe. Three moments in time are shown.

offset $\vec{r}_2$ the longitudinal *delta-function wake potential*, also simply called the *delta wake* [24]:

$$W_{\parallel}^{\delta}(\vec{r}_1, \vec{r}_2, \zeta) = \frac{1}{q} \int_{-\infty}^{\infty} E_z(\vec{r}_1, \vec{r}_2, \zeta, t = (\zeta + s)/c)\, ds, \tag{3.13}$$

where E_z is the longitudinal component of the electric field generated by the charge q, and c the velocity of light. The particle is assumed to have the velocity c.

The *wake potential* of a bunch with a longitudinal charge distribution, $\lambda(\zeta)$, can be derived from the delta wake by:

$$W_{\parallel}(\zeta) = \int_0^{\zeta} \lambda(\zeta_0) W_{\parallel}^{\delta}(\zeta - \zeta_0) d\zeta_0, \tag{3.14}$$

where ζ_0 is the longitudinal coordinate of the generating charge with respect to the beginning of the bunch (see below) and ζ is the location where the wake is calculated. $W_{\parallel}$ and $W_{\parallel}^{\delta}$ are measured in units of V/C. Here the wake potential was calculated at the same radial position as the generating charge: $\vec{r}_2 = \vec{r}_1$.

The longitudinal particle distribution of a bunch is characterized by the standard deviation, σ_z. For ultra-relativistic particles the relative longitudinal motion is "frozen" within the bunch, since the velocity is equal to c. In this case one can divide the bunch longitudinally into *slices*. The bunch is considered to start at position 0, neglecting the particles that come earlier. This fact was assumed in writing eq. 3.14. One can then successively add the effect of the wake fields generated by all previous slices. For Gaussian bunches, with $\lambda(\zeta) = 1/(\sqrt{2\pi}\sigma_z) \exp(-\zeta^2/2\sigma_z^2)$ (see Fig. 3.7), the beginning of the bunch may be considered to be at 4 or 5 σ_z ahead of the bunch center.

The transverse wake potential can be determined from the longitudinal one by using the Panofsky-Wenzel theorem:

$$\frac{\partial}{\partial \zeta} \vec{W}_{\perp}(\vec{r}, \zeta) = -\nabla W_{\parallel}(\vec{r}, \zeta) \cdot \vec{e}_{\perp}. \tag{3.15}$$

For rotationally symmetric structures and small particle offsets, the main contribution to the transverse wake fields is given by the dipole wakes, but there are also higher order contributions, such as from quadrupole wakes.

The wake potential can be calculated by means of numerical simulations. One can determine the wake of a bunch if it is not too short. The shorter the bunch, the longer is

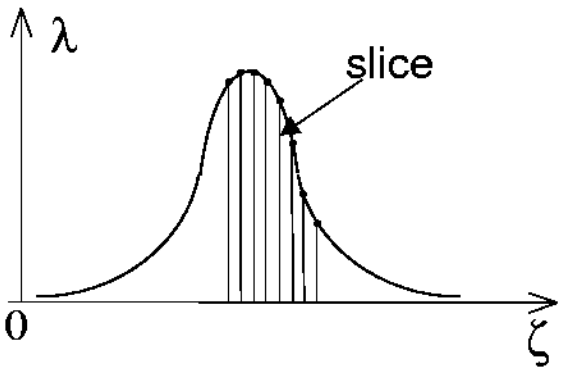

Figure 3.7: Longitudinal division into slices of a bunch with Gaussian charge distribution.

the required computation time, since one has to model the structure with a finer grid. Starting from the wake potential of a very short Gaussian bunch, one can calculate the wake potential of a longer Gaussian bunch, by convolution [26].

An example of an wake potential is given in Fig. 3.8. A Gaussian bunch with a length σ_z of 0.3 mm has been considered. The dipole wake field excited by this bunch in a 6 m long accelerating structure of the S-Band Linear Collider, described in Chapter 2, was computed in the time domain with the help of the MAFIA code (see [26], p. 50). It can be seen that the wake fields are damped relatively fast, apparently influencing only the particles in the generating bunch. The effect on a long time scale is described in the next chapter.

3.3.2 Long range wake fields. Higher Order Modes

The basic considerations of the previous section are also valid for the multi-bunch dynamics. Only the method of calculating the wakes is usually different.

The calculation of wake field in the time domain far behind a bunch requires significantly increased computational efforts. Therefore a frequency domain method is usually preferred. First, the resonant modes are calculated with the help of numerical codes. Although only one mode is excited by the RF power source and used for acceleration , *higher order modes* (HOMs) can be excited inside a cavity by the beam itself. These will oscillate in the structure with an amplitude determined by the loss factor of the mode and with a damping time given by the quality factor of the mode (see section 3.2). The longitudinal wake potential is obtained by summing the contributions of the individual modes:

$$W_{\parallel}^{\delta}(\zeta) = \begin{cases} \sum_l 2\,k_{\parallel l} \cos\left(\omega_l \frac{\zeta}{c}\right) \exp\left(-\frac{\omega_l}{2Q_l}\frac{\zeta}{c}\right), & \text{for} \quad \zeta > 0, \\ \sum_l k_{\parallel l}, & \text{for} \quad \zeta = 0 \quad \text{and} \\ 0, & \text{for} \quad \zeta < 0. \end{cases} \tag{3.16}$$

Here l is the index of the modes with longitudinal component of the electric field on

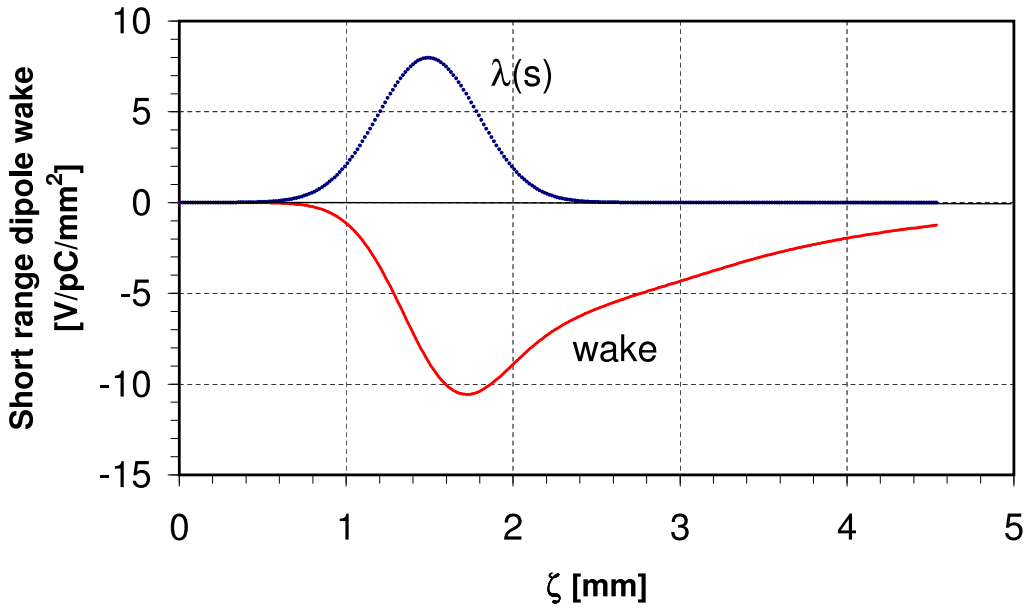

Figure 3.8: The short range wake potential (lower curve) excited by a Gaussian bunch (upper curve) with 0.3 mm rms length in an SBLC accelerating structure. The bunch moves to the left.

the axis.

For modes with higher azimuthal order (dipole, quadrupole etc.), the loss factor depends on the offset of the exciting particle. In the case of cylindrically symmetric structures, the loss factors for dipole modes are proportional to the square of the bunch offset for small offsets from the axis. This is due to the fact that the potential V_l depends linearly on the offset a where it is calculated, for small a. For quadrupole modes, the loss factor depends on the 4th power of the offset [24]. Therefore one uses a normalized transverse loss factor, $k_\perp^n$, that is independent of the offset. For a dipole mode it is given by:

$$k_{\perp l}^n = \frac{|V_l|^2}{4\,W_l\,a^2}. \tag{3.17}$$

$k_{\perp l}^n$ has units of V/Cm^2. The main contribution to the transverse wake potential is given by the dipole modes. The dipole delta wake, also normalized to a^2 is given by:

$$W_\perp^{n\delta}(\zeta) = \sum_l 2k_{\perp l}^n \frac{c}{\omega_l} \sin\left(\omega_l \frac{\zeta}{c}\right) \exp\left(-\frac{\omega_l}{2Q_l}\frac{\zeta}{c}\right), \quad \text{for } \zeta > 0. \tag{3.18}$$

In practice, the resonant modes are calculated up to a certain frequency. The error made by neglecting the modes with higher indexes is usually not large, since they have often low loss factors. But one has to be careful, since it has already been proved, both by calculations and by measurements, that some modes of higher frequencies may also have high loss factors (see section 5.3.2). Also, when going to very high frequencies, one comes in the short wake range.

In Fig. 3.9.a, the contribution to the dipole delta wake from the first dipole passband of the 6 m long accelerating structure of the SBLC is shown [3]. This was calculated using eq. 3.18. The resonant modes were obtained using the code MAFIA [27]. All modes are considered to have a quality factor of 15000 (undamped modes: Q is given by the losses in the copper walls of the structure). It can be seen that at the beginning the amplitude of the wake decreases, due to the decoherence of many modes, but after a re-coherence time it increases again. The re-coherence time is given by the mode spacing in this passband, which is about 2.5 MHz. In Fig. 3.9.b the wake for the first 5 m behind the exciting particle is shown. The location of several bunches is depicted, as foreseen for the SBLC. The bunches at 1.8, 3.6, 5.4 m etc. behind the generating one, see almost no field, being close to a zero of the wake envelope[2]. However, in the real structure, due to fabrication tolerances, the frequencies of the modes vary slightly (with about 1 MHz rms) so that the position of the zero of the wake is shifted. For a complete picture of the wake fields in the SBLC structure, one has to take into account the contribution of other passbands as well.

In this thesis I will deal only with wake fields generated by non-uniformities in the beam environment, in particular by the accelerating structures, giving the main contribution in the main linacs of a future linear collider. Apart from this, there are also wake fields caused by the resistivity of the walls [28]. A recently discovered wake is due to the surface roughness of the beam pipes [29]. This is the main contribution in an undulator, where very short bunches are used.

3.4 Wake Field Influence on the Beam Properties

The transverse motion of the particles in an accelerator in the presence of wake fields is governed by the equation [25]:

$$\frac{d}{ds}\left(\gamma(s,\zeta)\frac{dx}{ds}\right) + K_x(s,\zeta)\,\gamma(s,\zeta)\,x(s,\zeta) = -\frac{e^2}{m_0c^2}\int_0^{\zeta} \lambda(\zeta_0)\,W_\perp^{n\delta}(\zeta-\zeta_0)\,x(s,\zeta_0)\,d\zeta_0. \quad (3.19)$$

It is assumed that the particle has the nominal energy. From this equation one can determine the transverse motion of the bunches in the presence of the wake fields.

3.4.1 Short range effects

The longitudinal short range wakes lead to a change in the energy of each slice, depending on its position in the bunch. In this way the energy spread of a bunch is usually increasing. The transverse wake fields lead to a deflection of the slices with respect to the previous ones, so that the bunch is deformed. From the combined effects of the wake fields and the betatron oscillation, the bunch may have a so-called

[2]Nevertheless, this was not a design strategy.

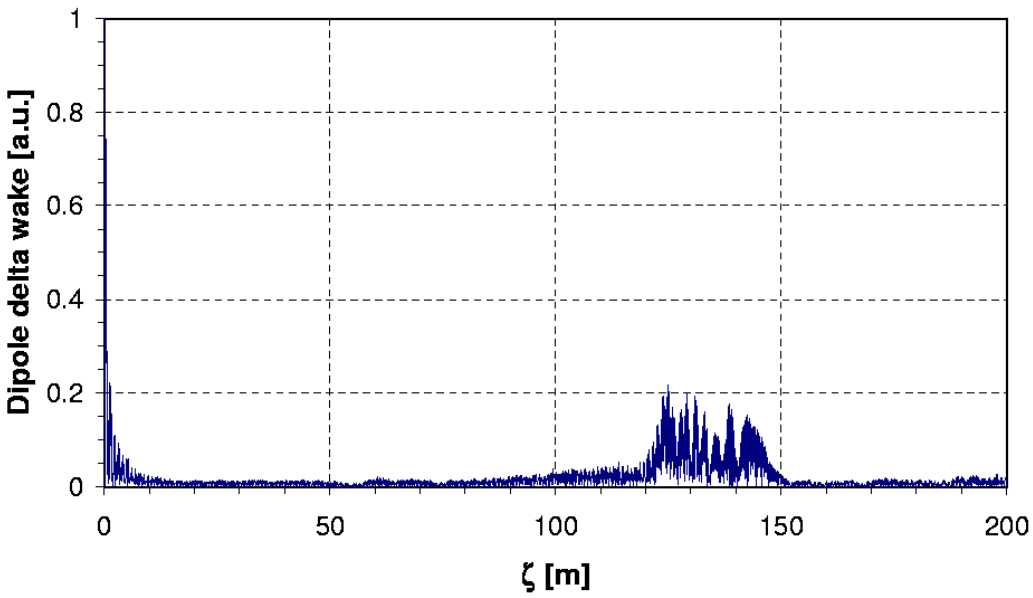

a.

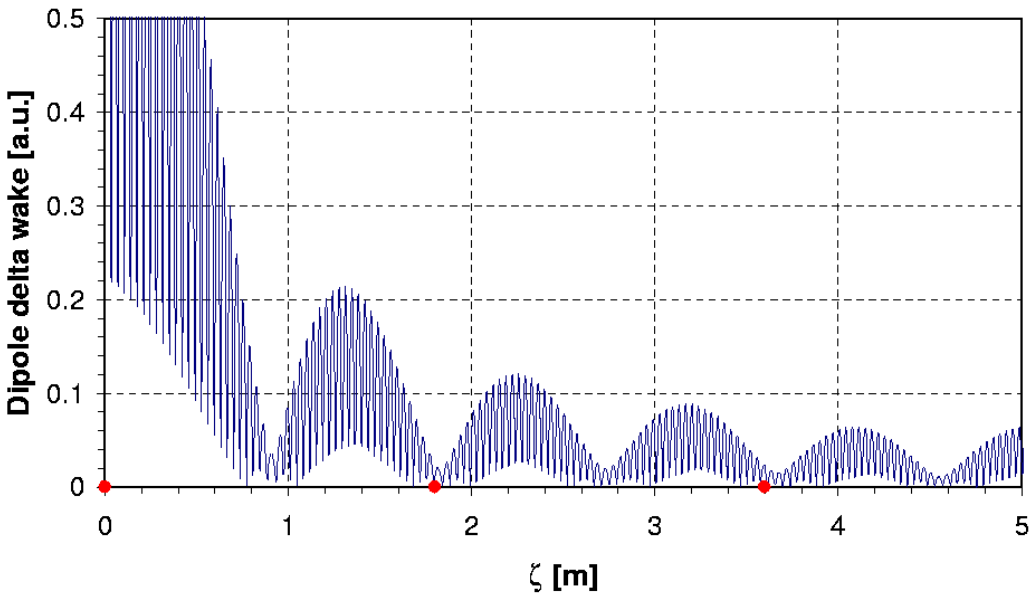

b.

Figure 3.9: In the upper plot, the long range dipole wake (envelope) for the SBLC structure given by the modes of the first dipole passband is shown. The modes are considered to be undamped ($Q = 15000$). The wake is normalized to the maximum value ($1.3 \cdot 10^{16}$ V/Cm^2). The generating bunch is in the origin of the time axis. The bottom plot depicts a detail for the first 5 m behind the generating particle. The position in time of several bunches, as designed for the SBLC (1.8 m spacing), is marked with black dots.

"banana" shape, particularly in long accelerators [30]. This leads to the deterioration of the transverse emittance, and to a decrease in luminosity.

As an example, in Fig. 3.10 the offsets of the slices of a bunch are shown after tracking through the main linac of the SBLC. The bunch is divided longitudinally into 31 slices and has an initial offset of 50 μm. The dipole wake shown in Fig. 3.8 has been used in the simulations. It has been assumed that no monopole wake is excited. The main parameters of the bunch and of the accelerating sections used in the simulations are given in Table 3.1 and correspond to the SBLC design values.

Gradient	[MeV/m]	17
Bunch charge	[nC]	1.8
Bunch length σ_z	[mm]	0.3
Initial energy	[GeV]	3.15
Final energy	[GeV]	250

Table 3.1: Parameters used in the simulations shown in Figs. 3.10 and 3.11.

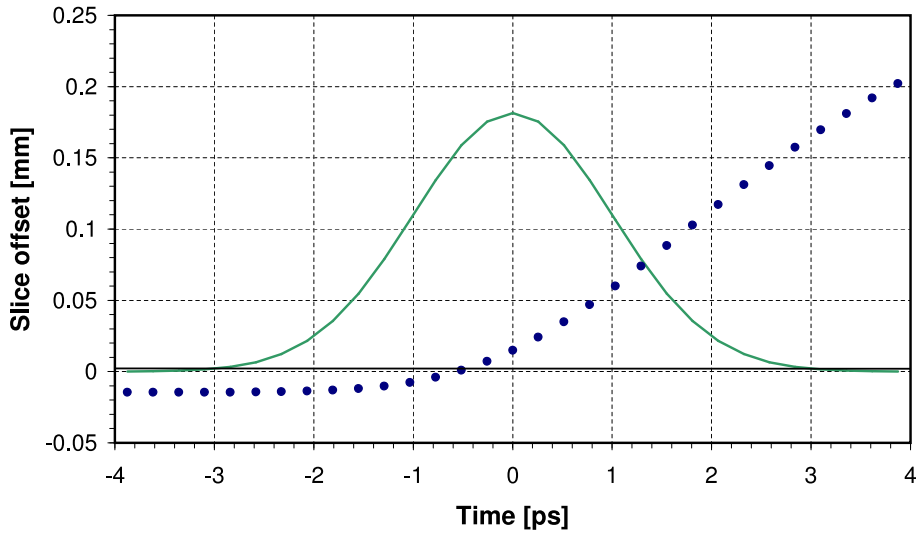

Figure 3.10: The offsets of the slices of a bunch at the end of the SBLC main linac. The initial offset of the bunch is 50 μm.

The "banana" shape mentioned above can be seen in the figure. The rms transverse beam size is 75 μm, which is about 8 times larger than the required one for the vertical plane. In Fig. 3.11 the increase in vertical emittance of the bunch along the linac is shown. An initial emittance of 0.2 mm·mrad is assumed, which is the value delivered by the damping ring (see section 2.1). The normalized emittance increases to about 4 mm·mrad, which is unacceptably large for the linear collider. Therefore a method to decrease this value has to be applied.

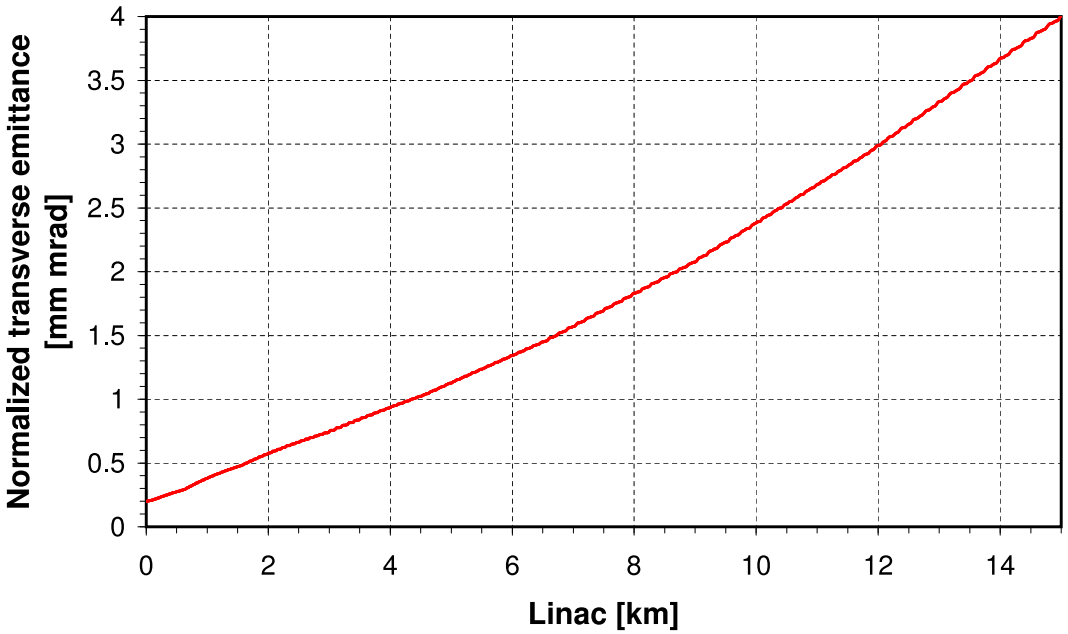

Figure 3.11: The vertical emittance along the main linac. An initial emittance of 0.2 mm·mrad has been assumed.

Method to reduce the effects of short range wake fields

A correction technique was devised by Balakin, Novokhatski and Smirnov [31], which is called *BNS damping*. If a bunch has a correlated energy distribution, then the various slices of the bunch are differently focused by the quadrupoles, which may lead to an emittance increase. This chromatic effect was neglected in the previous simulations. Since the dipole wake fields and the quadrupole effects have a similar behavior, by inducing a proper energy distribution along the bunch, the two effects can cancel each other.

BNS damping is achieved either with the help of a radio-frequency quadrupole, or by letting the tail of the bunch acquire less energy by choosing an appropriate phase in the accelerating sections. In the case of the SBLC a correlated energy distribution is induced by the longitudinal wake fields. In this way a big part of the effects of dipole wakes can be eliminated.

3.4.2 Long range effects

On a long time scale, the wakes induced by one bunch influence the following bunches. This is mainly of concern for beam dynamics in the transverse planes.

A wake is excited by each bunch of a train, leading to a deflection of the following bunches from the axis. Depending on the beam current and on the properties of the transverse modes, the deflection may increase along the accelerator and also towards the end of the bunch train, leading to the loss of the tail of the train. This is the so-called *beam break-up* (BBU) effect, first observed at the SLAC two-mile accelerator [32, 33].

To give an example for this phenomenon, the multi-bunch beam dynamics in the SBLC main linac has been simulated. The linac is structured in 8 sections, each being composed of FODO cells. The first section contains two accelerating structures per FODO cell, the second four and so on up to the eighth section with 16 structures per cell. The quadrupoles and RF structures are considered to be perfectly aligned. It is assumed that only the modes of the first dipole passband are excited. The modes are assumed to be undamped (quality factor of 15000) giving the long range wake shown in Figs. 3.9.

The bunches are treated as point charges and enter the linac with an offset of 50 μm. The main parameters used in the simulations are given in Table 3.1. The 333 bunches have a 6 ns spacing.

In Fig. 3.12 the bunch offsets at the end of the main linac are shown. The offsets increase towards the tail of the bunch train, reaching values of over 1 mm. A different illustration of the BBU effect can be seen in Fig. 3.13, where the evolution of the normalized multi-bunch emittance along the linac shows an exponential increase. The emittance at the end exceeds by far the maximum allowed vertical normalized emittance of a single bunch at the IP of 0.25 mm·mrad.

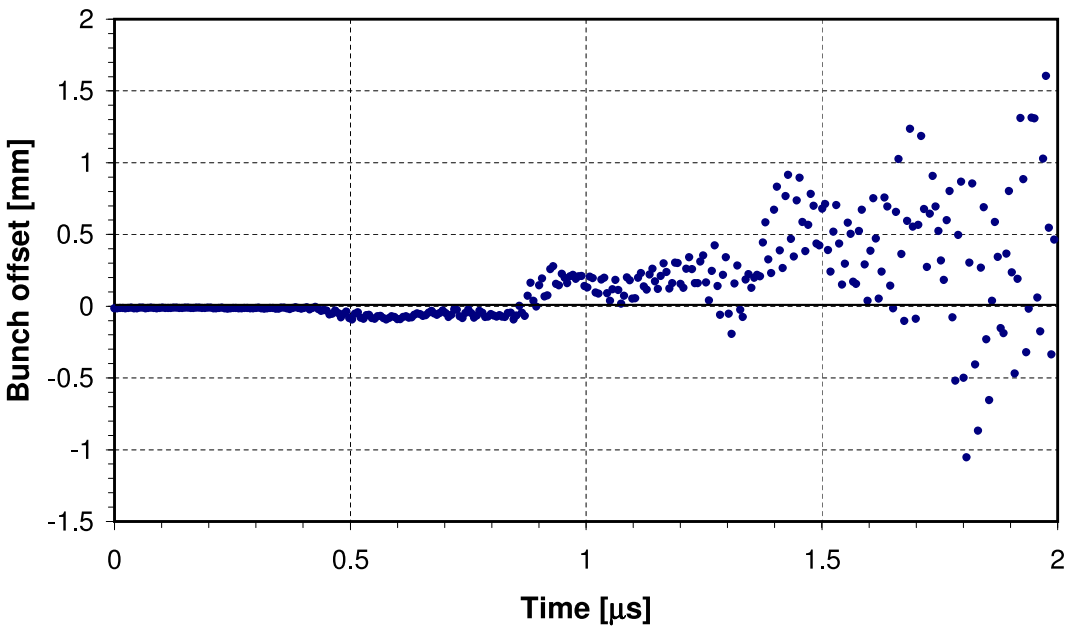

Figure 3.12: Bunch offsets at the end of the SBLC main linac. The initial transverse position of bunches is 50 μm. The structures are assumed to be perfectly aligned. The HOMs are undamped ($Q = 15000$).

In Figs. 3.14 and 3.15 the trajectories along the linac of the first and of the 321st bunch are shown. In the first plot, the envelope of the first bunch trajectory is drawn as well. The bunch executes betatron oscillations, whose amplitude is damped due to the increasing energy. One can also recognize the first steps between the 8 sections of the accelerators [3]. For the 321st bunch (Fig. 3.15) the contribution of the wake fields is dominant, leading to an increase of the bunch offset at the linac end.

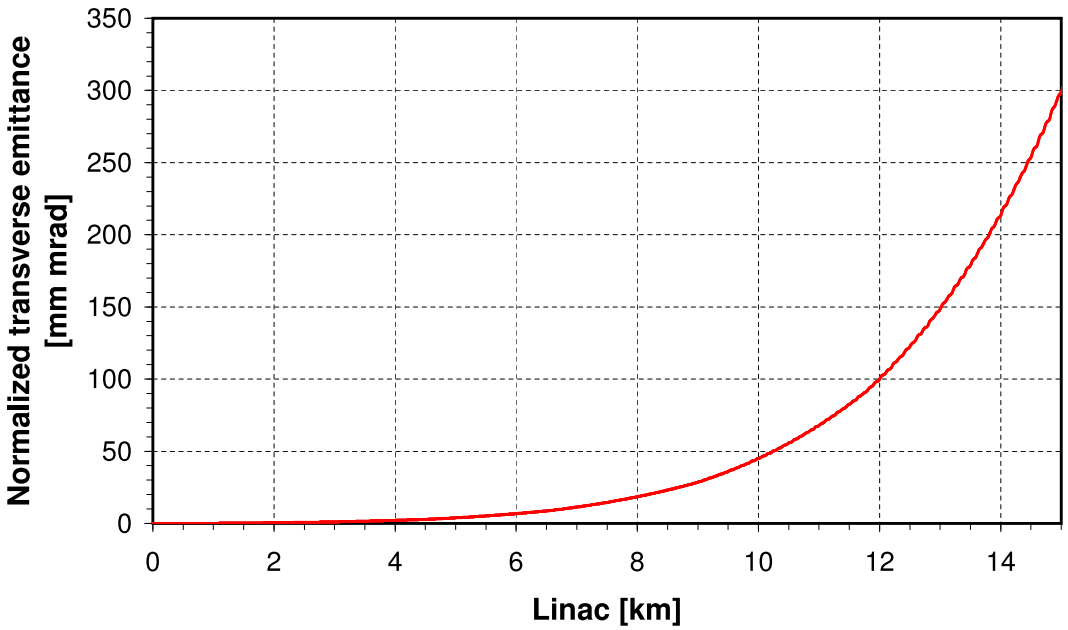

Figure 3.13: The multi-bunch emittance along the SBLC main linac. The structures are assumed to be perfectly aligned. The HOMs are undamped ($Q = 15000$).

The bunch offsets and multi-bunch emittance as obtained from these simulations may lead to the situation that positron and electron bunches do not meet at the interaction point. Therefore one has to take measures to reduce the effect of the wakes.

Techniques to decrease the effects of long range wake fields

The design of the accelerating structures aims to minimize the loss factors of HOMs and avoid trapped modes, which are confined in a section of the whole structure. Using numerical simulations one can obtain the frequencies of the modes of a cavity and the corresponding loss factors. Although a lot of progress has been made in this field, it is still a very difficult task to control so many modes in the quite complex resonators.

Moreover, one can *damp* the HOMs, i.e reduce their quality factors and therefore the time they oscillate in the cavity. One way to do this is to use special antennae, called *HOM couplers*, to extract the energy of the wake fields out of the resonators. The TESLA cavity is equipped with HOM couplers on both sides (see chapter 5). For normal-conducting structures one can use waveguide-like HOM couplers at more cells. At CERN, SLAC and KEK complex structures are developed (in the S- and C-band) that extract the HOM energy all along the structure [34, 35, 36]. Another way of damping the HOMs is to use *absorbing materials*. For the SBLC structure a layer of 10 to 20 μm stainless steel or Kanthal was planned to be applied on the tip of each iris. According to simulation, by this method all modes of the first dipole passband can be damped below Q = 4000 [49].

Another technique is to induce a spread in the frequency of the transverse modes in the individual cells of an accelerating section. This *cell-to-cell detuning* occurs automat-

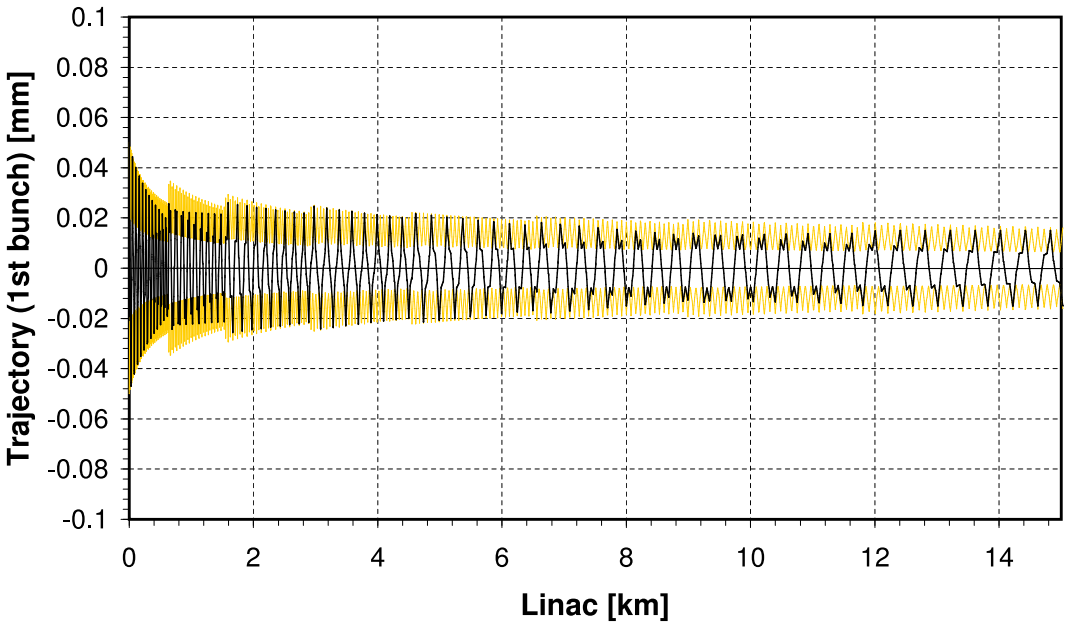

Figure 3.14: Trajectory of the first bunch in the train (solid line). This bunch is not affected by wake fields. The dashed line represents the beam envelope.

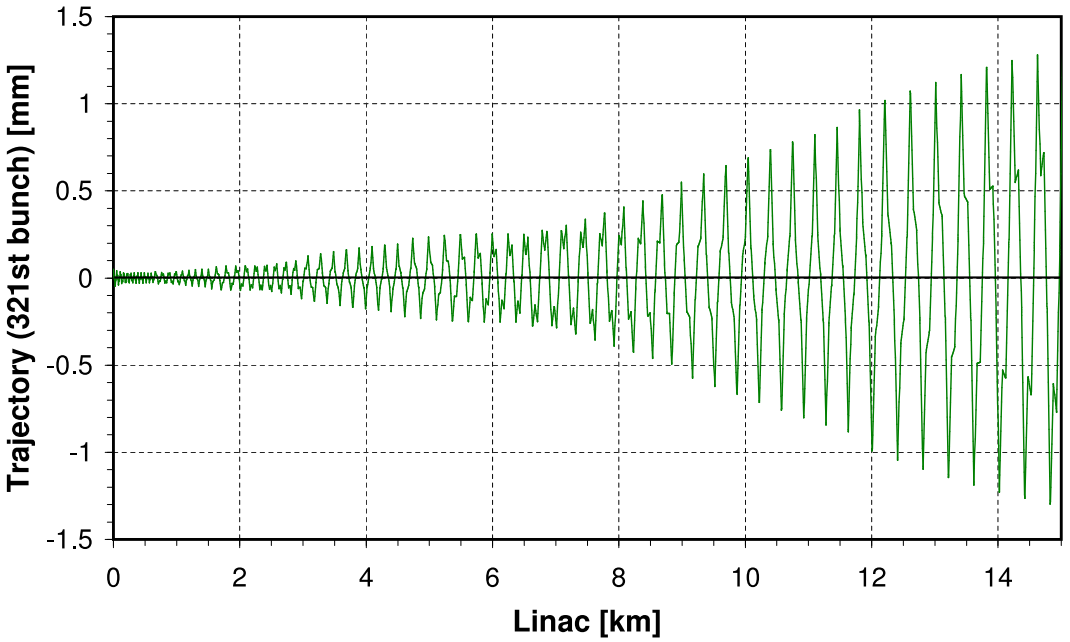

Figure 3.15: Trajectory of the 321st bunch in the train. The bunch is strongly affected by the wakes generated by all previous bunches.

ically in constant-gradient accelerating structures, where the diameter of the cells and of the irises decreases in such a way that the resonance frequency of the accelerating mode stays constant. At the same time, the amplitude of the electric field of the traveling wave is constant in all cells. On the other hand, the HOM frequencies increase toward the last cell, and as a result they can not add coherently along the structure. The disadvantage of this procedure is that many modes are now trapped within various sections of the accelerating structure, which makes their damping more difficult (see section 4.2). Detuning can be also applied from *cavity to cavity*, by slight deformation. Both detuning techniques are used for the SBLC structure, while only the second one is employed for the TESLA cavities. For the TESLA cavities one aims to avoid trapped modes inside the structure, through a slight asymmetry of the end cells.

In addition to the active methods described above, the misalignments of the accelerating structures reduces the effects of the wake fields. The misalignment tolerance for the SBLC structures is 50 μm, while for TESLA it is 500 μm.

Due to ground motion, the positions of the structures drift in time. This can be compensated by feedback systems. After longer periods of time, realignment of the structures has to be performed. For the SBLC an active structure alignment method was also foreseen, in order to minimize the excitation of HOMs. This method is based on using the signals from two symmetric HOM wave-guide pick-ups.

An illustration of the effectiveness of the above mentioned techniques for the SBLC case, is shown in Fig. 3.17. The accelerating structures are assumed to be damped, with all modes of the first dipole passband having $Q = 4000$. Ten different types of structures are assumed, having slightly different frequencies for each mode. They are randomly distributed in the linac. The frequency spread assumed is 0.4 % rms. The structures have a misalignment of 50 μm rms. The bunch train has an initial transverse offset of 50 μm. The other parameters of the linac and of the beam are the same as in the previous simulations. The transverse positions of the bunches at the end of the linac are shown in Fig. 3.16. The offsets are now below 25 μm. After about 1.3 μs a steady state is reached. In Fig. 3.17 the multi-bunch emittance increase in the linac is shown. The emittance at the end of the linac represents about 3 % of the single bunch emittance (0.25 mm·mrad), which is negligible. The damping and detuning of the modes lead to a very good beam quality.

3.4.3 Wake field measurements

In the case of long range wake fields, the properties of the individual modes are usually studied. The frequency and quality factors of each resonant field can be determined, for example, by measuring the scattering matrix (also referred to as S parameters) between two ports, with the help of a network analyzer [37]. This matrix gives the relationship between the waves going into and out of an RF structure through its ports. The frequency and quality factor of each resonance can be directly measured from the S11 (reflection) or S12 (transmission) curve. The quality factor is given by the resonance

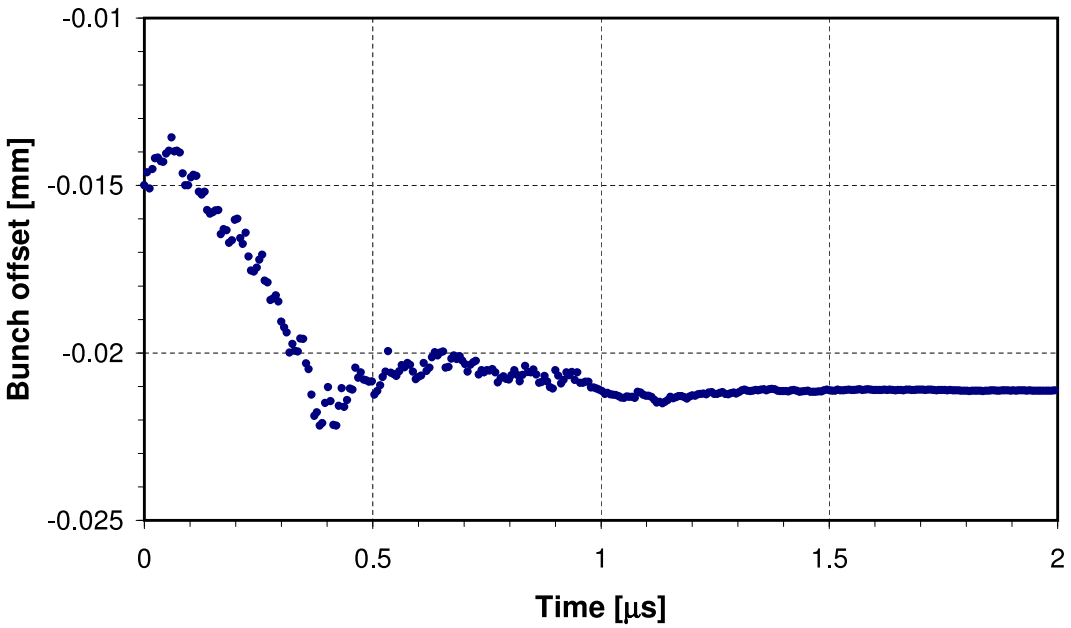

Figure 3.16: Transverse bunch positions at the end of the SBLC main linac. The transverse position of bunches at the beginning of the linac is 50 μm. The accelerating structures are assumed to be misaligned with 50 μm rms. They are also detuned, having a spread in frequency of 0.4 % rms. The HOMs are damped ($Q = 4000$).

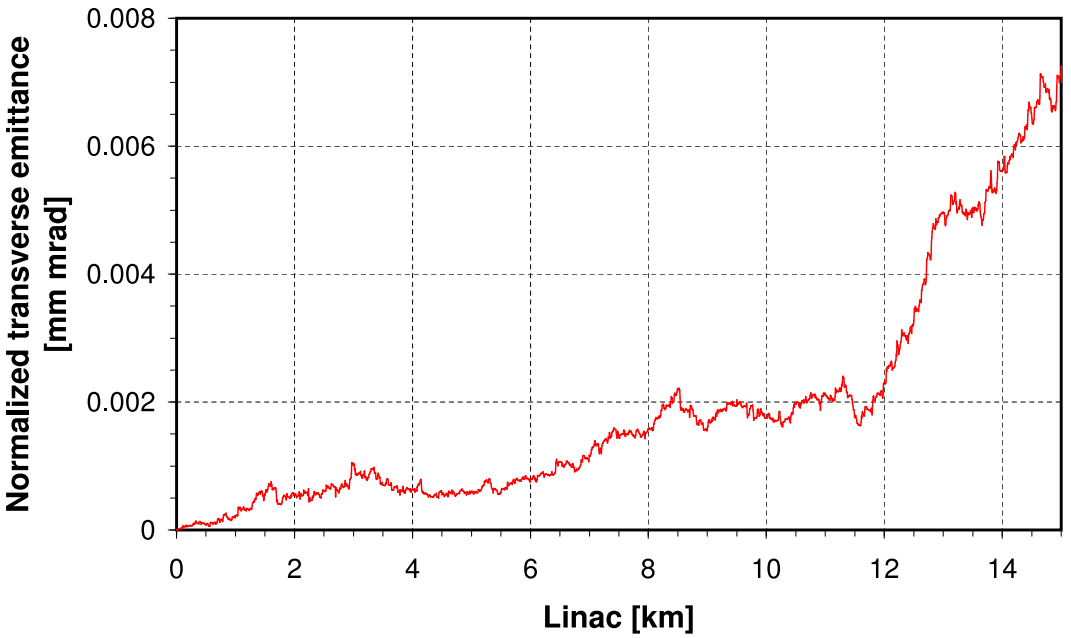

Figure 3.17: The multi-bunch emittance along the SBLC main linac. The accelerating structures are assumed to be misaligned with 50 μm rms. They are also detuned, having a spread in frequency of 0.4 % rms. The HOMs are damped ($Q = 4000$).

frequency ω and the full width at half maximum (FWHM) $\Delta\omega$ [38]:

$$Q = \frac{\omega}{\Delta\omega}. \tag{3.20}$$

The loss factor can be measured with more complex techniques. The bead-pull technique [38, 39] is based on measuring the detuning induced by a small metallic or dielectric bead. The bead is pulled through the structure by help of a thread causing a small perturbation. The field distribution along a structure can be determined. Another method is to send a current pulse through a wire placed inside the structure and compare it to the case of a reference object [39, 40]. This is the so called coaxial wire method. The loss factors can be determined from simulations that nowadays give quite accurate values.

HOMs can be excited also with the help of a bunch or a bunch train. One measures, in this case with a spectrum analyzer, the signal that couples out of the structure through HOM couplers, and get the frequency and quality factors of the modes. One can also measure the influence of wake fields on the beam with beam position monitors (BPM). From this, the loss factor can be determined. Measurements aiming to study HOMs using a beam are described in chapters 4 and 5.

A technique was developed at SLAC that enables the measurement of the wake field directly in time domain [41]. An Accelerator Structure Setup (ASSET) has been incorporated into the SLC. In this setup, a drive electron bunch goes off-axis through an accelerating structure, exciting a wake field. A test positron bunch travels on axis through the structure and is deflected by the wake field. Its offset is measured at a BPM behind the structure. The position in time of the test bunch with respect to the drive bunch can be varied to determine the temporal dependence of the transverse wake field.

Chapter 4

Higher Order Modes in the S-Band Accelerating Structure

The S-Band Test Facility (SBTF) was built in order to test various components of a high energy S-Band Linear Collider such as the thermionic gun, the 150 MW klystrons, modulators etc. One of the main parts is the accelerating structure. The studies made at the test facility on the long range wake fields, are presented in this chapter.

4.1 The S-Band Test Facility

The layout of the SBTF is shown schematically in Fig. 4.1 [42, 43]. The electron beam is generated by a thermionic gun. The pulses are compressed longitudinally by two standing wave sub-harmonic bunchers, working with 125 MHz and 500 MHz, as well as two S-band traveling wave structures. The beam energy is increased to about 100 MeV in a first 5 m long accelerating structure. This structure is similar to the ones used for Linac II, the electron injector linac for the DESY circular accelerators. The two next accelerating structures, specially designed for the SBLC, increase the electron energy to 300 MeV. The first and the second structures are fed through a power splitter by the same klystron [44], while a second klystron feeds the third one. Quadrupole triplets are placed after each accelerating structure. The beam is analyzed with the help of a spectrometer and then it is sent to a dump. The correctors, screens and bunch position monitors are not shown in the figure.

4.2 Accelerating Structure Design

4.2.1 The S-band structure

The second and third accelerating structures installed in the SBTF are identical to the ones foreseen for the SBLC, except for some minor details that will be mentioned later. The structures are based on the experience with the 3 m long 3 GHz structures used at

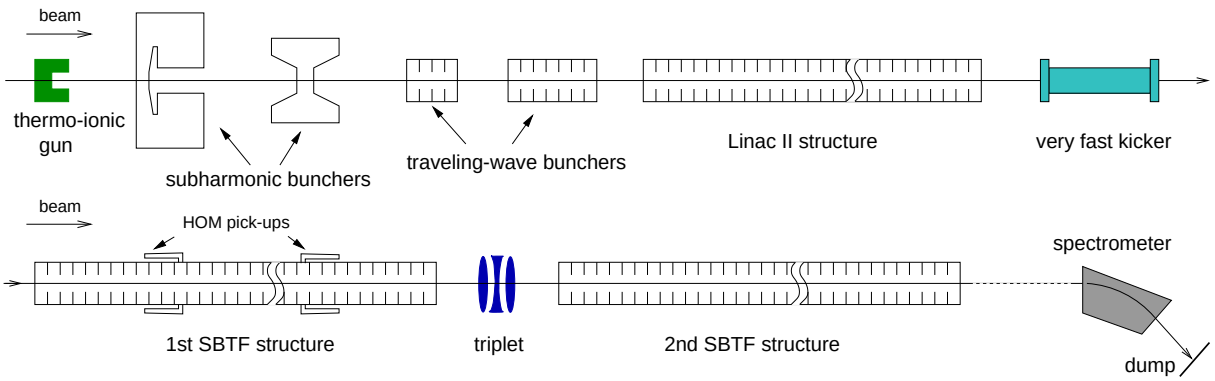

Figure 4.1: The SBTF layout.

SLAC [1]. The SBLC structure is a 6 m long normal conducting disk-loaded waveguide working in the $2\pi/3$ mode. In comparison to the structure of the Stanford linac, the length was increased to reduce the number of input couplers and simplify the power distribution system. On the other hand, the structure length is limited by the losses in the walls. For the SBLC structure, it was considered acceptable that at least one third of the power fed into the section reach the end of the section. Each of the 180 cells is 33 mm long, implying a wavelength of the accelerating mode $\lambda = c/f = 100$ mm. The cell and iris radii are tapered along the structure such that the gradient is constant while energy is transfered to the beam. The main characteristics of the SBLC structure are summarized in Table 4.1. The shunt impedance per unit length is defined as the square of the accelerating electrical field over the fraction of the input power lost per unit length in the structure walls. For a tapered section the shunt impedance varies with the cell number. The average shunt impedance is 53 $M\Omega/m$.

Special attention was given to reducing the wake fields. A symmetrical input coupler is used. The power is absorbed in the last eight cells of the structure by an integrated load, instead of the usual output coupler. The load consists of a layer of 0.1 mm thick Kanthal.

The tapering of the structure introduces a spread of the HOM frequencies along the structure. The dispersion diagram of this structure is given in Fig. 4.2 [3]. The simulation of the passbands of a long structure with different cell dimensions means a large numerical effort. Therefore dispersion curves are calculated for each cell with periodic boundary conditions. This method is justified by the small differences between neighboring cells. This procedure has been applied here. The lower and the upper curves for each passband correspond to the first and last cell or vice versa. Due to the large number of cells, the passband is quasi-continuous. A mode with a given frequency moves from one curve to another when propagating along the structure, changing the phase advance per cell.

Let us have a look at the sixth passband, at a given frequency above 9 GHz. A mode excited in the first cell (lower curve) propagates along the structure, changing its phase advance per cell, until it reaches the last cell (upper curve). In contrast, a mode in the first passband, excited in a certain cell, having a phase advance per cell close to zero

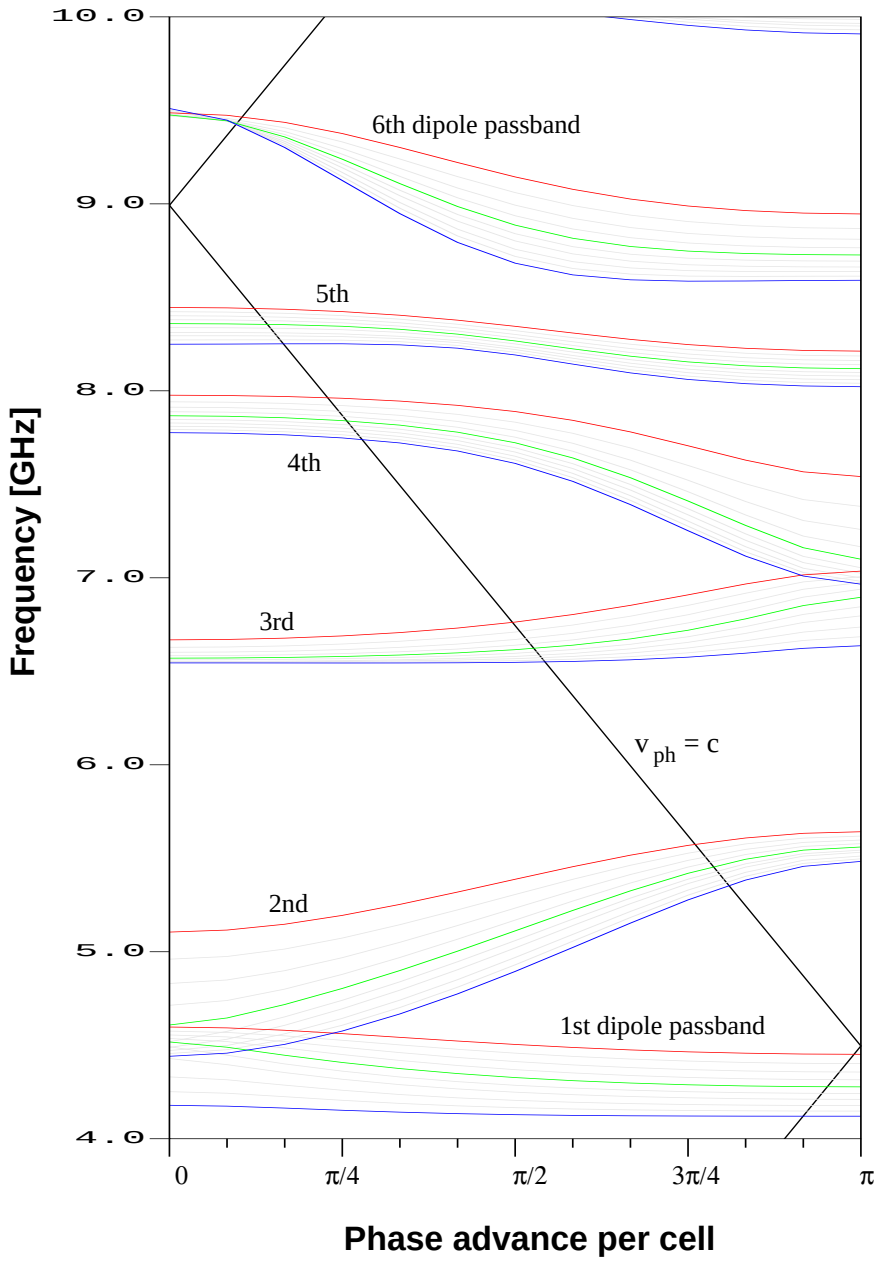

Figure 4.2: The dispersion diagram for dipole modes of the SBLC structure [3]. A curve is drawn for each cell, when taking periodic boundary conditions. The curves for each type of field distribution form a passband. The line represents the light velocity. The modes found at its intersection with the passbands have a phase velocity of c and can be therefore excited stronger by a ultra-relativistic beam.

(left in the figure) propagates toward the end of the structure. After a number of cells it has a phase advance of π and is reflected back. This is a trapped mode, that does not reach one of the end cells. It can be seen in the diagram that most of the modes in the first passband are trapped, as well as some modes in the third passband.

Examples of such trapped modes are given in Fig. 4.3 [27]. The field amplitude along the structure is represented. For each mode, the variation of the phase advance per cell from almost zero (left) to π can be observed. (The phase advance π is characterized by equal amplitudes with opposite signs in adjacent cells.)

The frequencies and loss factors of the modes of several passbands have been calculated by various methods, such as the mode matching technique and a double-band coupled oscillator model [46, 47, 48, 49]. The results are in good agreement with each other. The loss parameters of the modes of the first, third and sixth dipole passbands obtained in [49] are plotted in Fig. 4.4. These passbands give the main contribution to the transverse long range wake field [27]. The loss factors in the first passband are shown in more detail in Fig. 4.5. While the level of the loss factors in the first passband is about $4 \cdot 10^{15}$ V/Cm^2, in the sixth passband some modes reach $7 \cdot 10^{16}$ V/Cm^2 [48]. The wake field obtained with these modes of the first dipole passband, under the assumption that the modes are not damped ($Q = 15000$), is shown in Fig. 3.9.

Accelerating mode		$2\pi/3$
Frequency	[GHz]	2.998
Loss factor	[V/pC]	111
Quality factor		14000
Wavelength	[m]	0.1
Structure type		constant-gradient
Length	[m]	6
Cell length	[mm]	33.34
Number of cells		180
Attenuation		0.55
Cell radius		
- first cell	[mm]	41.358
- last cell	[mm]	39.992
Iris radius		
- first cell	[mm]	15.388
- last cell	[mm]	10.893
Group velocity		
- first cell	[% of c]	4.1
- last cell	[% of c]	1.3
Shunt impedance		
- first cell	[MΩ/m]	45
- last cell	[MΩ/m]	61

Table 4.1: Main characteristics of the SBLC accelerating structures.

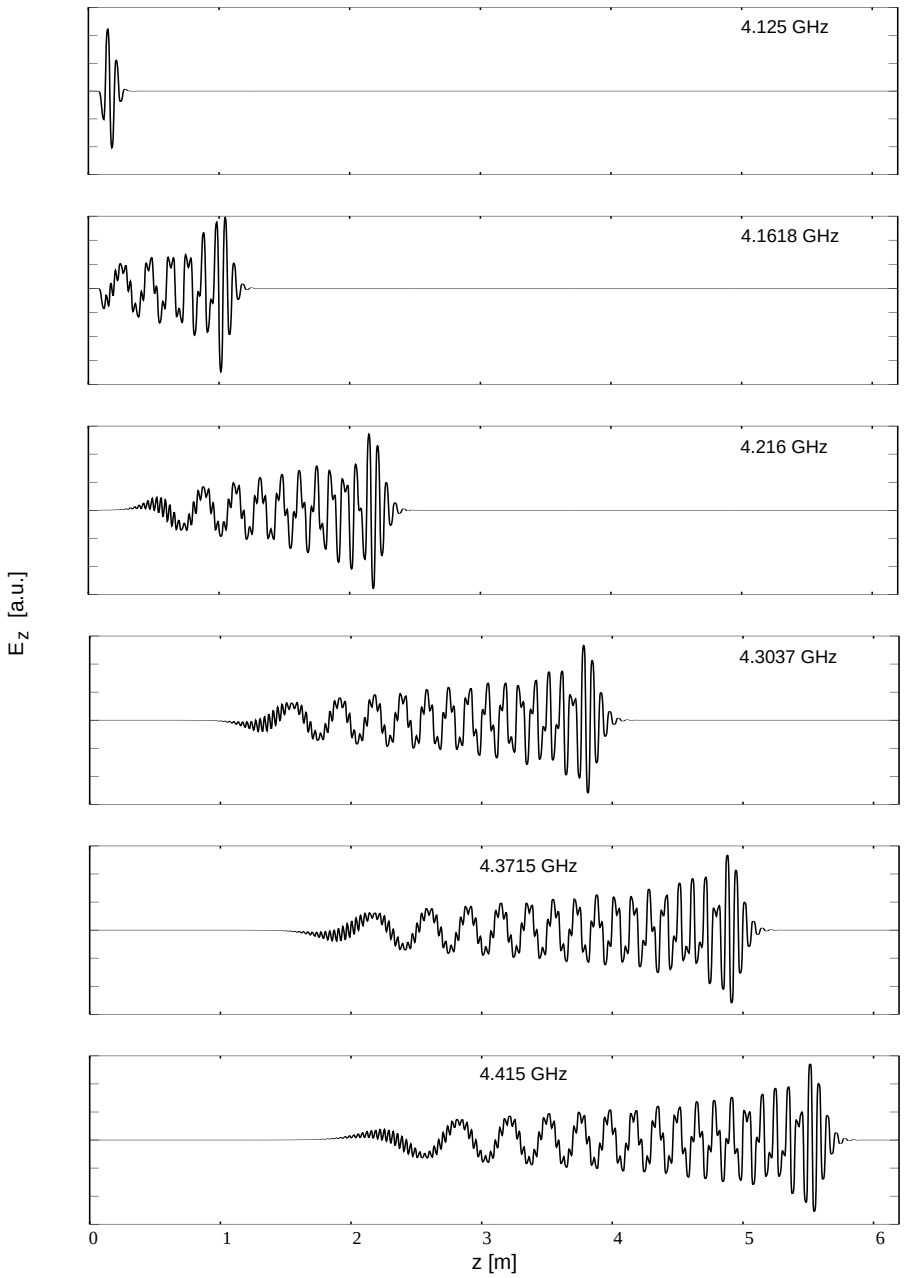

Figure 4.3: The field distribution along the structure of several trapped modes of the first dipole passband.

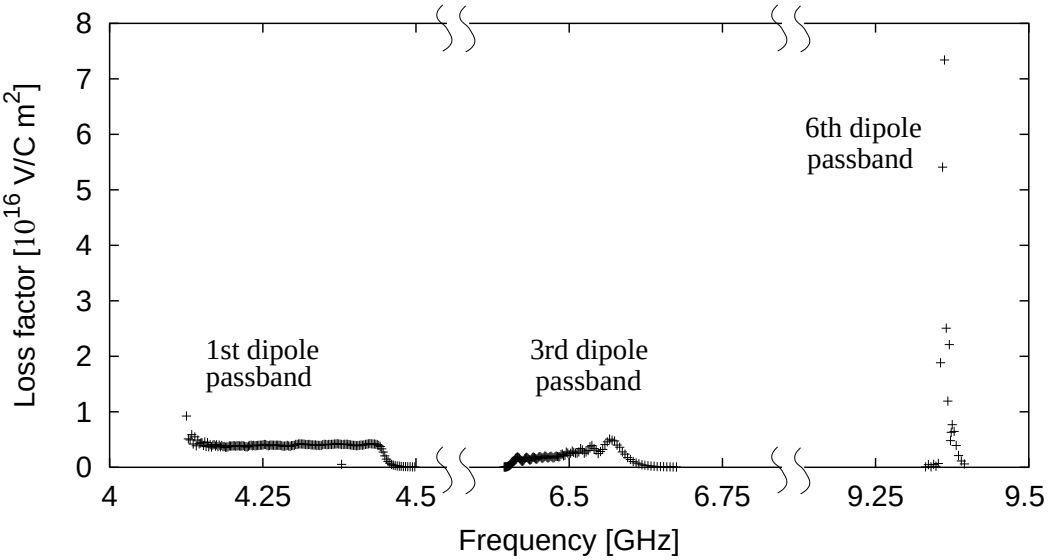

Figure 4.4: Loss factors of the modes of the first, third and sixth dipole passbands.

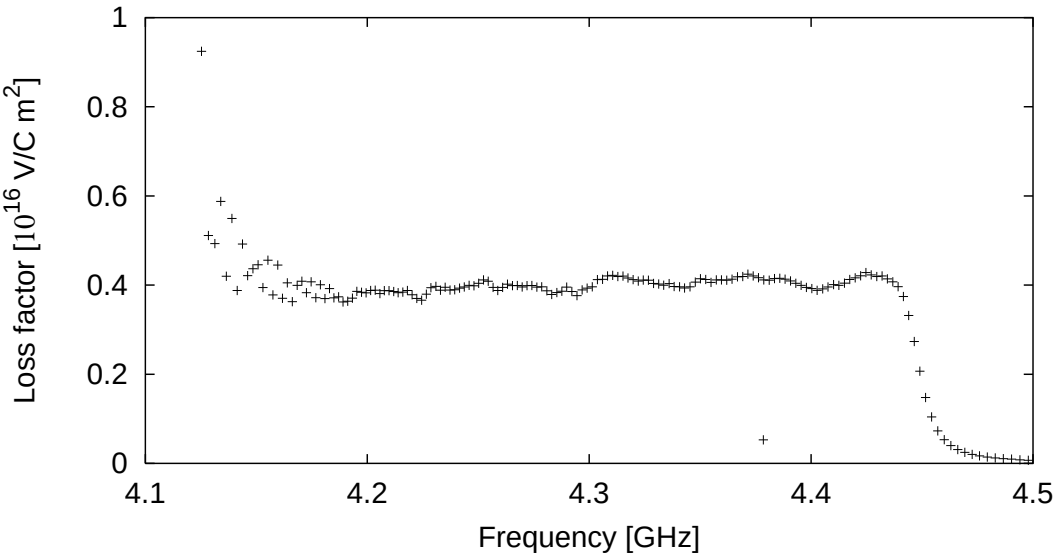

Figure 4.5: Loss factors of the modes of the first dipole passband.

The effect of this wake field must be reduced in order to preserve a good beam quality (see section 3.4.2). For the SBLC structure three different cures are foreseen:

- frequency detuning
- HOM damping
- active structure alignment

Detuning The cell dimensions vary along the structure such that the field amplitude and the frequency of the accelerating mode remain constant although the beam continuously extracts energy from the traveling wave. The frequency of the HOMs changes slightly from cell to cell. In this way a natural *cell-to-cell detuning* is achieved. This reduces the wake field before re-coherence occurs at a time scale given by the typical mode spacing (see Fig. 3.9). For the first passband where the mode spacing is about 2 MHz, the detuning is effective for the first about 70 bunches (arriving before the re-coherence) in the linear collider (bunch spacing 6 ns). The contribution of the modes from the sixth passband does not decohere so fast, dominating the wake seen by the first bunches [3].

In order to further decrease the effect of the wake field on the beam, *section-to-section detuning* introduces an additional artificial spread in the mode frequencies. Ten types of structures with a frequency spread of $\pm$ 18 MHz are achieved by changing the single cell geometry.

Damping In order to avoid a high emittance growth due to the re-coherence of the wake field of the first dipole passband after about 450 ns, their quality factors have to be lower than 4000 [3]. For the sixth passband, the maximum loss factor is higher than for the first passband, but due to the fact that there are few such modes, the maximum wake field is lower (0.25 V/pc/mm^2 compared to 1.3 V/pc/mm^2 for the first passband). Therefore, although the re-coherence time is shorter, the Q values of the modes in the sixth passband have to be reduced to only 8000. At least four dampers would be needed along the section, in order to achieve this damping, due to the many trapped modes. This would be not only costly, but would also affect the mode pattern. For the SBLC structure another solution is adopted: a thin layer of lossy material on the tip of the irises [49, 50]. A layer of 10-20 μm stainless steel or Kanthal leads to the required damping. The accelerating mode is less affected by the iris coating, since the surface currents in the iris tip are much lower than for dipole modes. The shunt impedance of the fundamental mode is therefore reduced by only a few percent [3].

While for the SBLC structure all irises would be coated with lossy material, at the two structures built in the SBTF only the iris tips of cells 3 to 14 and 113 to 123 have such a layer. Calculations show that about half of the modes of the first dipole band are damped to Q values less than 5000, while the rest are distributed between 5000 and 14000, the typical level for copper. Additionally, the colinear load in the last cells damps the modes that reach this part.

Active structure alignment The accelerating section can be aligned with respect to the beam with the help of the signals from two sets of four HOM waveguide pick-ups. These pick-ups are described in section 4.2.2. A bunch sent through the structure excites all modes. By moving the structure, which is placed on a girder, with the help of four micro-movers, the HOM signals can be minimized. In this way the structure is centered on the beam trajectory. A relative alignment of $\pm$ 10 μm can be achieved.

Another important aspect in building an accelerating structure is its *straightness*. Due to the misalignment of the individual cells with respect to each other, a mode is excited even if the average offset is zero. Since the modes of the first dipole passband, giving the highest contribution to the long range wakes, are trapped within 40 to 60 cm of the structure (typically), the accelerating section has to be straight within 30 μm rms over a length larger than 60 cm. For the 6 m long structure slightly larger values are accepted.

4.2.2 The HOM couplers

At two cells along the structure, two sets of four waveguide couplers are foreseen for HOM detection and analysis only, not for damping, in the SBLC section and were installed at one SBTF structure. They are designed such to have little influence on the mode pattern. Their design is shown in Fig. 4.6. A small fraction of the HOM energy is extracted through the azimuthal slots into the four symmetric waveguides, two for each polarization plane. The 3 GHz accelerating mode is below the cutoff of the waveguides (4 GHz) and its amplitude decreases exponentially along the waveguide.

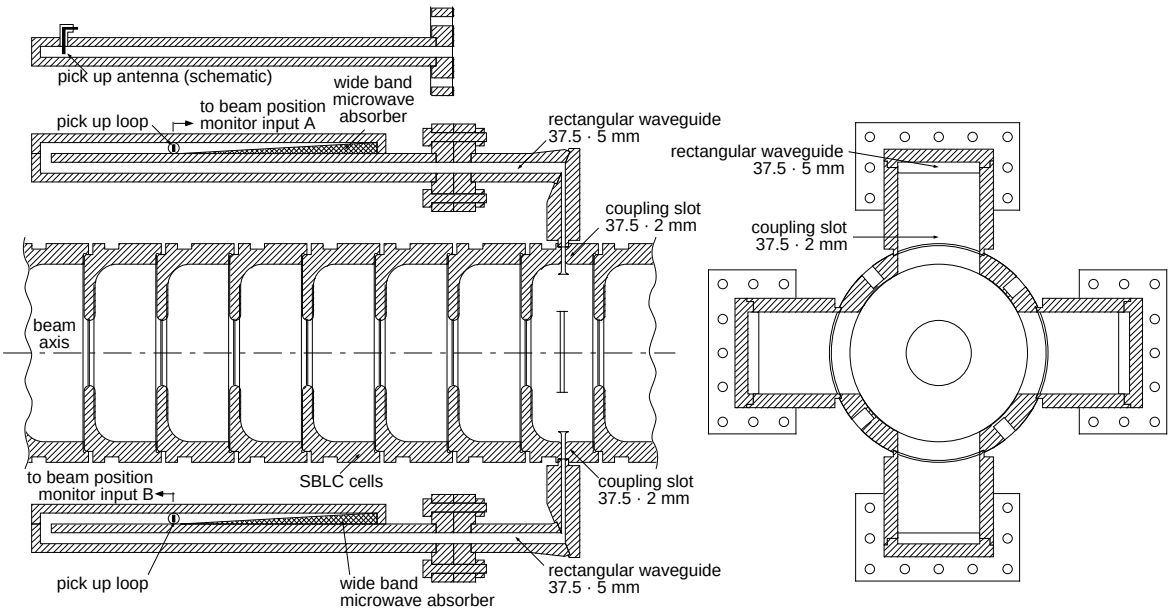

Figure 4.6: The HOM waveguide coupler. Four waveguides are coupled to one cell. Two design versions are shown [3].

Two designs are presented. The lower one, with a folded waveguide achieves a better rejection of the accelerating mode and avoids standing waves. On the other hand, it is more complicated to fabricate and more costly.

For the first SBTF structure, studied in this chapter, the upper option has been used. This structure is studied in this chapter. The two sets of HOM couplers are placed at cells 26 and 107. The second SBTF structure is not equipped with such HOM couplers. Instead, it has four pick-ups at a cell at the end of the section intended for the study of the sixth passband. These are sufficient to measure all modes with high loss factors of this passband since they are propagating along all the structure.

4.3 Single Bunch Frequency Spectrum

4.3.1 Experimental setup

The experimental setup is shown in Fig. 4.7. One bunch with 1.4 nC charge and 65 MeV energy is sent through the SBTF structure. The offset (and angle) of the bunch can be varied using a corrector magnet. The off-axis bunch excites wake fields in the first SBTF structure. The signal from the HOM couplers is viewed with a spectrum analyzer and an oscilloscope.

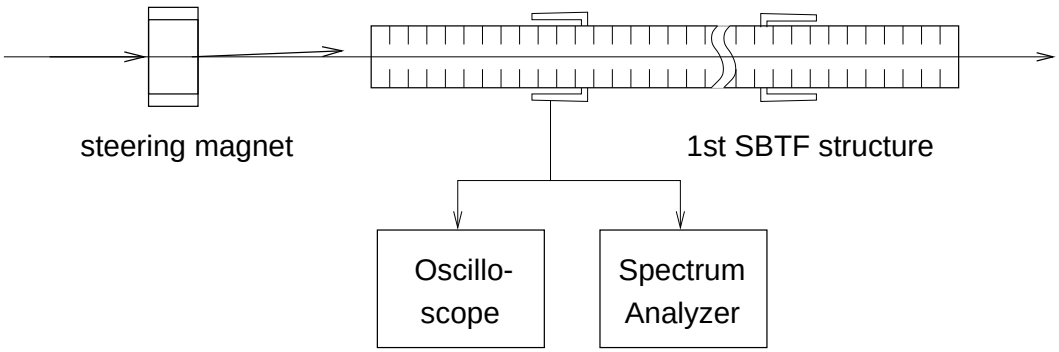

Figure 4.7: The experimental setup for the HOM measurements.

Since we are interested in dipole modes, a way to reduce the signal from the monopole modes that are above the cut-off is used. The signal of monopole modes at two opposite waveguides is equal in amplitude, being independent of the offset. The field at the coupling slots is parallel to the axis. Since the antennae are placed on the same side of the coupler (for example on the upper side of the up and down couplers), the two monopole signals are in anti-phase and cancel when the two outputs are added.

In contrast to this, signals from dipole modes are in phase, so that their addition leads to a double amplitude. A hybrid combiner is used for signal addition from the horizontal waveguides at cell 26. For the vertical signal a standard power combiner is used.

The oscilloscope signal is given by the wake fields excited by the beam and the RF power fed into the structure through the input coupler. The spectrum analyzer

measures the real part of the transverse impedance of the structure $Z_\perp$, given by a Fourier transform of the transverse wake [24, 25]:

$$Z_\perp(\omega) = \frac{-i}{c}\int_{-\infty}^{\infty} W_\perp(\zeta)\exp\left(-i\,\omega\,\frac{\zeta}{c}\right)d\zeta. \tag{4.1}$$

In case of a point-like charge all HOMs are excited:

$$Z_\perp^\delta(\omega) \propto (-i)\sum_l \frac{k_l}{\omega_l^2 - \omega^2 - i\,2\,\frac{1}{2Q_l}\,\omega_l\,\omega}. \tag{4.2}$$

For a Gaussian bunch with length σ_z a coupling impedance is measured, given by:

$$Z_{\perp g}(\omega) = \frac{1}{c}\exp\left(-\frac{\omega^2}{2\left(\frac{c}{\sigma_z}\right)^2}\right) Z_\perp^\delta(\omega). \tag{4.3}$$

Due to the exponential factor, the modes with a frequency higher than c/σ_z are strongly damped. Therefore we are able to excite only modes with frequencies $\omega_l < m \cdot c/\sigma_z$, where m is of the order 4-5.

4.3.2 Measurements and results

A typical signal in the time domain measured from the first pairs of pick-ups as seen on the oscilloscope is shown in Fig. 4.8. The envelope of the time signal is obtained with the help of a rectifying diode. At about 430 ns after the main signal peak (in about the center of the oscilloscope image), the first re-coherence signal given by the modes of the first passband can be recognized. This is in agreement with the mode spacing in this passband, slightly higher than 2 MHz. The second re-coherence can be also seen, after an equal time interval. The distinct signals that can be seen between the highest peak and the first re-coherence echo are most likely given by re-coherence of the modes in other passbands.

On the spectrum analyzer, modes could be measured up to about 15 GHz. Special attention was given to the first dipole passband in which most of the modes are trapped. In Fig. 4.9 the spectrum measured from the upstream horizontal waveguides (the sum signal from the power combiner) is shown. The frequency range measured from the first passband is 4.16 ÷ 4.3 GHz. Fig. 4.10 shows the signal from one downstream horizontal coupler. The downstream waveguides measure modes with frequencies between 4.28 and 4.45 GHz.

The measured frequency range for this passband is smaller as compared to the one obtained from simulation, 4.12 ÷ 4.45 GHz for modes with higher loss factor (see Fig. 4.5). The modes with frequencies below 4.16 GHz are trapped in the cells upstream of the first HOM coupler, and can not be detected. The modes with frequencies above 4.42 GHz reach the region with the colinear load at the end of the structure and are therefore damped.

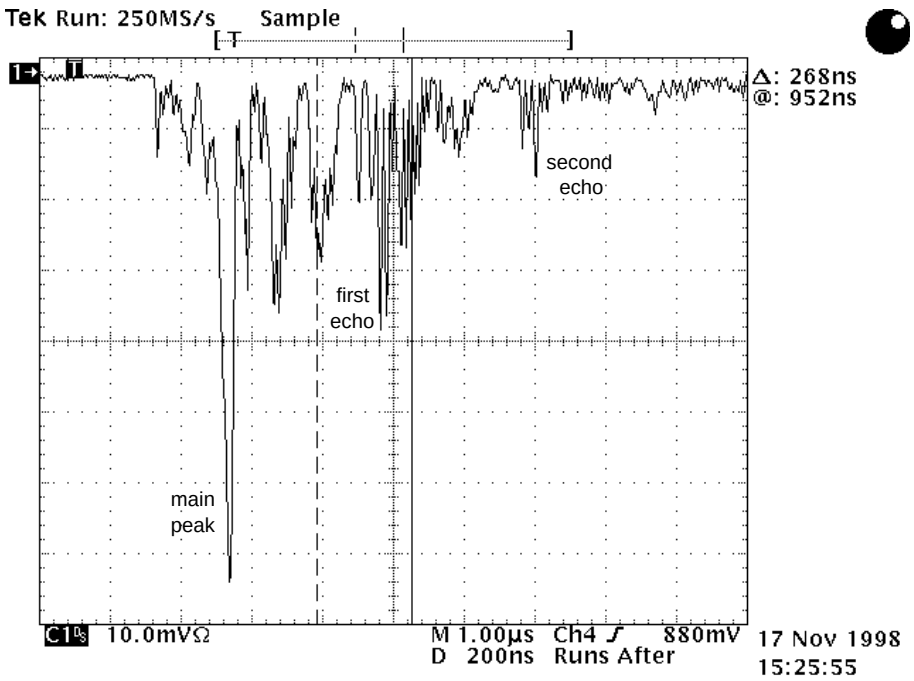

Figure 4.8: The time domain HOM signal obtained with one bunch per pulse from the two upstream horizontal waveguides summed in a power combiner. The time scale is 200 ns per division; the vertical scale is 10 mVΩ per division.

It is interesting to remark that the fundamental mode at 3 GHz could not be seen even before installing the power combiners. This shows a strong damping in the waveguides. On the other hand, its third and fourth harmonics have been clearly observed. The absence of the second harmonics at 6 GHz may be due to the absence of the second harmonic in the klystron.

An unexpected mode is measured at the upstream couplers, at 4.125 GHz (Figs. 4.9). It is well separated from the rest of the modes and has a $Q \approx 2000$, much lower than for the typical structure modes. By measuring the signal amplitude as a function of the beam offset, a linear dependence is found, indicating its dipole character. A similar mode is measured at the downstream HOM couplers at 4.135 GHz, not shown in Fig. 4.10. These additional modes are due to the coupler geometry and are localized around these.

For more modes of the first dipole band, the dipole character is checked. For cylindrically symmetric structures, the dipole contribution to the transverse wake function is proportional to the offset of the generating bunch [24]. In Fig. 4.11, the peak amplitude of the horizontal signal for a mode at 4.217 GHz is plotted as a function of the beam offset at the couplers. The linear character is clearly seen. For offsets larger than 5 mm, the amplitude decreases because part of the bunch hits the irises of the previous cells. The field minimum is not zero because of the straightness of the structure, meaning that this mode is always excited in some cells.

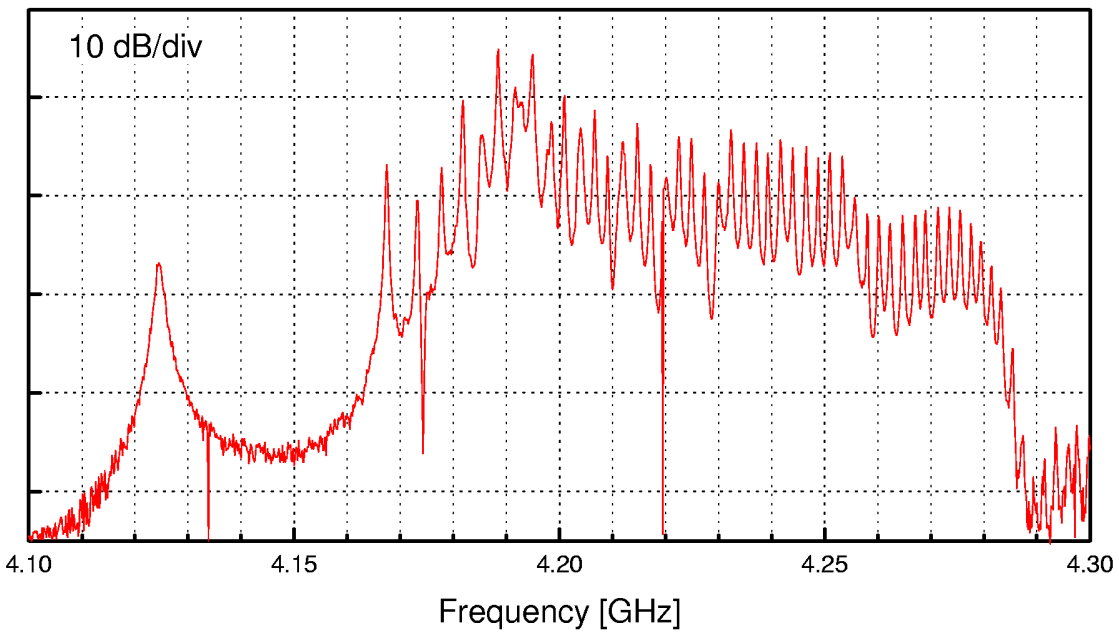

Figure 4.9: Frequency spectrum measured with the upstream horizontal HOM pick-ups summed in a power combiner.

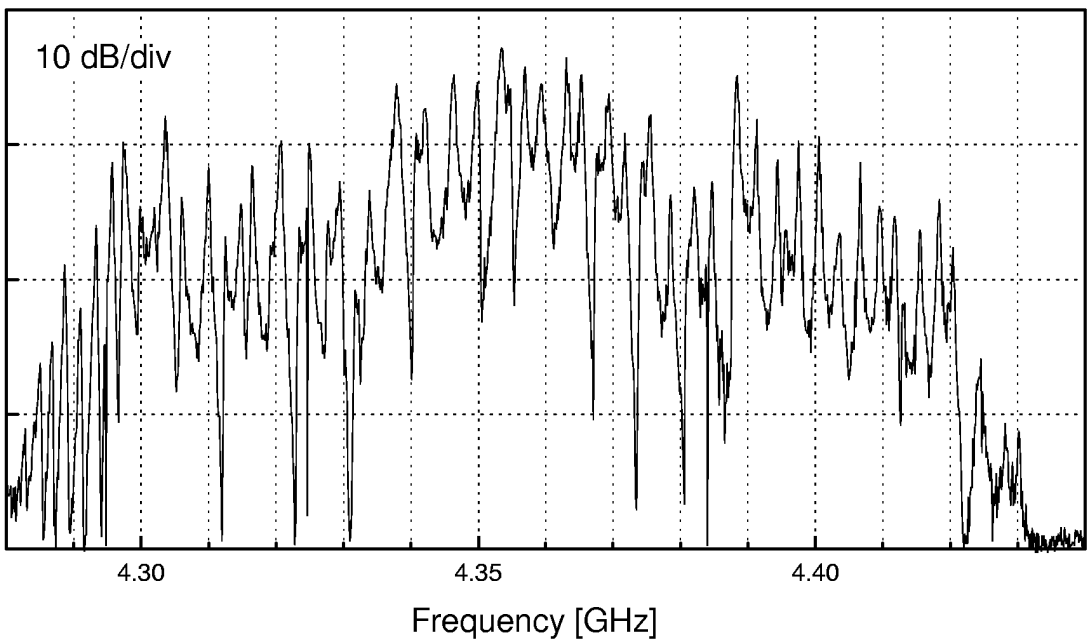

Figure 4.10: Frequency spectrum measured with the downstream left HOM pick-up.

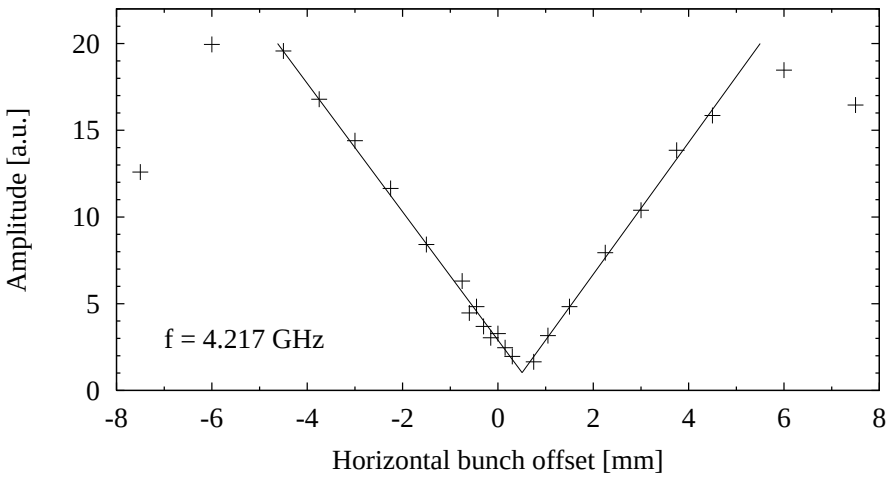

Figure 4.11: The field amplitude at the mode at 4.217 GHz measured at the horizontal upstream HOM pick-ups as a function of the bunch offset.

4.4 Bunch Trains. Amplification of Modes

4.4.1 Theory

When a bunch train passes off-axis through an accelerating section, each bunch, considered to be point-like, excites a transverse wake field $W_\perp^{n\delta}(\zeta)$. The total wake field produced by N bunches is given by:

$$\sum_{n=1}^{N} W_\perp^{n\delta}(\zeta - nct_b) = \sum_{n=1}^{N}\sum_{l} 2k_{\perp l}^{n}\frac{c}{\omega_l}\sin\left(\omega_l\frac{\zeta}{c} - nt_b\right)\exp\left(-\frac{\omega_l}{2Q_l}\left(\frac{\zeta}{c} - nt_b\right)\right), \qquad (4.4)$$

for $\zeta > Nct_b$, where t_b is the bunch spacing. The transverse coupling impedance is:

$$Z_{\perp t}(\omega) = \frac{\exp(-iN\omega t_b) - 1}{\exp(-i\omega t_b) - 1}\, Z_\perp^\delta(\omega). \qquad (4.5)$$

For Gaussian bunches one should substitute $Z_{\perp g}$ (eq. 4.2) for $Z_\perp^\delta$ in this equation.

In Fig. 4.12 the function $(\exp(-iN\omega t_b) - 1)/(\exp(-i\omega t_b) - 1)$ is plotted for a train of 20 bunches. Maxima are obtained for frequencies equal to multiples of ω_b. The sidebands are given by the limited train length. For increasing number of bunches, the maxima become narrower and the amplitude of the sidebands decrease.

Eq. 4.5 implies that the contribution to the total wake field is maximum for modes with

$$\omega_l = m\omega_b = m\frac{2\pi}{t_b}, \qquad (4.6)$$

while the other modes decohere. Therefore the modes satisfying eq. 4.6 are most dangerous for beam dynamics with long trains. Using accelerating sections with slightly different mode frequencies is a cure for this, as discussed in section 3.4.2.

It is interesting to mention here that the transverse effect on the bunches caused by a mode with a frequency exactly at a multiple of the bunch frequency is zero. Indeed, even if the field excited by each bunch adds coherently, the bunches are found at the zero-crossing of the field. A slight deviation from the multiple of the bunch frequency such that

$$\omega_l = m\omega_b \left(1 \pm \frac{1}{2Q_l}\right) \tag{4.7}$$

gives, on the contrary, a maximum effect on the bunch train [30].

4.4.2 Measurements and results

Bunch trains with 24 ns bunch spacing were sent off-axis through the structure. The pulses have 20 bunches and the bunch energy is 65 MeV.

In Fig. 4.13, the spectrum measured at the first horizontal waveguides is shown. It can be seen that, as compared to the single bunch case, the amplitude of the modes at around $m \cdot \omega_b/(2\pi) = 4.167$, 4.208 and 4.250 GHz had increased. The amplitude of the mode at 4.125 GHz, induced by the HOM coupler waveguides, is magnified as well. Due to the small number of bunches, more modes around these frequencies are amplified. For the same reason, harmonics are obtained at multiples of $1/(20 \times 24\ ns) =$ 2.1 MHz. These are easy to be seen for the mode at 4.125 GHz. The signals from modes with frequencies around $(m + 1/2)\ \omega_b/(2\pi)$ are attenuated.

4.5 Kicker Experiment

4.5.1 Principle of the experiment

The method described here gives the possibility to individually excite and study modes with high impedance. Before entering the accelerating section, the bunches are given different transverse positions with a sine modulation, using a fast kicker:

$$\delta x_n = \delta x\ \sin(n\omega_K t_b + \varphi), \tag{4.8}$$

where δx_n is the transverse offset of bunch n, δx is the maximum offset, $\omega_K/(2\pi)$ is the kicker frequency and φ the initial phase of the modulation.

In the accelerating structure the bunches are affected differently by the transverse wakes excited by the previous bunches. The kick on bunch n is given by:

$$\delta x'_n = q\frac{e}{E}\sum_{k=1}^{n-1} \delta x_n W_\perp^{n\delta}((n-k)\,ct_b). \tag{4.9}$$

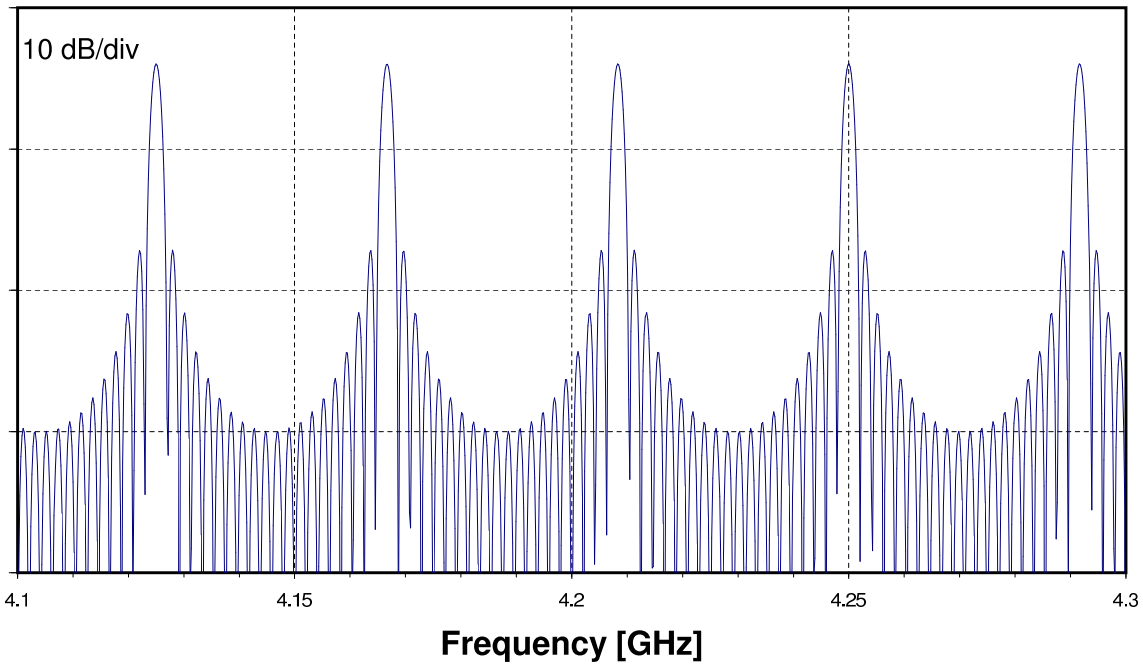

Figure 4.12: The function $(\exp(-iN\omega t_b) - 1)/(\exp(-i\omega t_b) - 1)$ describing the change in the coupling impedance for a bunch train with respect to a single bunch (eq. 4.5). A train with 20 bunches with a 24 ns spacing is considered.

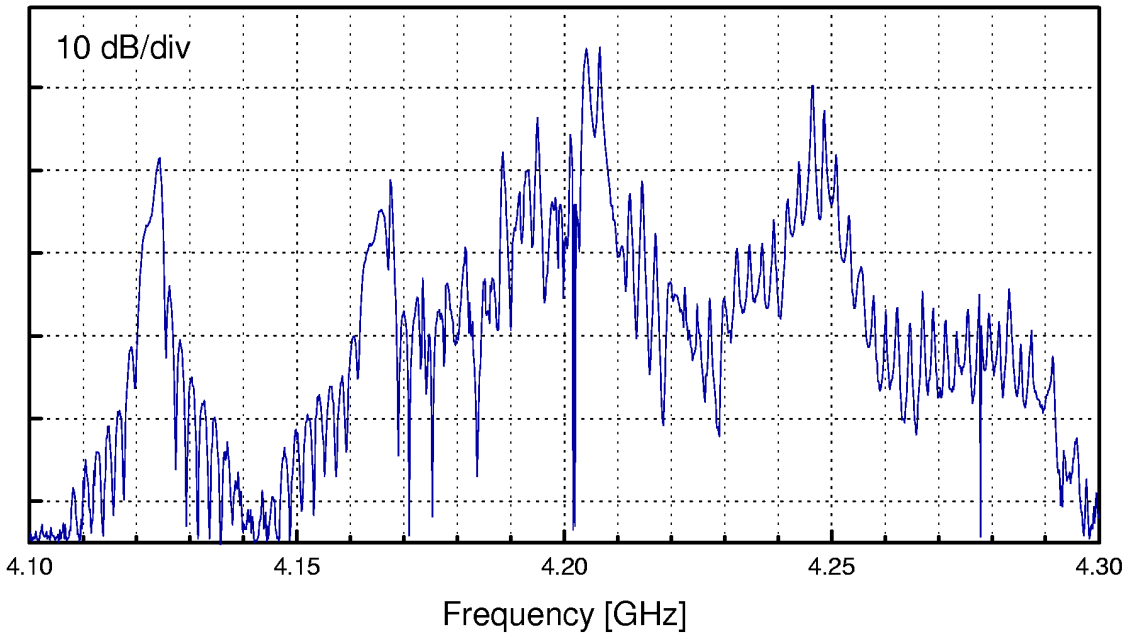

Figure 4.13: The frequency spectrum measured with 20 bunches at the upstream horizontal HOM pick-ups summed up through a power combiner.

In writing this relation, it is assumed that the change in the offset of bunch k within the structure is much smaller than δx_k and that the energy gain is much smaller than the initial energy.

For an infinite bunch train, the kick can be written as:

$$\lim_{n\to\infty} \delta x'_n \approx 2\,\delta x\, q\, c\, \frac{e}{E} \sum_l \frac{1}{\omega_l} k_l \Big[\quad \mathcal{A}_+(\omega_l t_b, Q_l, \omega_K t_b) \sin(n\omega_K t_b + \phi) - \\ - \quad \mathcal{A}_-(\omega_l t_b, Q_l, \omega_K t_b) \cos(n\omega_K t_b + \phi) \Big]. \tag{4.10}$$

The functions $\mathcal{A}_+$ and $\mathcal{A}_-$ are defined in Appendix A [51].

The functions $\mathcal{A}_+$ and $\mathcal{A}_-$ are periodic in ω_K with period ω_b. They are also symmetric and anti-symmetric, respectively, in ω_K. From the periodicity and symmetry properties it follows that $\mathcal{A}_+$ and $\mathcal{A}_-$ are symmetric also with respect to $\omega_b/2$, which limits the relevant interval for the modulation frequency to this value. $\mathcal{A}_-$ reaches its maximum when

$$\omega_{Kl0} = |\omega_l - m \cdot \omega_b|. \tag{4.11}$$

In this case:

$$\mathcal{A}_{-0} = \pm \frac{\omega_b}{\omega_l} \frac{Q_l}{2\pi} \qquad \text{and} \qquad \mathcal{A}_{+0} = 0. \tag{4.12}$$

The maximum and the minimum kick in the steady state are:

$$\delta x'_{0\,\substack{max\\min}} \propto \pm \mathcal{A}_{-0}. \tag{4.13}$$

When the modulation frequency is equal to:

$$\omega_{Kl1} = \omega_{Kl} \pm \omega_l/2Q_l \tag{4.14}$$

then $\mathcal{A}_+$ is maximum and equal to $\mathcal{A}_-$:

$$\mathcal{A}_{+1} = \mp \mathcal{A}_{-0}/2 \qquad \text{and} \qquad \mathcal{A}_{-1} = \mathcal{A}_{-0}/2. \tag{4.15}$$

In this case,

$$\delta x'_{1\,\substack{max\\min}} \propto \pm \frac{\sqrt{2}}{2} \mathcal{A}_{+0}. \tag{4.16}$$

By varying the kicker frequency, one can meet the resonance condition for each mode. When the resonance condition is fulfilled for one mode (eq. 4.11), one observes on the BPM an increase in the maximum offsets of the bunches. An alternative is to monitor the Fourier transform of the bunch offsets. Two peaks at either side of the bunch harmonics, separated from them by $\omega_K/(2\pi)$ are seen in this case. These peaks are always there, given the initial modulation of the bunch offsets, but they increase in amplitude at resonance due to the coherent addition of the HOM effect.

4.5.2 Measurements and results

The experimental setup is shown in Fig. 4.14. 40 bunches with 24 ns spacing and 35 MeV energy have been injected into the SBTF structure. An energy of 65 MeV, lower than the usual, is used in order to increase the HOM kicks (see eq. 4.10). The bunch offsets are modulated with the help of a very fast counter traveling-wave kicker [52]. The kicker consists of two opposite plates, through which two sine signals of opposite sign travel, generating an electromagnetic wave. The contributions of the kicks from the electric and magnetic fields add for charged particles that travel in the direction opposite to that of the wave and cancel out for particles traveling in the same direction. The kicker can impart on 35 MeV electrons a maximum kick of 400 μrad, which corresponds to an offset of 2.4 mm at the location of the BPM. The bunch horizontal positions are monitored at the stripline BPM. This BPM can measure individual bunches separated by less than 8 ns [45].

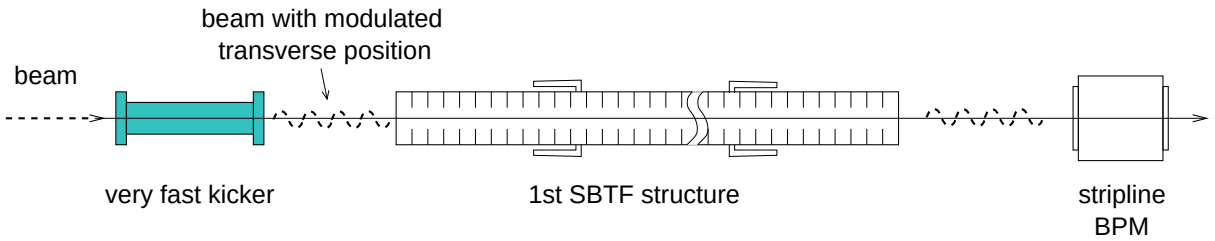

Figure 4.14: Experimental setup for the kicker experiment.

The modulation frequency $\omega_K/(2\pi)$ has been varied between 0 and 21 MHz (half the bunch frequency) in steps of 0.2 MHz. The difference and sum signals from the horizontal pick-ups of the BPM were monitored with the help of an oscilloscope. A Fourier transform has been performed on the difference signal directly on the scope. For each modulation step, the spectrum between 4.1 and 4.5 GHz from the first and second horizontal HOM waveguides has been also monitored by means of a spectrum analyzer. Most undamped modes are expected to be found in this frequency range due to trapping (see section 4.2). For many values of ω_K, the third and sixth passbands has been studied as well.

In Fig. 4.15, the difference and sum signals from the BPM are shown for a kicker modulation of 14 MHz. The sum signal, which is proportional to the bunch charge, is not constant, having a modulation of about 2.5 MHz. In Fig. 4.16 the Fourier transform of the BPM difference signal is shown for $\omega_K/(2\pi) = 14$ MHz. The central signal represents a harmonic of the bunch frequency. Two peaks separated from the bunch harmonics by 2.5 MHz can be seen. These signals are related to the non-uniformity of the bunch current (see Fig. 4.15). This charge modulation can be also seen with the current monitors placed after the Linac II section and after the SBTF structure. The signals from these monitors are shown in Fig. 4.17 together with that from a current monitor after the injector section.

In Fig. 4.16 the two peaks on either side of the central signal, 14 MHz apart from this, are generated by the modulation in the transverse position of the bunches. This

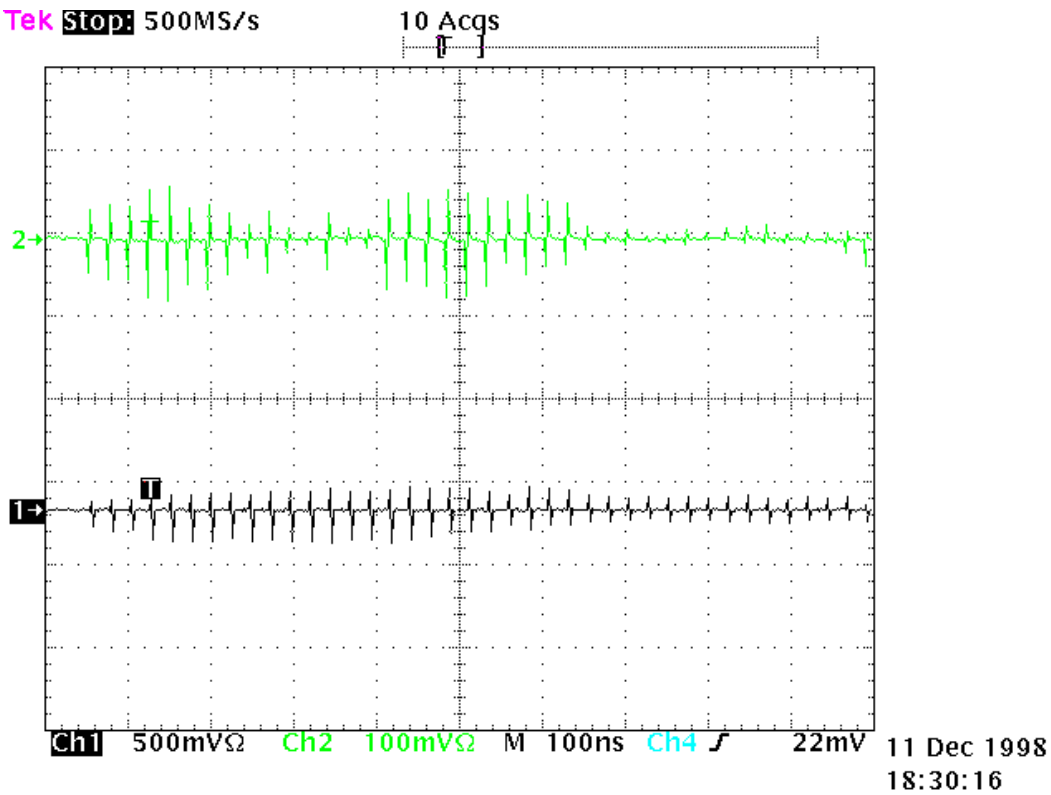

Figure 4.15: BPM difference (upper trace) and sum signals (lower trace) measured at the upstream horizontal HOM pick-ups. The time scale is 100 ns per division. The amplitude of each complete oscillation is proportional to the bunch offset for the upper trace and to the charge for the lower trace. The modulation of the transverse bunch positions is 14 MHz, corresponding to a period of 71 ns. An additional modulations of 2.5 MHz can be observed on both signals.

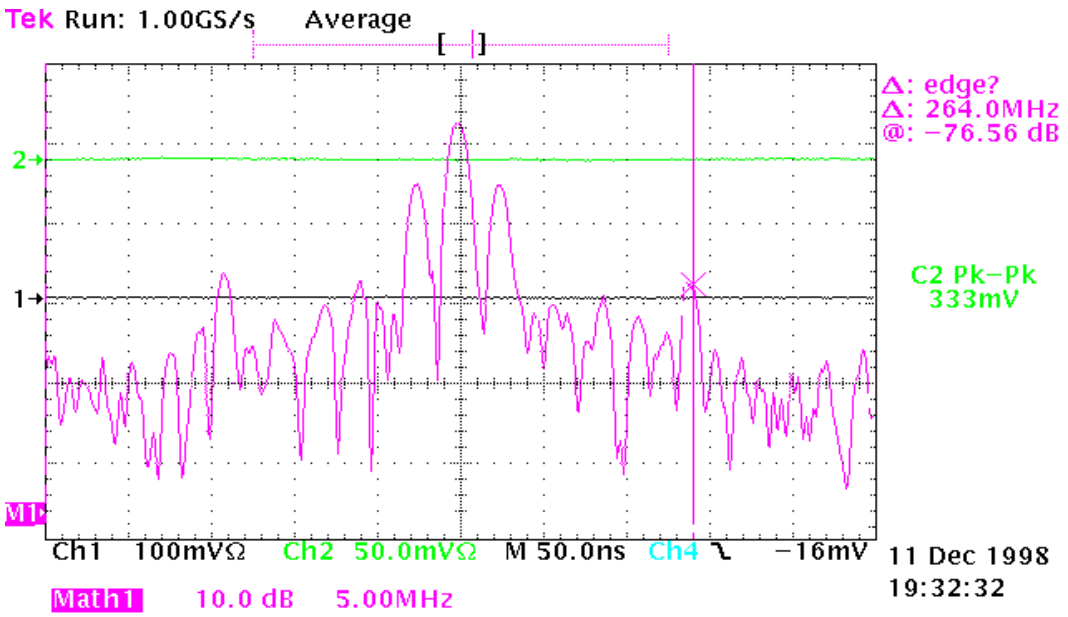

Figure 4.16: Fourier transform of the BPM difference signal shown in Fig. 4.15.

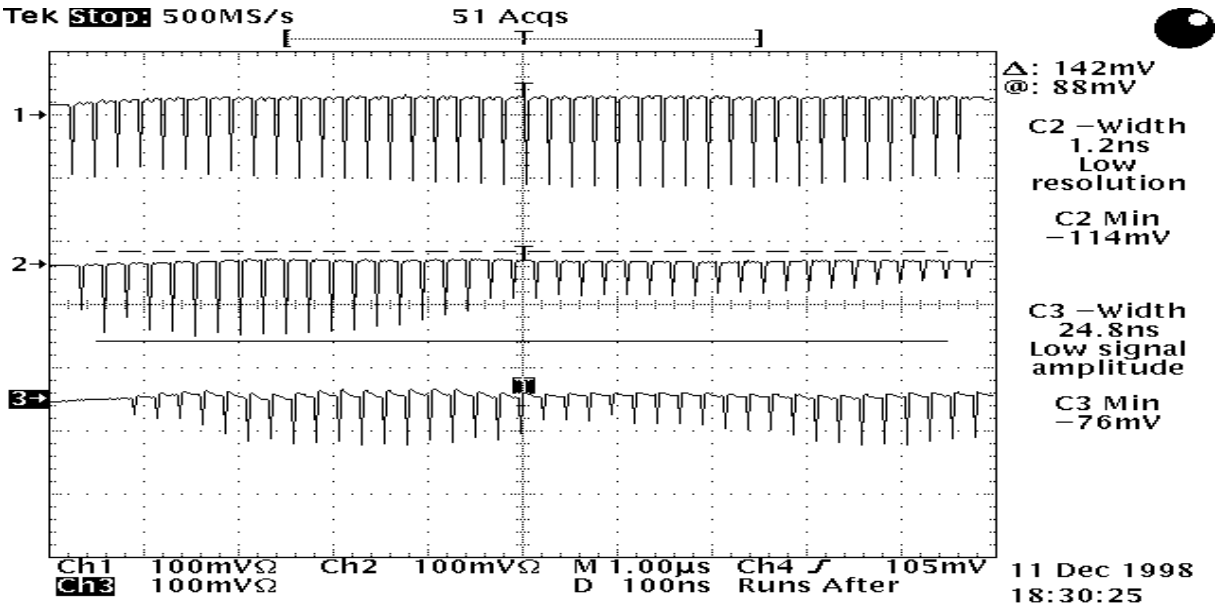

Figure 4.17: Current monitor signals: trace 1 - before the Linac II structure; trace 2 - before the SBTF structure; trace 3 - after the SBTF structure.

signal is always present, its amplitude varies only slightly during the scan. This fact made it difficult to say with certainty whether a high impedance mode is excited or if this comes from the harmonics of the number of bunches (1 MHz). With a much longer bunch train, the effect of the HOMs would be much larger. Nevertheless, using the spectrum analyzer no mode amplification for any step in the scan was observed.

Chapter 5

Higher Order Modes in the TESLA Cavities

The main goal of the TESLA Test Facility (TTF) is to prove that accelerating gradients of 15 MV/m or more are achievable with superconducting cavities and that long pulses of electron bunches with parameters close to the TESLA design can be accelerated [12]. Up to now, gradients beyond 23.4 MV/m, the TESLA goal, were reached in many cavities. Bunch trains of a up to 800 μs were accelerated to a maximum electron energy of 330 MeV. A maximum beam current of 8 mA was produced.

Apart from the cavities, many other components are being 'tested, starting with the high charge low-emittance photo-electric gun up to the diagnostics tools. One of the research programs is the study of higher order modes (HOMs) in the superconducting cavities. At 1.3 GHz, wake fields are low when compared to accelerating cavities in higher frequency linacs. Nevertheless, high quality factors of modes with higher loss factors may lead to a resonant addition of kicks on subsequent bunches and to a high multi-bunch emittance.

In this chapter, after a general description of TTF, the design of the TESLA cavity is presented. Then the principle of the experiments made with a beam with modulated intensity is explained. This kind of experiment was initially made in 1998 and repeated with the present configuration of the linac. The results of the recent experiment and comparison with predictions are summarized.

One result of the experiment made in 1998 was the discovery of a dipole mode at about 2.58 GHz belonging to the third passband with an unexpected high impedance. The investigations on this particular mode, concerning the reason of its insufficient damping in some cavities, are described in the last section.

5.1 The TESLA Test Facility

The present configuration of TTF is shown in Fig. 5.1. The electrons generated by a photo-cathode with the help of a laser beam are accelerated by a RF cavity to about 4 MeV [12, 53, 54]. A booster cavity (also called capture cavity) increases the energy

to 16 MeV. A magnetic spectrometer in this linac section can be used for energy and energy spread measurements. The first cryo-module (ACC1) accelerates the electrons to about 120 MeV. The bunch compressor reduces the length of the bunches. The RF phase is set in ACC1 such that the head of the bunch receives less energy than the tail. Therefore the head will have a longer path in the four magnets so that the tail has time to catch up. A second module (ACC2) brings the electrons to 230 MeV. They are then sent through the undulator where intense, very short pulses of coherent light are produced [55]. The collimator protects the undulator from halo particles. At the end of the linac, the energy distribution of the electrons is measured with a second magnetic spectrometer. Not shown in Fig. 5.1 are quadrupoles and corrector dipoles used to focus and steer the beam, beam position monitors (BPM), current monitors and screens to measure and adjust the beam quality.

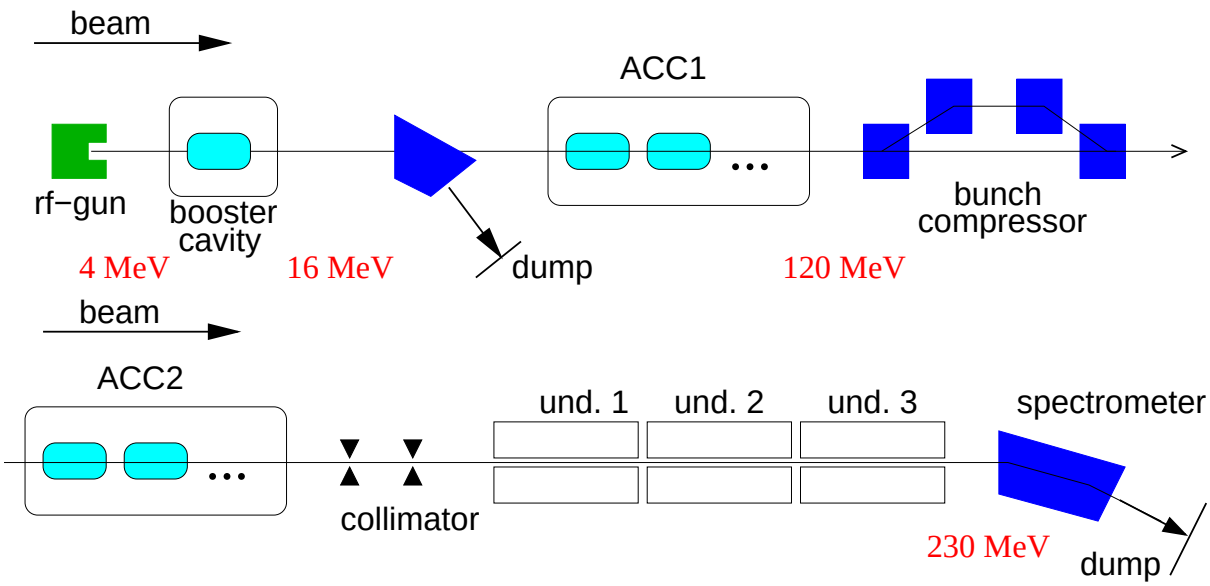

Figure 5.1: The present layout of the TTF linac. ACC1, ACC2: first and second accelerating sections; und. 1-3: undulator module 1-3. Typical energies are shown.

Each cryo-module contains eight 9-cell accelerating cavities and a quadrupole doublet (see Fig. 5.2). The superconducting cavities and quadrupoles are cooled down to 2 K. The accelerating cavity will be presented in the next section.

The HOMs in the cavities are the object of this study. Such investigations have already been made with a previous configuration of the linac: A thermionic gun [12, 56], generated low energy electrons at 217 MHz. They were accelerated to about 10 MeV by the booster cavity. The beam was then accelerated by the first cryo-module built for TTF. The bunch compressor, the second module, the collimator and the undulator were not yet installed.

The experiments made in August 1998 (section 5.3.2) studied the HOMs in the cavities of module 1, while the recent experiments did so at module 3, that replaced module 1 in TTF (section 5.3.4). The bunch train properties are listed comparatively in Table 5.1 for injectors 1 and 2, with the parameters that have been used for the HOM studies.

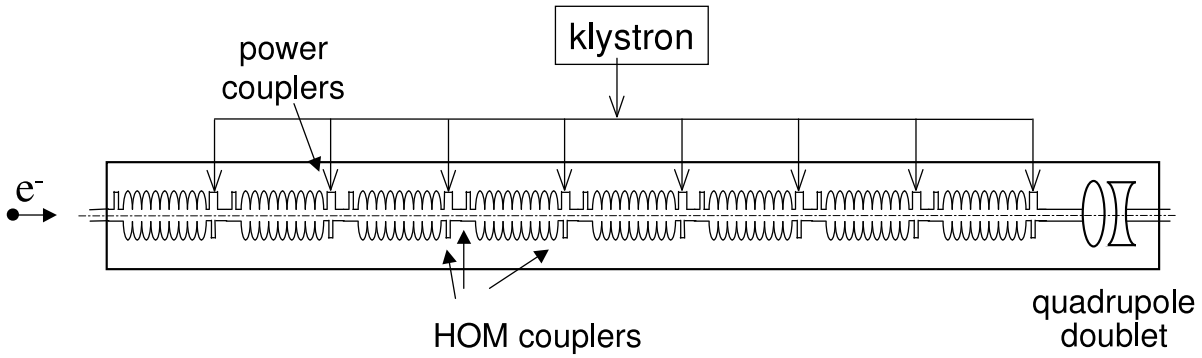

Figure 5.2: Layout of the TTF cryo-module. Eight 9-cell accelerating cavities are powered by a single klystron. A superconducting quadrupole doublet is added to the string.

		Injector 1	Injector 2	
Bunch frequency $\omega_b/(2\pi)$	[MHz]	216.6666	54.16665 *	27.083325 *
Average bunch charge q_0	[nC]	0.037	0.15	0.3
Average current / pulse	[mA]	8	8	8
Energy at entrance of module ACC1	[MeV]	10	16	16

* Modified for HOM experiments (standard frequency: 1.003086111 MHz)

Table 5.1: Beam parameters for the HOM experiments. For injector 2, two options are given.

5.2 The TESLA Cavity

The accelerating cavity design is shown in Fig. 5.3 [2, 57]. It is a standing wave 9-cell 1 m long structure made of niobium. The fundamental mode is a π mode (the direction of the electric field alternates from cell to cell) and has a frequency of 1.3 GHz. The shape of the cells was optimized in order to avoid high local fields. The end half-cells have a slightly different shape in order to ensure the field flatness in all cells. The power coupler is placed downstream.

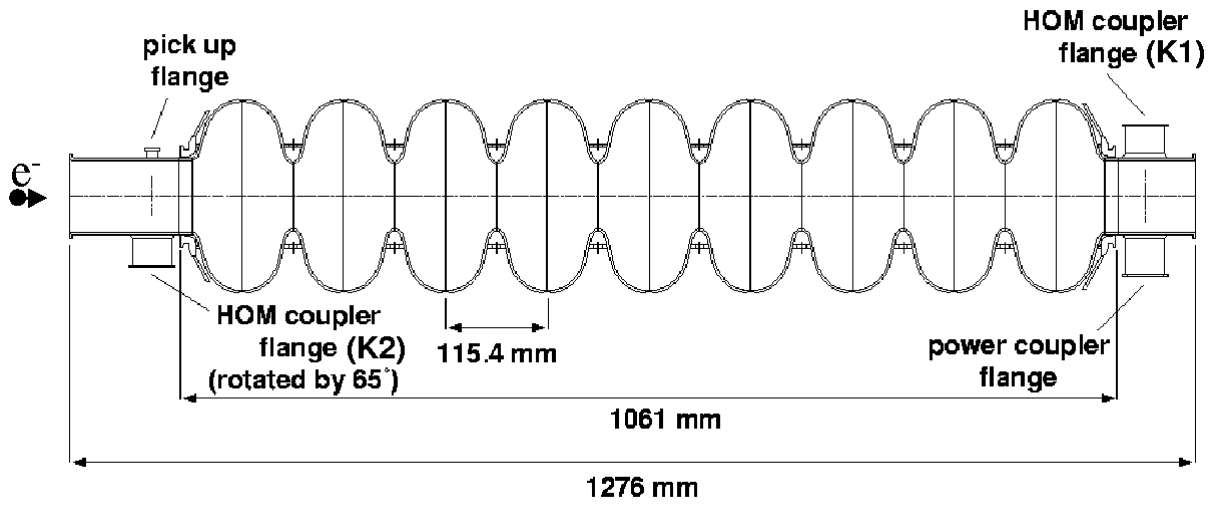

Figure 5.3: Design of the TESLA accelerating cavity [57]. The cavity is positioned in the module such that the beam comes from left. When viewed from the right end, the HOM couplers make with the power coupler angles of 145° (K1) and 30° (K2) clockwise.

The HOM couplers

One HOM coupler is mounted on the beam tube at either side. They reduce the effect of the HOMs by extracting their stored energy. They are almost perpendicular to each other in order to ensure damping of both polarizations of the dipole modes. The angle is not exactly 90 °, but 115 °, in order to damp also quadrupole modes.

Two types of HOM couplers, one demountable and the other welded, were tested and used at the cavities for TTF. Their designs are shown in Fig. 5.4. In both cases, the coupling to the RF field is made through a loop whose plane is orthogonal to the beam axis. The loop couples to the electric and magnetic fields of the modes. It is capacitively coupled to an external load. A notch filter prevents energy being extracted from the accelerating mode.

In the presence of the HOM couplers, the effective quality factor of a mode changes.

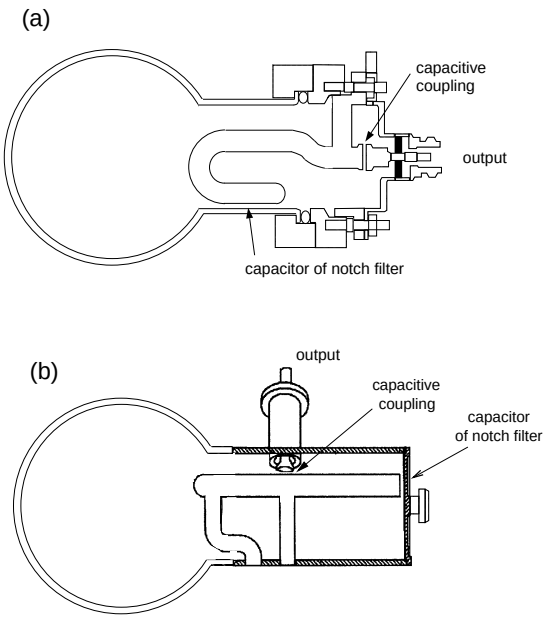

Figure 5.4: HOM couplers installed at either side of the TESLA cavities. Two types are used at the TTF cavities: (a) a demountable type and (b) a welded type [2].

The total Q is given by:

$$Q_{tot} = \frac{\omega W}{P_{tot}}, \tag{5.1}$$

where W is the total energy stored in the mode and P_{tot} is the total power loss. A fraction of the power is lost in the cavity walls, that determines the quality factor Q_0 of the mode in the cavity without couplers. A much larger fraction is coupled out through the couplers, defining the external quality factor Q_{ext}. Therefore one can write the following relation for the total Q, also called *loaded* Q:

$$\frac{1}{Q_{tot}} = \frac{1}{Q_0} + \frac{1}{Q_{ext}}. \tag{5.2}$$

For a superconducting cavity, Q_0 is of the order of $10^8 \div 10^9$ and $Q_{tot} \approx Q_{ext} \ll Q_0$. At room temperature, the total Q is dominated by Q_0, of the order of a few thousands up to 10^4. Q_{ext} practically does not depend on the temperature.

Higher Order Modes

The dispersion diagram for the dipole modes of the TESLA cavity is given in Fig. 5.5 [58]. The first two passbands, are below the cut-off of the beam pipe connecting the cavities (about 2.25 GHz for TE-like modes). This means that they can not propagate between cavities and may not reach the HOM couplers. While designing the HOM couplers, special attention was payed to these passbands, as well as to the second

monopole passband, situated around 2.4 GHz. The modes of the other dipole passbands can propagate into the beam pipes. Nevertheless some of these higher order modes are trapped into the cavity, i.e. their field amplitude in the end cells is low, most of the energy being concentrated in the middle cells. Such are the modes belonging to the fifth passband. Trapped modes may not reach the location of the HOM couplers and therefore may be not damped. In order to avoid such a situation, the end half-cells of the cavity were made slightly asymmetric.

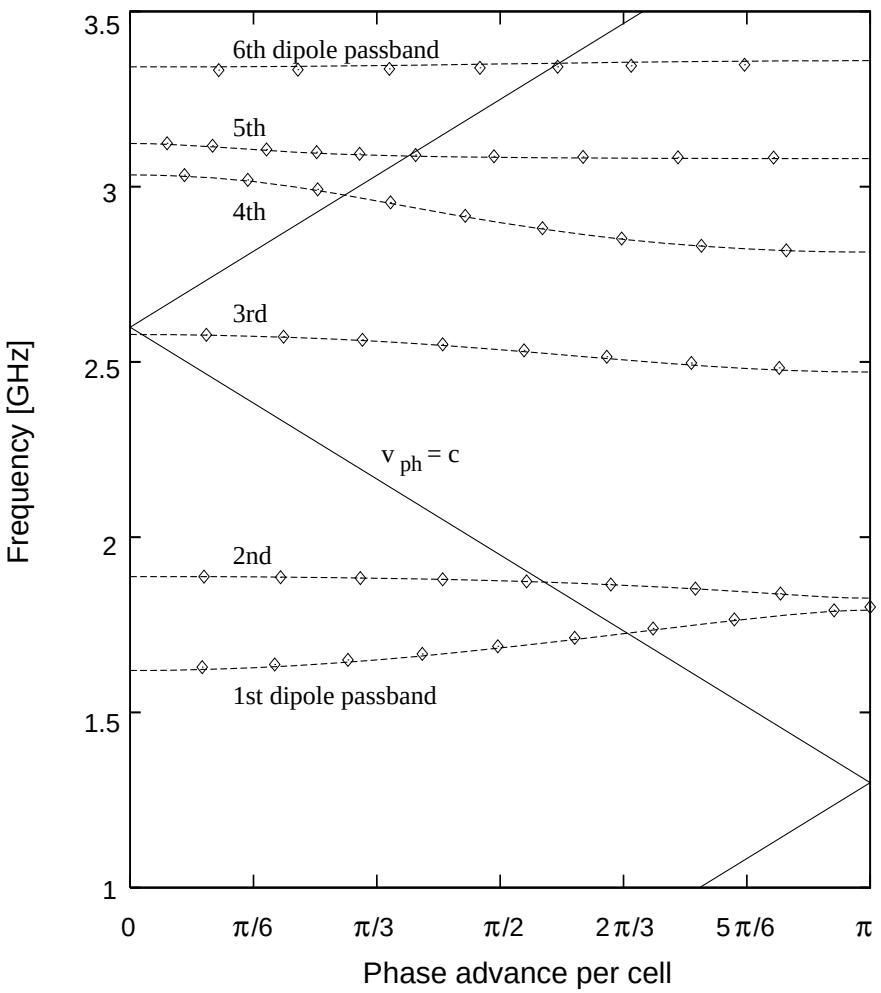

Figure 5.5: Dispersion diagram for the dipole modes of the TESLA cavity [58]. The diamond symbols represent individual modes. The velocity of light line is shown as well. Its intersection with the passbands marks the modes with highest impact on the beam.

In Fig. 5.6 the first monopole passband is shown. The accelerating mode is the last in this passband, having a phase advance per cell of π and a frequency of 1.3 GHz.

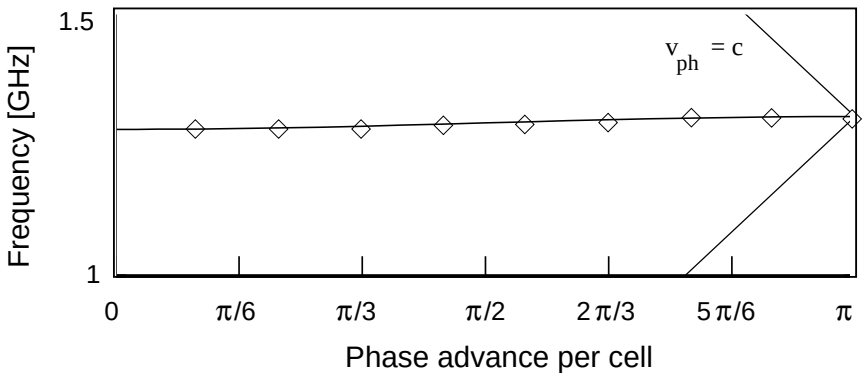

Figure 5.6: Dispersion diagram for the first monopole passband of the TESLA cavity. The mode with π phase advance per cell is used for acceleration.

5.3 HOM Excitation with an Intensity Modulated Beam

5.3.1 Principle of the experiment

For the S-band accelerating structures two methods were used in order to resonantly excite individual modes (see sections 4.4 and 4.5). In the first method the modes whose frequencies are at multiples of the bunch frequency (eq. 4.6) are excited in phase by each bunch of a long train. When looking at the frequency spectrum, these modes are amplified with respect to the case of using one bunch, while the excitation of other modes averages to zero for an infinite bunch train. The drawback of this method is that only few modes satisfy eq. 4.6.

The second method is to excite single modes by using a bunch train with modulated transverse positions at the entrance of the accelerating structure. If the modulation frequency ω_{mod} is varied from 0 to $\omega_b/2$, with $\omega_b = 2\pi/t_b$ the bunch repetition angular frequency, all modes can be excited, when the following relation is fulfilled:

$$\omega_{mod\,l} = |\omega_l - m \cdot \omega_b|, \tag{5.3}$$

where ω_l is the angular frequency of the excited mode and m an integer.

In [51] it has been proposed to excite single modes by a charge modulation:

$$q_n = q_0\,(1 + \lambda \cdot \sin(n\,\omega_{mod}\,t_b + \phi)), \tag{5.4}$$

where n is the bunch index, q_0 the average charge, t_b the bunch spacing, ω_{mod} the angular frequency of the modulation signal. λ is the modulation amplitude and ϕ its initial phase. The transverse wake potential seen by the bunch with the index n in the train contains the contributions of the wakes excited by all previous bunches, being proportional to:

$$\propto \sum_{k=1}^{n-1} q_k W_\perp^{n\delta}((n-k)ct_b), \tag{5.5}$$

where $W_{\perp}^{n\delta}$ is the delta-like transverse wake potential per accelerating structure (see chapter 3). The bunches are considered to be point-like.

If we consider the kick to be concentrated in the middle of the accelerating cavity, the kick received by bunch number n is approximately:

$$\delta x'_n = \delta x_0 \frac{e}{E} \sum_{k=1}^{n-1} q_k W_{\perp}^{n\delta}((n-k)\, ct_b), \tag{5.6}$$

where δx_0 is the initial offset of the bunches with respect to the cavity axis, same for all bunches, and E is the energy of the bunches in the middle of the cavity. For an infinitely long train (reaching the steady state, i.e. the bunches have the same phase space coordinates) $\delta x'_n$ can be written as a sum of three terms:

$$\begin{aligned} \lim_{n\to\infty} \delta x'_n \approx \delta x_0\, q_0\, \frac{c}{2}\, \frac{e}{E} \sum_l \left(\frac{R}{Q}\right)_l \quad & \Big\{ \quad p_r(\omega_l t_b, Q_l) + \\ + \lambda \quad & \Big[\quad \mathcal{A}_+(\omega_l t_b, Q_l, \omega_{mod} t_b) \sin(n\omega_{mod} t_b + \phi) - \\ - \quad & \mathcal{A}_-(\omega_l t_b, Q_l, \omega_{mod} t_b) \cos(n\omega_{mod} t_b + \phi) \Big] \Big\}. \end{aligned} \tag{5.7}$$

Here and throughout this chapter, the R/Q parameter is used instead of the loss factor ($(R/Q)_l = 4k_l/\omega_l$), because it is used in most of the literature about the TESLA cavity. The functions p_r, $\mathcal{A}_+$ and $\mathcal{A}_-$ are defined in Appendix A [51]. The first term does not depend on the current modulation and is determined only by the mode properties and by the bunch spacing. p_r reaches its maximum:

$$p_{r_{max}} = \pm \frac{\omega_b}{\omega_l} \frac{Q_l}{2\pi} \tag{5.8}$$

for modes with the frequency:

$$\omega_l^{p_r} = n\omega_b \left(1 \pm \frac{1}{2Q_l}\right). \tag{5.9}$$

The second and third terms in relation 5.7 are exactly the same as for the case of a train with modulated transverse bunch positions (Chapter 4, eqs. 4.10 to 4.16).

If a mode is excited on resonance (eq. 5.3), then from eqs. 5.7, 4.12 and 4.13 it results that the offset amplitude Δx, i.e. the difference between the extreme transverse positions in the bunch, at a certain location after the cavity, is given by:

$$\Delta x = \delta x_{max} - \delta x_{min} \;\propto\; \delta x'_{max} - \delta x'_{min} = c\, \delta x_0\, \lambda \left(q_0 \frac{\omega_b}{2\pi}\right) \frac{e}{E} \frac{1}{\omega_l} \left(\frac{R}{Q}\right)_l Q_l. \tag{5.10}$$

The experiment consists in sending off-axis a long bunch train with intensity modulation through an accelerating cavity. By slowly variation of the modulation frequency ω_{mod} the resonance condition given by eq. 5.3 is met for each mode. The transverse

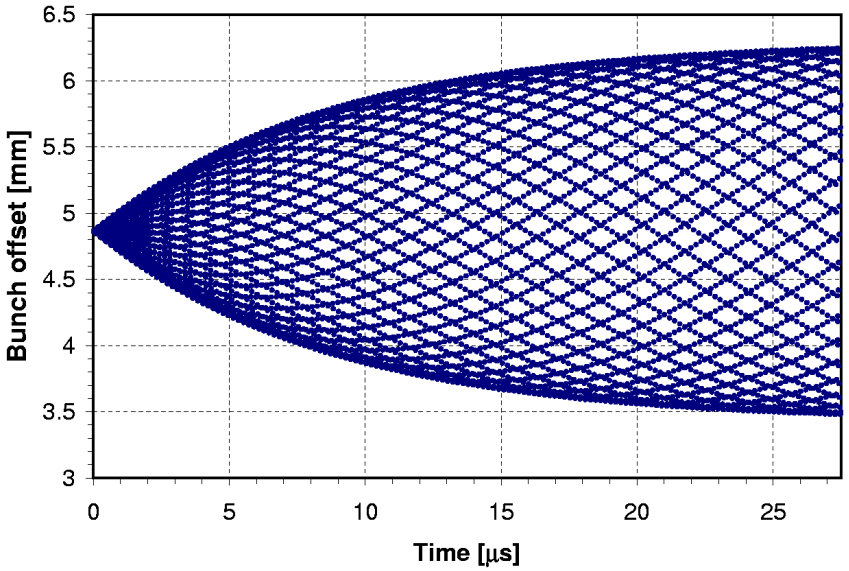

Figure 5.7: Bunch offsets at the BPM location for the case of exciting a dipole mode on resonance in cavity 8. The envelope of the transverse positions describe the build-up of the HOM resonance. Bunch properties: $\omega_b/(2\pi)$ = 216 MHz, q_0 = 0.037 nC, I_0 = 8 mA, δx_0 = 10 mm, E_0 = 16 MeV. Gradient 2 MV/m. HOM properties: $\omega_l/(2\pi)$ = 1.876 GHz, R/Q = 9 Ω/cm^2, $Q = 5 \cdot 10^4$. Modulation: $\omega_{mod}/(2\pi)$ = 74 MHz (resonant mode excitation), amplitude λ = 80 %. Distance cavity-BPM: 6.5 m.

positions of the bunches are monitored with a BPM. At resonance, the BPM signal changes from showing a constant transverse position of the bunches in the train, to a pattern similar to the one in Fig. 5.7. This figure is obtained through simulations, by subsequent addition of the fields excited by all previous bunches, assumed to be point-like. The pulse is long enough to approach the steady state. In practice, the average offset of the train, which is induced by the initial beam offset, can be reduced to zero using deflecting magnets.

The frequency resolution of this type of experiment depends on the repetition frequency of the bunches. The higher ω_b, the better the various modes can be resolved from each other, i.e. the resonant frequencies of the modulation are distributed over a wider frequency range. This was the argument for choosing to do this experiment at TTF with injector 1, working at a frequency of 216 MHz. Injector 2 works at a bunch repetition frequency of 1 MHz, where the probability that, for a given ω_{mod}, more modes are simultaneously and quasi-resonantly excited is much higher.

5.3.2 First experimental results

A HOM experiment with modulated beam intensity has been carried out with an older setup of TTF, when injector 1 has been used to generate electron bunches. The experimental setup is shown in Fig. 5.8. A thermionic gun delivers a bunch train with 8 mA current and a pulse duration of up to 800 μs. The bunch repetition frequency is

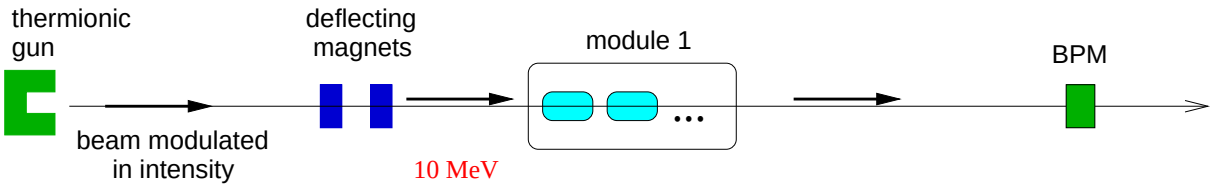

Figure 5.8: Experimental setup used in 1998. The intensity modulated beam generated by the thermionic gun receives an offset with the help of a deflecting magnet pair. When in one cavity of module 1 a mode is excited, its effect on the bunch offsets is measured at the BPM.

216 MHz. Using a voltage modulator at the gun grid, the bunch charge is modulated with an amplitude of up to 100 %. A pair of horizontally deflecting dipole magnets is used to vary the transverse position of the bunch train. The maximum offset is $\pm$ 20 mm. Then the train travels through the eight cavities of the first cryo-module built for TTF (module 1). A broad-band BPM is used to measure the position of the bunches about 10 m downstream the module. The sum and the difference of the two opposite horizontal pick-ups of the BPM are observed on an oscilloscope. In order to make more sensitive measurements, the train is centered in the BPM. In the neighborhood of the BPM center, the response is linear with the bunch offset. This procedure is justified since we are interested only in the bunch offsets relative to each other, and not in the absolute transverse position of the beam pulse. The beam enters the module with an energy of 10 MeV. The accelerating gradient is reduced to 2 MV/m in order to maximize the kicks received by the beam from the higher order modes. The quadrupoles situated between the module and the BPM are switched off. The above mentioned parameters are summarized in Table 5.1 (injector 1).

We mention here that modes can be excited in any of the eight cavities of the module. A kick in cavity 8 leads to a smaller maximum offset read at a BPM situated in the bunch compressor section than a similar kick in the first cavity, due to the shorter distance from cavity to BPM.

At the beginning of the modulation frequency scan, at $\omega_{mod}/(2\pi) = 15$ MHz, a resonance was observed on an analog oscilloscope, as shown in Fig. 5.9 [59]. In the left picture the BPM difference signal in the absence of any HOM resonance is shown. At the beginning of the pulse, the signal has a higher amplitude due to an overshoot of the bunch charge. In the right picture, the maximum offset in the train increases, reflecting a HOM resonance. In Fig. 5.9, the oscillation on the envelope is due to an offset of the modulation frequency from resonance by 8 kHz.

The resonance disappears when the third cavity is detuned, i.e. the frequency of the modes changes and eq. 5.3 is not satisfied anymore for the given modulation frequency. With the cavity tuned back, with the help of a spectrum analyzer at one of the HOM couplers of cavity 3, the mode is found to have a frequency of 2.585 GHz. Its dipole character is indicated by the linear dependence of the HOM peak amplitude with the beam offset. In the time domain the damping time of the mode is measured: τ = 110 μs. From here the quality factor is estimated to $Q = \omega\tau/2 \approx 9 \cdot 10^5$. The quite strong maximum kicks on the bunches, even for short pulses of 35 μs, indicates that

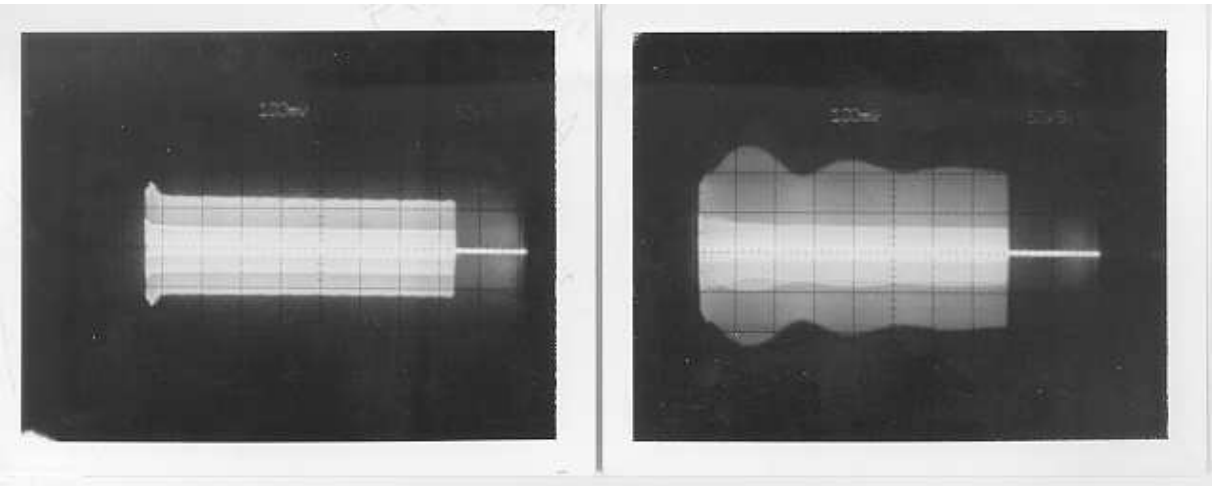

Figure 5.9: BPM difference signal evidencing HOM resonance (right) in comparison to the signal for the unmodulated beam (left) [59]. The abscissa represents the time axis, while the ordinate is the BPM difference signal. The pulse length is 400 μs.

this mode should have a high R/Q as well. Indeed, a value of 15 Ω/cm^2 is given by URMEL simulations[1] [61]. For comparison we mention here that the highest R/Q obtained from simulations for modes in the first two dipole passbands is 15 Ω/cm^2.

The time allocated for this experiment allowed the study of three more modes. None of them is as pronounced as the one described above. All modes are listed in Table 5.2. The last mode given in the table has a Q at about the beam breakup limit indicated in [11]. The second and third modes have $(R/Q)Q$ below the value for the mode at 1.876 GHz. But the biggest question is about the cause of the poor damping of the mode at 2.58 GHz. The investigations regarding this issue are presented in section 5.4.

$\omega_{mod}/(2\pi)$ [MHz]	$\omega_l/(2\pi)$ [GHz]	$(R/Q)_l$ [Ω/cm^2]	τ_l [μs]	Q_l	$((R/Q)Q)_l$ [MΩ/cm^2]	passband	cavity number
15.022	2.585	15	110	$9{\cdot}10^5$	13.50	3rd (TE)	3
14.04	2.586	15	8	$6.5{\cdot}10^4$	0.98	3rd (TE)	6
22.475	2.5775	1	22	$1.8{\cdot}10^5$	0.18	3rd (TE)	3
74.03	1.876	9	20	$1.2{\cdot}10^5$	1.08	2nd (TM)	3

Table 5.2: HOMs excited by an intensity modulated beam generated by injector 1.

Since time did not allow for scanning over the complete frequency range and since these results showed the importance of studying the HOMs with a high impedance, it was decided to continue the experiments with injector 2. The estimations regarding these experiments are given in section 5.3.3, while the experiment results are presented in section 5.3.4.

[1] MAFIA simulations give $R/Q = 23\ \Omega/\text{cm}^2$ [60]

5.3.3 Simulations

Choice of bunch repetition frequency

The present injector of the test facility operates at 1 MHz. In order to increase the resolution of the experiment, the frequency is modified to 54 MHz, the maximum possible frequency with this injector. Since it seemed easier to obtain a bunch frequency of 27 MHz rather than 54 MHz, the question arose if the experiment could be made at this frequency. In order to illustrate the role of the bunch frequency, an example with two modes that can be excited in the whole module, in the 4th and 8th cavity, respectively, is given. The characteristics of the modes are given in Table 5.3. The frequencies of the modes were artificially chosen (but realistic ones) such that the modulation frequencies in the case of using $\omega_b/(2\pi)$ = 27 MHz needed to excite the two modes resonantly are separated by only 10 kHz from each other, while for the 54 MHz case, they are better resolved. The amplitudes of the kicks in the steady state due to the two modes differ by approximately a factor 2, given the same $(R/Q)Q$ and the difference in frequency (see eq. 5.10).

	Mode				Resonant modulation	
	$\omega/(2\pi)$ [GHz]	R/Q [Ω/cm^2]	Q	$(R/Q)Q$ [$\mathrm{M}\Omega/\mathrm{cm}^2$]	$\omega_{mod}/(2\pi)$ [MHz] for 54 MHz	$\omega_{mod}/(2\pi)$ [MHz] for 27 MHz
Mode 1 in cav. 4	1.770416	10	10^5	1	17.083	10
Mode 2 in cav. 8	2.555843	5	$2{\cdot}10^5$	1	10.01	10.01

Table 5.3: HOM properties chosen for the illustration of the differences between bunch frequencies of 54 and 27 MHz and the necessary modulation frequencies to excite them resonantly in the HOM experiment.

In Fig. 5.10 scans around the resonant ω_{mod} for each mode are simulated for $\omega_b/(2\pi)$ = 54.16665 MHz and 27.083325 MHz. The offset amplitude Δx is shown as a function of the modulation frequency. For the 54 MHz case (upper graphic), the two modes can be clearly distinguished during the scan. For 27 MHz, the two modes can not be separated in the BPM signal anymore. The signal from the second mode, excited in cavity 8, is practically covered by the other one, which gives a higher Δx.

If the two modes are in the same cavity, both resonances for a bunch frequency of 54 MHz (upper graphic) have the same amplitude. For 27 MHz (lower curve) one would see an enlarged peak.

Figs. 5.11 and 5.12 show the evolution of the offsets of the bunches at various positions in the module and at the BPM for the two cases of bunch frequencies, for a modulation frequency of 10.01 MHz. With 54 MHz, the offset is changing only due to focusing up to cavity 8, where mode 2 is excited. At the exit of this cavity one can see

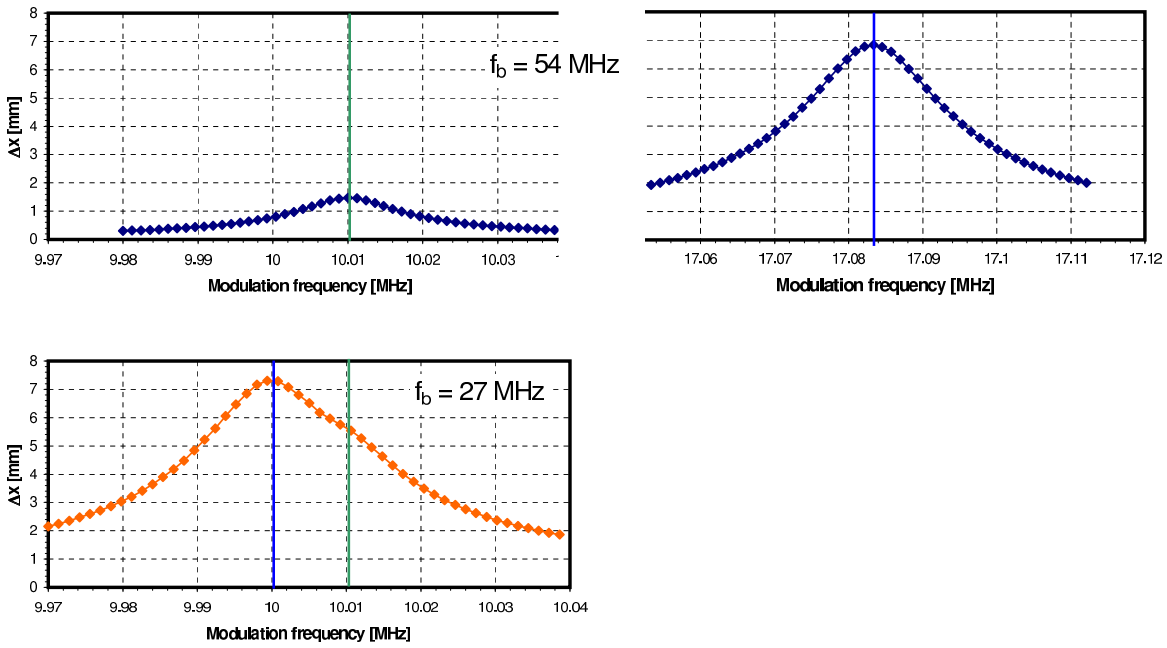

Figure 5.10: Δx variation with the modulation frequency around the resonances for the two modes listed in Table 5.3, for $\omega_b/(2\pi) = 54.17$ MHz (above) and 27.08 MHz (below).

that the sine modulation of the bunch charges is reflected by the modulation in transverse positions. The amplitude of this transverse position modulation increases at the BPM. For a bunch frequency of 27 MHz (Fig. 5.12), mode 1 is excited in cavity 4. In cavity 8 mode 1 is excited, leading to an addition to the offset amplitude.

The above example shows that the resolving power is higher at higher bunch frequency, but it does not state that such a resonance overlapping necessarily occurs in practice. This depends on the frequencies of the modes with high impedance. It is also to remark that at very high bunch frequency the time required to scan the whole frequency range $(0 \div \omega_b/2)$ is longer since the scan step does not depend on ω_b.

If several resonances overlap, it is possible to identify the modes by looking at the signal picked up from the HOM couplers with a spectrum analyzer. One has to search for modes in each of the eight cavities and around all frequencies that satisfy relation 5.3. This procedure is very time consuming.

A faster method may be to detune, for each resonance, the cavities one by one, until the mode frequency does not satisfy the resonance condition anymore and Δx is reduced to the BPM resolution level. If, in spite of a large detuning one would observe that the resonance amplitude is only diminished without disappearing, then a mode is excited in another cavity as well. By keeping the first cavity detuned, one can detune further the other cavities until the resonance vanishes completely. In this way one can identify the cavities where HOMs are excited. The next step is to find the frequency of the modes using a spectrum analyzer.

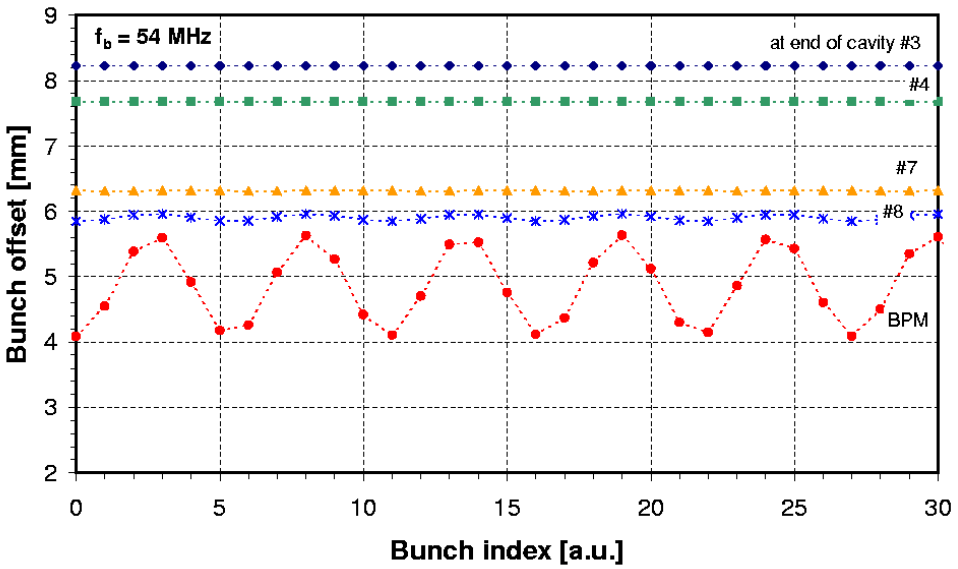

Figure 5.11: Evolution of the bunch offsets at the exits of various cavities along module ACC1 and at the BPM, for a bunch frequency of 54 MHz and a modulation frequency of 10.01 MHz. The bunch train enter the first cavity with an offset of 10 mm. The bunches are in the steady state of the pulse. Only mode 2 in cavity 8 (Table 5.3) is excited .

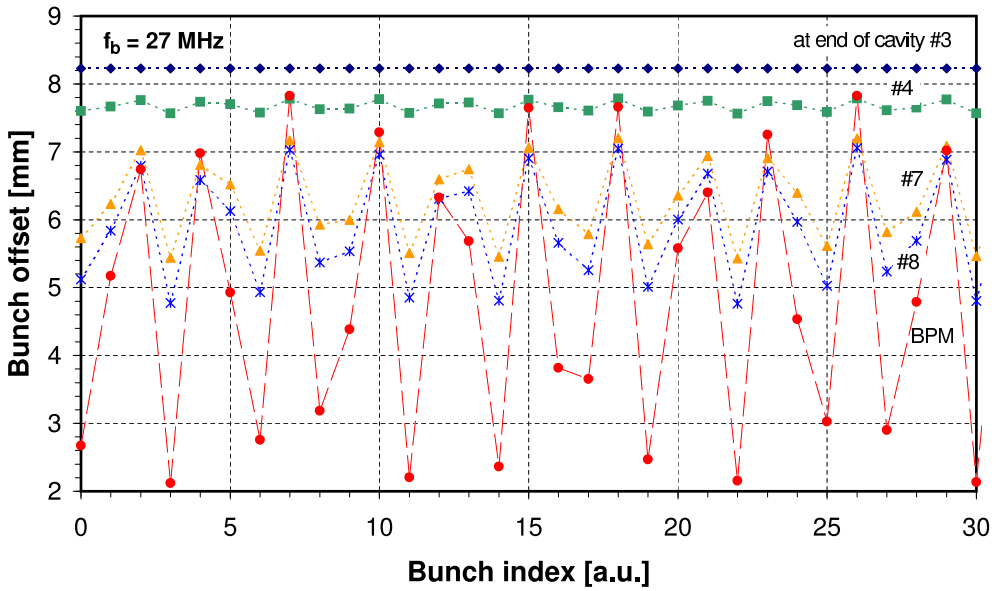

Figure 5.12: Evolution of the bunch offsets at the exits of various cavities along module ACC1 and at the BPM, for a bunch frequency of 27 MHz and a modulation frequency of 10.01 MHz. The bunch train enter the first cavity with an offset of 10 mm. The bunches are in the steady state of the pulse. Mode 1 is excited in cavity 4 and then mode 2 in cavity 8.

Expected BPM signal

The experimental conditions with the present linac are different compared to the previous ones (section 5.3.2). The bunch frequency is different, but also other parameters (Table 5.1): The energy at the entrance of the module is 16 MeV instead of 10 MeV. The BPM has been moved upstream in the straight section of bunch compressor, being now at 6.5 m (instead of 10 m) behind the end of the module. At the same time, the cryo-module placed at position ACC1 is a different one (see Fig. 5.1): Module 1 was replaced by module 3.

In Fig. 5.7 an example was given for the BPM pulse pattern when using injector 1 ($\omega_b/(2\pi)$ = 216 MHz), when exciting a mode on resonance. The same mode excited resonantly with injector 2 with a bunch frequency of $\omega_b/(2\pi)$ = 54 MHz, is shown in Fig. 5.13. In order to compare to Fig. 5.7, the same parameters were chosen in both cases, as given in Table 5.4. As it can be seen, the offset amplitude, Δx is the same in both cases (Figs. 5.7 and 5.13). This follows from eq. 5.10: for the same average current, Δx obtained by exciting a mode is the same for both injectors. The time needed to reach the steady state is also the same with both injectors.

In Fig. 5.14 a possible scenario for exciting the beam off-resonance is shown. The modulation frequency is chosen away from resonance: $\omega_{mod}/(2\pi) = \omega_{mod1}/(2\pi)(1 + 0.005)$. The maxima of the amplitudes are spaced by about 10 μs, that corresponds

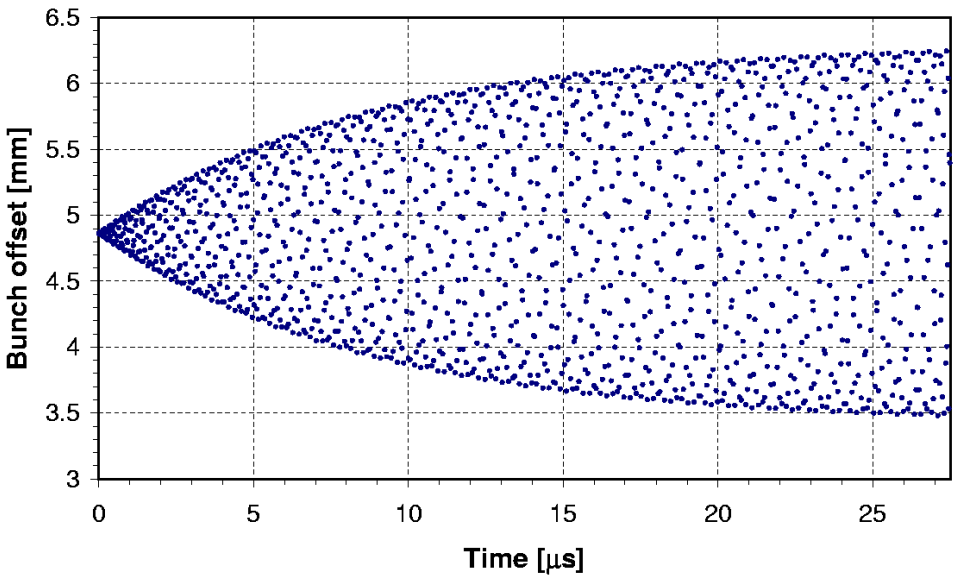

Figure 5.13: Bunch offsets at the BPM location for the case of exciting a dipole mode on resonance in cavity 8, with a 54 MHz beam. The same mode was excited and the similar beam and machine properties (as in the present linac) were used as in Fig. 5.7. Bunch properties: $\omega_b/(2\pi)$ = 54 MHz, q_0 = 0.15 nC, I_0 = 8 mA, δx_0 = 10 mm, E_0 = 16 MeV. Gradient 2 MV/m. HOM properties: $\omega/(2\pi)$ = 1.876 GHz, R/Q = 9 Ω/cm^2, $Q = 5 \cdot 10^4$. Modulation: $\omega_{mod}/(2\pi)$ = 19.833 MHz (resonant mode excitation), amplitude λ = 80 %. Distance cavity-BPM: 6.5 m.

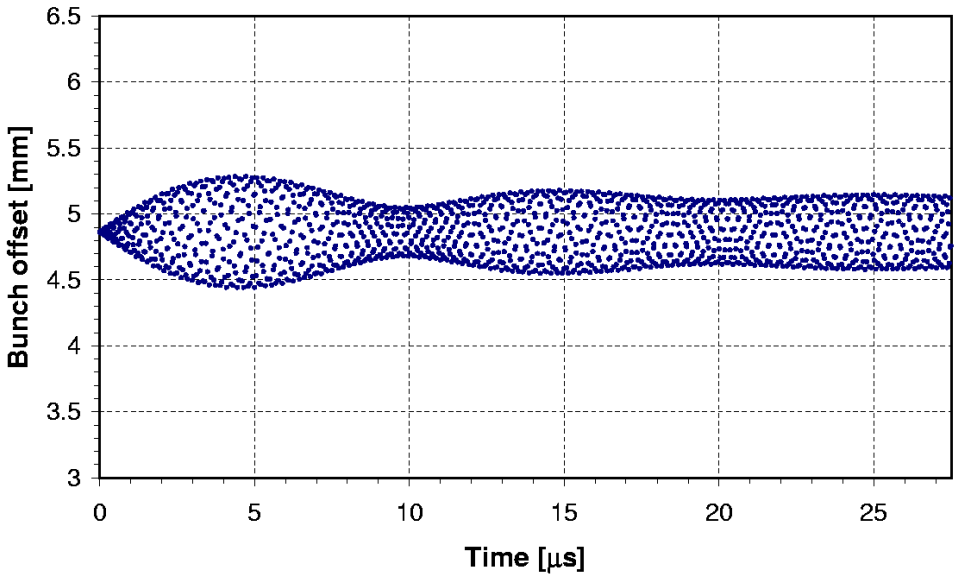

Figure 5.14: Bunch offsets at the BPM location for the case of exciting a dipole mode off resonance ($\omega_{mod}/(2\pi)$ = 19.833 + 0.099 MHz) in cavity 8, with a 54 MHz beam. The beam parameters are the same as in Fig. 5.13.

Bunch frequency $\omega_b/(2\pi)$	[MHz]	54.17
Average bunch charge q_0	[nC]	0.15
Average beam current	[mA]	8.13
Modulation amplitude λ	%	80
Gradient	[MV/m]	2
Energy at entrance of		
- cavity 1	[MHz]	16
- cavity 8	[MHz]	30
Distance end of cav. - BPM		
- cavity 1	[m]	16.182
- cavity 8	[m]	6.488

Table 5.4: Beam parameters used for simulation of HOM experiments with injector 2.

to the offset from resonance of 99 kHz. At the same time, Δx is also drastically reduced. In this example Δx may still be distinguished on the BPM, but for other modes this may come too close to the BPM resolution, which is 100 μm [61]. Therefore the step size used in the modulation frequency scan should be chosen small enough in order to not miss any important resonance. If we assume that the highest Q that a mode may have is in the order of 10^6, which is the highest value previously measured for a HOM in a TESLA cavity, then the smallest full width at half maximum (FWHM) is of the order of 2 kHz.

In Fig. 5.15 a scan of the current modulation frequency is simulated around the resonance for a mode with $Q = 10^6$. The initial energy and the BPM position are the ones used in the present linac. It is assumed that the mode is excited in cavity 8, the

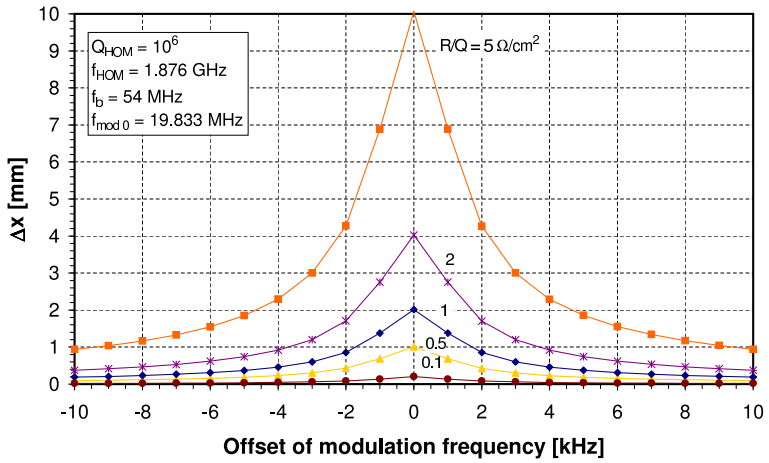

Figure 5.15: Scans of the modulation frequency around the resonance for a hypothetical mode at 1.876 GHz in cavity 8. Different values are assumed for R/Q, while Q is the same for all curves.

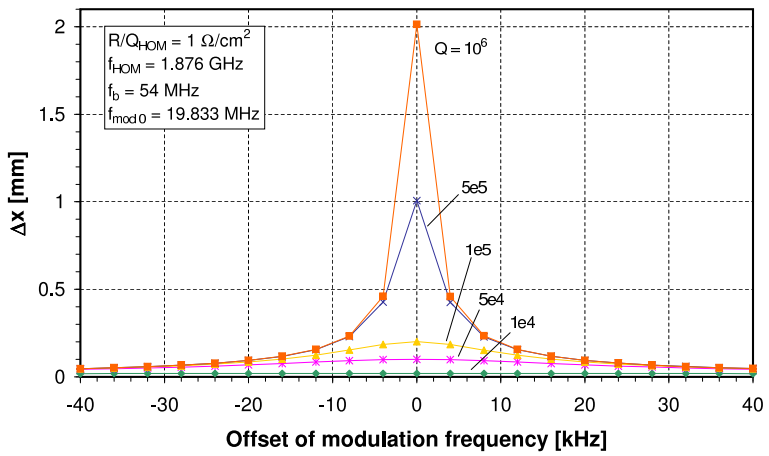

Figure 5.16: Scans of the modulation frequency around the resonance for a hypothetical mode at 1.876 GHz in cavity 8. Different values are assumed for Q, while R/Q is the same for all curves.

last of the module, which is the most unfavorable case. The other characteristics of the mode and of the bunch train are given in the figure. Different values for R/Q are considered. As it can be seen, for a given Q, the R/Q determines the magnitude of Δx at the BPM and the various curves have similar shape. The lowest curve with $R/Q = 0.1\ \mathrm{M\Omega/cm^2}$ gives a maximum $\Delta x = 200\ \mu$m. An offset of $\omega_{mod}/(2\pi)$ of 1.7 kHz reduces this value to about half (for this Q) which is about at the resolution limit of the BPM. Therefore we deduce that for modes with $Q = 10^6$ and $R/Q \geq 0.1\ \mathrm{M\Omega/cm^2}$ a step of 2 kHz, that is less than FWHM, is about the largest that still allows the detection of the mode, under the assumptions made for the beam in this simulation and summarized in Table 5.4

In Fig. 5.16, scans are made around the resonance for the same mode, for various Q values. R/Q is 1 $\Omega/\mathrm{cm^2}$. For $Q = 10^5$, the resonant amplitude is 200 μm. An offset of the modulation frequency of 16 kHz reduces Δx by a factor two. From Figs. 5.15 and 5.16 we can deduce the necessary step size for the frequency scan. If we want to study all modes with a $(R/Q)Q > 0.1\ \mathrm{M\Omega/cm^2}$ and if we assume that the highest Q is 10^6, then the most unfavorable case ($R/Q = 0.1\ \Omega/\mathrm{cm^2}$ and $Q = 10^6$) is shown in Fig. 5.15. Then a step of 1 kHz is sufficient in order to excite such a mode during the modulation scan and obtain a Δx above the resolution of the BPM. To the questions what modes we can "see" with this kind of experiment, I will come back in the next paragraph.

Simulation of a modulation frequency scan

The frequencies and quality factors for both polarizations of most of the modes of the first and second dipole passbands have been measured with a network analyzer at the cavities of module 3 [62]. The R/Q values are known from simulations [60]. One polarization of each mode was used to simulate the HOM experiments, as listed in Table 5.5. In some cavities a mode in the third passband could be measured as well. The beam parameters are as given in Table 5.4.

First, the resonant excitation of each mode of index l is calculated, with a frequency of the intensity modulation given by eq. 5.3. It is assumed that only one mode can satisfy the resonance condition for a given ω_{mod}. The beam is injected with a 10 mm offset in cavity 1 and then transported to the entrance of the middle of the cavity where mode l is excited. The offset amplitude of the bunch train in the steady state is then calculated with eq. 5.10. From here the offset amplitude Δx at the BPM is obtained, by further beam transport.

The resulting offset amplitude caused by the modes of cavity 8 is plotted against $(R/Q)Q$ in Fig. 5.17. The dependence is almost linear. The slight deviations from linearity are due to the difference in frequency of the modes (see eq. 5.10).

This plot gives us the possibility to estimate which modes can be studied with the experimental method described in this chapter, with the present linac setup. A mode with $(R/Q)Q = 0.05\ \mathrm{M\Omega/cm^2}$ leads to a magnitude of about 100 μm, which is the BPM resolution. For the modes in the first cavities, a higher offset amplitude at the BPM is achieved. A mode with $(R/Q)Q = 0.02\ \mathrm{M\Omega/cm^2}$ in the first cavity leads to an offset amplitude at the BPM higher than 200 μm.

Cavity							
#1	#2	#3	#4	#5	#6	#7	#8
TE_{111}-like							
1.617079 $8.5 \cdot 10^5$	1.616201 $8.5 \cdot 10^5$	1.622150 $7.1 \cdot 10^5$		1.618742 $5.2 \cdot 10^5$	1.618229 $4.2 \cdot 10^5$	1.622908 $4.2 \cdot 10^5$	1.617510 $5.6 \cdot 10^5$
1.625270 $1.6 \cdot 10^5$	1.623986 $2.1 \cdot 10^5$	1.629685 $1.5 \cdot 10^5$		1.626876 $1.1 \cdot 10^5$	1.625813 $1.1 \cdot 10^5$	1.630580 $1.1 \cdot 10^5$	1.625999 $1.6 \cdot 10^5$
1.638514	1.637066 $1.1 \cdot 10^5$	1.642157 $2.1 \cdot 10^4$		1.639050 $1.5 \cdot 10^4$	1.639172 $5.6 \cdot 10^4$	1.643758 $3.7 \cdot 10^4$	1.638941 $4.8 \cdot 10^4$
1.655608 $9.2 \cdot 10^3$	1.655410 $6.9 \cdot 10^4$	1.660232 $6.1 \cdot 10^4$		1.657696 $3.6 \cdot 10^4$	1.657335 $4.0 \cdot 10^4$	1.661562 $2.7 \cdot 10^4$	1.656011 $4.1 \cdot 10^4$
	1.677916 $4.5 \cdot 10^4$	1.682453 $4.3 \cdot 10^4$		1.679891 $1.4 \cdot 10^4$	1.679550 $2.1 \cdot 10^4$	1.684032 $1.6 \cdot 10^4$	1.679989 $2.1 \cdot 10^4$
	1.703379 $4.1 \cdot 10^4$	1.708446 $1.9 \cdot 10^4$			1.705162 $1.4 \cdot 10^4$	1.709871	1.705160 $5.3 \cdot 10^3$
	1.731503 $2.8 \cdot 10^4$	1.735716 $1.0 \cdot 10^4$			1.732980 $3.3 \cdot 10^3$	1.737385 $7.8 \cdot 10^3$	1.731928 $4.9 \cdot 10^3$
	1.759601 $2.0 \cdot 10^4$	1.763793 $3.1 \cdot 10^4$		1.761332 $5.3 \cdot 10^3$			
1.787634 $5.2 \cdot 10^3$	1.786911 $1.0 \cdot 10^4$			1.787691 $2.0 \cdot 10^3$			
TM_{110}-like							
1.797261 $5.5 \cdot 10^3$	1.796301 $2.3 \cdot 10^4$	1.797838 $9.7 \cdot 10^3$		1.797060 $3.0 \cdot 10^3$	1.797594 $4.1 \cdot 10^3$	1.795788 $3.7 \cdot 10^3$	1.797002 $6.3 \cdot 10^3$
1.837920 $2.4 \cdot 10^4$	1.837506 $1.0 \cdot 10^5$	1.844618 $2.4 \cdot 10^4$		1.839634 $1.3 \cdot 10^4$	1.839524 $2.5 \cdot 10^4$	1.847363 $5.2 \cdot 10^4$	1.839458 $5.1 \cdot 10^4$
1.853905 $1.1 \cdot 10^4$	1.852563 $6.5 \cdot 10^4$			1.854967 $2.3 \cdot 10^4$	1.854147 $1.7 \cdot 10^4$	1.858570 $2.3 \cdot 10^4$	1.855466 $4.0 \cdot 10^4$
1.866031 $1.4 \cdot 10^4$	1.864410 $5.8 \cdot 10^4$	1.868574 $6.9 \cdot 10^4$		1.866244 $1.8 \cdot 10^4$	1.866055 $2.1 \cdot 10^4$	1.868064 $4.7 \cdot 10^4$	1.866405 $4.2 \cdot 10^4$
1.874507 $2.4 \cdot 10^4$	1.873320 $4.8 \cdot 10^4$			1.875091 $2.5 \cdot 10^4$	1.874920 $2.9 \cdot 10^4$	1.874861 $3.9 \cdot 10^4$	1.874458 $3.0 \cdot 10^4$
1.880750 $3.9 \cdot 10^4$	1.879626 $2.6 \cdot 10^5$	1.881683 $1.9 \cdot 10^4$		1.880819 $3.4 \cdot 10^4$	1.880790 $3.4 \cdot 10^4$	1.879206 $4.5 \cdot 10^4$	1.880845 $4.6 \cdot 10^4$
1.884660 $5.7 \cdot 10^4$	1.883320 $2.8 \cdot 10^5$	1.885119 $6.0 \cdot 10^4$		1.884814 $5.6 \cdot 10^4$	1.884670 $7.0 \cdot 10^4$	1.882098 $8.0 \cdot 10^4$	1.884952 $1.1 \cdot 10^5$
1.887038 $1.1 \cdot 10^5$	1.886775	1.887134 $5.7 \cdot 10^4$		1.887104 $1.1 \cdot 10^5$	1.887068 $1.3 \cdot 10^5$	1.884059 $9.4 \cdot 10^4$	1.884952 $1.1 \cdot 10^5$
1.888228 $3.5 \cdot 10^5$	1.885566 $5.6 \cdot 10^5$	1.888140 $2.0 \cdot 10^5$		1.888363 $4.5 \cdot 10^5$	1.888143 $2.3 \cdot 10^5$	1.884641 $1.9 \cdot 10^5$	1.887818 $2.2 \cdot 10^5$
TE-like							
2.577227 $9.1 \cdot 10^4$						2.590641 $6.5 \cdot 10^5$	2.579804 $1.4 \cdot 10^5$

Table 5.5: Dipole modes measured in the cavities of module 3 [62]. One polarization of each dipole mode is listed, as used for the simulation of the HOM experiment. For cavity 4 as well as for some modes of the other cavities no data are available. In each cell of the table, the upper number is the frequency in GHz and the lower number is the quality factor.

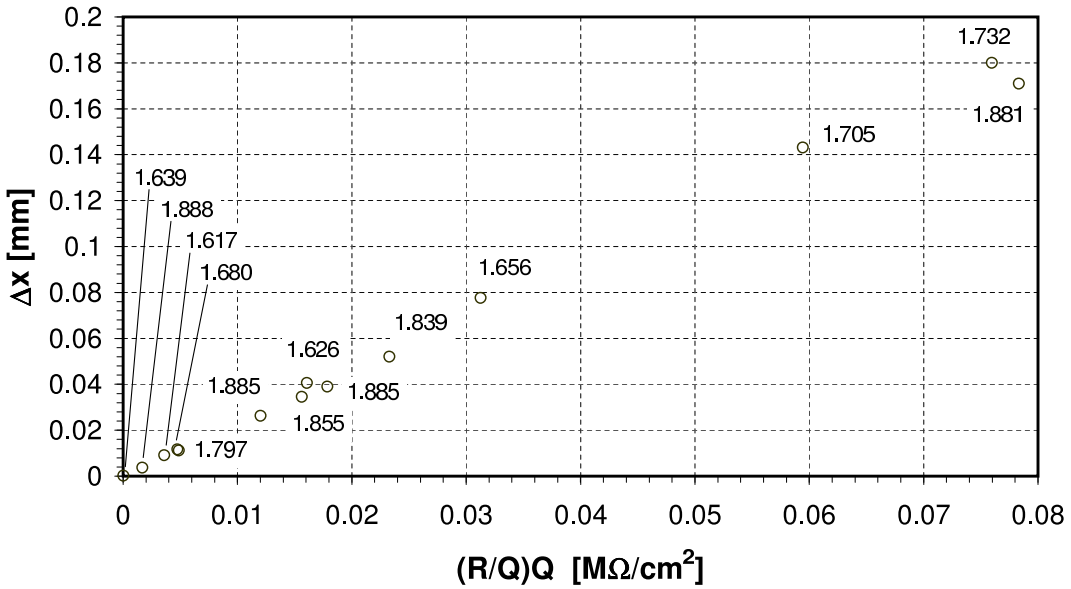

Figure 5.17: Calculated offset amplitude Δx at the BPM as a function of the $(R/Q)Q$ of the resonantly excited dipole modes of cavity 8. The number attached to each point represents the frequency of the excited mode (in GHz).

In making the above estimations about which modes can be detected, we assume the parameters from Table 5.4 and that the modes are excited on resonance. The quadrupoles between cavity 8 and the BPM are switched off. Also, the assumption is made that the modes have a horizontal polarization. This is the optimal case in our experiment since we produce horizontal offsets and hence measure horizontal deflections. Since, in reality, the modes can have other polarization directions as well, the measured Δx is expected to be smaller than the ones obtained in the simulations.

If ω_{mod} is only near a resonance, then Δx depends on the frequency offset as shown in Figs. 5.15 and 5.16. By considering the modes already measured at the cavities of module 3 (Table 5.5), a scan of the modulation frequency is simulated. It is considered that the bunch train is long enough so that the steady state is achieved. The maximum and minimum of the bunch offset is calculated and from here Δx. A frequency step of 10 kHz is assumed. In Fig. 5.18 the computed Δx is displayed as a function of $\omega_{mod}/(2\pi)$. On the same plot, the circles represent the case of exciting each mode on resonance (eq. 5.10). In some cases, due to the offset of ω_{mod} with respect to resonant frequency or to the cancelation of the effect of 2 or more modes, the amplitude is diminished, for example at about 9.2 and 16.2 MHz. Other peaks, like the ones at about 4.7 and 15 MHz, result from excitations of two or more modes.

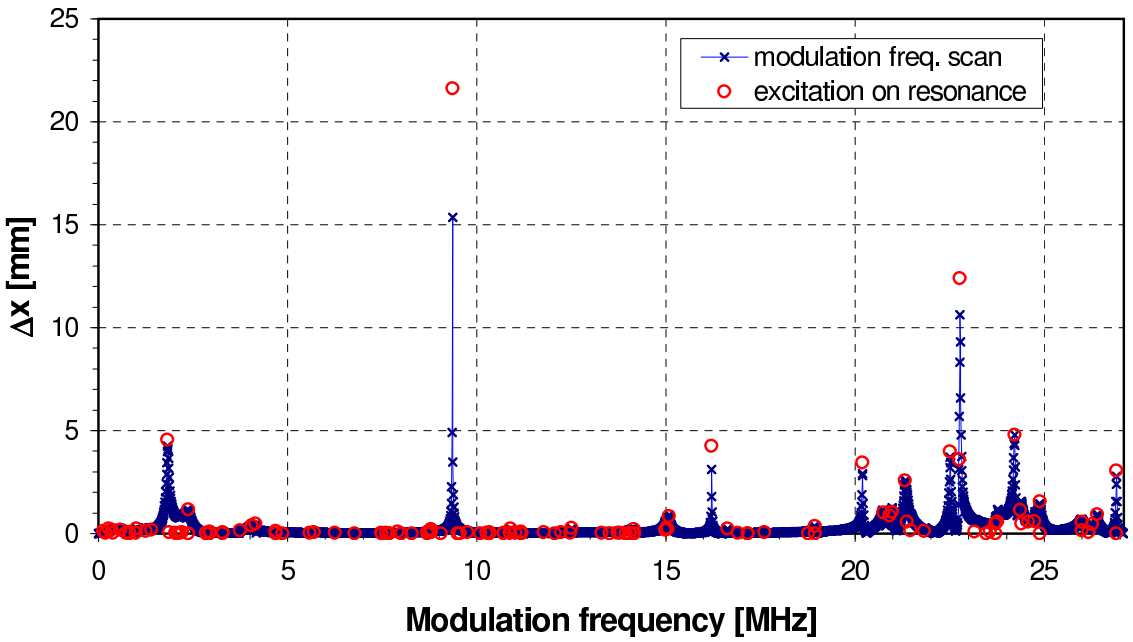

a.

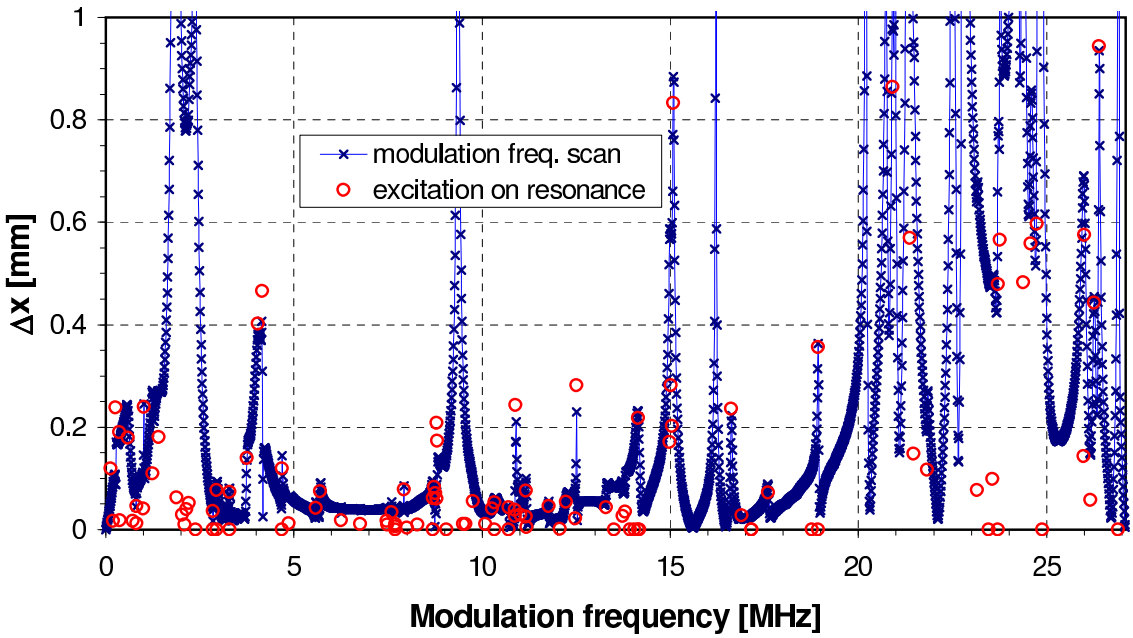

b.

Figure 5.18: (a) Simulated scan of the modulation frequency with a bunch frequency of 54 MHz. The known modes of module 3 can be excited. The modulation frequency step is 10 kHz. The circles represent the case of exciting the modes on resonance. (b) Enlarged view.

5.3.4 Measurements and results

Experimental setup

The experimental setup is shown in Fig. 5.19 [63]. The charge of the bunches was modulated by a sinusoidal modulation of the polarization of the photo-cathode laser [64]. Pulses of up to 800 μs length, an average current of 2 to 8 mA and an energy of 16 MeV, was sent through the accelerating module (TTF module 3). A pair of deflecting magnets was used to transversely shift the bunch train by up to $\pm$ 20 mm. The transverse positions of the bunches were measured by a broad-band BPM [65]. The quadrupoles between the module and the BPM were switched off. The electrons traveled then through a second module (TTF module 2). The final energy of the beam was below 50 MeV, low enough to allow its dumping in the collimator [66] in order to protect the undulator.

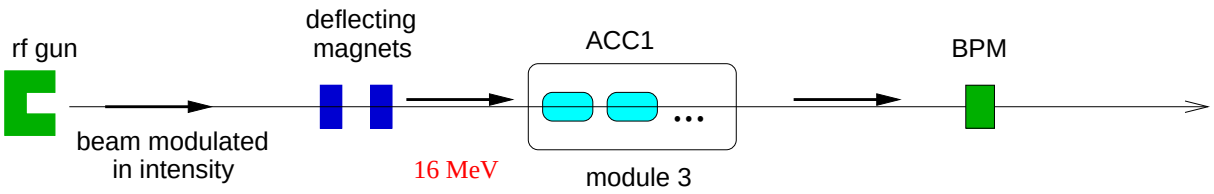

Figure 5.19: Setup for experiment with intensity modulated beam.

BPM signal

The sum of the signals of two opposite horizontal pick-ups is proportional to the bunch charges, while the difference contains information about the transverse position of the bunches multiplied by the charge. An example of the BPM difference signal, measured for a frequency of the charge modulation of 23.765 MHz, is given in Fig. 5.20. The BPM gives a symmetric signal, not differentiating between displacements to the right or to the left. The beam was centered in the BPM by minimizing the amplitude of the signal. The first 50 μs of the beam are not modulated. This part of the beam was used for the fast protection system of the accelerator. The signal increase reflects the increase in current, since it is not normalized to the charge.

About 400 μs of the train are modulated in intensity. The modulation amplitude is in this case $\pm$ 80 %. The signal magnitude increases due to the increase in the average bunch charge. The amplitude of the signal varies from pulse to pulse due to variations in beam current and position.

The experiment started with the excitation of known modes which in simulations gave large effects of the transverse position of the bunches (see Fig. 5.18). We note that the simulations assumed that all modes have a horizontal polarization. Two such modes are listed in Table 5.6. Their frequencies and quality factors have been previously measured with a network analyzer (precision $\pm$ 10 kHz).

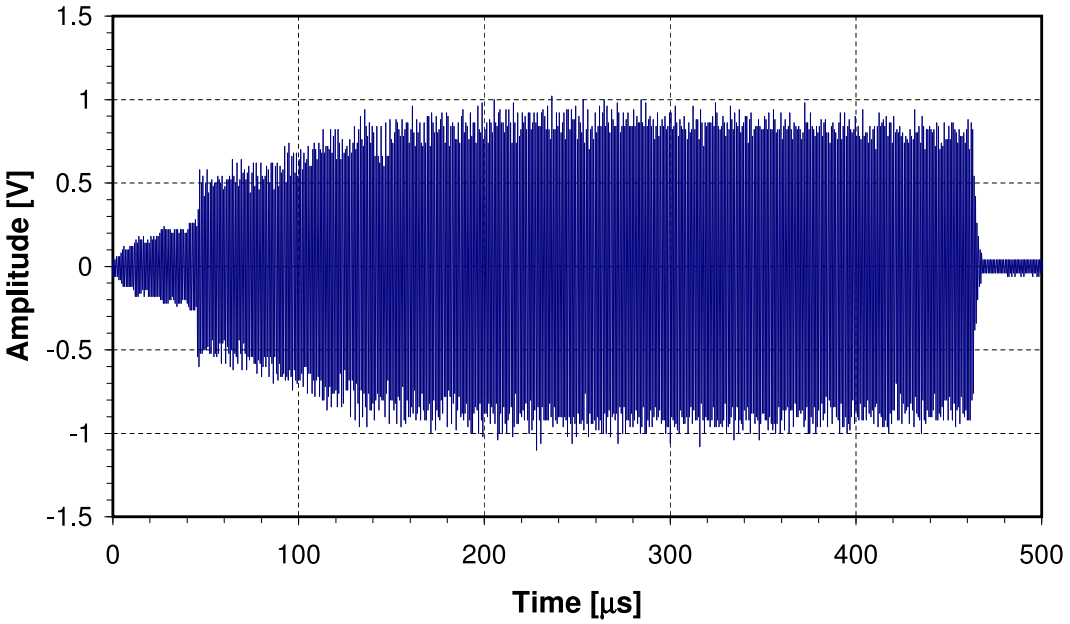

Figure 5.20: BPM difference signal, for a modulation frequency of 23.765 MHz. The first 50 μs of the train are not modulated in intensity.

Cavity	Dipole passbd.	$\omega_l/(2\pi)$ [GHz]	$(R/Q)_l$ [Ω/cm^2]	Q_l	$((R/Q)Q)_l$ [$\mathrm{M}\Omega/\mathrm{cm}^2$]	$\omega_{mod}/(2\pi)$ [MHz]	Δx [mm]
1	2nd	1.8747432	8.7	$1.14 \cdot 10^5$	1	21.089596	11
7	3rd	2.590641	15	$6.46 \cdot 10^5$	9.7	9.3582	20

Table 5.6: Two dipole modes in cavities of module 3, that in simulation give a maximum Δx at the BPM (last column) by assuming that the mode is horizontally polarized. The mode frequency and quality factor are measured values. R/Q is taken from simulations. The modulation frequency ω_{mod} is given by eq. 5.3.

The modulation frequency was varied around the resonance value. A change in the amplitude of the BPM signal was expected, similar to Fig. 5.9. But in spite of the maximum beam current and offset and careful design of electronics for the BPM, no change was observed in the BPM signal with ω_{mod}. The changes in the BPM signal with the modulation frequency are most likely smaller than the instability of the beam current and position. Therefore the BPM signal was filtered around the resonance frequency.

Filtered BPM signal

The resonance could be detected by frequency analyzing the BPM difference signal, filtered around 650 MHz $\pm\ \omega_{mod}/(2\pi)$, where 650 MHz is the resonance frequency of the BPM ($Q = 4$). In Fig. 5.21 the spectrum of the BPM difference signal is schematically shown. The central signal represents a bunch harmonic. In particular, the harmonics which are near a main resonance of the BPM are chosen. On either side of it, at $\pm\omega_{mod}$, a signal given by the modulation of the bunch charges is present. The signal is filtered around one sideband with the help of a spectrum analyzer (Fig. 5.22) and plotted in time domain.

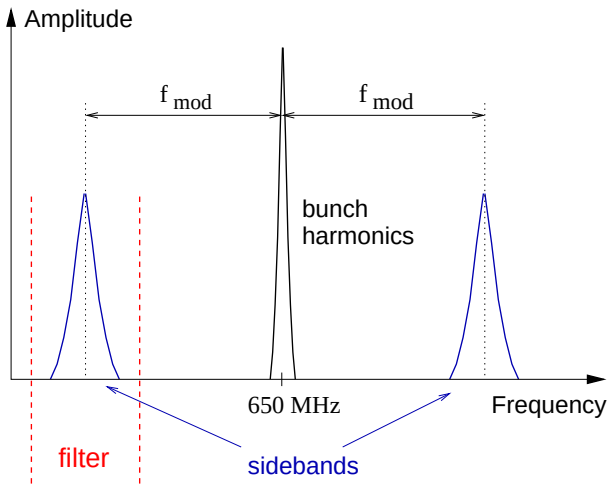

Figure 5.21: Spectrum of the BPM difference signal schematically drawn. The central peak represents a bunch harmonics. On either side of it there is a signal from the current modulation. The BPM signal is filtered around one of the side bands, as shown in Fig. 5.22.

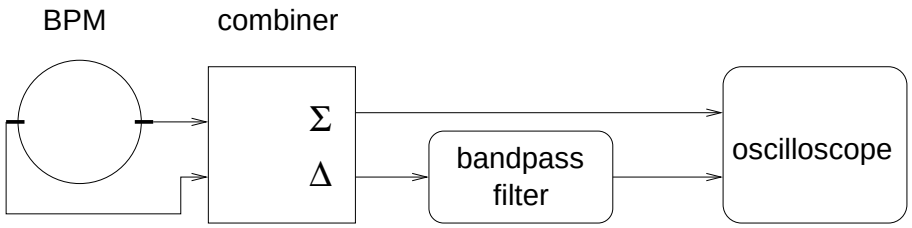

Figure 5.22: Setup for filtering the BPM difference signal. A spectrum analyzer is used as a bandpass filter.

The filtered BPM difference signal is shown in Fig. 5.23 for two values of $\omega_{mod}/(2\pi)$ around 21.09 MHz, which is the resonant frequency for the first mode listed in Table 5.6. The origin of the time coordinate marks here the beginning of the current modulation. The envelope of the bunch offsets is shown. The current is modulated

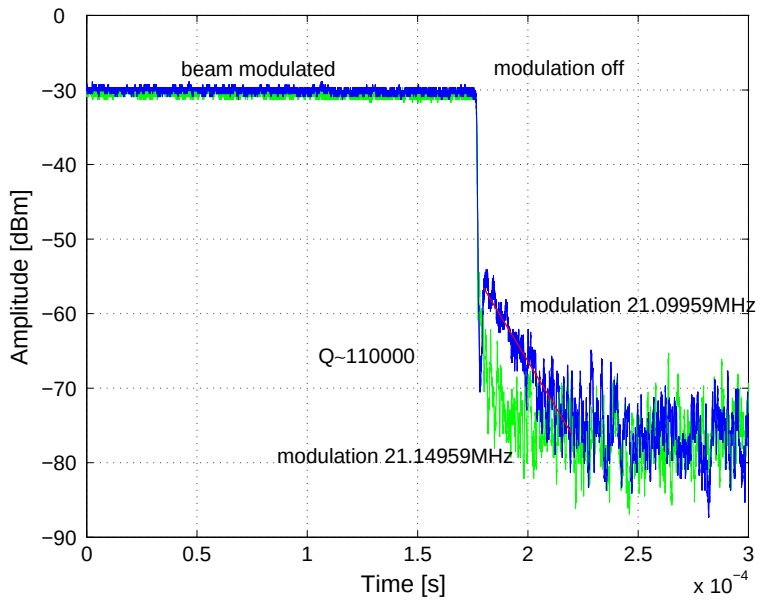

Figure 5.23: Filtered BPM difference signal for $\omega_{mod}/(2\pi) = 21.09959$ (on resonance) and 21.14959 MHz (off resonance) [67].

over 180 μs. The last part (the tail) of the bunch train is not modulated. The total length of the bunch train is 500 μs.

If no HOM satisfies eq. 5.3, the bunches of the unmodulated tail do not change their offsets. At the BPM, the constant offsets give no signal after filtering. This is the case in the lower curve in the figure. If a mode is resonantly excited, then, the electromagnetic field continues to oscillate after the modulated part of the beam has exited the cavity. Its amplitude decays exponentially in time (see eq. 3.16):

$$\propto \exp\left(-\frac{\omega_l}{2Q_l}t\right) = \exp\left(-\frac{t}{\tau_l}\right), \tag{5.11}$$

where τ_l is the decay time of mode with index l. The bunches of the tail of the train are deflected by the field, sampling the field strength. The bunch offsets at the BPM are modulated with a frequency given by ω_{mod}. The filtered signal is then proportional to the amplitude of the modulation of the transverse positions, that decays like the mode in the cavity. This case is illustrated by the upper curve in Fig. 5.23 ($\omega_{mod}/(2\pi)$ = 21.09959 MHz). The decay time is estimated with the help of a linear fit (in the logarithmic scale) to 19 μs and the quality factor is $1.1 \cdot 10^5$, in good agreement with previous measurements.

Fig. 5.24 shows the BPM signal (in linear scale) around another resonance, at $\omega_{mod}/(2\pi)$ = 23.776 MHz. When no HOM is resonantly excited (a), the bunches in the tail of the beam give zero signal. As a mode starts to be excited the tail of the bunch is deflected (b). At the same time on the modulated part of the beam an oscillation on the envelope is visible, similar to Fig. 5.9. This is another sign that we approach a resonance (about 15 kHz off resonance). As the modulation frequency is further increased, the offset of the bunches in the beam tail increases (c) and is maximum at resonance

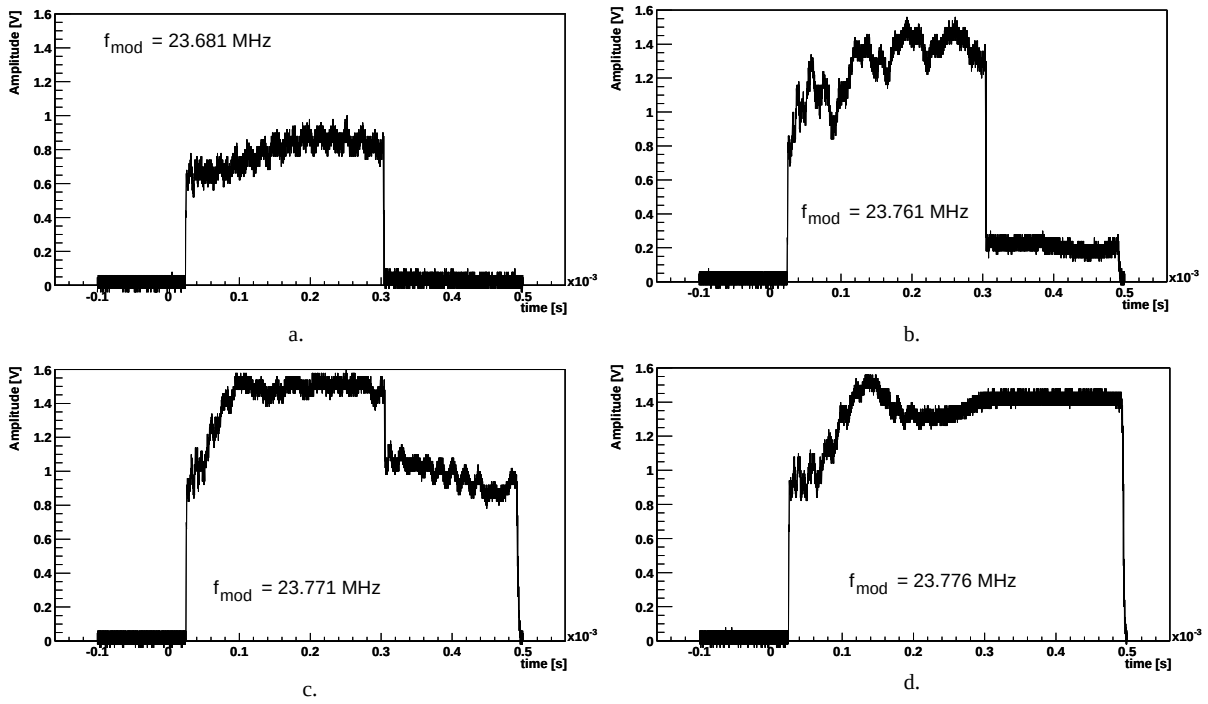

Figure 5.24: Filtered BPM difference signal for $\omega_{mod}/(2\pi)$ around 23.776 MHz. The signal approaches a resonance as the modulation frequency is increased.

(d). The very slow decay indicates a very high Q value of the excited mode. The slow decay of the relatively short bunch train made it impossible to estimate the quality factor with a good accuracy. Saturation of the BPM electronics is observed at maximum resonance, when the BPM signal is above 1.5 V. This corresponds to a displacement of 3.6 mm.

Scan of modulation frequency

In order to find the strongest HOM resonances, a scan of the modulation frequency was made in 1 kHz steps. For each step, the amplitude of the filtered BPM signal for the unmodulated tail of the bunch train was measured, at the moment when the modulation ceases. If the modulated part of the beam is long enough so that on resonance the steady state is reached, then this value, which is proportional to the field amplitude of the excited mode with index l, is proportional to Δx (eq. 5.10) and to:

$$\frac{1}{\omega_l}\left[\left(\frac{R}{Q}\right)Q\right]_l. \tag{5.12}$$

In some cases this is not true because the steady state is not reached, like in Fig. 5.24. The signal of the modulated part of the beam reaches a constant value due to the saturation of the electronics.

In Fig. 5.25 a section of the scan is compared to the simulations presented in section 5.3.3. Apart from the resonance at 24.2 MHz, no resonance from known modes can be

identified. The vertical scales for the two curves are different. Some other resonances are found at the expected values (e.g. at 24.7 MHz), but their width indicates a different Q and therefore a different excited mode. Some resonances from unknown modes are found, that were not taken into account in the simulations. The strongest effect in the figure can be seen for modulation frequencies of 24.32 and 23.75 MHz. The last one corresponds to the BPM signal shown in Fig. 5.24.

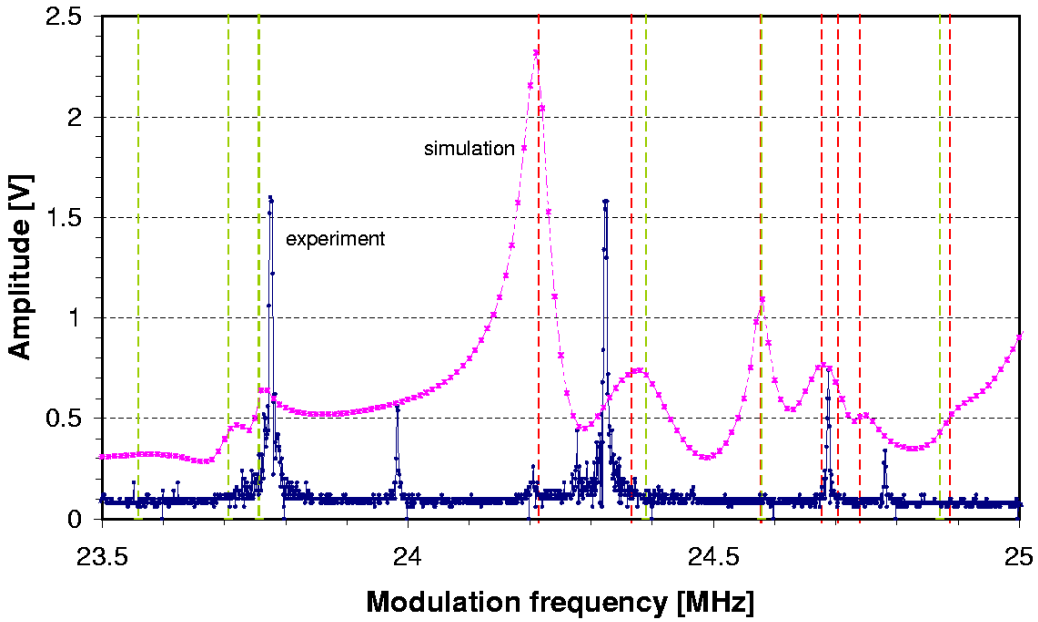

Figure 5.25: Modulation frequency scan for $\omega_{mod}/(2\pi)$ between 23.5 and 25 MHz (lower curve). The simulation result, based on the known modes with horizontal polarization (see section 5.3.3), is shown for comparison as well (upper curve). The dashed vertical lines mark the frequencies where resonances from previously measured modes of modules 3 (both polarizations) were expected.

Mode identification

For each resonance found on the BPM signal, the frequencies of the excited HOMs were determined using a spectrum analyzer connected to the HOM couplers [45]. The measurements were done in time domain for all frequencies that satisfy eq. 5.3. The beam was in this case modulated over the entire train length, except for the first 50 μs. When a mode was excited, the decay time of the mode in the cavity could be seen and measured. Often more modes were found, in various cavities, for the same resonance frequency.

An example of a HOM signal at resonance is given in Fig. 5.26 for $\omega_{mod}/(2\pi)$ = 23.776 MHz. The intensity modulated part of the beam covers the time interval from 50 to about 250 μs. The mode has a frequency of 3.06372405 GHz. The quality factor is determined from the decay time and is equal to $2 \cdot 10^6$. For the same modulation frequency, several other weaker modes were excited as well.

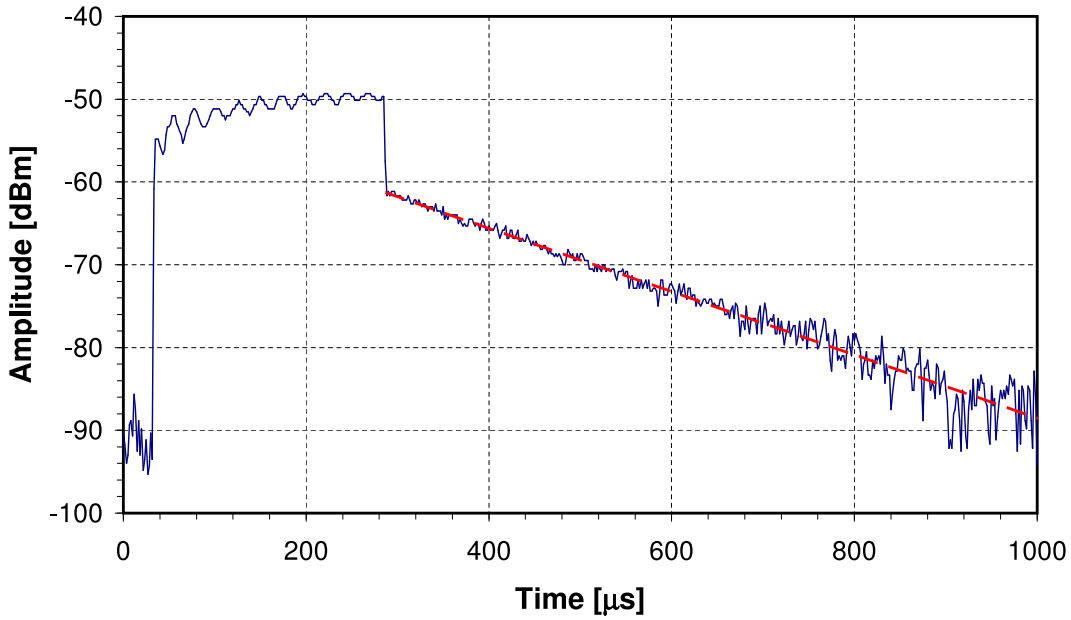

Figure 5.26: Time domain signal from a HOM coupler of cavity 1 measured with a spectrum analyzer. The signal was bandpass filtered around a mode at 3.06372405 GHz in the fifth passband.

For the mode of cavity 1 at 1.874 GHz (Table 5.6), the quality factor obtained from the signal at the HOM couplers is $1 \cdot 10^5$. This is in very good agreement with the value derived from the BPM difference signal (see page 5.23) and with previous measurements made with a network analyzer.

Polarization angle

The modes given in Table 5.6 showed a weaker BPM signal than in the simulations. In particular the mode at 2.59 GHz was difficult to identify. One reason could be that the polarization of the mode is not horizontal.

One can estimate the polarization direction of a mode by measuring the amplitude at a HOM coupler for equal horizontal and vertical offsets. When the beam goes with an offset δx through a cavity (see Fig. 5.27), then the amplitude of the excited field at the coupler location is proportional to the projection of the offset to the polarization direction.

$$A(\delta x, \delta y = 0) \propto \delta x \cdot \cos\varphi \qquad \text{and} \qquad A(\delta x = 0, \delta y) \propto \delta y \cdot \sin\varphi. \tag{5.13}$$

For $\delta x = \delta y$ then

$$\tan\varphi = \frac{A(\delta x = 0, \delta y)}{A(\delta x, \delta y = 0)}. \tag{5.14}$$

The amplitude of the signal at a coupler of cavity 7 centered on a frequency of 2.5906 GHz was measured as a function of the horizontal and vertical displacement

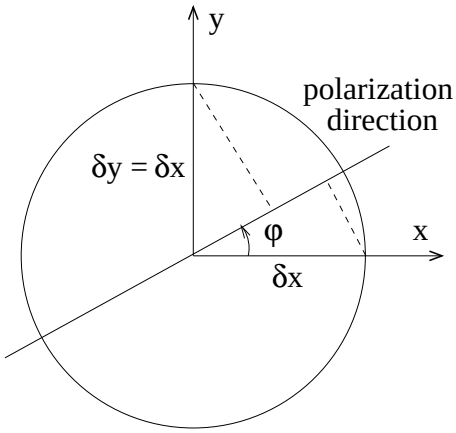

Figure 5.27: Sketch of mode polarization with respect to the axes.

of the beam. The curves obtained are shown in Fig. 5.28. The polarization angle is obtained from the ratio of the vertical and horizontal slopes. An angle of $77^\circ \pm 8^\circ$ is deduced. This explains in part why the effect at the BPM was much smaller than in the simulations, where a horizontal polarization was assumed. For a mode at 1.874 GHz in cavity 1, a polarization angle of $70^\circ \pm 7^\circ$ was measured.

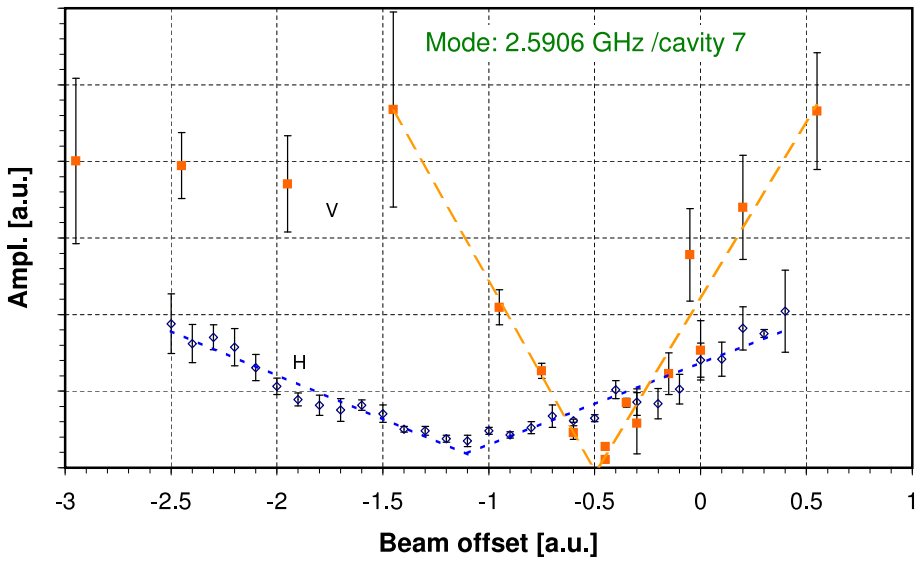

Figure 5.28: Amplitude of signal from HOM couplers as a function of the horizontal and vertical beam offset.

The R/Q values

The R/Q can be determined with help of eq. 5.10 by measuring the kick amplitude on the beam. In the right hand term a factor $\cos\varphi$ has to be introduced. For the mode at 1.874 GHz in cavity 1, a maximum offset amplitude of the beam (of the unmodulated part of the tail) Δx of 1.8 mm was measured. This translates into a kick amplitude of 200 μrad in the cavity. The beam characteristics are as follows: initial beam offset δx_0 = 19 mm, energy E = 16 MeV, current I_0 = 4 mA, modulation amplitude λ = 90 %. If we assume a horizontal polarization of the mode, then the computed R/Q is 1.8 Ω/cm^2. Taking into account the polarization measured for this mode of $70^\circ \pm 7^\circ$ (previous paragraph), then the result is $5.4\,^{+3.4}_{-1.5}$ Ω/cm^2. The upper value is close to the value given by simulations, of 8.7 Ω/cm^2.

During the scans, resonances from quadrupole modes were found as well (around 2.3 GHz and 2.79 GHz). Nevertheless they give only a second order effect on the transverse beam dynamics. Table 5.7 summarizes several dipole modes that were found in various cavities [61]. They have a high quality factor, that in a few cases were cross-checked by measurements with a network analyzer. These modes require future analysis. More results of the HOM experiment will be presented in [69].

$\omega/(2\pi)$ [GHz]	Cavity	Δx [mm]	Q (measured with beam)	Q (measured with NA)	R/Q (calculated) [Ω/cm^2]
2nd dipole passband					
1.8869	2 & 8	1.66	$4 \cdot 10^5$		
1.8805	1	2.94	10^5		2
3rd dipole passband					
2.5758	all	7.00	$3 \cdot 10^5$	$2.3 \cdot 10^5$ (through all module)	
4th dipole passband					
2.7924	6	0.96	$4.6 \cdot 10^6$		
5th dipole passband					
3.0637	1	> 7.2 (saturation)	$1.7 \cdot 10^7$	$1.7 \cdot 10^7$	1
3.0682	1	> 7.2 (saturation)	$7 \cdot 10^7$		
6th dipole passband					
3.3535	2 & 3	3.4	$6 \cdot 10^5$		
3.3567	3	> 7.2 (saturation)	$2 \cdot 10^5$		

Table 5.7: Dipole modes excited in the HOM experiment.

5.4 Investigations on Cavities of Module 1

In designing the HOM couplers for the accelerating cavities, special attention was given to the modes with high R/Q of the first and second dipole passbands. One of these is the mode studied in the HOM experiments described in section 5.3 with a frequency of 1.876 GHz, having $R/Q \approx 9$ MΩ/cm^2. In the third cavity of module 1, this mode was found to have $Q = 1.2 \cdot 10^5$, which is at the upper limit given in [11].

The third dipole passband is above the cut-off for TE modes in the beam pipe (approx. 2.25 GHz), and therefore it should propagate in the beam pipe and reach the HOM coupler locations. The HOM antennae (see section 5.2) couple to the electric and magnetic field. Two couplers are used in each 9-cell cavity, one on either side, that are positioned at a relative angle of 115 °. Therefore if the field of one mode does not couple to one antenna, it should couple to the other one, or even to the couplers belonging to the neighboring cavities (see Fig. 5.2).

Surprisingly, a mode was found to be badly damped in this passband, at 2.585 GHz. The R/Q of this mode is about 15 Ω/cm^2, which is very high. The studies made on this mode in order to find out why it is not well damped in some cavities are presented in this section.

5.4.1 Last mode of the third dipole passband

The frequency of the weakly damped mode in cavity 3 of the TTF module 1 is 2.585 GHz, about twice that of the accelerating mode. This mode is close to the light velocity curve on the phase diagram (see page 58), therefore its interaction with relativistic beams is particularly efficient. The group velocity is almost zero, which means that the energy can not propagate within the cavity and to the coupler, even if it is above the cut-off in the beam pipe.

In Figs. 5.29 and 5.30 the spectra of the 3rd passband for the second and third cavity in the module are shown. In both cases, many peaks at different frequencies can be seen. Individual modes (represented by the peaks) are hard or impossible to identify. For a single cavity, one passband is formed by 9 modes (equal to the number of cells), each with two polarizations (field directions). Therefore the frequency spectrum of a passband shows in general 9 double peaks. When 8 cavities are coupled by beam pipes and form a module, then each mode splits into more modes forming sub-passbands. If the cavities are identical, the frequencies of the new modes are close to those in the individual cavity. If in one cavity the last mode is higher in frequency, then in the cavity chain it can be identified as an individual mode, even if its properties are affected by the presence of the other cavities [71]. In the figures, the sub-passbands are mixed. The last mode of cavity 3 at 2.5845 GHz (marker 1 in Fig. 5.30) is higher in frequency than in the others, especially than in the neighboring cavities (the highest frequency for cavity 2 is 2.5796 GHz as seen in Fig. 5.29) and therefore can be clearly distinguished.

The same mode (the last of the third dipole passband) could be identified and measured at other cavities of the first 3 TTF modules where this passband is higher in frequency than in the neighboring ones. The measurements are summarized in Ta-

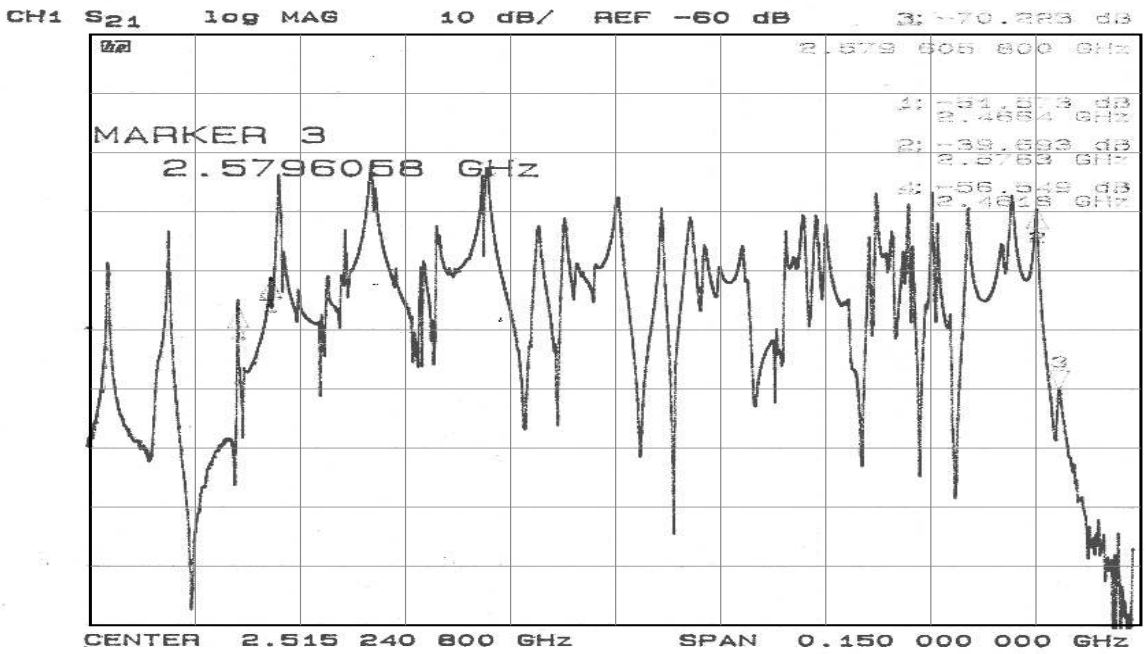

Figure 5.29: Transmission (S_{21} parameter) for cavity 2 (S8) of module 1 measured between its two HOM couplers (C2K1-C2K2). The frequency range is 2.4402408 ÷ 2.5902408 GHz, covering the third dipole passband. The vertical scale is logarithmic, with 10 dB per division[3].

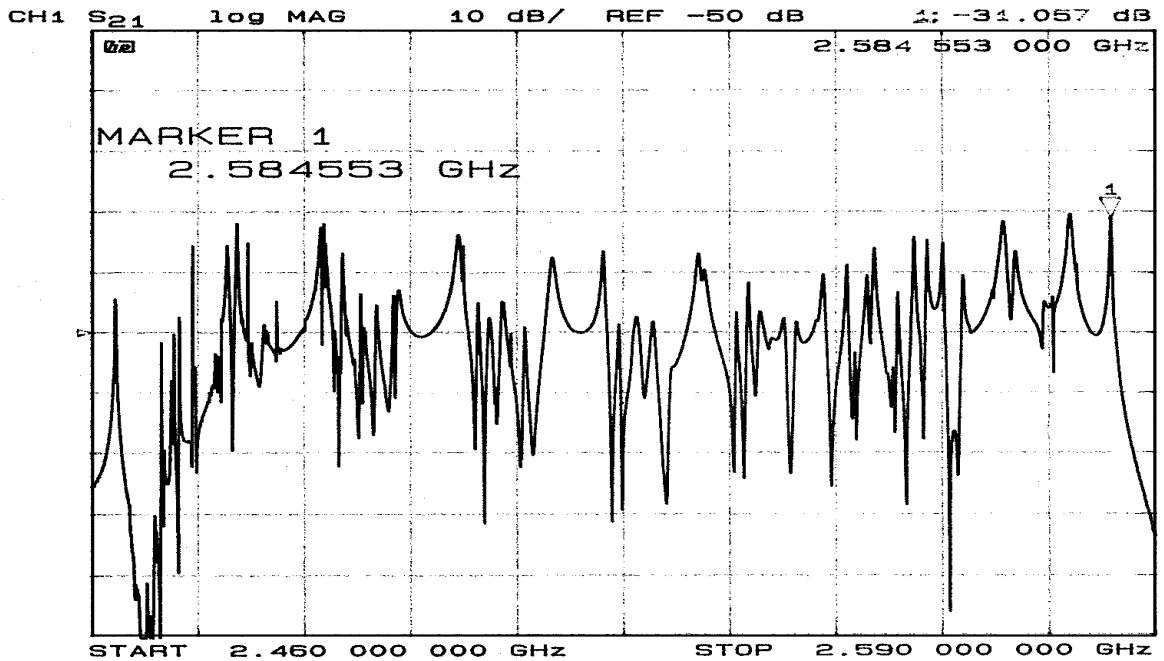

Figure 5.30: Transmission (S_{21} parameter) for cavity 3 (S10) of module 1 measured between its two HOM couplers (C3K1-C3K2). The frequency range is 2.46 ÷ 2.59 GHz, covering the third dipole passband. The vertical scale is 10 dB per division.

ble 5.8. Both polarizations of the mode are listed. The names of the cavities are also indicated beside their position in the module. In all cases the polarization with higher quality factor is the one with higher frequency. The other polarization had always a much lower Q, below $2 \cdot 10^4$. As seen, high Q modes were found also in the fifth cavity of module 2 and the seventh of module 3.

Cavity nr./ module	1st polariz.		2nd polariz.	
	Freq. [GHz]	Q	Freq. [GHz]	Q
#3 (S10) / 1	2.5845	$1.6 \cdot 10^4$	2.5850	$1.1 \cdot 10^6$
#6 (S11) / 1	2.5859	$1.3 \cdot 10^4$	2.5862	$8.6 \cdot 10^4$
#5 (A15) / 2	2.5832	$1.1 \cdot 10^4$	2.5844	$4.2 \cdot 10^5$
#7 (S28) / 3	2.5904	$1.6 \cdot 10^4$	2.5906	$6.5 \cdot 10^5$

Table 5.8: High-Q polarization of the last mode of the third dipole passband as measured with a network analyzer.

A few questions arise when looking at this table:

- is this mode better damped in the other cavities, where it could not be measured with a network analyzer?
- how dangerous is this mode for the beam dynamics in the TESLA main linac?
- are the HOM couplers of these cavities defective?
- is the higher Q-value correlated with the higher mode frequency?

In order to answer the first question, we made detailed measurements of the third dipole passband for all cavities of module 1. No mode was found to have a very high Q.

The second question is studied in chapter 6, where the multi-bunch beam dynamics in the TESLA main linac is simulated. It is assumed that in each cavity the 10 most dangerous modes as given in [11] can be excited and in one cavity of each module additionally the mode with 2.585 GHz and $Q = 10^6$. The result is an emittance growth of over 50 % which is not tolerable. Therefore the understanding of the mechanisms of the mode damping is important for the linear collider.

The other questions will be addressed in the rest of this chapter.

The module

Table B.1 in appendix B shows the cavities composing the 3 modules. The cavities are named with a different letter according to the firm that produced it. The 4 "bad" cavities are marked with a *, that is the cavities where high Q values were measured for the last mode of the third dipole passband (Table 5.8).

There are two types of input power couplers: one designed by DESY, the other by FNAL. It can be seen that the "bad" cavities contain both types. The same, there are

two types or HOM couplers: one designed by DESY, that is welded to the beam pipes, the other by CEA Saclay, which is mounted with a flange (see section 5.2). Again, both types are found at the bad cavities. From here we may conclude that most likely there is no design problem of one or the other type of coupler or a concept of both.

Third passband

In Fig. 5.30 the third passband is shown for cavity 3 (S10). The last mode, highest in frequency, is the one that interests us in this study. Actually the peak that can be seen has a low Q of $1.6{\cdot}10^4$. The quality value is obtained with eq. 3.20. The other peak is here not seen, because it is too narrow. It can be visualized by reducing the frequency span, as in Fig. 5.31. The two peaks here are the two polarizations of the mode, one broad, with low Q, and the other narrow, having a high Q value. The mode is much better seen when measuring between one HOM coupler of cavity 3 (C3K2) and a coupler of cavity 4 (C4K2) (see Fig. 5.32). The measured Q is $1.1 \cdot 10^6$, value given in Table 5.8.

A comparison of the frequency range of this passband for the various cavities is not easy, since the modes belonging to the third passband and to a certain cavity can not be identified. Therefore we compare in Fig. 5.33 the monopole passband TM_{011} that is lower in frequency. It is remarkable that the frequency range for the 4 bad cavities is higher than for the other ones.

The passband ranges are related to the cavity lengths, as seen in the lower plot of the same figure and in Fig. 5.34. The length after the final tuning is given, i.e. the length variation until the fundamental mode reaches 1.3 GHz. Due to the geometrical tolerances in cavity production, the frequency of the higher order modes differ, even if the accelerating mode has the same frequency in all cavities. The "bad" cavities, that are marked with solid symbols, are shorter than the design value, and than the other cavities. The correlation of the frequency to the cavity length is not linear, due to cell shape deformation.

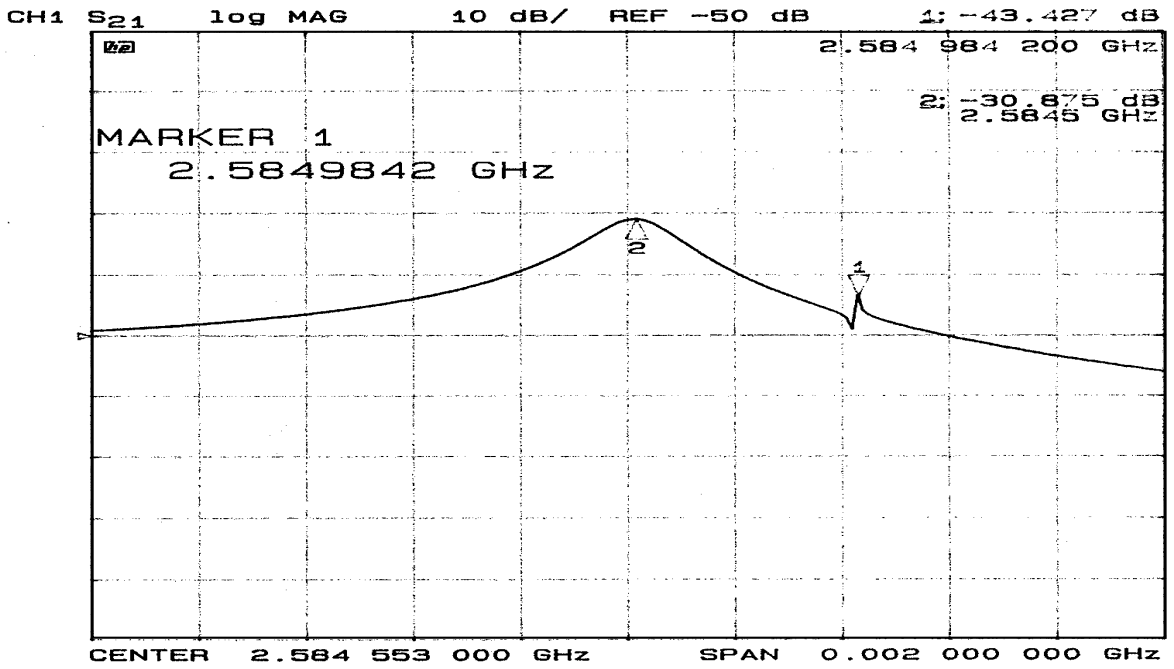

Figure 5.31: Last mode (with the two polarizations) of the third dipole passband of cavity 3 (S10) of module 1 measured between its HOM couplers (C3K1-C3K2). The frequency range is 2.583553 ÷ 2.585553 GHz. The vertical scale is 10 dB per division.

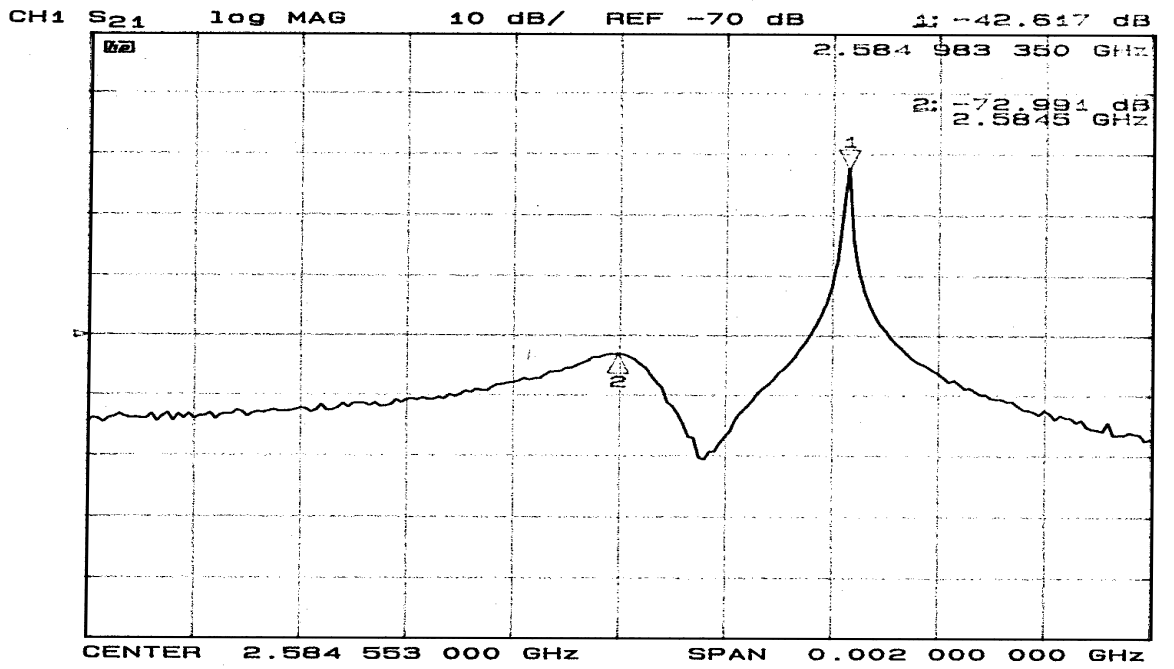

Figure 5.32: Last mode (with the two polarizations) of the third dipole passband of cavity 3 (S10) of module 1 measured across cavity 3 plus the tube between cavities 3 and 4 (C3K2-C4K2). The frequency range is 2.583553 ÷ 2.585553 GHz. The vertical scale is logarithmic, with 10 dB per division.

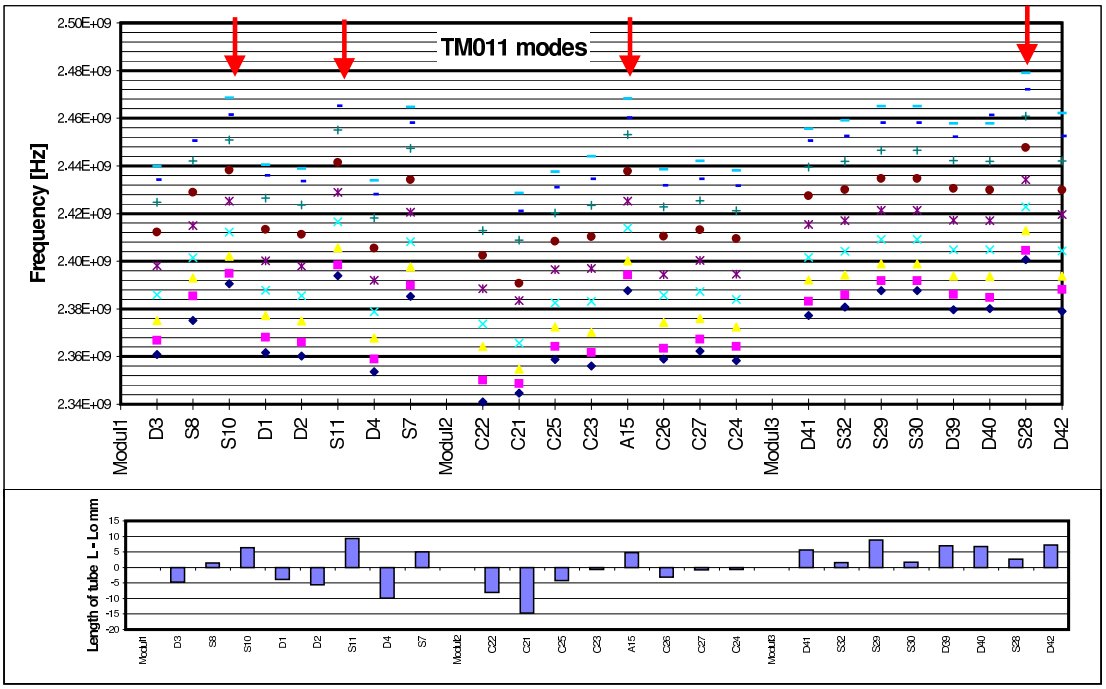

Figure 5.33: TM_{011} modes in the cavities of the first three TTF modules [62]. On the abscissa, the cavities are ordered as in the modules. The frequency differences between cavities is similar to the frequency difference for the 3rd dipole passband, higher in frequency. The lower graphic shows the difference in cavity length with respect to the design value.

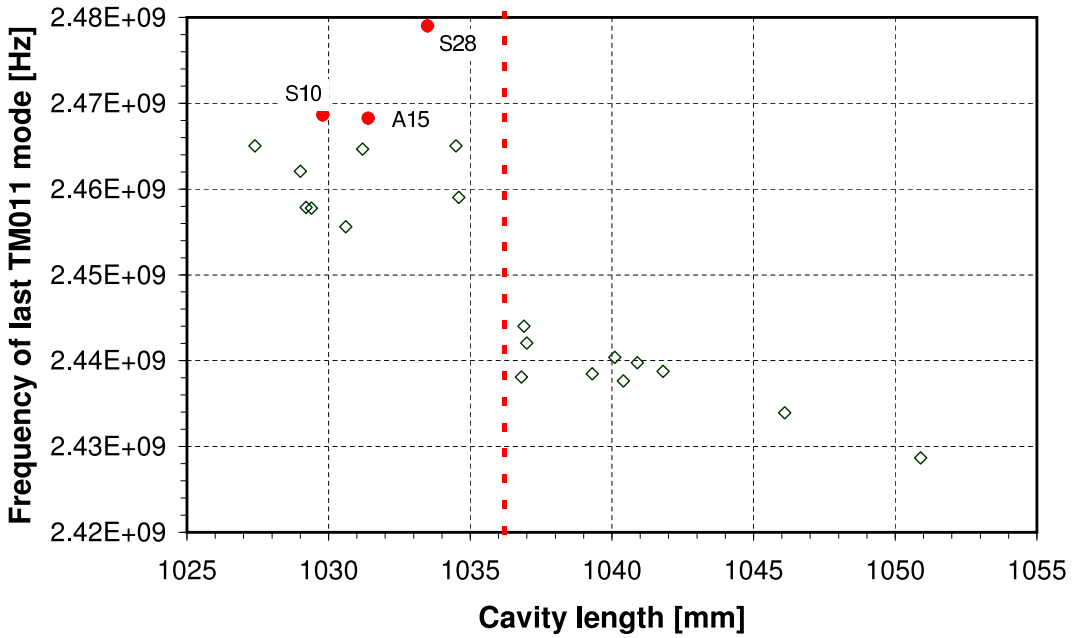

Figure 5.34: Frequency of the last mode of the TM_{011} passband as a function of the cavity length. The cavities with high Q mode in the third passband are marked with solid symbols. The vertical dashed line represents the design length of the cavity.

Measurements at module 1 at room temperature

Module 1 was warmed to the room temperature and taken out of the linac in order to be disassembled The transmission across cavities was measured again. The results show a shift down to lower frequencies by about 5.5 MHz for the third passband, due to the cavity dilatation. The measured passband for cavity 3 (S10) is shown in Fig. 5.35. The power couplers were detached and their ports were left open. The spectrum is essentially the same as for the cold cavity (see Fig. 5.30). The detailed spectrum for the last mode is shown in Fig. 5.36. When measuring the transmission between C3K2 and C4K2, the spectrum looks like in Fig. 5.37.

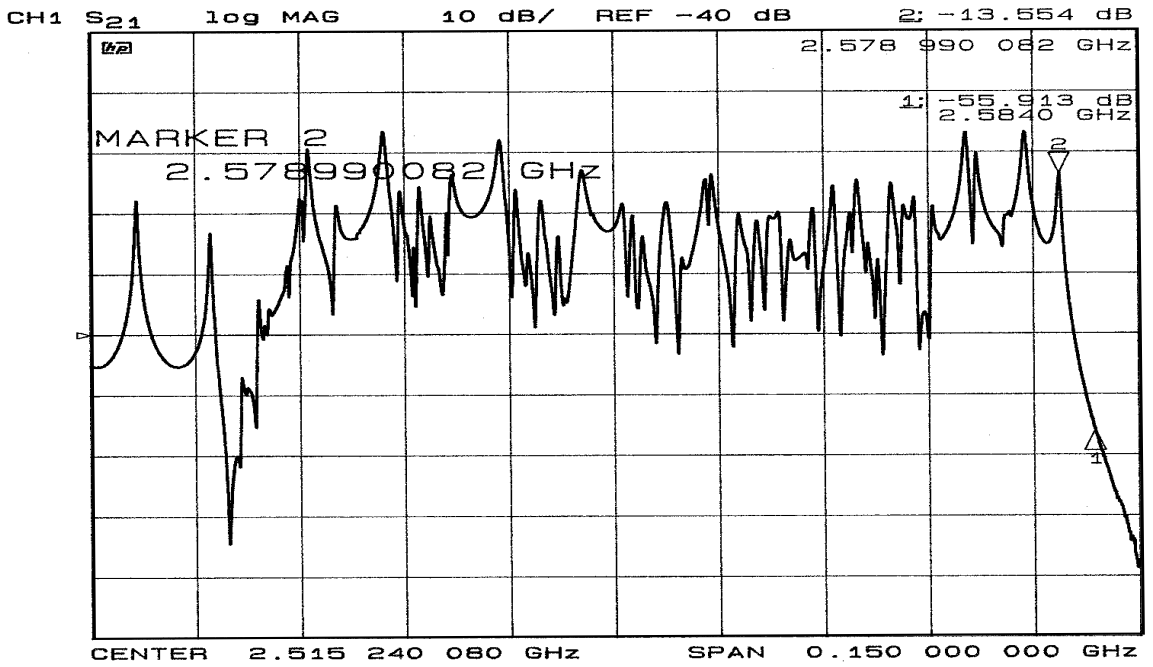

Figure 5.35: Transmission (S_{21} parameter) for cavity 3 (S10) of module 1 at room temperature measured between its two HOM couplers (C3K1-C3K2). The cavity string was taken out of the cryo-module. The input power couplers were detached and the respective ports were open. The frequency range is 2.44024008 ÷ 2.59024008 GHz, covering the third dipole passband. The vertical scale is 10 dB per division.

5.4.2 Measurements on individual cavities from module 1

Module 1 was taken out of the linac in spring 1999 and disassembled. The four best cavities were planned to be installed into a new module and the other four were available for investigations regarding the high Q mode at 2.58 GHz. These are cavities S7, S8, S10 and D4. The HOM couplers were still installed, while the power couplers have been removed. In most of the studies, the port for the input coupler was closed with a metallic plate.

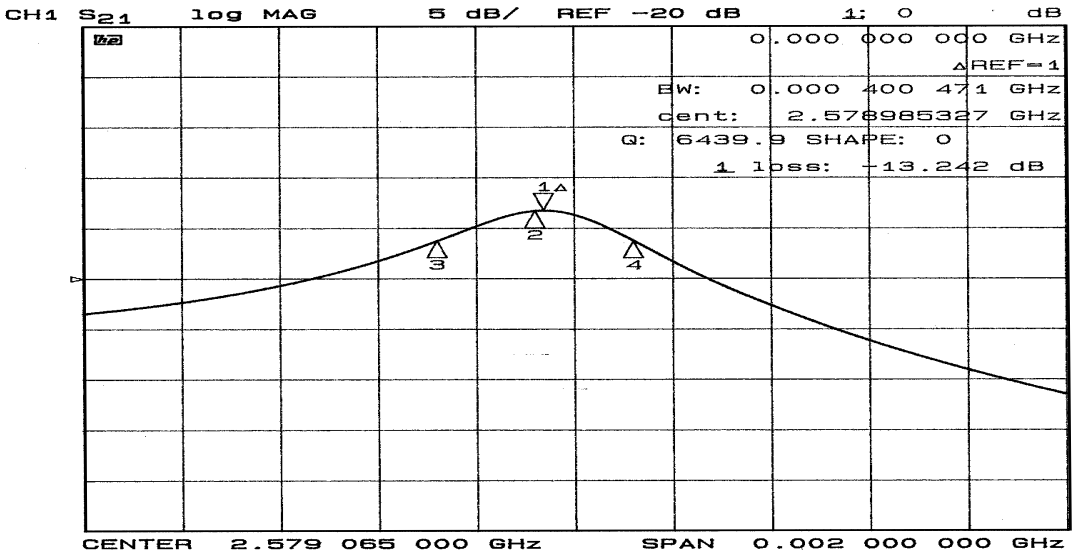

Figure 5.36: Last mode of the third dipole passband of cavity 3 (S10) of module 1 at room temperature measured between its two HOM couplers (C3K1-C3K2). Only the mode with lower Q in the superconducting cavity can be seen. The frequency range is 2.578065 ÷ 2.580065 GHz. The vertical scale is 5 dB per division.

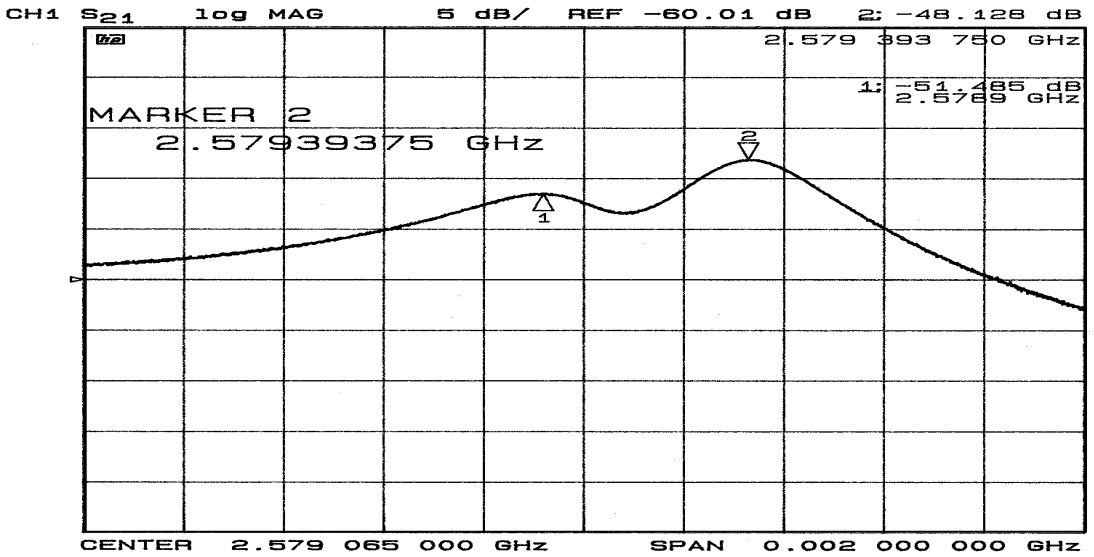

Figure 5.37: Last mode (both polarizations) of the third dipole passband of cavity 3 (S10) of module 1 at room temperature measured across cavity 3 plus the tube between cavities 3 and 4 (C3K2-C4K2). The frequency range is 2.578065 ÷ 2.580065 GHz. The vertical scale is 5 dB per division.

Transmission spectra

The transmission curves (S_{21} parameter) were first measured with open beam tubes, between the two HOM couplers of each cavity (see Fig. 5.3). The frequency spectrum for the third passband of cavity S10 is given in Fig. 5.38. For each mode only one peak (one polarization) can be seen. The quality factor of the last mode was found to be about 3000. It is not clear what polarization we see here, whether the well damped or the poorly damped one (see Fig. 5.32). When the tubes were closed with metallic plates, the spectrum changed like shown in Figs. 5.39. The last mode is shown in more detail in Fig. 5.40. The Q increased to about 7000. This is caused by the fact that the power flowing out of the structure in the first case is now confined inside. About half of the dissipated energy in the case of open tubes is in the couplers and walls, the rest flowing outside through the tubes.

The similar spectrum for cavity D4, considered to be a good cavity, shown in Figs. 5.41 and 5.42 (with open and closed ends, respectively), do not show essential differences to the ones for cavity S10, except the lower mode frequencies. The quality factors are about 1500 (but the measurement is affected by the mode with slightly lower frequency) and 6000, respectively.

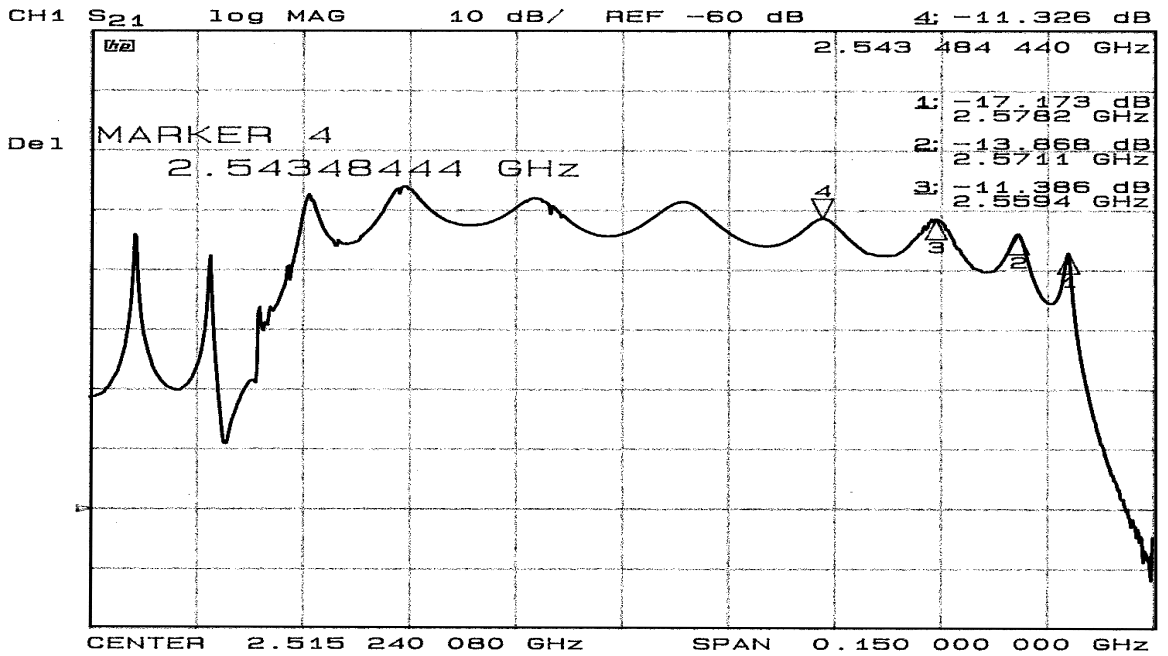

Figure 5.38: Transmission (S_{21} parameter) between the HOM couplers of cavity S10 when the tube ends are open. The frequency range is 2.44024008 ÷ 2.59024008 GHz, covering the third passband. The vertical scale is 10 dB per division.

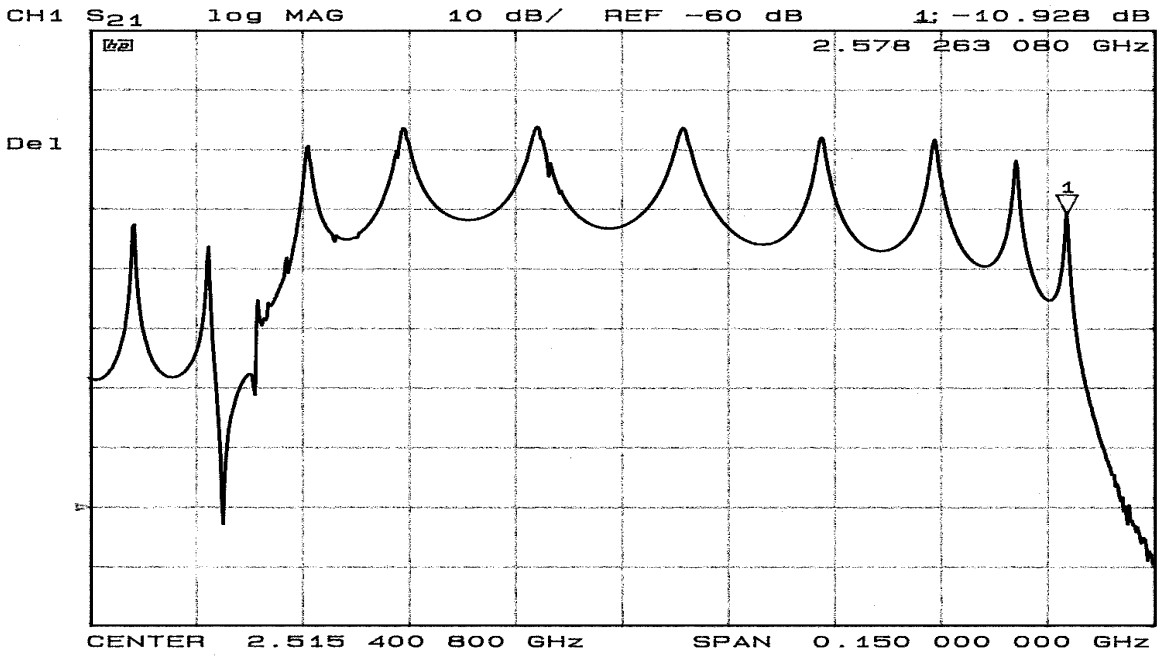

Figure 5.39: Transmission (S_{21} parameter) between the HOM couplers of cavity S10 when the tubes are closed with metallic disks. The frequency range is 2.44024008 ÷ 2.59024008 GHz, covering the third passband. The vertical scale is 10 dB per division.

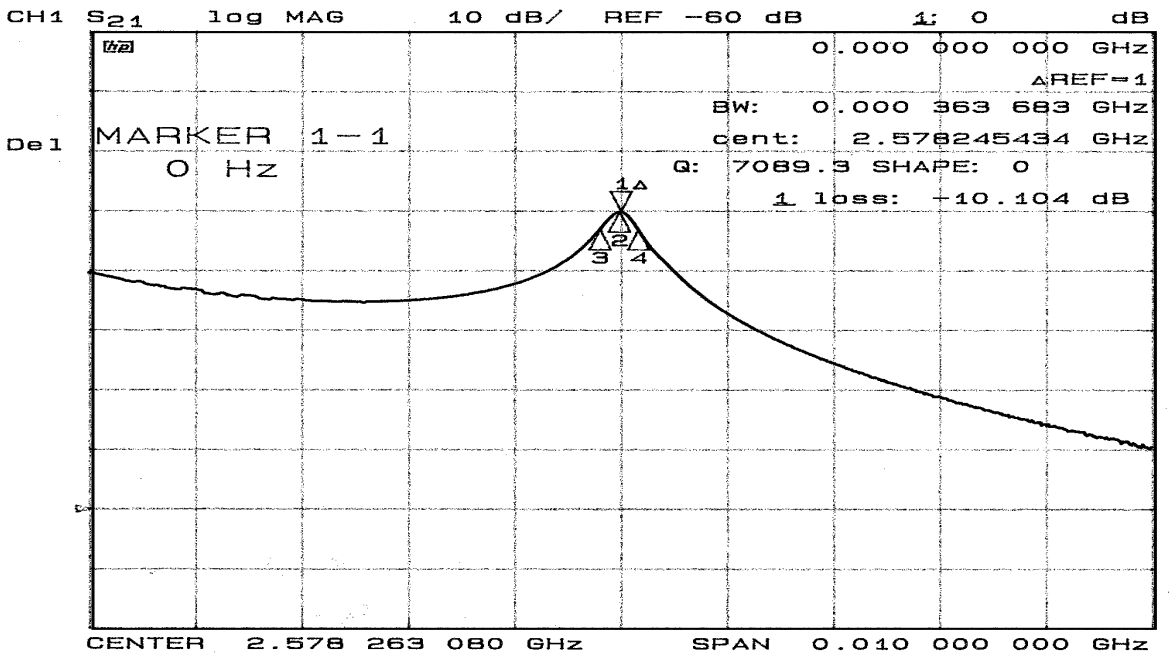

Figure 5.40: Transmission (S_{21} parameter) between the HOM couplers of cavity S10 when the tubes are closed with metallic disks. The frequency range is 2.57326308 ÷ 2.58326308 GHz, covering the last mode of the third passband. The vertical scale is 10 dB per division.

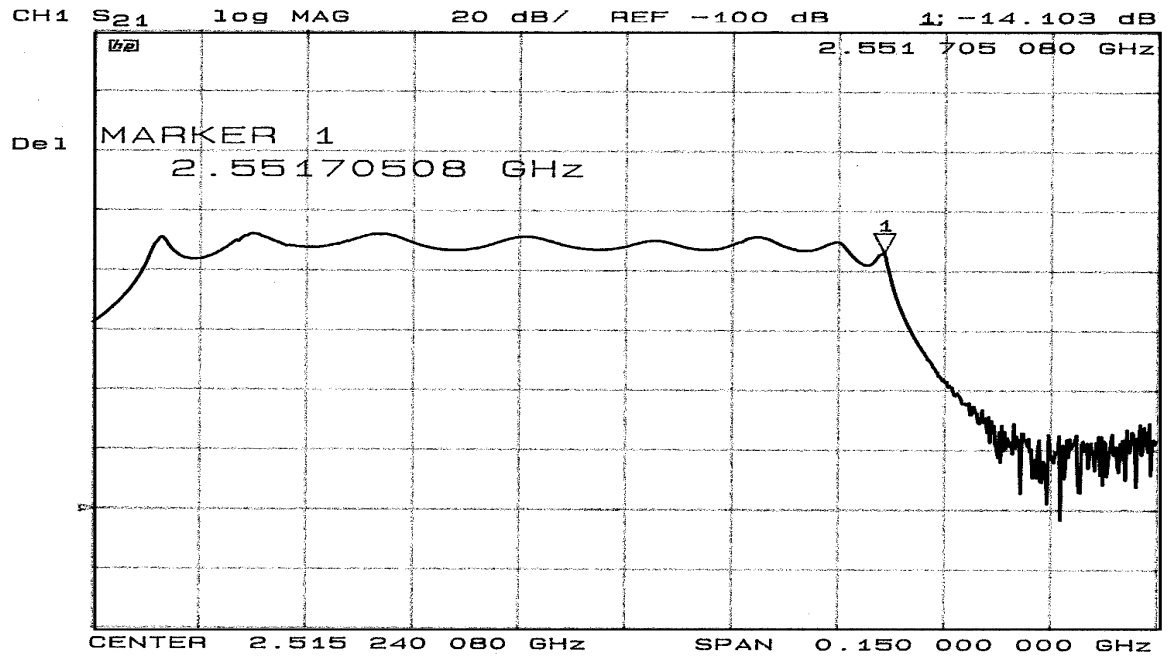

Figure 5.41: Transmission (S_{21} parameter) between the HOM couplers of cavity D4 when the tube ends are open. The frequency range is 2.44024008 ÷ 2.59024008 GHz, covering the third passband. The vertical scale is 20 dB per division.

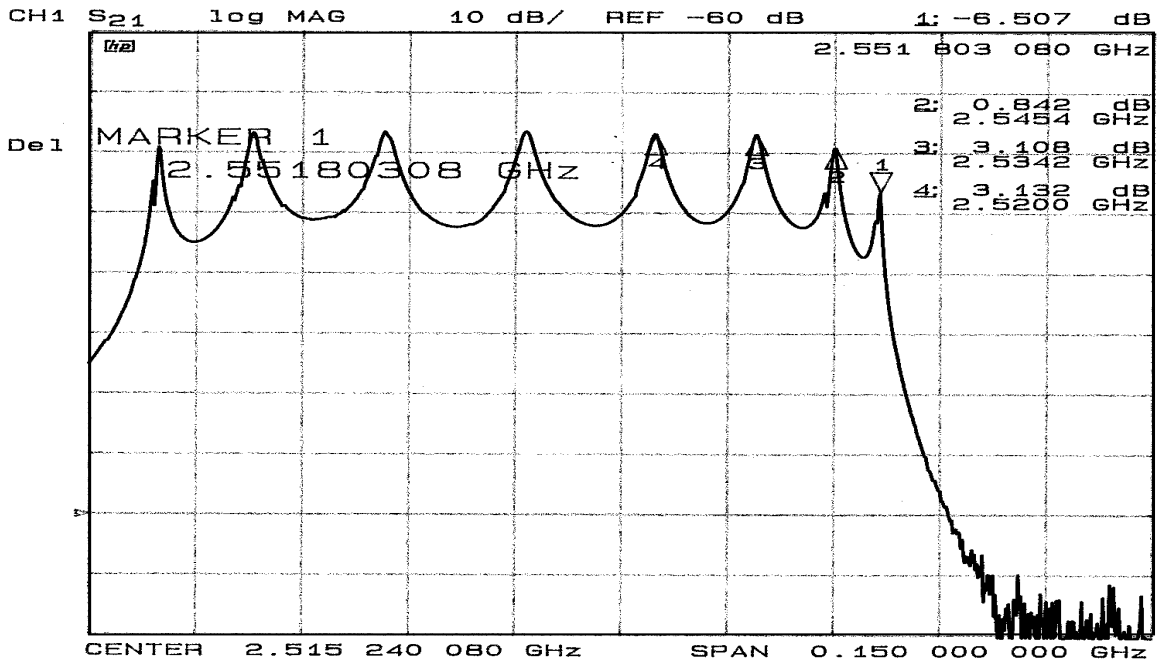

Figure 5.42: Transmission (S_{21} parameter) between the HOM couplers of cavity D4 when the tubes are closed with metallic disks. The frequency range is 2.44024008 ÷ 2.59024008 GHz, covering the third passband. The vertical scale is 10 dB per division.

Study of HOM coupler effect

The HOM couplers of cavities S10 and S7 could be detached and were interchanged one by one between the cavities. The coupler angle was kept the same with an error of about $\pm$ 2°. The transmission curves were again measured. The curves obtained were exactly the same as with the original couplers. The amplitude of the last mode varied by less than $\pm$ 1 %. The quality factor when using various HOM couplers at cavity S10 was between 7000 and 7100. The similar behavior of the couplers is an indication that they are identical.

Estimation of the external Q of HOM couplers from cavity S10

To the beam pipes of cavities D4 and S10, copper tubes were attached on either side, as shown in Fig. 5.43. These tubes have the same inner diameter as the beam pipes and were provided with holes at many angles and longitudinal positions. Movable metallic disks in the tubes set the boundary conditions. Small antennae were placed in each tube and used to measure the transmission coefficient S_{21} across the cavity. The angular and longitudinal position of the antennae was chosen so that to have a good signal of the mode, and to distinguish the dangerous polarization. Here by polarizations the peaks that can be distinguished on the spectrum are meant, that are separated by 300-500 kHz.

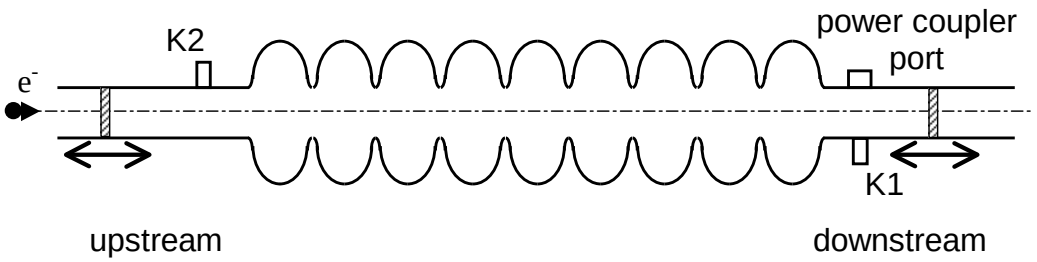

Figure 5.43: Measurement setup. Tubes are attached to the cavity beam pipes. Metallic disks can be moved inside the disks. K1 and K2 denote the HOM couplers. The power coupler port was closed with a metallic plate. The terms "upstream" and "downstream" refer to the position of the cavity in the module with respect to the beam direction.

By placing a 50 Ω load on the connector of one HOM coupler, the quality factor of the dangerous mode was measured for the case of having the other coupler loaded with 50 Ω and opened, respectively. Although the antennae were not calibrated, this method gives us a rough estimation of the external quality factor of the second coupler. If we assume that the antennae have a small coupling to the field, then the loaded Q is given approximately by eq. 5.2: When the coupler to be measured is left open or a short is connected to it, then one measures approximately $Q_{short} \approx Q_0$. With a load, the coupler is absorbing the energy it sees from the field of the mode so that the measured

Q is $Q_{load} \approx Q_{tot}$. From these considerations it results that:

$$\frac{1}{Q_{ext}} \approx \frac{1}{Q_{load}} - \frac{1}{Q_{short}}. \tag{5.15}$$

With this relation only low values of Q_{ext} can be estimated.

The results of the measurements with cavities D4 and S10 with various boundary conditions are given in Table 5.9.

Upstream tube length [mm]	Downstream tube length [mm]	Q_{ext1}	Q_{ext2}
Cavity D4			
253	253	$5.5 \cdot 10^4$	$5.5 \cdot 10^4$
306	253	$2.5 \cdot 10^5$ §	*
253	311	*	$> 10^6$ §
Cavity S10			
252	238	10^6 §	$6 \cdot 10^5$ §
287	238	$> 4 \cdot 10^6$ §	$5 \cdot 10^4$

* could not be measured because other polarization was too close

§ Q values higher than 10^5 can not be determined exactly by this method; the numbers indicate rather the order of magnitude

Table 5.9: Estimated Q_{ext} for the two HOM couplers of cavities D4 and S10, for various boundary conditions. The tube lengths are effective tube lengths from end of cavity to the position of metallic disk (see Fig. 5.43).

For D4, the external Q is of the order of $5 \cdot 10^4$ for tube lengths of 253 mm on either side (symmetrical boundaries). For the other two boundary conditions, one can only say that Q_{ext} of each of the couplers is very high, even if a precise value can not be measured. For cavity S10, the Q_{ext} of both couplers is very high for the case of quasi-symmetrical boundaries, on the contrary to the case of D4. For asymmetric boundaries, Q_{ext2} is much lower, indicating more field at this coupler, while the other coupler sees less (or no) field, indicated by the tendency of Q_{ext1} to higher values. If we assume that the mode have about the same radial distribution in both cavities for any boundary conditions, the difference in Q_{ext} to the case of cavity D4 (a "good" cavity) indicates lower field at the coupler location. (The polarization problem was not studied and will be the subject of future investigations.)

Effect of boundary conditions

The transmission through the cavity was measured with the setup from Fig. 5.43. The position of the metallic disk was varied and the frequencies of the last 4 modes of the passband were measured. The other disk was kept fixed. The curves obtained for cavity S10 are shown in Fig. 5.44. One observes that for each mode, when decreasing the tube length, the frequency increases about linearly up to a region where the

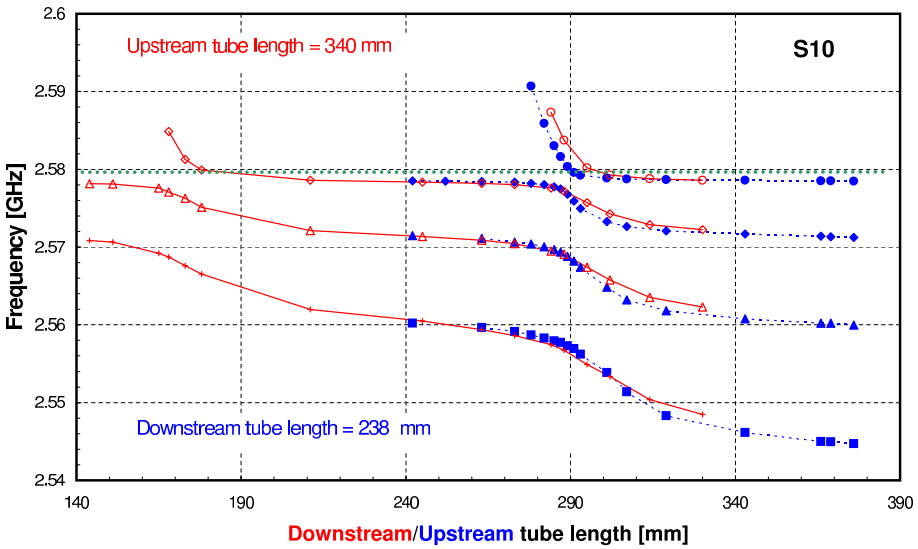

Figure 5.44: Frequencies of the last 4 modes of the third dipole passband for cavity S10, as a function of one tube length, while the length of the other tube is kept fixed. The curves with open symbols are for the case of varying the downstream tube length (see Fig. 5.43).

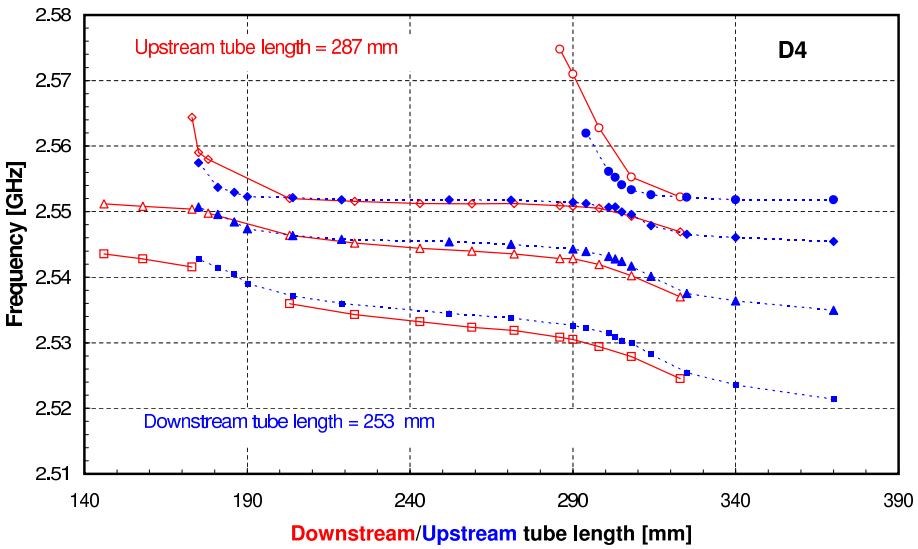

Figure 5.45: Frequencies of the last 4 modes of the third dipole passband for cavity D4, as a function of one tube length, while the length of the other tube is kept fixed. The curves with open symbols are for the case of varying the downstream tube length (see Fig. 5.43).

mode transforms rapidly into the one immediately higher in frequency. In this transition region, one observes in the whole passband 10 modes instead of the usual 9. It is remarkable that for the last mode, the curve is pretty flat, the boundary does not influence it much, which means that the field level in the tube is very low. The mode is quasi-trapped. In the transition region, the field contents in one tube is much increased, but at this state another mode is taking its place. The fixed disk is kept on the linear region (tube length between 190 and 270 mm) when the other one is moved.

The frequency versus the tube length for cavity D4 is given in Fig. 5.45. The linear region for the last mode has also a small slope, which means the field in the tubes is also low.

Field distribution

For various boundary conditions defined by the metallic disks (Fig. 5.43), the field distribution was measured. For this purpose the bead-pull technique was used [38, 39]. A short dielectric cylinder, with a length of 4 mm and a diameter of 4 mm, was moved along the cavity, on the axis. The radial electric field on the axis was measured for each location of the bead.

When one disk is kept fixed, and on the linear region in Fig. 5.44 (or Fig. 5.45 for cavity D4), then the field distribution inside the cavity is essentially stable when moving the other disk on the linear region. In the tube, the distribution is changing, allowing more or less peaks of the field.

The field distribution is shown comparatively in Fig. 5.46 for cavities S10 and D4 for the same, symmetrical boundaries. The field amplitude drops faster at the cavity

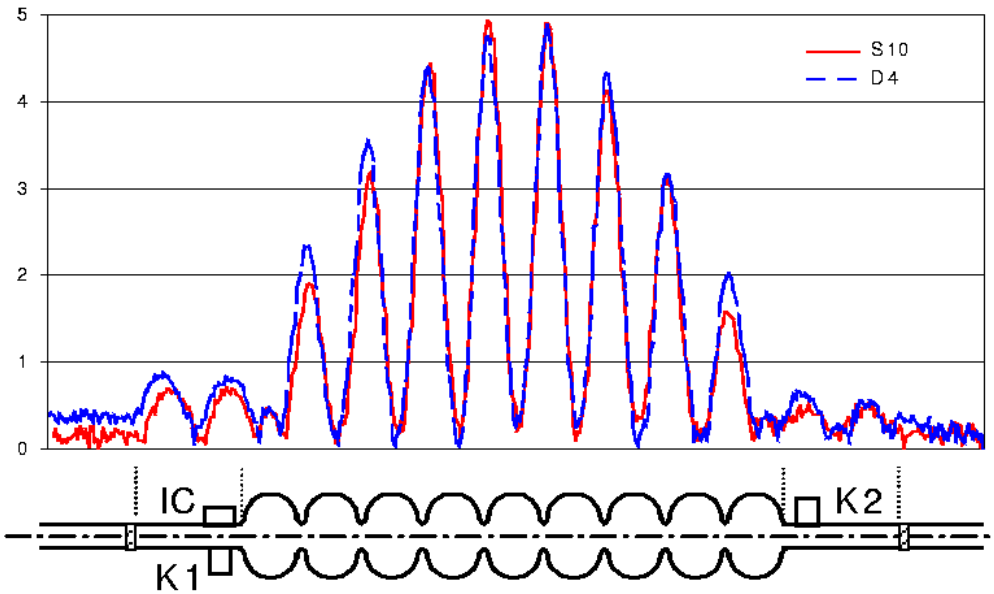

Figure 5.46: Field distribution E_r on the axis of cavities S10 and D4 for symmetrical boundary conditions; both tube lengths are equal to 223 mm.

sides for S10 than for D4. But the field is quasi-trapped in both cases, as predicted by the Figs. 5.44 and 5.45, and the small difference in field level at the coupler location can not account for the big differences in the mode damping.

The difference in the field level in the end cells is related to the shorter length of cavity S10. The design cavity length is 1.036 m, while cavity S10 has 1.029 m and D4 1.044 m. A uniform reduction of the cell length explains the higher mode frequency for S10, but not the difference in field distribution. The attention was then given to the end cells that are by design shorter. Simulations show that an increase in the length of one end cell increases the trapping of the mode, i.e. the field amplitude drops faster in the end cells and is lower in the tube [61, 70].

In order to find out whether the length reduction of cavity S10 is distributed uniformly or rather concentrated in the end cells, the cell lengths were measured by an optical method [72]. (I remind here that the cavity is built into a tank that makes this measurement impossible from the outside.) By help of a rigid endoscope that was introduced in the cavity on the axis, the reflection of light on a point near the iris was seen. It was assumed that the cell curvature is about the same for all cells in the neighborhood of the iris. The limits of the last cells could not be measured, since there the geometry is different (due to the connection to the beam pipe). The precision of the measurement is $\pm$ 0.2 mm. The measurement results are given in Table 5.10.

Cell	Length [mm]	
	measured	design
1	*	113.7
2	114.16	115.4
3	114.31	115.4
4	114.89	115.4
5	114.43	115.4
6	114.06	115.4
7	114.35	115.4
8	114.43	115.4
9	*	114.7
total	1029	1036

* could not be measured

Table 5.10: Cell length for cavity S10 measured by an optical endoscope (precision $\pm$ 0.2 mm). The cells are numbered starting with the power coupler side.

All inner cells are shorter than the design value. By subtracting from the total length of this cavity the lengths of the inner cells, we find out that the sum of the end cells is equal to the sum of the ideal end cells (that are not identical). If both end cells have the design lengths, then the field distribution for cavity S10 is the same as in a design cavity with longer end cells. Then the higher field trapping for cavity S10 than for D4 shown in Fig. 5.46 can be explained based on the above mentioned simulations [61, 70].

In case one disk is in the transition region of the curve of Fig. 5.44, then the field

distribution is asymmetric, for example as shown in Fig. 5.47. There is no field in one tube, which explains the situations when we obtained very high Q_{ext} at one coupler with asymmetric tube lengths (see Table 5.9).

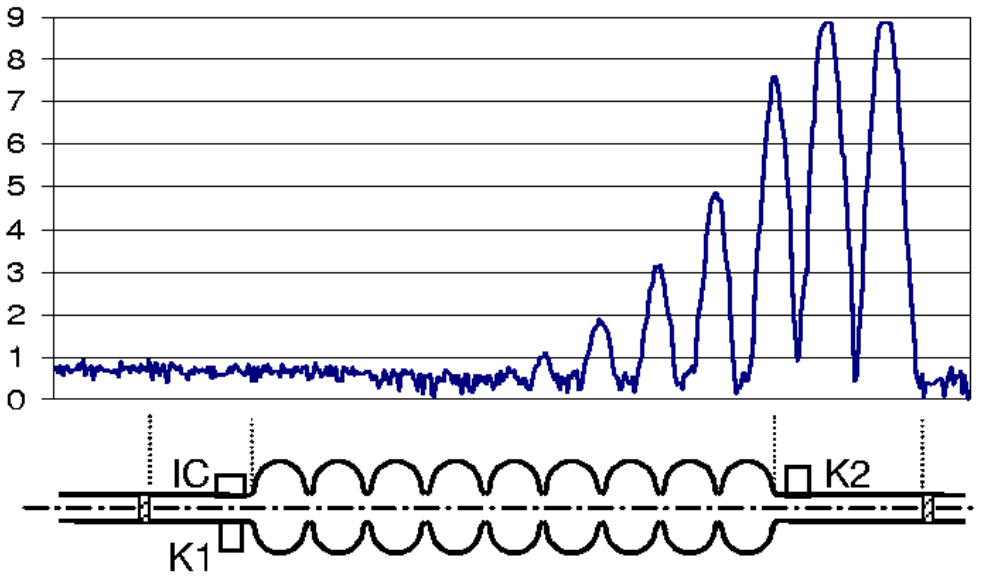

Figure 5.47: Field distribution E_r on the axis of cavity S10 asymmetrical boundary conditions; the upstream tube length is 283 mm, the downstream tube length is 223 mm.

We do not know the boundary conditions in module 1, imposed by the neighboring cavities of S10. Looking at the results of these measurements, a few hypotheses seem plausible, each with question marks:

- If the boundaries in the TTF module were such that the field is asymmetrical in the "bad" cavity like in Fig. 5.47, one expects that the HOM absorber couples very well and damps the mode. A field minimum at the location of the coupler may be then the cause of the bad damping. But it seems quite unlikely that there are two minima at both absorbers that are placed in one tube, and that this happens at least at four of 24 cavities, for which a high Q was measured for this mode.

- For a symmetrical field distribution (Fig. 5.46), the field in the tube may be too low for a good mode damping. But for other modes in the 3rd passband similar field levels were measured in the tubes as well. Again a more plausible explanation is a field minimum at both couplers (plus the two of the neighboring cavities).

- Another cause of the bad damping may be a "wrong" polarization direction of the field that may lead to the cancelation of the electric and magnetic coupling. (I remind here that the other polarization of this mode is well damped, see Table 5.8) But if this happens at the location of one coupler, the other one should couple well to the field, since they are at a relative angle of 115 ° to each other.

The investigations made to further clarify the situation are presented in the next section.

5.4.3 Experimental study of boundary conditions

Simulations have shown that, depending on the position of the metallic disks fixing the boundaries in Fig. 5.43, a situation may occur when only about 0.4 % of the total energy of the mode is outside the cavities [71, 70]. In obtaining this, the mode properties obtained from simulations for a design cavity were used. The quality factor of the mode is in the order of 10^7 when no HOM coupler is installed in the tubes.

When HOM couplers are also taken into account, the quality factor of a mode is given by:

$$Q = \frac{\omega_l W_{tot}}{P_{abs}}, \tag{5.16}$$

where W_{tot} is the total energy stored in the mode and P_{abs} the power absorbed by the HOM couplers. If a is the voltage normalized to the square root of an arbitrary impedance of the field of the mode propagating from the cavity in the beam tube (see Fig. 5.48), then the power absorbed by the couplers can be written by help of the S-parameters:

$$P_{abs} = \frac{1}{2}|a|^2 \left(|S_{01}|^2 + |S_{02}|^2\right) = \frac{1}{2}|a|^2 S^2. \tag{5.17}$$

We call S the coupling efficiency. The energy stored in the beam pipe W_{pipe} can be written as:

$$W_{pipe} \approx \frac{1}{2}|a|^2 \frac{2l}{v_{gr}}, \tag{5.18}$$

where $1/2|a|^2$ is the power coming from the cavity, v_{gr} is the group velocity of the wave propagating out of the cavity. l/v_{gr} is the time needed to reach the reflection plane. The factor 2 comes from the fact that the wave reflects back. It was assumed that no losses are in the tube walls and that there is a full reflexion at the right plane. Then the quality

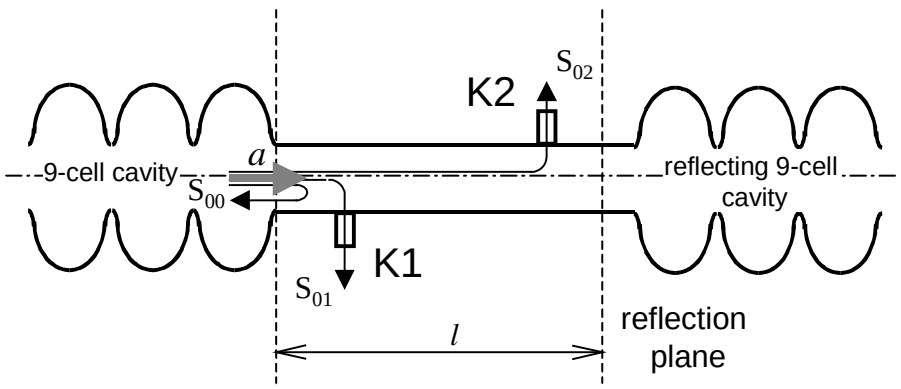

Figure 5.48: Definition of the coupling efficiency.

factor can be written as:

$$Q \approx \frac{\omega}{v_{gr}} \frac{2l}{S^2} \frac{W_{tot}}{W_{pipe}}. \tag{5.19}$$

The quality factor was calculated for various values of l and S. A total Q higher than 10^6 can be obtained only if the coupling efficiency between the field and the HOM absorbers is below 5 %. Boundary conditions equivalent to the ones from this simulation can be explained by a lower frequency of the neighboring cavity by a few MHz [71, 70].

A coupling efficiency below 5 % is rather unrealistic. In order to check if this can occur, we have reconstructed the geometry of the tube between two cavities, as shown in Fig. 5.49. The angles and positions of the couplers are the ones used in the module. K1 and K2 denote the HOM couplers. The couplers from cavity S10 were mounted at the angular positions used in the TESLA cavities. The power coupler port was closed with a metallic disk. The bellow is an original one, that has been used in module 1. On one side, a so-called adapter was attached that insured an optimum matching for frequencies around 2.585 GHz. Four antennae were used, two (e and g) in the power coupler plane, and the others (f and h) in the perpendicular plane. At the other side, a metallic disk could be moved inside the tube to vary the distance L1 from coupler K1.

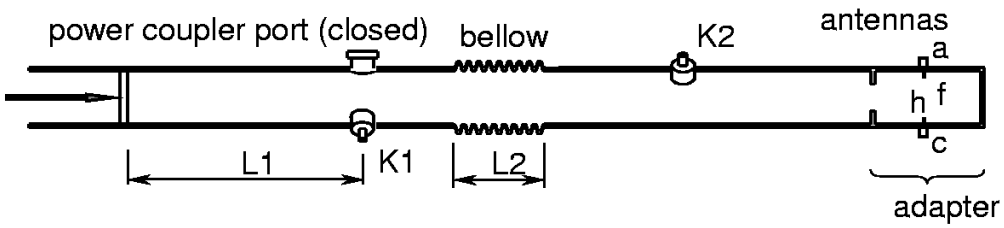

Figure 5.49: Experimental setup for study of influence of boundary conditions on the coupling efficiency to the HOM absorbers.

The boundary condition was varied by changing L1 in small steps. For each case the transmission from antennae g and h to K1 and K2 was measured. By a linear combination of the results, the transmission could be calculated for each polarization angle:

$$S_{\varphi \to \frac{K1}{K2}}(\omega) = S_{h \to \frac{K1}{K2}}(\omega) \cos\varphi + S_{g \to \frac{K1}{K2}}(\omega) \sin\varphi. \tag{5.20}$$

It was found that for two values for L1 and two particular angles the transmission to both couplers has steep minima. In Figs. 5.50 and 5.51 the transmission level from the adapter to K1 and K2, respectively, is displayed as a function of L1 for the two particular angles for a frequency of 2.582 GHz. S_φ represents the effective absorption to both couplers:

$$S_\varphi = \sqrt{S^2_{\varphi \to K1} + S^2_{\varphi \to K2}}. \tag{5.21}$$

It is remarkable that the considered planes are approximately perpendicular to K2 and K1, respectively (see Fig. 5.52), which means a bad coupling of the electric field

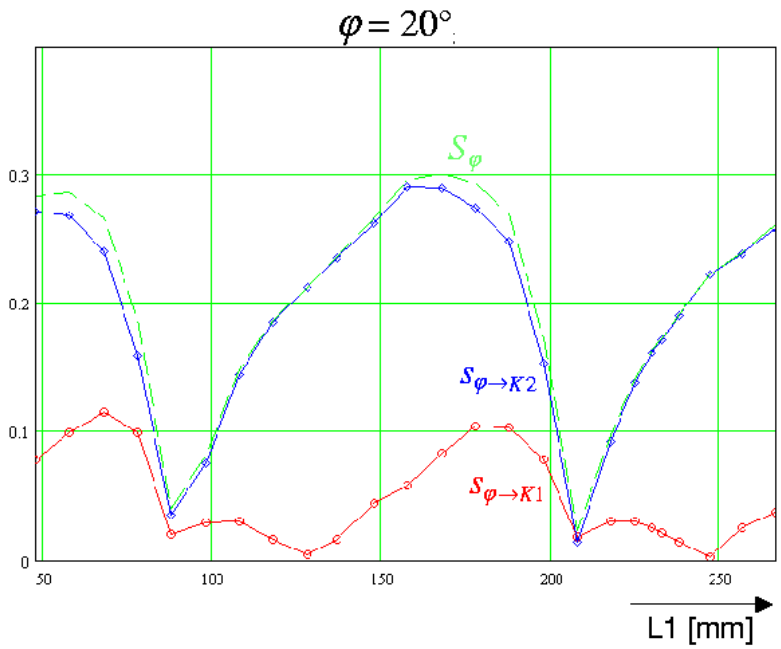

Figure 5.50: Transmission level from the adapter to K1 and K2 as function of L1, for a frequency of 2.582 GHz and an angle $\varphi = 20°$ with respect to the plane of antenna *h* (see Fig. 5.52).

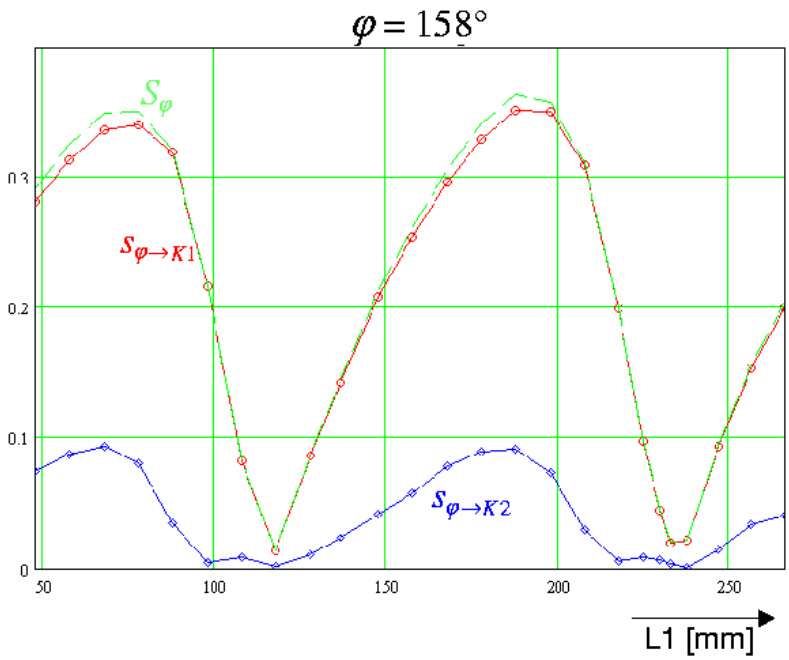

Figure 5.51: Transmission level from the adapter to K1 and K2 as function of L1, for a frequency of 2.582 GHz and an angle $\varphi = 158°$ with respect to the plane of antenna *h* (see Fig. 5.52).

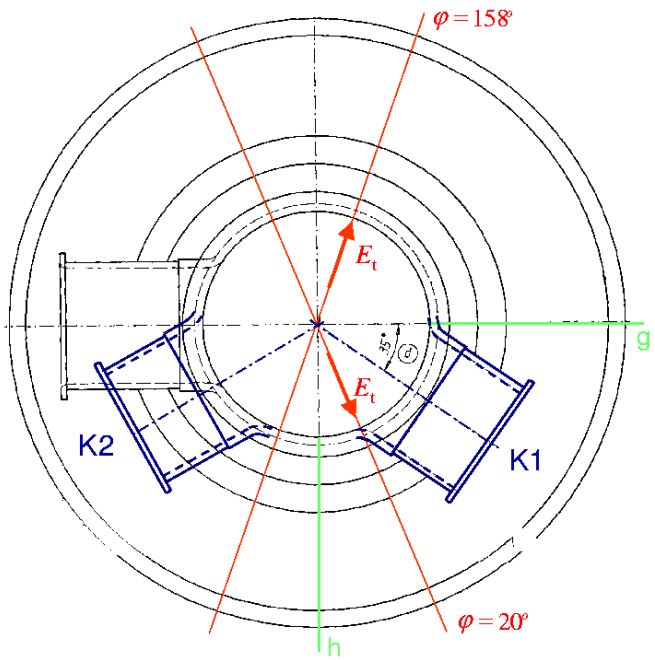

Figure 5.52: Angles of polarizations with low transmission to both couplers in the beam tube. View from upstream direction (see Fig. 5.3).

of the given polarization to this coupler. The curves do not change much with the frequency.

The results of the studies presented in this section show that the bad damping of one polarization of the last mode in the third dipole passband at some TTF cavities can be understood if a combination of factors act together:

- low field in the tubes due to cavity deformation and to the boundary conditions and
- an unfavorable angle polarization of the mode.

A neighboring cavity whose frequency is a few MHz lower leads to boundary conditions as the unfavorable ones found above. This is in agreement with the observation that the "bad" cavities are always higher in frequency. The polarization direction of the mode and the causes of it (for example the ellipticity of the cavity) were not the object of this study and will be approached in future investigations.

Chapter 6

Emittance Growth in the TESLA Main Linac

As mentioned in section 2.2, an alternative design of the accelerating structure for the TESLA linear collider has been proposed. This is the so-called superstructure, that is now under study, in parallel to the reference 9-cell cavities. In this chapter, after a brief review of the designs for the accelerating structure, the simulations for the beam dynamics in the TESLA main linac with superstructures are presented. The results are then compared to the case of the design with 9-cell cavities.

6.1 Alternative Design of the Accelerating Structure

6.1.1 General considerations

In [11] (Conceptual Design Report - CDR) eight 9-cell resonators were proposed to be grouped together in a cryo-module and used for acceleration in the TESLA main linac. This type of cryo-module is used in the TESLA Test Facility (TTF). The performance of the cavities was extensively studied. Many cavities achieved gradients beyond 25 MV/m, the initial goal for TESLA. In the updated TESLA design, 16 m long cryo-modules with twelve 9-cell cavities and a slightly different beam optics are foreseen [2]. In this chapter, the simulations involving 9-cell cavities are made with the CDR design. The results with the reference design (twelve 9-cell cavities per module) are expected to be similar, as will be seen later in this chapter.

For a linear collider, it is desirable to maximize the fill factor and reduce costs by using accelerating structures with as many cells as possible. On the other hand, with long structures, the field homogeneity is more difficult to achieve and many modes may be trapped. The 9-cell cavity is a good compromise between these requirements. The limitations on the number of cells per structure can be avoided by joining several multi-cell cavities together into a so-called *superstructure* [2, 73]. The interconnection tubes permit the energy flow from cavity to cavity. The whole chain is fed through one power coupler. Two types of superstructures are being investigated at present: one

with four 7-cell cavities and the other with two 9-cell cavities. The second one is the preferred solution. The simulations for the alternative design of the TESLA main linac have been made with the first version of the superstructure because a copper model of such a superstructure has been thoroughly studied.

A sketch of the superstructure with four 7-cell cavities is shown in Fig. 6.1. The shape of the inner cells is the same as in the 9-cell cavities (Fig. 5.3). The geometry of the end cells is adapted to the larger diameter of the interconnecting tubes. HOM couplers are placed in each interconnection tube. One such coupler can be placed in each end tube as well.

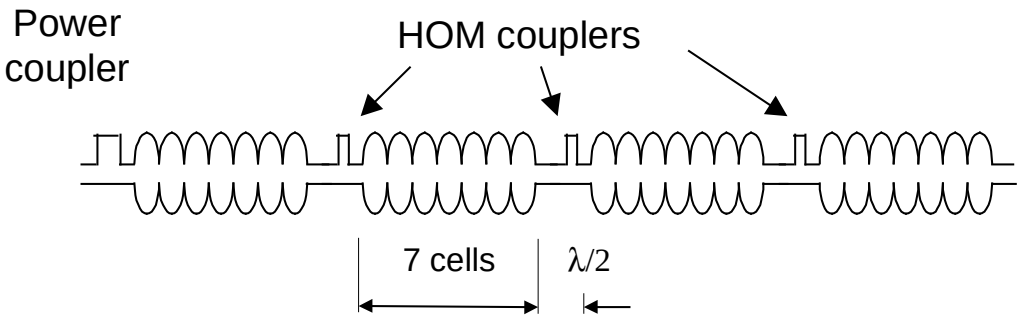

Figure 6.1: Superstructure made of 4×7-cell cavities.

For both designs used here for simulations, the length of the cryo-module is the same. There are eight 9-cell cavities per module in the CDR design and three superstructures in the alternative design. For both cases, the main linac is divided into three sections (see Fig. 6.2). The first section is made of FODO cells with four modules per cell and accelerates the beam from 3.2 to 50 GeV. The second linac section has six modules per cell, while the third one has eight. The energy increases to 150 GeV in the second and to 250 GeV in the last section. The focusing strength is chosen such that the phase advance per cell is equal to 60°. The beta function is shown in Fig. 6.3. The three sections are connected by matching sections.

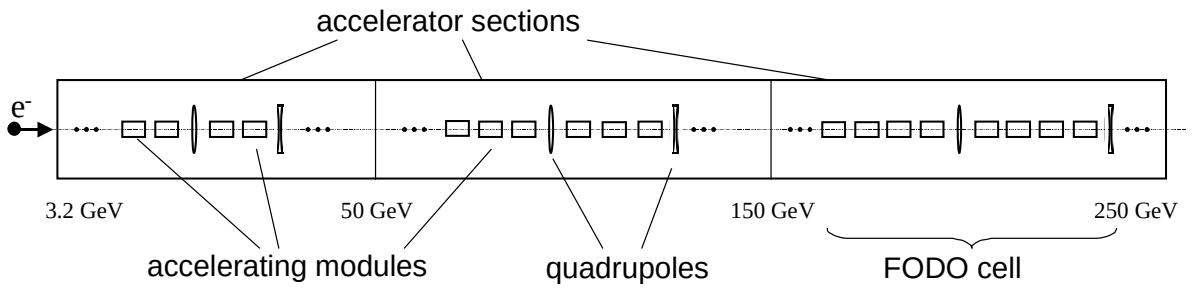

Figure 6.2: Main linac layout as used for the present simulations. The linac is divided into 3 sections with FODO cells comprising 4 modules per cell from 3.2 to 50 GeV, 6 modules from 50 to 150 GeV and 8 modules per cell from 150 to 250 GeV.

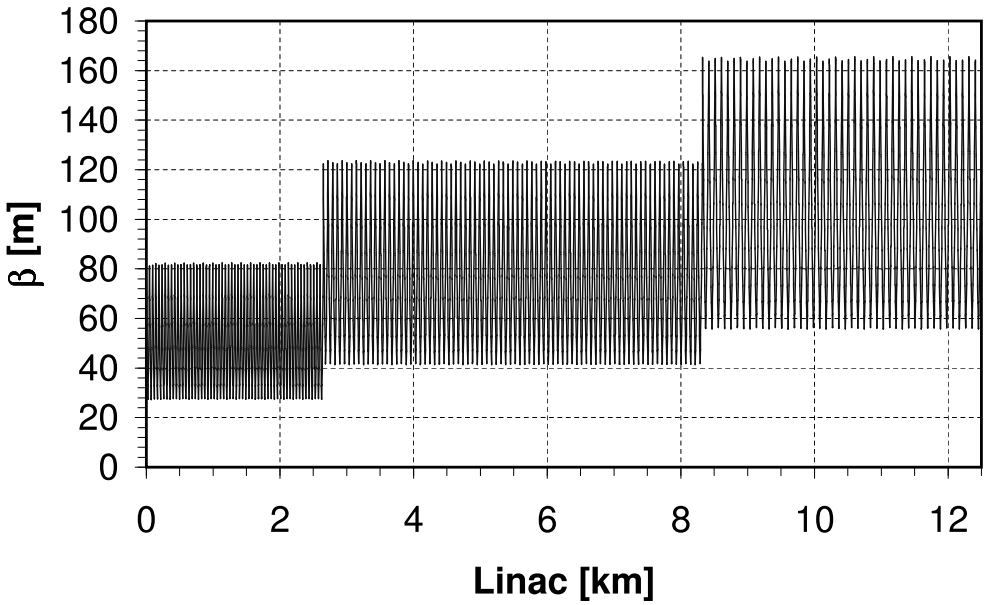

Figure 6.3: Beta function along the TESLA main linac (same for both designs listed in Table 6.1).

The gradient used with the superstructures is 21.7 MV/m instead of 25 MV/m in the case of the CDR design. The design current is 9.5 mA instead of 8 mA in the CDR design. The bunches have a lower charge, but the bunch spacing is smaller and the pulse length is longer. The main characteristics of the two designs used in this chapter, regarding the accelerating structures, modules, structuring of the main linac and the beam properties, are summarized in Table 6.1.

6.1.2 Higher Order Modes

The 9-cell cavity and the superstructure are expected to possess similar higher order modes due to the identical cell shape (with the exception of the end cells). In order to make a rough comparison, we consider first a simplified case. Let us think of two accelerating structures with the same cell geometry but a different number of cells. The group velocity is very small in comparison to the velocity of light. Therefore the energy propagates very slowly from cell to cell. If a point-like charge travels through the structure with the velocity of light, it will excite a delta wake field, $W^{\delta}(\zeta)$ (longitudinal and transverse). If we consider that the particle has the same offset and angle in each cell (the change along the cells is much smaller than the initial offset and angle) and taking into account the much lower velocity of the energy flow than the particle velocity, then the wake field excited will be about the same in each cell.

$$W_n^{\delta} \approx \text{const.}, \tag{6.1}$$

Design		**CDR**	**alternative**
Main linac			
accelerating structure		9-cell cavity	superstructure
length of acc. str.	[m]	1.036	3.577
number of acc. sec./module		8	3
length of module*	[m]	10.7	11
linac sections		3	3
1st section			
modules/FODO cell		4	4
energy	[GeV]	$3.2 \rightarrow 50$	$3.2 \rightarrow 50$
2nd section			
modules/FODO cell		6	6
energy	[GeV]	$50 \rightarrow 150$	$50 \rightarrow 150$
3rd section			
modules/FODO cell		8	8
energy	[GeV]	$150 \rightarrow 250$	$150 \rightarrow 250$
phase advance/FODO cell	[°]	60	60
accelerating gradient	[MV/m]	25	21.7
Beam			
current	[mA]	8	9.5
bunch charge	[nC]	5.8	3.2
bunch spacing	[ns]	708	337
number of bunches/pulse		1130	2820
pulse length	[μs]	800	950

* From beginning of first cavity to the end of last cavity;
(no quadrupoles are included)

Table 6.1: Main characteristics of the main linac and of the beam in the two designs, as used for the simulations in this chapter.

where n is the cell index. This is true for each passband. From eq. 3.16

$$W_n^{\delta}(\zeta = 0) = \sum_l \frac{k_l}{N}, \tag{6.2}$$

where k_l/N is the loss factor per cell of the mode with index l. The number of modes in a passband is given by the number of cells N in the accelerating structure. From here it follows that for each passband of two accelerating structures with N_1 and N_2 cells, respectively, one has:

$$\sum_{l_1}^{N_1} \frac{k_{l_1}}{N_1} \approx \sum_{l_2}^{N_2} \frac{k_{l_2}}{N_2} \tag{6.3}$$

This relationship enables us to compare the loss factors for the 9-cell cavity and for the superstructure, normalized to the number of cells. For the latter, some influence is expected from the interconnecting tubes interrupting the periodicity of the structure.

The frequencies and impedances of the modes of the first higher order monopole passband and of the first three dipole passbands of the superstructure were obtained with the MAFIA code [74]. Two-dimensional simulations have been performed. The monopole modes with $k_{loss} > 3$ V/nC ($R/Q \geq 1\ \Omega$) are given in Table 6.2[1] [74]. For comparison, the monopole modes in the 9-cell cavity are presented in Table 6.3. The dipole modes with loss factors higher than 10 V/pC/m^2 ($R/Q \geq 0.3\ \Omega/\text{cm}^2$) are listed in Table 6.4. Table 6.5 shows the dipole modes for the 9-cell cavity. The measured frequencies and quality factors in the 9-cell TTF cavities will be discussed in section 6.3.1.

Simulations were carried out for the third dipole passband as well. The interest in this passband resides in the fact that for the 9-cell cavities one mode of this passband has a high impedance ($R/Q \approx 23\ \Omega/\text{cm}^2$). Moreover, it was found by beam experiments at TTF that this mode is poorly damped by the HOM couplers in some cavities [59]. The studies of this mode are presented in Chapter 5.

The R/Q values of the HOMs of the superstructure are compared in Fig. 6.4 and 6.5 with the ones for the modes of the reference 9-cell cavity [60]. The values were normalized in both cases to the number of cells. This allows a rough comparison of the two structures as discussed above. It can be seen that the impedances in both cases are indeed comparable. The sums of the loss factors per cell were calculated for the first two dipole passbands (considering all modes in each passband) and are presented in Table 6.6. The agreement between the two accelerating structures is quite good. The values are in general smaller for the superstructure, which is due to the perturbation of the cell periodicity by the beam tubes.

Although the HOMs in the superstructure and 9-cell cavities are similar, simulations were needed for the alternative design of the TESLA main linac, using superstructures. These simulations are presented in the next section and compared to the CDR design in section 6.3.

[1] R/Q (eq. 3.12) is preferred in most literature about the TESLA cavities, instead of the loss factor.

Frequency [GeV]	Loss factor [V/nC/ss.]	R/Q [Ω/ss.]	Q (meas.)
TM_{011}-like			
2.0303	41.5	13	$1.8 \cdot 10^3$
2.0281	41.4	13	$1.9 \cdot 10^3$
2.1230	13.3	4	$1.6 \cdot 10^3$
2.1258	13.4	4	$8.0 \cdot 10^2$
2.1237	13.3	4	$1.5 \cdot 10^3$
2.1587	101.7	30	$2.9 \cdot 10^3$
2.1558	101.6	30	$2.2 \cdot 10^3$
2.3052	7.2	2	$2.1 \cdot 10^3$
2.3061	7.2	2	$2.0 \cdot 10^3$
2.3084	7.3	2	$1.8 \cdot 10^3$
2.4149	3.8	1	$2.81 \cdot 10^4$
2.4170	3.8	1	$5.92 \cdot 10^4$
2.4198	3.8	1	$1.28 \cdot 10^4$
2.4226	3.8	1	$1.96 \cdot 10^4$
2.4338	19.1	5	$1.82 \cdot 10^4$
2.4405	613.4	160	$1.93 \cdot 10^4$
2.4519	1155.4	300	$1.45 \cdot 10^4$
2.4539	123.3	32	$2.44 \cdot 10^4$
2.4546	161.9	42	$2.05 \cdot 10^5$
2.4612	34.8	9	$1.12 \cdot 10^4$

Table 6.2: Monopole modes in the superstructure as obtained from MAFIA [74]. The measured Q-values will be discussed in section 6.2.2.

Frequency (simulation) [GHz]	Ave. frequency (measured) [GHz]	Loss factor (simulation) [V/nC/9-cell]	R/Q (simulation) [Ω/9-cell]	Q (meas.)
TM_{011}-like				
2.3787	2.3718	0.05	0.014	$1.5 \cdot 10^6$
2.3842	2.3774	0.02	0.006	$5.0 \cdot 10^5$
2.3939	2.3857	0.16	0.041	$5.0 \cdot 10^5$
2.4042	2.3964	0.40	0.105	$2.5 \cdot 10^5$
2.4166	2.4092	3.65	0.962	$1.0 \cdot 10^5$
2.4292	2.4222	0.005	0.001	$1.0 \cdot 10^5$
2.4402	2.4349	83.39	21.757	$5.0 \cdot 10^4$ *
2.4480	2.4465	602.25	156.622	$7.5 \cdot 10^4$ *
2.4520	2.4517	548.79	142.488	$2.5 \cdot 10^5$ *

* modes used for simulations in section 6.3.1

Table 6.3: Monopole modes in the 9-cell cavities as obtained from simulations [60] and from measurements at the cavities of the first 3 cryo-modules of TTF (see section 6.3.1).

Frequency [GeV]	Loss factor [V/pC/m^2 /superstr.]	R/Q [Ω/m^2 /superstr.]	Q (meas.)
TE_{111}-like			
1.4377	26.7	1.18	$1.64 \cdot 10^5$
1.4367	26.7	1.18	$8.16 \cdot 10^4$
1.4370	26.7	1.18	$1.31 \cdot 10^5$
1.6547	12.9	0.50	$2.04 \cdot 10^5$
1.6839	13.1	0.50	$3.03 \cdot 10^4$
1.6871	19.9	0.75	$5.67 \cdot 10^4$
1.6926	80.0	3.01	$1.11 \cdot 10^4$
1.6941	31.1	1.17	$1.76 \cdot 10^4$
1.7182	405.9	15.04	$1.3 \cdot 10^3$
1.7226	943.8	34.88	$5.56 \cdot 10^4$
1.7267	127.6	4.70	$1.63 \cdot 10^4$
1.7281	168.5	6.21	$9.57 \cdot 10^4$
1.7613	112.4	4.06	$1.3 \cdot 10^3$
1.7638	512.4	18.50	$7.9 \cdot 10^3$
TM_{110}-like			
1.8491	41.0	1.41	$1.87 \cdot 10^4$
1.8521	146.2	5.02	$2.4 \cdot 10^3$
1.8540	72.7	2.50	$4 \cdot 10^3$
1.8649	119.0	4.06	$7.8 \cdot 10^3$
1.8664	208.3	7.10	$8.1 \cdot 10^3$
1.8734	37.7	1.28	$2.89 \cdot 10^4$
1.8745	309.1	10.50	$2.19 \cdot 10^4$
1.8749	290.3	9.86	$2.09 \cdot 10^5$
1.8758	20.7	0.70	$2.77 \cdot 10^4$
1.8803	9.5	0.32	$8.17 \cdot 10^4$
1.8806	28.4	0.96	$7.22 \cdot 10^4$
1.9042	28.7	0.96	$5.21 \cdot 10^4$
1.9028	28.7	0.96	$5 \cdot 10^5$
1.9043	28.7	0.96	$3.35 \cdot 10^4$
TE-like			
2.5751	977.3	24.16	$1.44 \cdot 10^4$
2.5762	116.5	2.88	$1.66 \cdot 10^4$
2.5758	1009.9	24.96	$1.32 \cdot 10^4$

Table 6.4: Dipole modes in the superstructure as obtained from MAFIA [74]. The measured Q-values will be discussed in section 6.2.2.

Frequency (simulation) [GHz]	Ave. frequency (measured) [GHz]		Loss factor (simulation) [V/pC/m^2 /9-cell]	R/Q (simulation) [Ω/cm^2 /9-cell]	Q (meas.)	Q (BBU limit [11])
	1st pol.	2nd pol.				
TE_{111}-like						
1.6289	1.6110	1.6114	0.16	0.01	$1.0{\cdot}10^6$	
1.6369	1.6188	1.6195	2.67	0.10	$5.0{\cdot}10^5$	
1.6506	1.6321	1.6316	0.02	0.001	$2.0{\cdot}10^5$	
1.6669	1.6500	1.6506	19.98	0.76	$7.0{\cdot}10^4$ *	
1.6888	1.6725	1.6727	6.05	0.23	$5.0{\cdot}10^4$	
1.7137	1.6978	1.6991	301.86	11.21	$5.0{\cdot}10^4$ *	$8.4{\cdot}10^3$
1.7383	1.7260	1.7252	423.41	15.51	$2.0{\cdot}10^4$ *	$7.2{\cdot}10^3$
1.7652	1.7554	1.7545	59.86	2.16	$2.0{\cdot}10^4$ *	
1.7909	1.7827	1.7831	49.20	1.75	$7.5{\cdot}10^3$ *	$7.2{\cdot}10^3$
TM_{110}-like						
1.7991	1.7949	1.7948	21.70	0.77	$1.0{\cdot}10^4$ *	
1.8392	1.8342	1.8334	13.28	0.46	$5.0{\cdot}10^4$ *	$4.7{\cdot}10^4$
1.8531	1.8509	1.8511	11.26	0.39	$2.5{\cdot}10^4$ *	$5.2{\cdot}10^4$
1.8647	1.8643	1.8635	191.56	6.54	$5.0{\cdot}10^4$ *	$7.6{\cdot}10^4$
1.8727	1.8731	1.8732	255.71	8.69	$7.0{\cdot}10^4$ *	$1.2{\cdot}10^5$
1.8783	1.8795	1.8798	50.80	1.72	$1.0{\cdot}10^5$ *	$1.9{\cdot}10^5$
1.8820	1.8837	1.8841	3.17	0.11	$5.0{\cdot}10^5$	$3.3{\cdot}10^5$
1.8842	1.8864	1.8868	4.72	0.16	$7.0{\cdot}10^5$	$6.7{\cdot}10^5$
1.8852	1.8877	1.8881	2.31	0.01	$1.2{\cdot}10^6$	
TE-like						
2.5630	no		42.41	1.05	$1.0{\cdot}10^5$ *	arbitr.
2.5704	statistics		20.05	0.50	$1.0{\cdot}10^5$ *	chosen
2.5751			961.28	23.80	$5.0{\cdot}10^4$ *	

* modes used for simulations in section 6.3.1

Table 6.5: Dipole modes in the 9-cell cavities as obtained from simulations [60] and from measurements at the cavities of the first 3 cryo-modules of TTF (see section 6.3.1).

Passband	9-cell cavity	Superstructure	
TE_{111}-like	96	89	V/pC/m^2/cell
TM_{110}-like	61	55	V/pC/m^2/cell

Table 6.6: Comparison of sum of the loss factors per cell for the first two dipole passbands of the 9-cell cavity and the superstructure.

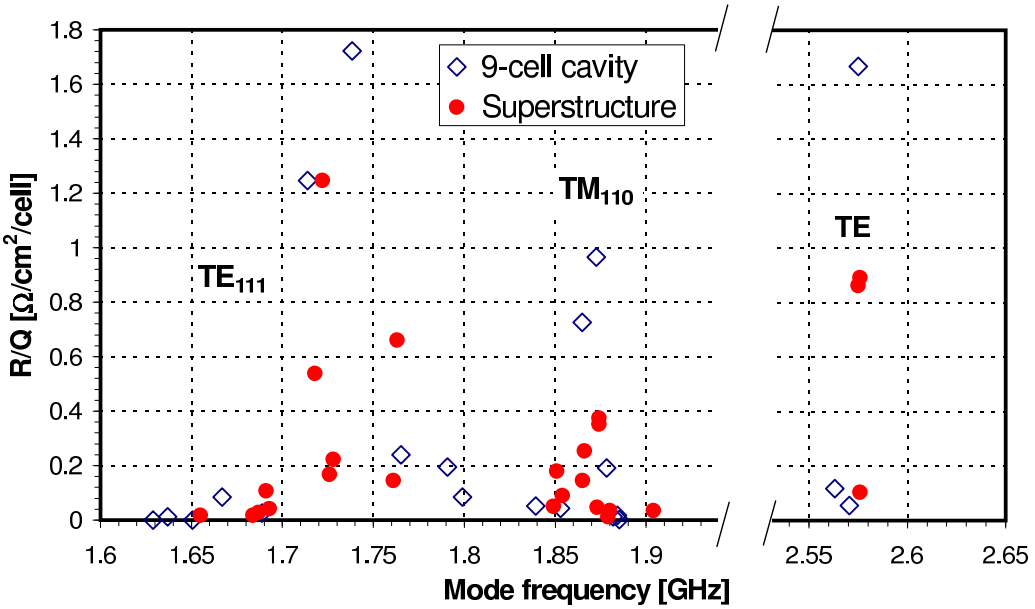

Figure 6.4: R/Q for the dipole modes of the 9-cell cavity and of the superstructure. The values are normalized to the number of cells.

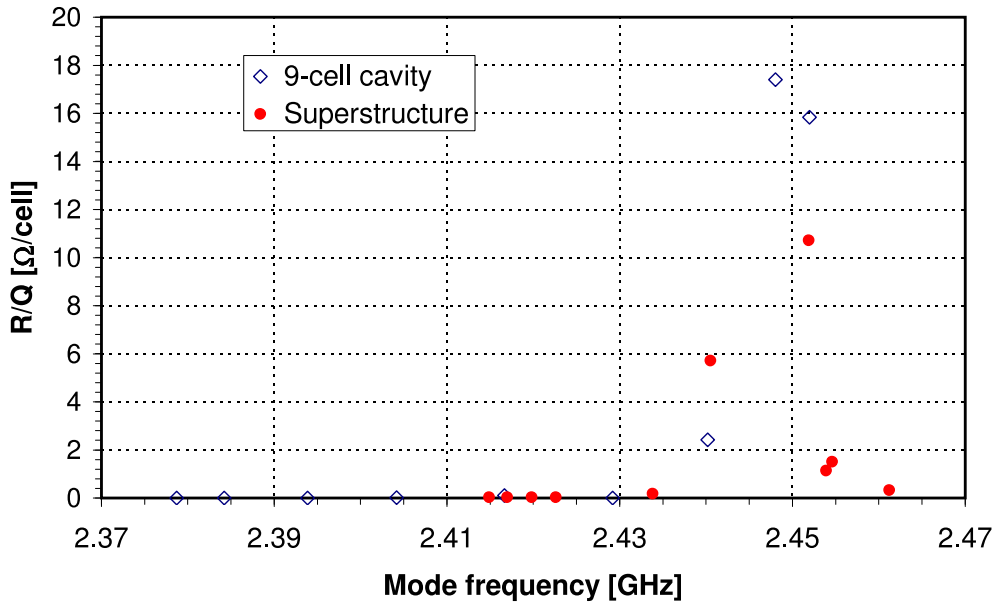

Figure 6.5: R/Q for the monopole modes of the 9-cell cavity and of the superstructure. The values are normalized to the number of cells.

6.2 Beam Dynamics with the TESLA Alternative Design

6.2.1 Required HOM damping in the superstructure

Simulations were carried out for the beam dynamics in the main linac of TESLA, in order to determine the amount of damping needed for the HOMs in the superstructure. The conditions were looked for, for which the bunch train properties satisfy the requirements of the high energy physics experiments: a small transverse spread in the beam offset and a small multi-bunch emittance at the IP. The estimation parameter is the multi-bunch emittance (see section 3.1) which should be negligible in comparison to the design single bunch emittance ($3 \cdot 10^{-8}$ m·rad in the vertical plane). The multi-bunch *emittance growth* is defined as the percent of the multi-bunch emittance at the end of the linac from the desired single bunch emittance.

The code L is used for the simulations [75]. The cryo-module with superstructures and the main linac is made up as described in section 6.1. The beam parameters are given in Table 6.1. The bunches are assumed to be rigid. The gradient is 21.7 MV/m. The cavities are misaligned with 500 μm rms, while the quadrupoles are considered to be perfectly aligned. The effect of quadrupole misalignment and orbit motion is discussed in section 6.2.3.

The short range wakes are not taken into account. They are of little concern here since only the effect of HOMs is studied. Both monopole and dipole modes are considered, as presented in Tables 6.2 and 6.4. The HOMs are assumed to be equally distributed within the accelerating sections. The kick from each mode is assumed to be concentrated in the center of the structure. The error introduced by this assumption is usually negligible [26]. The cavities are assumed to be slightly deformed (cavity-to-cavity detuning) in such a way as to obtain ten types of cavities with different HOM frequencies. This frequency spread among the cavities is required to avoid the resonant addition of the long range wake fields in various cavities (see section 3.4.2). The assumed frequency spread is 0.1 % rms reflecting the production tolerances.

The higher order modes are assumed to be damped to various levels. For each case, ten machines are considered: These differ by the various offsets and HOM frequencies of the cavities. For each set of quality factors, the same ten machines are considered. This allows us a comparison between the various damping levels of the modes. The loss factors are taken from simulations (Tables 6.4 and 6.2).

First, the quality factors Q of all HOMs are set to $5 \cdot 10^5$, except for the four dipole modes with a loss factor higher than 500 V/pC/m^2 (R/Q bigger than 15 Ω/cm^2) and two monopole modes with loss factors over 500 V/nC ($R/Q > 150$ Ω), for which a Q of $1 \cdot 10^5$ was assumed. The highest R/Q for a dipole mode is 35 Ω/cm^2, while for the monopole modes it is 300 Ω. The longitudinal multi-bunch energy spread obtained is negligible, of the order of 10^{-6}, but the transverse normalized multi-bunch emittance is quite large, being close to the vertical design emittance at the interaction point, $3 \cdot 10^{-8}$ m·rad.

In the next step, the Q-values of the four dipole modes with the highest impedance were lowered to $5 \cdot 10^4$ without much change in the emittance. All other modes are

assumed then to be damped as well from $5 \cdot 10^5$ to $2 \cdot 10^5$. Now the multi-bunch emittance obtained is well below the maximum admissible value. The beam dynamics has been simulated for some more cases as well. A summary of the results is given in Table 6.7. The maximum normalized multi-bunch emittance ε_n obtained in the ten random simulations done for each case is given.

Number of dipole modes	Q	R/Q [Ω/cm^2 /superstr.]	max ε_n [m·rad]
27	$5 \cdot 10^5$	≤ 15	$5 \cdot 10^{-8}$
4	$1 \cdot 10^5$	> 15	
27	$5 \cdot 10^5$	≤ 15	$3.5 \cdot 10^{-8}$
4	$5 \cdot 10^4$	> 15	
27	$2 \cdot 10^5$	≤ 15	$9 \cdot 10^{-9}$
4	$5 \cdot 10^4$	> 15	
24	$2 \cdot 10^5$	< 10	$8 \cdot 10^{-9}$
7	$5 \cdot 10^4$	> 10	
27	$2 \cdot 10^5$	≤ 15	$1 \cdot 10^{-8}$
4	$1 \cdot 10^5$	> 15	
31	$2 \cdot 10^5$		$3 \cdot 10^{-8}$

Table 6.7: Normalized multi-bunch emittance for various choices for Q. The maximal emittances obtained from the 10 random simulations for each case are compared.

As it can be seen, damping most of the modes to a level of $2 \cdot 10^5$ is sufficient, except for the ones with $R/Q > 15\ \Omega/\mathrm{cm}^2$, for which values under $5 \cdot 10^4$ are desirable. Still, a stronger damping for these modes will be aimed for in the real structure, as well as for the modes with $R/Q > 10\ \Omega/\mathrm{cm}^2$, since locally they can give a very strong kick to the beam. In practice, only some of the 27 modes considered in the simulations will reach $2 \cdot 10^5$, which relaxes even more the damping level required for the others. The standard deviation in the transverse bunch position is in all cases smaller than 10 μm and can be easily corrected by a feedback system.

In Figs. 6.6 and 6.7, one of the worst results obtained from the simulations done for the case of 27 modes having $Q = 2 \cdot 10^5$ and four with $5 \cdot 10^4$ is shown. The bunch offsets in the vertical plane at the end of the linac are plotted in Fig. 6.6 while Fig. 6.7 shows the normalized multi-bunch emittance along the accelerator in the same plane. After about 150 μs a steady state is reached, all bunches have the same transverse position (Fig. 6.6). This means that only less than 10 % of the train contributes to the multi-bunch emittance.

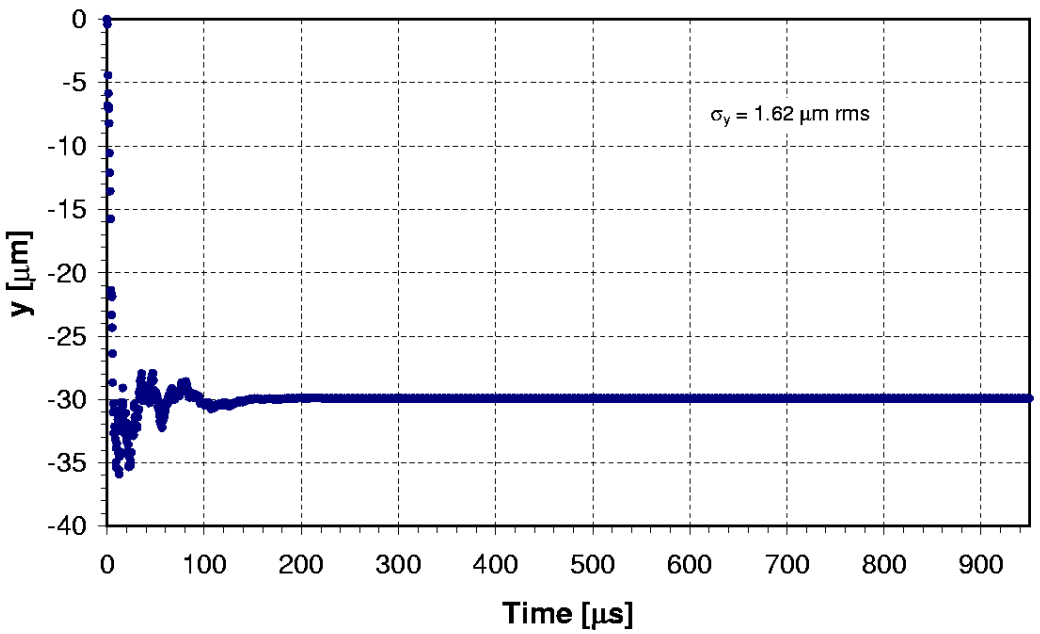

Figure 6.6: Bunch offsets at the end of linac for the case when all modes have $Q = 2 \cdot 10^5$, except for 4 modes with $R/Q = 15\ \Omega/\mathrm{cm}^2$ that have $Q = 5 \cdot 10^4$. σ_y is here the standard deviation of the vertical position of the bunches.

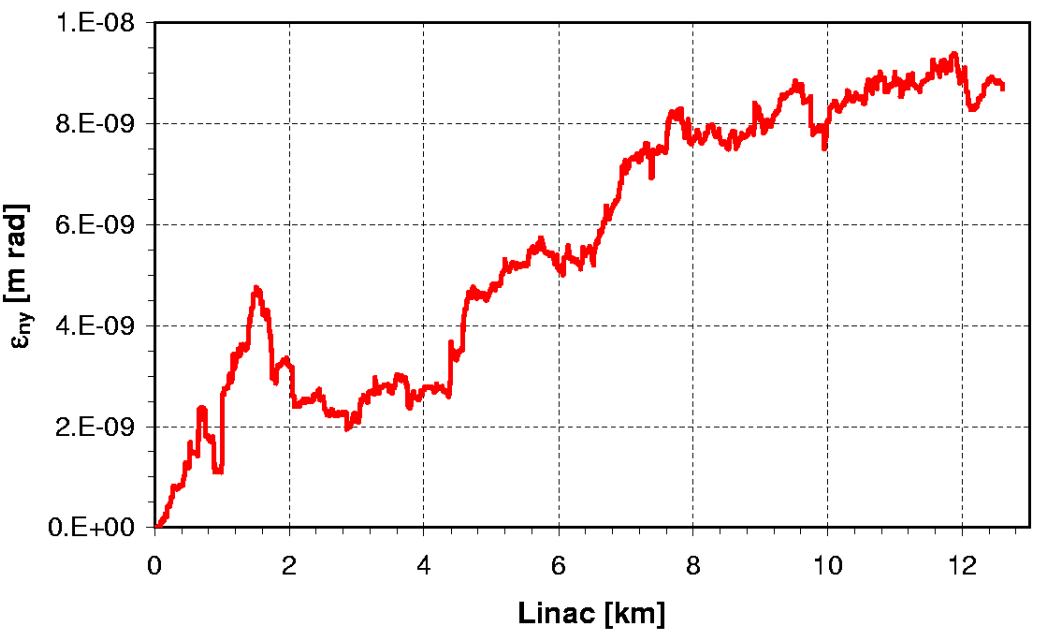

Figure 6.7: Normalized multi-bunch emittance along the main linac. Worst result obtained for the case when all modes have $Q = 2 \cdot 10^5$, except for 4 modes with $R/Q = 15\ \Omega/\mathrm{cm}^2$ that have $Q = 5 \cdot 10^4$.

6.2.2 Multi-bunch emittance growth

Measurements of external Q in a copper model of the superstructure

The external quality factors Q_{ext} were measured in a copper model of the superstructure [76], with three HOM couplers placed at the interconnecting tubes and two at the end tubes. The couplers are identical to those of the 9-cell cavities. The quality factor Q_{ext} was measured for all modes up to 3 GHz for various angular positions of the couplers.

The various sets of measurements, for different combinations of the coupler angles, are comparable to each other. Some modes are better damped in a certain case, while others achieve a lower Q for other angular positions of the HOM couplers. In all cases, most of the modes could be damped to a Q-level below $2 \cdot 10^5$, as approximately required in the previous section.

One set of results was chosen and the measured quality factors for the dipole modes are shown in Fig. 6.8 [77]. Only three modes exceed $2 \cdot 10^5$ and they have an R/Q below 10 Ω/cm^2. Two of them, shown in the chart, have Q close to the limit value, while a third mode has $Q = 5 \cdot 10^5$, but a quite low R/Q of 0.96 Ω/cm^2.

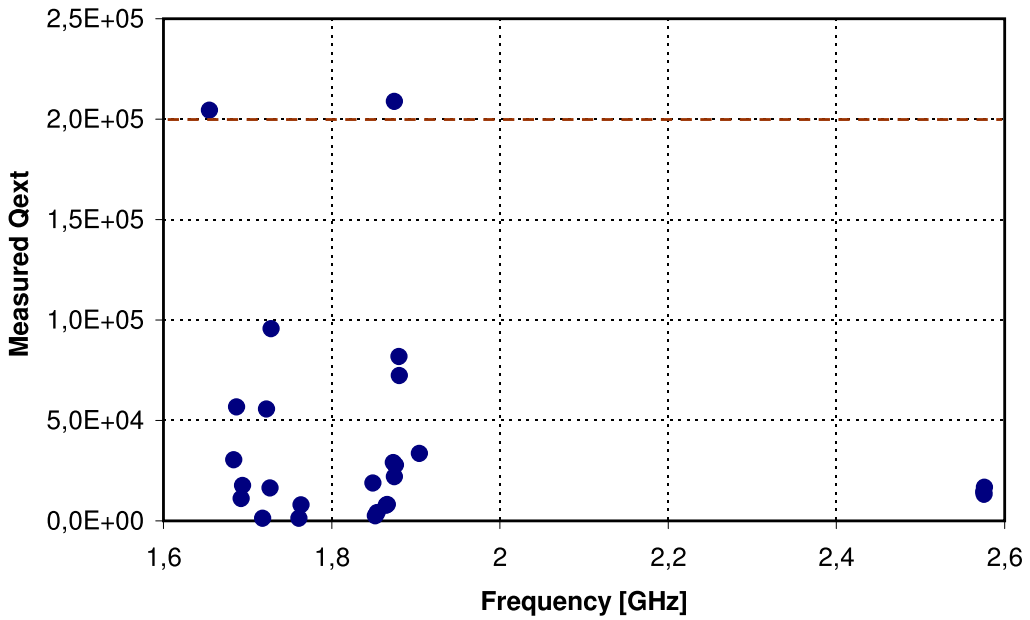

Figure 6.8: Measured Q_{ext} in the copper superstructure model. The dipole modes of the first three passbands with the highest R/Q are shown. Only three modes are above the estimated limit of $2 \cdot 10^5$. One of them has a higher Q but a low R/Q and is not shown in the figure.

Simulations with measured quality factors

The measured Q_{ext} of the modes were used for new simulations. Again ten random machines were considered. The average multi-bunch emittance along the linac is shown in Fig. 6.9. The obtained emittance growth of 4 % is negligible.

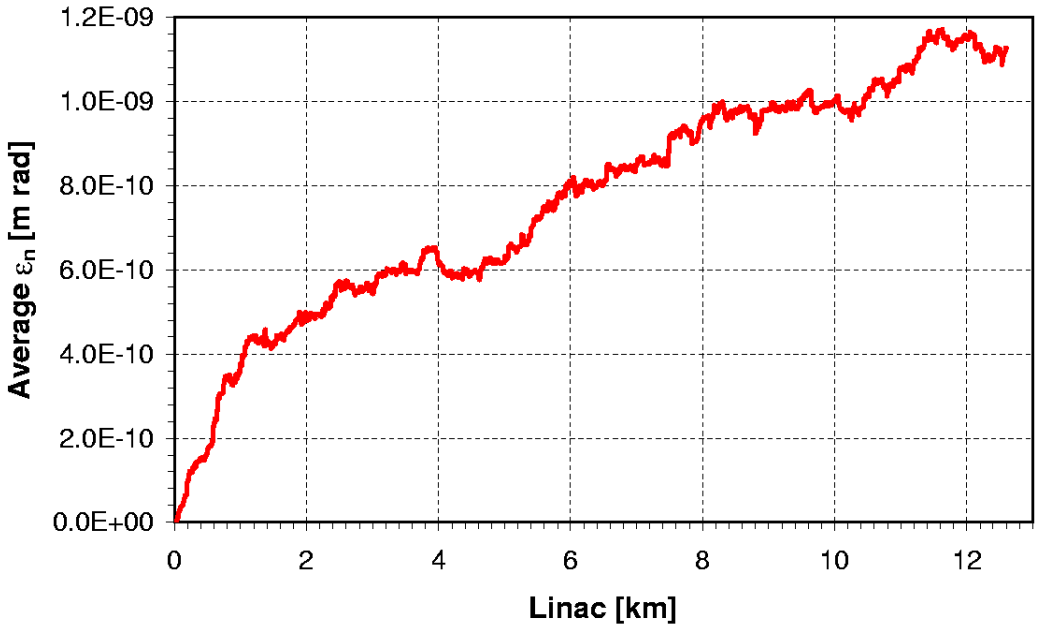

Figure 6.9: Normalized multi-bunch emittance along the main linac for the alternative design. The simulations were made with measured Q_{ext}. The average emittance of the 10 simulations is shown. Average emittance growth is 4 %.

The validity of the results of these simulations depends on whether one achieves the same damping level with a niobium superstructure as with the copper model. A structure consisting of two 7-cell cavities is now being built and is planned to be tested at TTF. The HOMs will also be studied at this superstructure.

6.2.3 Pulse-to-pulse orbit jitter

The individual bunch offsets within a bunch train (see the example of Fig. 6.6) can be corrected with an adaptive feed-forward system, provided that the bunch pattern does not change much from pulse to pulse. A slow pulse-to-pulse orbit jitter can be corrected with a fast feedback system placed in the beam delivery system [78, 79]. In this section, the variation of the multi-bunch pattern at the linac end due to ground motion, injection error and charge fluctuation is studied.

For the simulations presented in this section, a slightly different linac layout is used. As it will be seen, there is no essential difference between this layout and the one considered above. Each module contains 4 superstructures. The initial energy of the bunches is 5 GeV. The linac is divided into only two sections: The first one accelerates

the bunches to about 125 GeV and contains 4 modules per FODO cell. The second, from 125 to 250 GeV, has 6 modules per FODO cell. The bunch train is the same as used above with the alternative design (Table 6.1). The higher order modes used are the ones measured on the copper model of the superstructure (Tables 6.4 and 6.2). The mode frequencies have a spread of 0.1 % rms. In order to save computation time, only 500 bunches are considered from a total of 2820. This is justified by the fact that we want to compare bunch trains under various assumptions, and the steady state is rapidly reached, where all bunches have the same offsets and angles.

A first simulation was done with a misalignment of the accelerating structures of 0.5 mm rms. The quadrupoles are perfectly aligned. The bunches are injected on axis. The emittance is calculated by assuming a full length bunch train, with the 501st to the 2820th bunches in the steady state. The emittance growth obtained is about 3 %, comparable to the results of the previous section.

Ground motion

Starting from this linac, with no quadrupole misalignment, ground motion is simulated by randomly moving the quadrupoles and the superstructures according to the ATL law:

$$< \Delta y^2 >= A \cdot T \cdot L, \tag{6.4}$$

where Δy is the relative vertical displacement of two points separated by the distance L, after a time T. A is a coefficient depending on the geological conditions. Here the same value is taken as for the HERA accelerator [80] $A = 4 \cdot 10^{-6}$ μm^2/m·s. The simulations are done in steps of 0.2 s, since the pulse repetition frequency is 5 Hz.

The rms position error of the quadrupoles in time is shown in Fig. 6.10. The effect of the ground motion on the average offset of the bunch train is shown in Fig. 6.11. A drift of a few μm after 120 s can be observed.

In Fig. 6.12, two bunch trains are compared, one at the initial time, the other after 1 min. The difference between the two bunch patterns, after subtracting the average offset, is smaller than 8 nm in this case, which means that the change in the effect of the HOMs due to the different orbit of the beam in the accelerating structures is very small. The shift of the whole pattern is due to the quadrupole kicks. An adaptive feed-forward system can easily remove the bunch-to-bunch offset variation.

Injection offset

The bunch train is injected with a vertical offset of 18 μm (one bunch sigma) in the same machine. The quadrupoles have no misalignment. The result is compared to the case of injection on-axis in Fig. 6.13. The rms variation of the bunch positions is 17 nm (after subtraction of the average position), which is negligible.

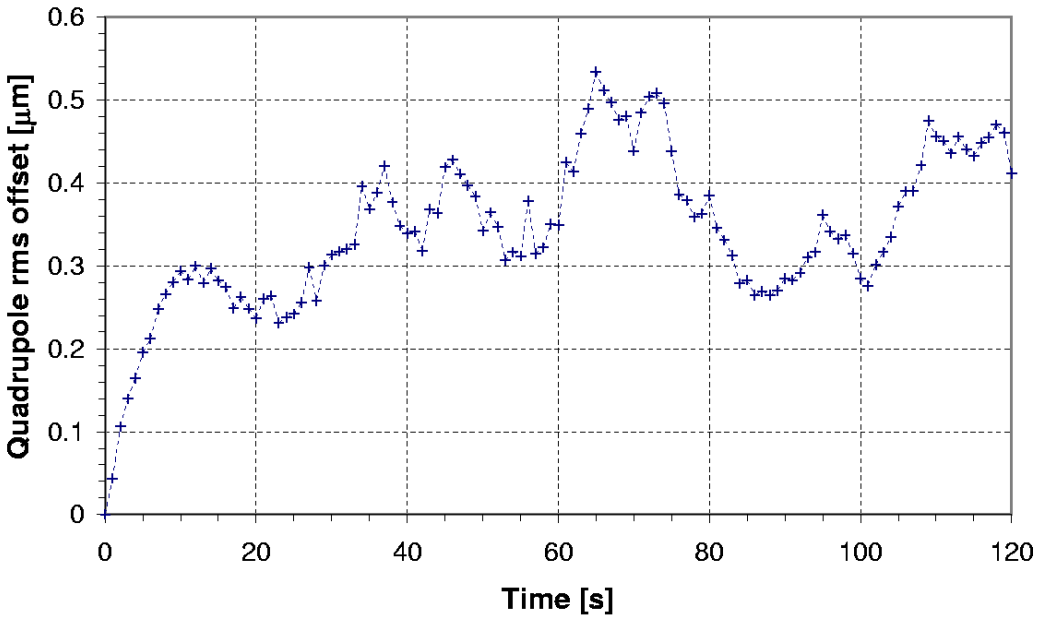

Figure 6.10: The rms offset of the quadrupoles versus time, due to ground motion.

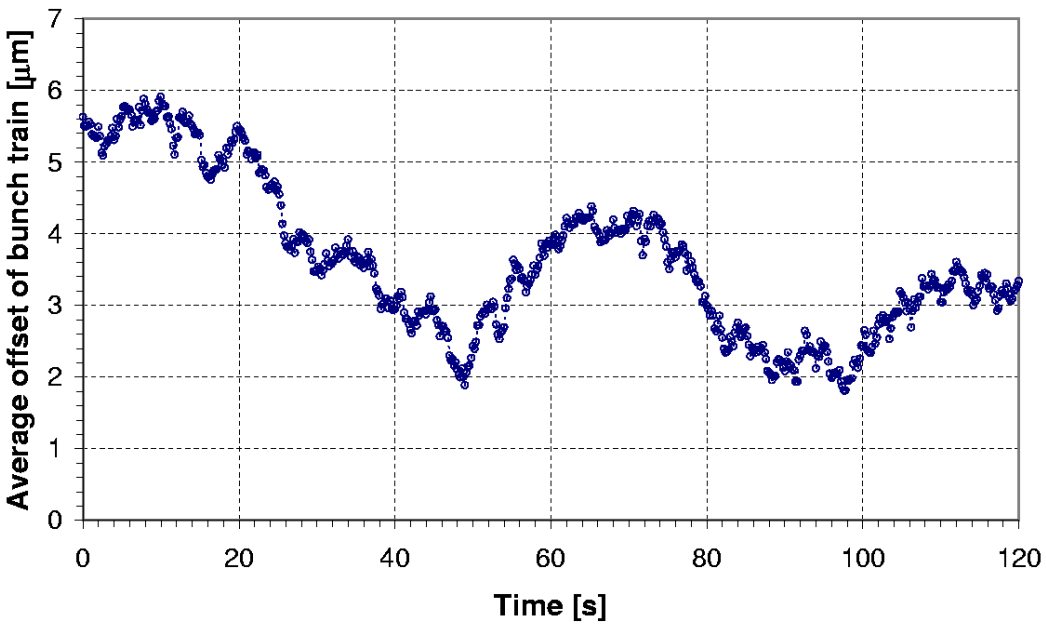

Figure 6.11: The average offset of the bunch train at the linac end versus time, caused by ground motion.

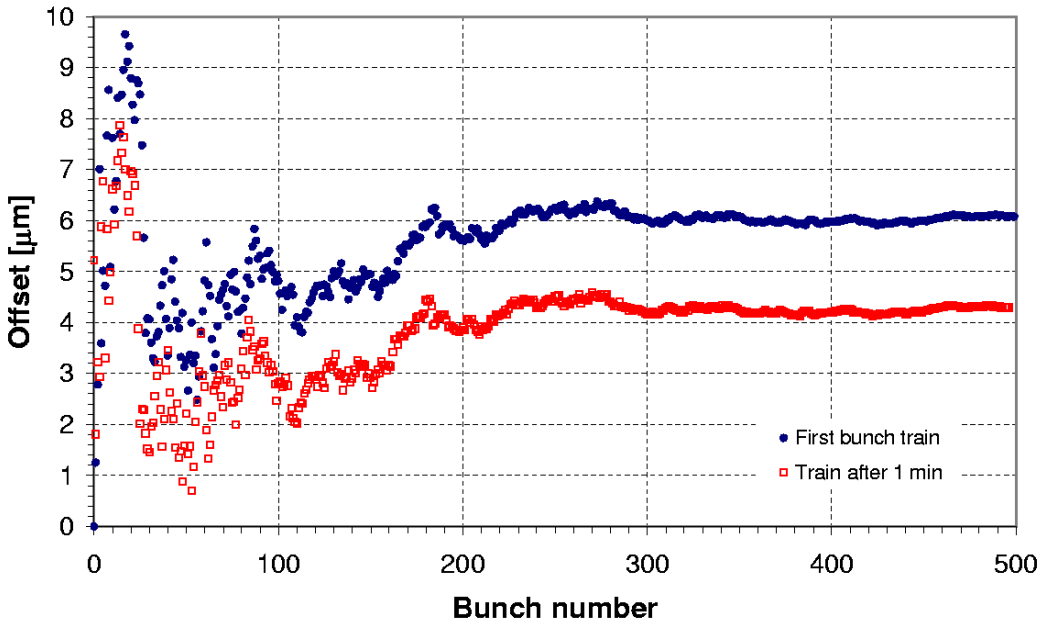

Figure 6.12: Bunch offsets of two pulses: at the initial time moment (quadrupoles perfectly aligned) and after 1 min of ground motion.

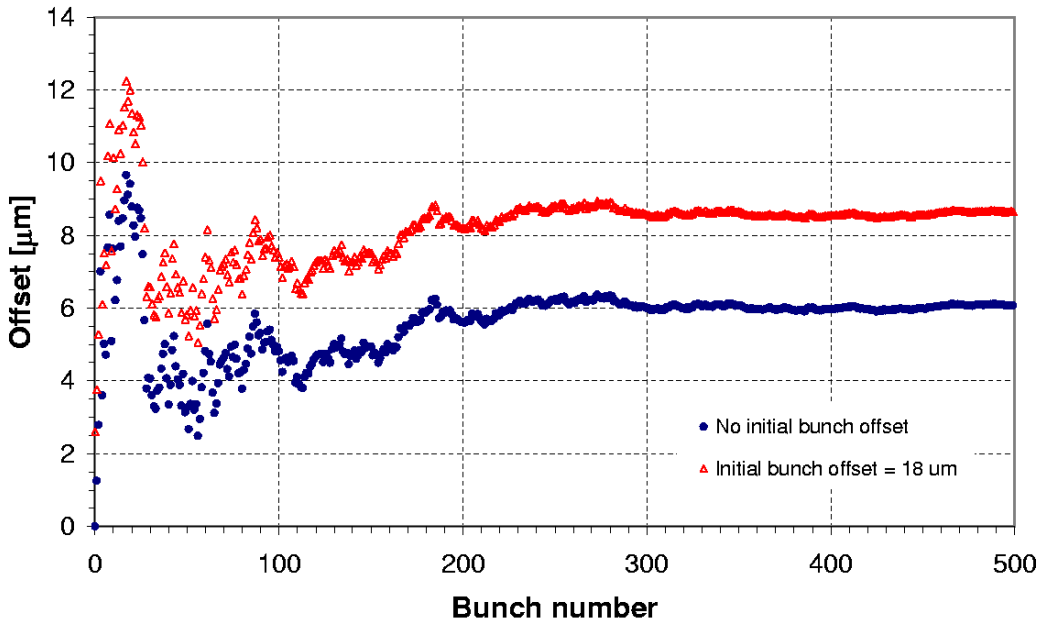

Figure 6.13: Bunch offsets for two pulses: with no initial offset of the bunches, and with an offset of 18 μm (one σ_y, where σ_y is the transverse rms bunch size). The quadrupoles are perfectly aligned.

Charge fluctuation

A charge fluctuation of 1 % from bunch-to-bunch induces a negligible change on the bunch offsets, as can be seen in Fig. 6.14.

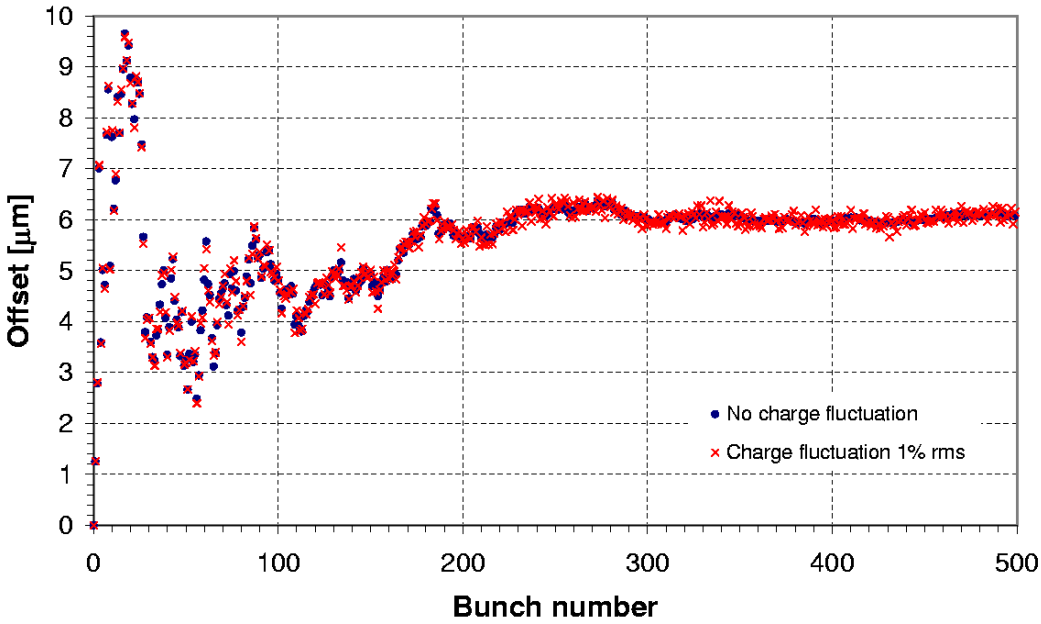

Figure 6.14: Bunch offset for two pulses: with constant charge for all bunches, and with 1 % charge fluctuation. The quadrupoles are perfectly aligned.

All three effects on the beam stability studied above, ground motion, injection error and charge fluctuation, show an essentially static beam pattern [81]. A feed-forward system can correct bunch-to-bunch offset variations, while the general feedback system can correct the pulse-to-pulse orbit jitter.

6.3 Comparison to the CDR Design

6.3.1 Beam dynamics with the TESLA CDR design

Similar simulations, as for the main linac with superstructures, were made for a main linac containing 9-cell accelerating cavities, in order to compare the results. The beam parameters used are given in Table 6.1 (CDR design). The accelerating module contains eight 9-cell cavities. The main linac is structured as described in section 6.1.1. Ten types of cavities are considered with an rms frequency spread of 0.1 %. Ten runs were carried out with various misalignment of cavities and various mode frequencies. Two sets of simulations were performed, differing only in the HOMs used, as described below.

Simulations with HOMs from CDR

First the 10 dipole modes given in [11] as being the most dangerous are considered. They are listed in Table 6.8.

Frequency [GHz]	Loss factor [V/pC/m^2 /9-cells]	R/Q [Ω/cm^2 /9-cells]	Q
TE_{111}-like			
1.709	306.03	11.40	$8.40 \cdot 10^3$
1.736	403.58	14.80	$7.20 \cdot 10^3$
1.763	47.08	1.70	$7.20 \cdot 10^3$
TM_{110}-like			
1.837	14.43	0.50	$4.68 \cdot 10^4$
1.853	8.73	0.30	$5.15 \cdot 10^4$
1.865	186.90	6.38	$7.56 \cdot 10^4$
1.874	253.45	8.61	$1.20 \cdot 10^5$
1.880	56.70	1.92	$1.94 \cdot 10^5$
1.884	1.48	0.05	$3.31 \cdot 10^5$
1.887	4.74	0.16	$6.73 \cdot 10^5$

Table 6.8: Dipole modes used for simulations (see CDR [11]).

One typical result for the bunch train pattern at the end of the main linac is shown in Fig. 6.15. It can be seen that after about 100 μs the steady state is reached, which is less than 15 % of the train. The average multi-bunch emittance increase along the linac is shown in Fig. 6.16. The emittance obtained is much smaller than the vertical normalized emittance at the IP of $3 \cdot 10^{-8}$ m·rad. The multi-bunch emittance growth is of 4 %. This agrees with [11] and is similar to the one obtained for the design with superstructures (section 6.2.2).

Simulations with HOMs from measurements at the TTF cavities

One question that arises is how realistic is the damping level given in [11] (Table 6.8) and used for simulations in the previous paragraph. Since 1997, three cryo-modules have been built and tested at TTF, containing a total of 24 9-cell cavities. The higher order modes of the first and second dipole passbands as well as for the second monopole passband were measured for each cavity [62].

The average frequency measured for each mode, for both polarizations, is given in Tables 6.5 and 6.3, in comparison to the ones obtained from simulations [60]. In Fig. 6.17 the average frequencies for each polarization of the modes are plotted against the simulated values. The frequency spread is in most cases $\pm$ (0.5 $\div$ 0.6) % rms for the TE_{111}-like modes, while for the TM_{110}-like modes it is lower, $\pm$ (0.05 $\div$ 0.2) %. The spread is smaller for the second passband, but the band itself is also narrower, the

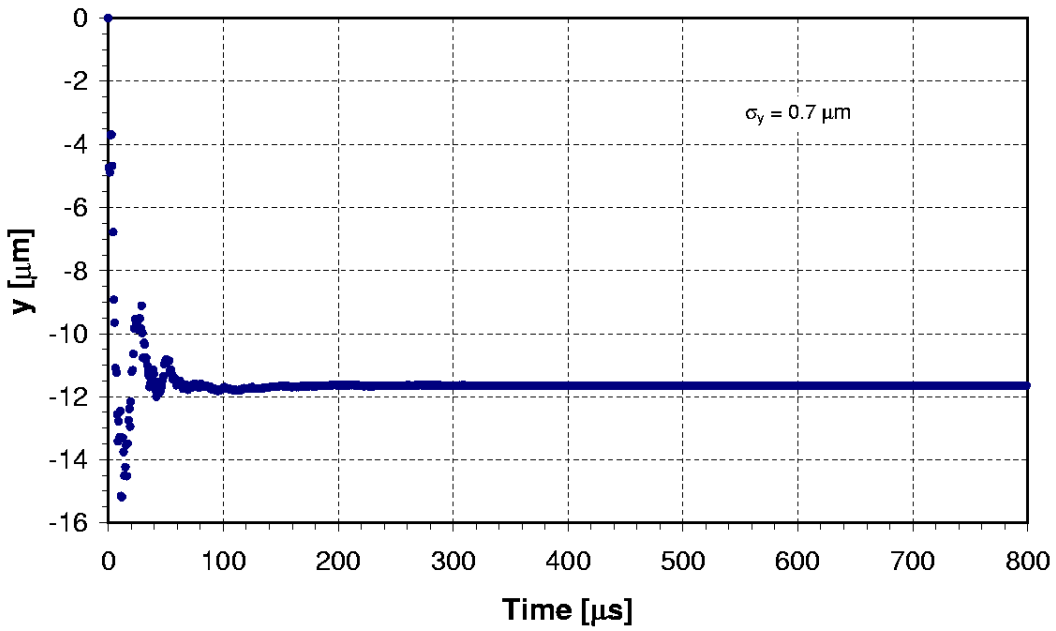

Figure 6.15: Typical bunch train offsets at linac end for the CDR design. The modes from CDR [11] were used (see Table 6.8). σ_y is here the standard deviation of the vertical position of the bunches.

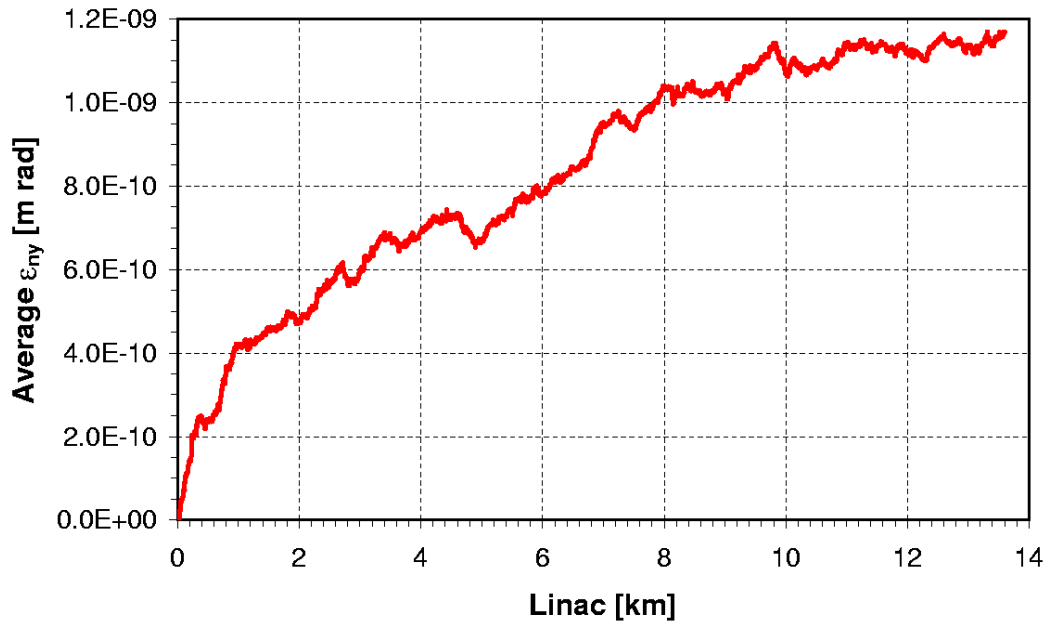

Figure 6.16: Normalized multi-bunch emittance along the main linac for the CDR design. The modes from CDR [11] were used (see Table 6.8). The average emittance is shown. Average emittance growth is 4 %.

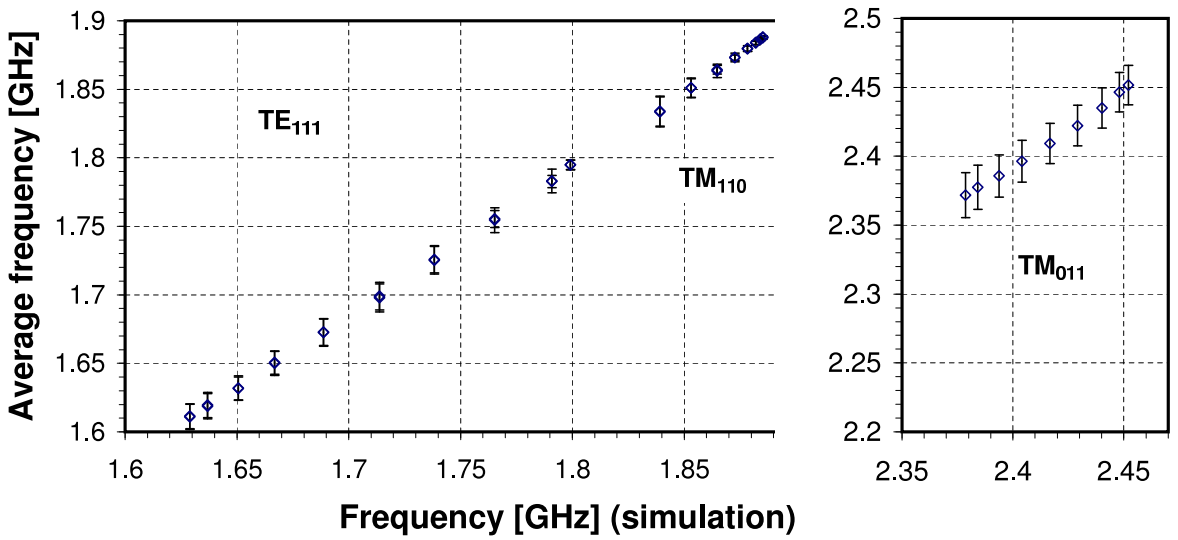

Figure 6.17: Average mode frequencies for passbands TE_{111}, TM_{110} and TM_{011} measured at the cavities of the first 3 TTF modules plotted against the values obtained from simulations.

difference in frequency between the modes being smaller. For the monopole band, the frequency spread of the cavities is around $\pm$ 0.6 % rms.

For the quality factors of the modes, similar statistics is not possible, due to the wide spread in the values. Instead, a histogram analysis is presented, counting the number of modes found in various intervals of Q-values. An example of such a histogram is shown in Fig. 6.18. In some cases a maximum can be seen, with the number of cavities having higher and lower values decreasing when one goes further from this "center". In order to make a prediction of the beam dynamics in the main linac of TESLA, considering the CDR design, a value was picked for each mode closer to the maximum values than to the "center". The Q-values chosen for our next simulations are given as well in Table 6.5 and 6.3. For comparison, the Q-values from the modes given in Table 6.8, and used for simulation in the previous paragraph, are also listed in the last column. It is remarkable that most of the modes have lower or similar Q-values for the measurements. Noticeable differences can only be seen for two TE_{111} modes at 1.7137 and 1.7383 GHz. One should keep in mind that the quality factors taken from the measurements are rather pessimistic values.

In Table 6.5 some modes of the third dipole passband are given as well. Although the frequencies and quality factors could not be measured due to the degeneration of the modes in the module with 8 cavities (see section 5.4), this passband is also of interest for reasons mentioned for the superstructure case: on one hand one mode has very high R/Q of 23.8 Ω/cm^2, on the other, at several TTF cavities, this mode was found to have a very high Q, between $8 \cdot 10^4$ and 10^6. The fact that many cavities have higher Q-values than desired does not yet mean that they are already "dangerous",

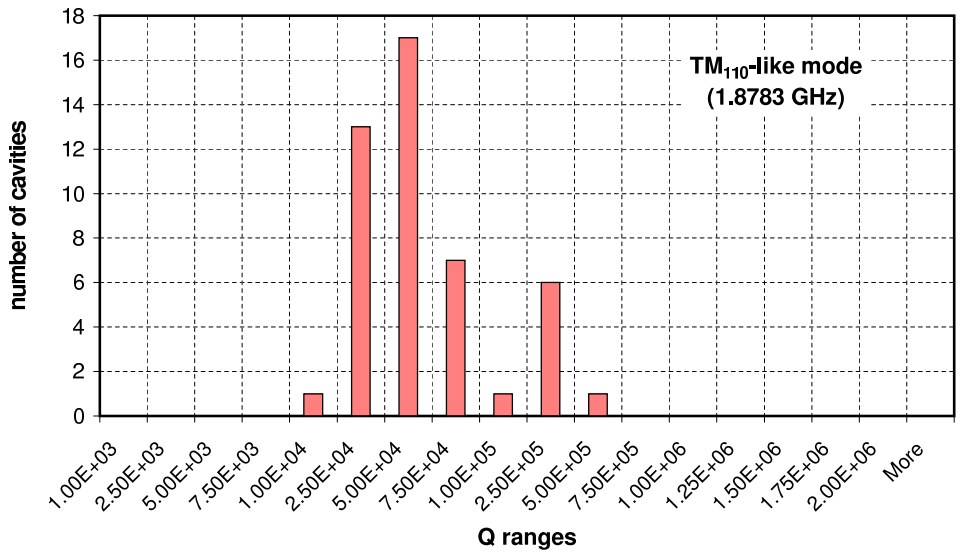

Figure 6.18: Example of a histogram with measured Q-values at the cavities of the first 3 TTF modules for a TM_{110}-like mode.

since one can not set an absolute limit. The simulations presented here answer the question, how would the beam dynamics look like in a linac where the cavities would resemble the ones in TTF.

For the simulations, the dipole modes with a loss factor higher than 0.3 V/pC/m^2 and the monopole modes with the loss factor exceeding 1 V/nC were chosen, in Tables 6.5 and 6.3 marked with a *. One polarization was chosen for each mode. The simulations done with the other polarization of each mode give comparable results. The Q-values are the ones derived from the measurements at the TTF cavities. The average vertical emittance obtained is shown in Fig. 6.19. The emittance growth is 5 %, comparable to the results presented in the previous paragraph.

6.3.2 Comparison

The results of the multi-bunch beam dynamics simulations are summarized in Table 6.9. In all cases, the emittance growth is a few percent, which is fully acceptable for the beam quality. This result is justified by the similar $(R/Q)Q$ of the modes for the two

Design	CDR		Alternative
	modes from CDR [11]	modes meas. at TTF	
Emittance growth $\Delta\varepsilon$ [%]	4	5	4

Table 6.9: Summary of the simulations for the alternative and CDR designs.

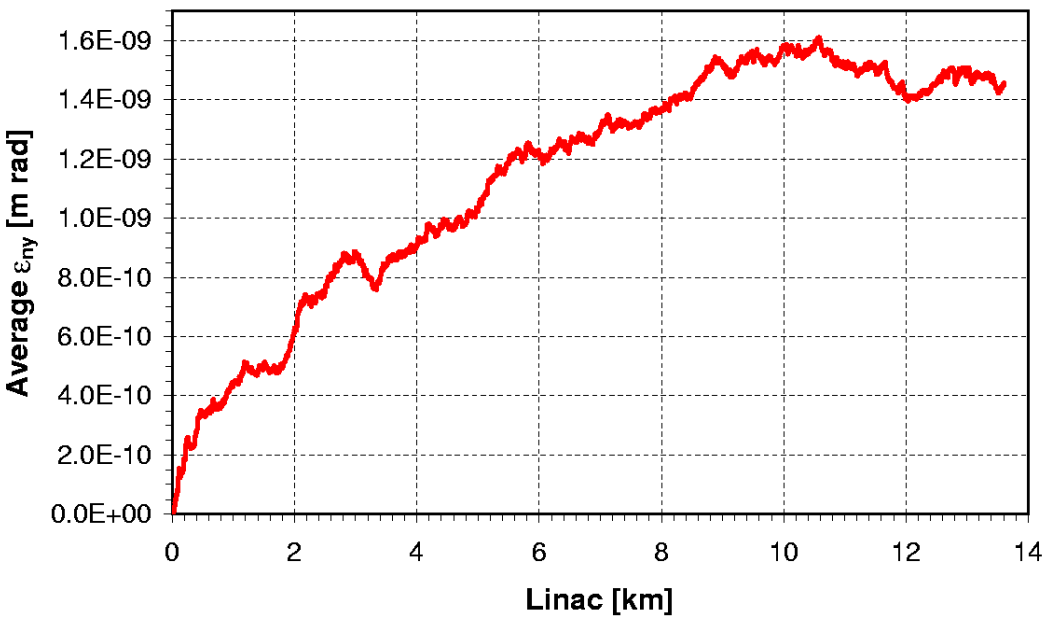

Figure 6.19: Normalized multi-bunch emittance along the main linac for the CDR design. The mode measurements at TTF were used (see Table 6.8). The average emittance is shown. Average emittance growth is 5 %.

structure types as shown in Fig. 6.20. Here, the values for the 9-cell cavity and for the superstructure, normalized to the number of cells, are shown.

The comparable results of the beam dynamics simulations for the case of using superstructures or 9-cell cavities lead us to expect similar results with other options for the acceleration sections.

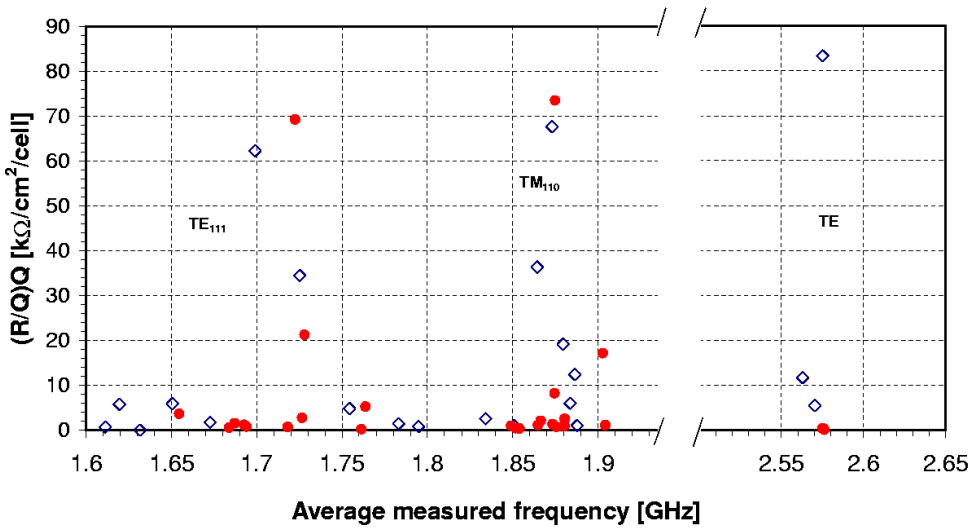

Figure 6.20: Comparison of the $(R/Q)Q$ per cell for the first 3 dipole passbands for the 9-cell cavity and for the superstructure.

6.4 Beam Dynamics in the Presence of an Insufficiently Damped Mode

The simulation that is presented in this section shows the importance of damping the modes, in particular a high impedance mode in the third dipole passband. As described in sections 5.3.2 and 5.4, a mode with the frequency around 2.58 GHz and $R/Q = 23.8\ \Omega/\mathrm{cm}^2$ was found to be badly damped in several TTF cavities. The measured Q-values are between $8.6 \cdot 10^4$ and $1 \cdot 10^6$ (see Table 5.8). In at least one cavity of each module, this mode has a Q above 10^5.

For the simulation, it was assumed that in each cavity the 10 modes from Table 6.8 can be excited, while one cavity of each module (containing 8 cavities in total), randomly placed within it, has an additional mode with frequency 2.585 GHz, $R/Q = 23.8\ \Omega/\mathrm{cm}^2$ (loss factor 9.6 $\mathrm{V/pC/m^2}$), and $Q = 10^6$. The linac is separated into three sections as described in section 6.1 and in Table 6.1. The bunch train properties are given in the same table (CDR design).

A typical result for the bunch train at the end of the linac is shown in Fig. 6.21. Compared to the bunch pattern for the CDR and the alternative design (Fig. 6.15), the steady state is reached after a longer time, due to the very high quality factor of the mode. The average multi-bunch emittance along the linac is plotted in Fig. 6.22. The average emittance growth is 54 %, which is not acceptable for the beam quality. The worst case obtained in the random simulations gives an emittance growth over 120 %.

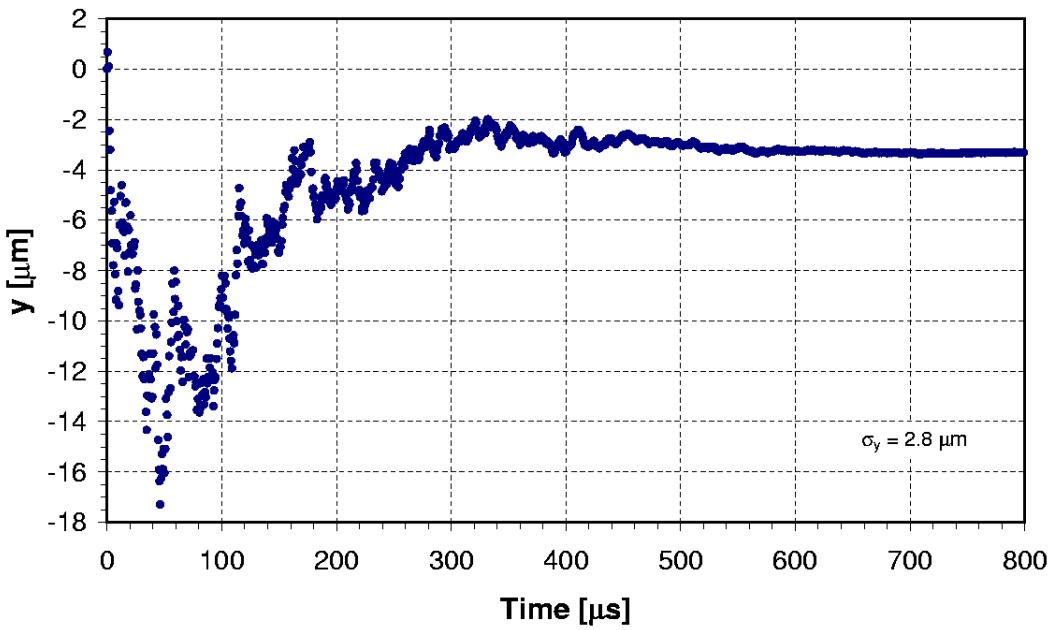

Figure 6.21: Typical bunch offsets at linac end for the CDR design. The modes from CDR [11] are present in each cavity. One cavity, randomly placed within each module, has an extra mode with frequency 2.584 GHz, $R/Q = 23.8\ \Omega/\mathrm{cm}^2$ and $Q = 10^6$. σ_y is the standard deviation of the vertical position of the bunches.

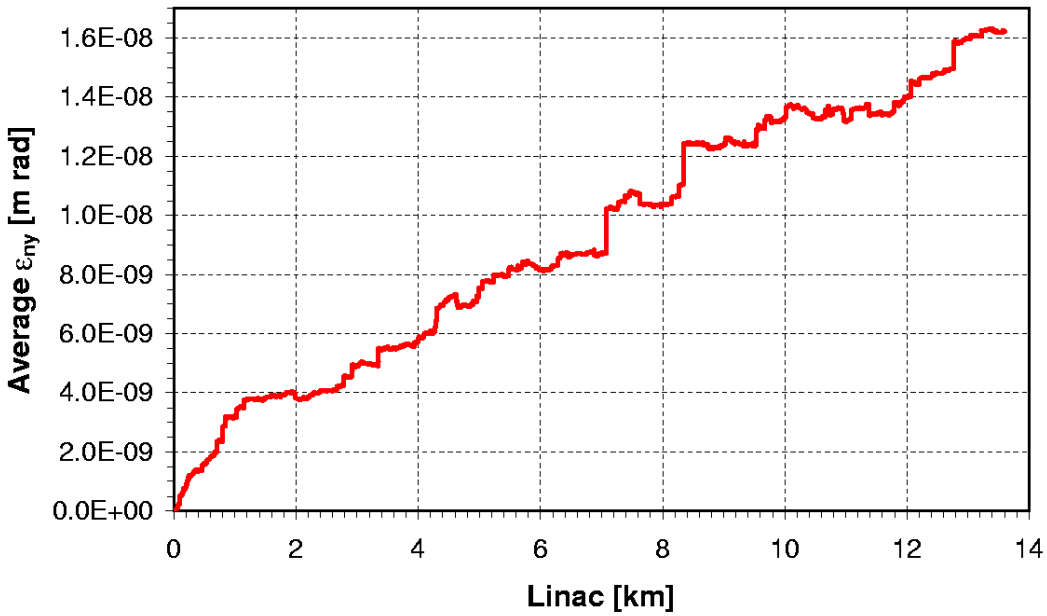

Figure 6.22: Normalized multi-bunch emittance along the main linac for the CDR design. One cavity randomly placed within each module has an extra mode with frequency 2.584 GHz, $R/Q = 23.8\Omega/\text{cm}^2$ and $Q = 10^6$. The average emittance is shown. Average emittance growth is 54 %.

The results of these simulations show how important it is to study the causes of such a bad damping for this mode. The studies done in this sense were presented in section 5.4. Nevertheless, even if such a situation occurs as the one given by the simulations in this section, an adaptive feed-forward can correct the bunch-to-bunch offset variations, provided that the bunch offsets pattern from pulse to pulse does not change much.

Chapter 7

Summary

Long range wake fields are studied in accelerating structures for high energy electron-positron linear colliders. The two linear collider concepts, the SBLC and TESLA, are based on different types of accelerating structures: The SBLC uses 6 m long normal conducting structures working at 3 GHz RF frequency, while TESLA is based on 1 m long superconducting cavities operating at 1.3 GHz. The superconducting version is technically more challenging, but it provides a much better performance for such a future colliding beam facility because of its higher acceleration efficiency, excellent beam stability and high luminosity.

Wake fields are excited by charged particles in the accelerating structures, and act back on the following particles. They typically lead to an increase in the beam energy distribution and transverse emittance. The longitudinal wake fields are roughly proportional to the square of the frequency of the accelerating mode and the transverse ones to the third power of the frequency. For this reason, the wake fields are smaller in TESLA than in the SBLC. Various methods are used in order to decrease the wake fields and their effects: extraction of their energy (damping), decoherence of effects from individual structures or cells (detuning), compensation of the wake field effects (BNS damping). One can distinguish between short range wake fields, with effects within the bunch, and long range ones, acting on the following bunches. The long range wake field can be written as a sum of higher order modes (HOM) that oscillate in the cavities. These modes can be grouped in passbands, frequency ranges where a number of modes are densely spaced.

Both theoretical and experimental methods have been used to study the HOMs in the accelerating sections:

Through simulations, the effects of the wake fields on the multi-bunch beam dynamics in the TESLA main linac were estimated (chapter 6). For these, the frequency, loss factor and quality factor of the modes obtained with the MAFIA code were used. The deflection of each individual bunch was calculated by adding the wake fields excited by all previous bunches.

Experimental studies of the HOM properties were performed with different methods:

- *Without beam*, the scattering matrix between special pick-ups of the accelerating structures were measured, by means of a network analyzer. By a perturbation technique, the field distribution of individual modes was determined. These methods were used to study TESLA cavities (section 5.4).
- Wake fields were excited *with bunched electron beams* and detected either directly with HOM pick-ups, using a spectrum analyzer, or indirectly at a position monitor through their effects on the beam. Several cases can be distinguished:
  - One short bunch excites all modes when traveling through an accelerating structure (section 4.3).
  - A bunch train leads to the amplification of the higher order modes which are at a multiple of the bunch frequency (section 4.4).
  - Single modes can be excited using a train with modulated transverse bunch positions (section 4.5) or with modulated bunch charge (section 5.3).

The HOM damping in the accelerating structure of the SBLC is achieved by an absorbing thin layer on the iris tips. HOM waveguide couplers are used only for measurements and not for damping. Some dipole passbands could be identified and compared to results of simulations. A dipole mode is induced by the HOM couplers, and is localized around them. When using a bunch train with modulated transverse positions, no resonant HOM amplification was observed.

Measurements with a beam modulated in intensity at the TESLA Test Facility have indicated modes with very high quality factors in several cavities, indicating their insufficient damping. For a mode at 2.58 GHz, investigations in the RF laboratory have shown that a possible reason for the poor damping are the boundary conditions imposed by the neighboring cavities. Depending on the frequency of this mode in different cavities which are connected by beam tubes, the electromagnetic field can have such a distribution that it couples badly to the HOM dampers.

Beam dynamics simulations carried out with the modes of the first two dipole passbands measured at the first three TTF cryo-modules show a negligible multi-bunch emittance growth in the TESLA main linac. The presence of a poorly damped mode from the third passband leads to a higher emittance growth. Nevertheless, the poor damping occurs only in few cavities, which indicates that it can be avoided. The simulations of the beam dynamics in the TESLA main linac when using superstructures for acceleration, groups of cavities fed together through one power input coupler, have given similar results to the case of using 9-cell cavities.

The HOMs of the TESLA cavities require further studies. For the mode at 2.58 GHz the causes that may lead to a rotation of the polarization direction have to be investigated. The results of the experiment at the TTF using a beam with modulated intensity have to be further analyzed. The effect on the beam dynamics of the other HOMs found to be poorly damped in some cavities of the TTF has to be studied through simulations. Nevertheless the feed-forward system will most likely be able to correct for the bunch to bunch offset variations caused by these HOMs.

Appendix A

Auxiliary Functions

Auxiliary functions describing the behaviour of a bunch train with a sinusoidal modulation of the transverse bunch positions or of the bunch charges (sections 4.5 and 5.3) [51]:

$$p_r(\omega t, Q) = \frac{1}{2} \frac{\sin(\omega t)}{\cosh\left(\frac{\omega t}{2Q}\right) - \cos(\omega t)} \tag{A.1}$$

$$\mathcal{A}_+(\omega t, Q, \Omega t) = \frac{1}{2} \frac{\sin(\omega t)\left(\cosh\left(\frac{\omega t}{2Q}\right)\cos(\Omega t) - \cos(\omega t)\right)}{\left(\cosh\left(\frac{\omega t}{2Q}\right) - \cos(\omega t - \Omega t)\right)\left(\cosh\left(\frac{\omega t}{2Q}\right) - \cos(\omega t + \Omega t)\right)} \tag{A.2}$$

$$\mathcal{A}_-(\omega t, Q, \Omega t) = \frac{1}{2} \frac{\sin(\omega t)\sinh\left(\frac{\omega t}{2Q}\right)\sin(\Omega t)}{\left(\cosh\left(\frac{\omega t}{2Q}\right) - \cos(\omega t - \Omega t)\right)\left(\cosh\left(\frac{\omega t}{2Q}\right) - \cos(\omega t + \Omega t)\right)} \tag{A.3}$$

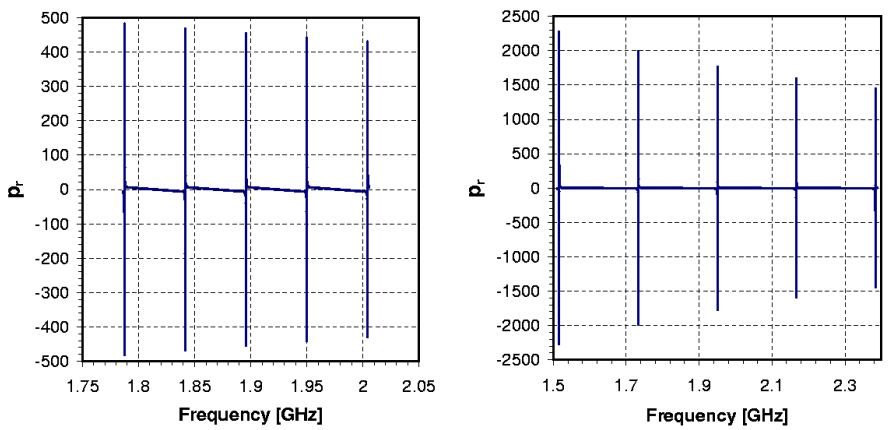

a. b.

Figure A.1: $p_r(\omega t, Q_l)$ as a function of $\omega/(2\pi)$ for (a) $1/t$ = 54 MHz and (b) $1/t$ = 216 MHz ($Q_l = 10^5$).

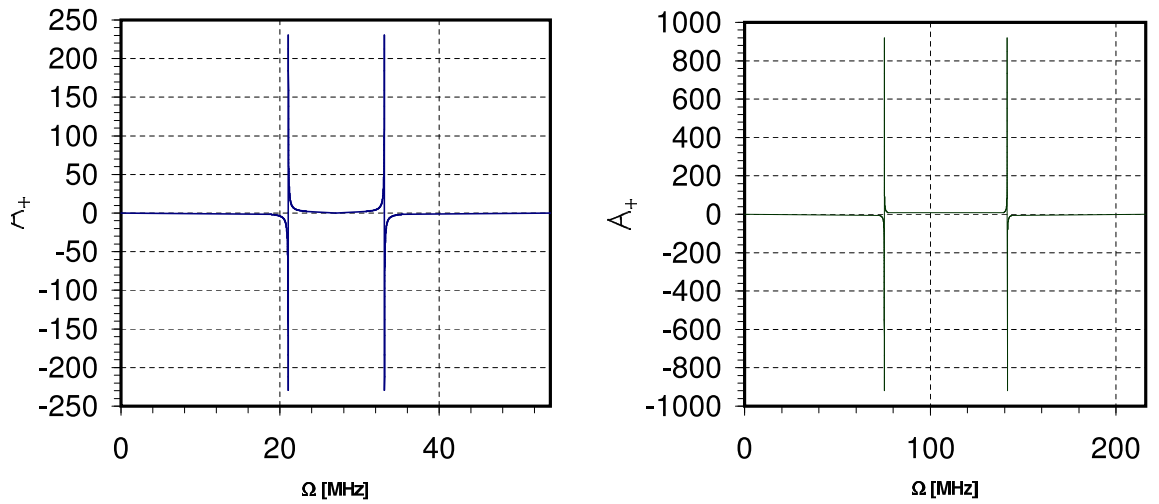

Figure A.2: $\mathcal{A}_+(\omega_l t, Q_l, \Omega t)$ as a function of $\Omega/(2\pi)$ for (a) $1/t$ = 54 MHz and (b) $1/t$ = 216 MHz (ω_l = 1.8748 GHz, $Q_l = 10^5$).

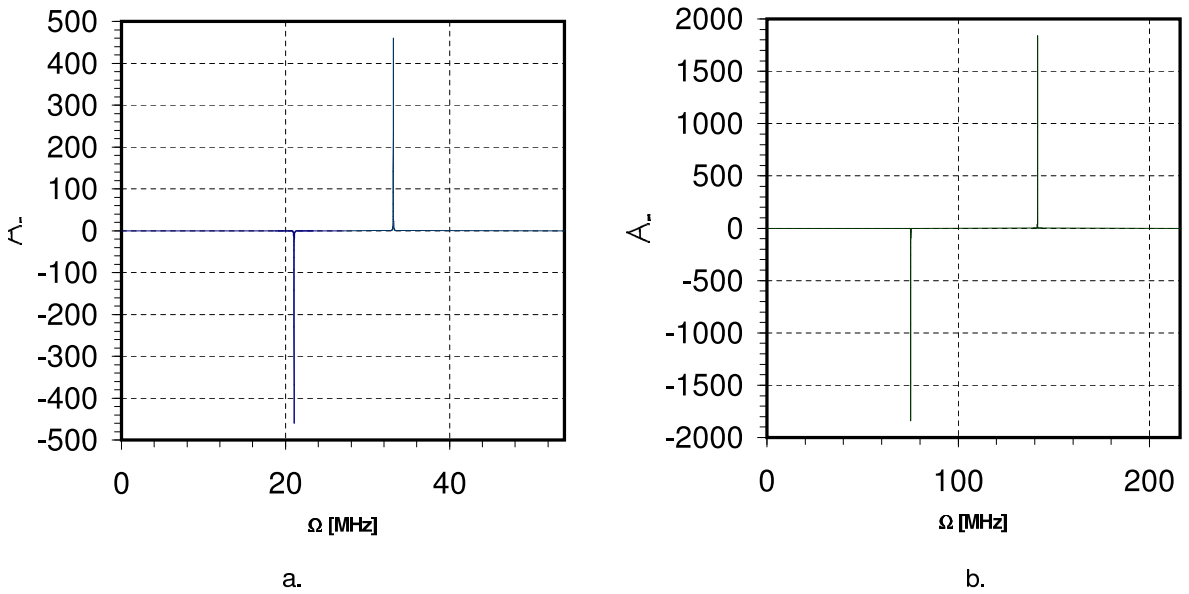

Figure A.3: $\mathcal{A}_-(\omega_l t, Q_l, \Omega t)$ as a function of $\Omega/(2\pi)$ for (a) $1/t$ = 54 MHz and (b) $1/t$ = 216 MHz (ω_l = 1.8748 GHz, $Q_l = 10^5$).

Appendix B

TTF Module 1

Module 1								
Cavity	D3	S8	* S10	D1	D2	* S11	D4	S7
Power coupler	FNAL	DESY	DESY	FNAL	FNAL	DESY	FNAL	FNAL
HOM couplers	DESY	Saclay	Saclay	DESY	DESY	Saclay	DESY	Saclay
Module 2								
Cavity	C22	C21	C25	C23	* A15	C26	C27	C24
Power coupler	FNAL	FNAL	FNAL	FNAL	FNAL	FNAL	FNAL	FNAL
HOM couplers	Saclay	Saclay	Saclay	Saclay	DESY	Saclay	Saclay	Saclay
Module 3								
Cavity	D41	S32	S29	S30	D39	D40	* S28	D42
Power coupler	DESY	DESY	DESY	DESY	AC	AC	DESY	AC
HOM couplers	DESY	DESY	DESY	DESY	DESY	DESY	Saclay	DESY

Table B.1: Components of the TTF cryo-modules 1, 2 and 3. Note: The DESY type power couplers used in module 1 had another design than the ones presently used (including the ones for module 3)

Bibliography

[1] R. Erickson (Ed.), *SLC Design Handbook*, Stanford, USA: SLAC (1984)

[2] R. Brinkmann, K. Flöttmann, J. Rossbach, P. Schmüser, N. Walker and H. Weise (eds.), *TESLA. The Superconducting Electron-Positron Linear Collider with an Integrated X-Ray Laser Laboratory. Technical Design Report*, Part II: *The Accelerator*, DESY Report: DESY 2001-011, ECFA 2001-209, TESLA Report 2001-23, TESLA-FEL 2001-05 (2001)

[3] R. Brinkmann, G. Materlik, J. Rossbach and A. Wagner (eds.), *Conceptual Design of a 500 GeV e^+e^- Linear Collider with Integrated X-ray Facility*, Chapter **4**: *S-Band Linear Collider*, DESY Report: DESY 1997-048 (1997)

[4] C. Adolphsen et al. (International Study Group), *International Study Group Progress Report on Linear Collider Development*, SLAC Report 559; KEK Report 2000-7 (2000)

[5] G. Guignard (ed.), *A 3 TeV e^+e^- Linear Collider Based on CLIC Technology*, CERN Report 2000-008 (2000)

[6] *International Linear Colliders Technical Review Committee Report 1995*, SLAC Report: SLAC-R-471 (1995)

[7] R. Brinkmann, *Technology and Challanges of Linear Colliders*, Proc. 18th Part. Accel. Conf. (PAC99), p. *16*, New York, USA, Mar. 29 - Apr. 2, 1999

[8] T. Raubenheimer, *The Generation and Acceleration of Low Emittance Flat Beams for Future Linear Colliders*, PhD Thesis at the Stanford University, California, USA; SLAC Report: SLAC-387 (1991)

[9] R. Brinkmann, Y. Derbenev and K. Flottmann, *A Low Emittance, Flat-Beam Electron Source for Linear Colliders*, Proc. 7th Europ. Part. Accel. Conf. (EPAC 2000), p. *453*, Vienna, Austria, Jun. 26-30, 2000

[10] K. Flöttmann, *Investigation Toward the Development of Polarized and Unpolarized High Intensity Positron Sources for Linear Colliders*, PhD Thesis at Universität Hamburg, Germany; DESY Report: DESY 93-161 (1993)

[11] R. Brinkmann, G. Materlik, J. Rossbach and A. Wagner (eds.), *Conceptual Design of a 500 GeV e^+e^- Linear Collider with Integrated X-ray Facility*, Chapter **3**: *TESLA Linear Collider*, DESY Report: DESY 1997-048 (1997)

[12] D.A. Edwards (ed.), *TESLA Test Facility Linac - Design Report*, DESY Report: TESLA 95-01 (1995)

[13] G. Materlik and Th. Tschentscher (eds.), *TESLA. The Superconducting Electron-Positron Linear Collider with an Integrated X-Ray Laser Laboratory. Technical Design Report*, Part V: *The X-Ray Free Electron Laser*, DESY Report: DESY 2001-011, ECFA 2001-209, TESLA Report 2001-23, TESLA-FEL 2001-05 (2001)

[14] C. Adolphsen et al., *RF Processing of X-Band Accelerator Structures at NLCTA*, Proc. 20th Int. Linac Conf. (Linac 2000), Monterey, California, Aug. 21-25, 2000

[15] W. Wuensch, I. Wilson, H. Braun and M. Luong, *A Very-High-Gradient Test of a 30 GHz Single-Cell Cavity*, Proc. 7th Europ. Part. Accel. Conf. (EPAC 2000), p. *271*, Vienna, Austria, Jun. 26-30, 2000

[16] H. Wiedemann, *Particle Accelerator Physics*, Vol. I, Springer-Verlag, Berlin Heidelberg, Germany (1993)

[17] K. Wille, *Physik der Teilchenbeschleuniger und Synchrotronstrahlungsquellen*, B. G. Teubner, Stuttgart, Germany (1996)

[18] J. Rossbach and P. Schmüser, *Basic Course on Accelerator Optics*, in Proc. CERN Accelerator School, University of Jyväskylä, Finland, p. *17* (1992)

[19] J. Buon, *Beam Phase Space and Emittance*, in Proc. CERN Accelerator School, University of Jyväskylä, Finland, p. *89* (1992)

[20] The MAFIA collaboration, *MAFIA: User Guide*, CST GmbH, Darmstadt (1996)

[21] J. le Duff, *Dynamics and Acceleration in Linear Structures*, in Proc. CERN Accelerator School, University of Jyväskylä, Finland, p. *253* (1992)

[22] M. Weiss, *Introduction to RF Linear Accelerators*, in Proc. CERN Accelerator School, University of Jyväskylä, Finland, p. *913* (1992)

[23] J.D. Jackson, *Electrodinamica clasică* (*Classical Electrodynamics)*, Editura Tehnică, Bucureşti, România (1991)

[24] T. Weiland and R. Wanzenberg, *Wake Fields and Impedances*, Joint US-CERN Accelerator Course, Hilton Head, So. Carolina, U.S.A., 1990; DESY Report: DESY M-91-06 (1991)

[25] A. Chao, *Physics of Collective Beam Instabilities in High Energy Accelerators*, John Wiley & Sons, New York, U.S.A. (1993)

[26] M. Drevlak, *On the Preservation of Single- and Multi-Bunch Emittance in Linear Accelerators*, PhD Thesis at Technische Hochschule Darmstadt, Germany; DESY Report: DESY 95-225 (1995)

[27] A. Jöstingmeier, Private communication

[28] H. Schlarb, *Resistive Wall Wake Fields*, Diploma Thesis at Universität Hamburg, Germany; DESY Report: TESLA 97-22 (1997)

[29] A. Novokhatski, M. Timm and T. Weiland, *The Surface Roughness Wakefield Effect*, Proc. Int. Comput. Accel. Phys. Conf. (ICAP'98), Monterey, California, U.S.A., Sep. 14-18, 1998; DESY Report: TESLA 99-17 (1999)

[30] A. Mosnier, *Instabilities in Linacs*, CERN Advanced Accel. Phys. Course, Rhodes, Greece, Sep. 20 - Oct. 1, 1993; CEA Saclay Report: DAPNIA/SEA 93-19 (1993)

[31] V. Balakin, A. Novokhatsky and V. Smirnov, Proc. 12th Int. Conf. High Energy Accel., Fermilab, Batavia, U.S.A. (1983)

[32] R.B. Neal (Ed.), *The Stanford Two-Mile Accelerator*, Stanford University, W.A. Benjamin, Inc., New York (1968)

[33] W.K.H. Panofsky and M. Bander, *Asymptotic Theory of Beam Break-Up in Linear Accelerators*, Rev. Sci. Instr. **39**, p. *206* (1968)

[34] I. Wilson and W. Wuensch, *The CLIC Main Linac Accelerating Structure*, Proc. 20th Int. Linac Conf. (Linac 2000), Monterey, California, U.S.A., Aug. 21-25, 2000

[35] *Zeroth Order Design Report for the Next Linear Collider*, SLAC Report: SLAC-R-0474 (1996)

[36] R.M. Jones et al., *Advances in the SLAC RDDS: Modeling Manifold Damping and its Effect on the Wake Field for the Next Linear Collider*, Proc. 7th Europ. Part. Accel. Conf. (EPAC 2000), p. *821*, Vienna, Austria, Jun. 26-30, 2000

[37] F. Caspers, *Basic Concepts II*, in Proc. CERN Accelerator School: RF Engineering for Particle Accelerators, Exeter College, Oxford, UK, p. *125* (1991)

[38] H. Klein, *Basic Concepts I*, in Proc. CERN Accelerator School: RF Engineering for Particle Accelerators, Oxford, UK, p. *97* (1991)

[39] B. Zotter and S.A. Kheifets, *Impedances and Wakes in High-Energy Particle Accelerators*, World Scientific, Singapore (1998)

[40] M. Sands and J. Rees, *A Bench Measurement of the Energy Loss of a Stored Beam to a Cavity*, SLAC Report: PEP-95 (1974)

[41] C. Adolphsen et al., *Measurement of Wakefields Generated in Accelerator Test Structures Using the SLC*, Proc. 15th Int. Conf. on High Energy Accel. (HEACC'92), Hamburg, Germany, Jul. 20-24, 1992; SLAC Report: SLAC-PUB-5941 (1992)

[42] M. Schmitz, *Performance of the First Part of the Injector for the S-Band Test Facility at DESY*, Proc. 18th Int. Linear Accel. Conf. (Linac 96), p. *788*, Geneva, Switzerland, Aug. 26-30, 1996

[43] M. Schmitz for the SBLC study group, *The S-Band Linear Collider Test Facility at DESY*, Proc. 17th Part. Accel. Conf. (PAC97), Vancouver, Canada, May 12-16, 1997

[44] S. Choroba, J. Hameister and M. Kuhn, *Performance of the Klystron Modulators at the S-Band Test Facility at DESY*, Proc. 19th Int. Linear Accel. Conf. (Linac 98), Chicago, USA, Aug. 23-28, 1998

[45] W. Radloff and M. Wendt, *Beam Monitors for the S Band Test Facility*, Proc. 16th Part. Accel. Conf. (PAC95) and Int. Conf. on High Energy Accel. (IUPAP), p. *2616*, Dallas, Texas, May 1-5, 1995

[46] U. v. Rienen, *Higher Order Mode Analysis of Tapered Disc-Loaded Waveguides Using the Mode Matching Technique*, Part. Accel. **41**, p. *173* (1993)

[47] U. v. Rienen, *Numerical Methods in Computational Electrodynamics*, Springer-Verlag, Berlin Heidelberg, Germany (2001)

[48] A. Jöstingmeier, M. Dohlus, C. Rieckmann and A.S. Omar, *Application of the GSM Method and TD Computation of the Long Range Wake in Linear Accelerator Structuress*, Proc. 17th Part. Accel. Conf. (PAC97), Vancouver, Canada, May 12-16, 1997

[49] M. Dohlus et al., *Higher Order Mode Damping by Artificially Increased Surface Losses*, DESY Report: DESY-96-169 (1996)

[50] M. Dohlus et al.,, *High Power Test of the Iris Coating in the S-Band Linear Collider*, DESY Report: DESY-M-96-19 (1996)

[51] S. Fartoukh, *A New Method to Detect the High Impedance Dipole Modes of TESLA Cavities*, DESY Report: TESLA 98-13 (1998)

[52] B.I. Grishanov, F.V. Podgornii, J. Rummler and V.D. Shiltsev, *Very Fast Kicker for Accelerator Applications*, DESY Report: TESLA 96-11 (1996); Nucl. Instr. Meth. **A369**, p. *28* (1997)

[53] S. Schreiber, *Performance Status of the RF-Gun Based Injector of the TESLA Test Facility Linac*, Proc. 7th Europ. Part. Accel. Conf. (EPAC 2000), p. *309*, Vienna, Austria, Jun. 26-30, 2000

[54] S. Schreiber, D. Sertore, I. Will, A. Liero and W. Sandner, *Running Experience with the Laser System for the RF Gun Based Injector at the TESLA Test Facility Linac*, Nucl. Instrum. Meth. **A445**, p. *427* (2000)

[55] J. Andruszkow et al., *First Observation of Self-Amplified Spontaneous Emission in a Free-Electron Laser at 109 nm Wavelength*, Phys. Rev. Lett. **85**, No. 18, p. *3825* (2000)

[56] M. Jablonka, E. Klein, *A High Charge per Bunch Injector for the TESLA Test Facility using a Normalconducting Capture Cavity*, DESY Report: TESLA 93-05

[57] B. Aune et al., *The Superconducting TESLA Cavities*, Phys.Rev. ST Accel. Beams, vol. 3 (2000)

[58] R. Wanzenberg, Private communication

[59] S. Fartoukh et al., *Evidence for a Strongly Coupled Dipole Mode with Insufficient Damping in TTF First Accelerating Module*, Proc. 18th Part. Accel. Conf. (PAC99), p. *922*, New York, USA, Mar. 29 - Apr. 2, 1999

[60] C. Tang, Private communication

[61] C. Magne, Private communication

[62] G. Kreps, Private communication

[63] We thank all TTF operators and coordinators who took part in the experiment

[64] We thank A. Liro and I. Will for making the special setup needed for the charge modulation

[65] We thank A. Goessel for preparing the interface to the BPM and the signal generator driving the charge modulation

[66] H. Schlarb, Private communication

[67] M. Hüning, Private communication

[68] We thank M. Wendt for preparing the setup and interface for this measurements

[69] C. Magne et al., *Measurement with Beam of the Deflecting Higher Order Modes in the TTF Superconducting Cavities*, to be presented at the 19th Part. Accel. Conf. (PAC 2001), Chicago, USA, June 18-22, 2001

[70] N. Baboi, M. Dohlus, C. Magne, A. Mosnier, O. Napoly, H.-W. Glock, *Investigation of a High-Q Dipole Mode at the TESLA Cavities*, Proc. 7th Europ. Part. Accel. Conf. (EPAC 2000), p. *1107*, Vienna, Austria, Jun. 26-30, 2000

[71] M. Dohlus, Private communication

[72] We thank H. Sandvoss for doing this measurement

[73] J. Sekutowicz, M. Ferrario and C. Tang, *Superconducting superstructure for the TESLA Collider: A Concept*, Phys. Rev. ST Accel. Beams, vol. 2, No. 6, 1999

[74] H. Chen, Private communication

[75] The MAFIA collaboration, *MAFIA: L - The Linear Accelerator Tracking Code*, CST GmbH, Darmstadt (1994)

[76] H. Chen, G. Kreps, M. Liepe, V. Puntus and J. Sekutowicz, *RF Measurements on Cu Model of the Superstructure for the TESLA Linear Collider*, Proc. of 9th Workshop on RF Superconductivity (RFSC99), Santa Fe, USA, Nov. 1-5, 1999

[77] M. Liepe, Private communication

[78] R.-D. Kohaupt and I. Reyzl, *Fast Feedback Systems for Orbit Correction in the TESLA Linear Collider*, Proc. 18th Part. Accel. Conf. (PAC99), p. *1171*, New York, USA, Mar. 29 - Apr. 2, 1999

[79] H.-Th. Duhme et al., *Feedbackelektronik TTF*, Proc. of the HERA/TTF Seminar, p. *171*, Grömitz, Sept. 25-29, 2000

[80] R. Brinkmann and J. Rossbach, *Observation of Orbit Motion in HERA Covering Eight Decades in Frequency*, Nucl. Instr. Meth. **A350**, p. *8* (1994)

[81] N. Baboi and R. Brinkmann, *Higher Order Mode Effects and Multi-Bunch Orbit Stability in the TESLA Main Linac*, DESY Report: TESLA 2000-28 (2000)

Index

9-cell cavity
    higher order modes, 107

absorbing materials, 27
accelerating structure, 14
    constant gradient, 14
    constant impedance, 14
    design, 27
    for SBLC, 33
    for TESLA
        9-cell cavity, 56
        superstructure, 106
adiabatic damping, 13

BBU, 25
bead-pull measurement, 31, 97
beam break-up, 25
beta function, 12
betatron oscillations, 12
BNS damping, 25

cavity, 14
CDR, 105
cell, 14
Conceptual Design Report, 105
coupling efficiency, 100
Courant-Snyder invariant, 12
cryo-module, 54
    design
        alternative design, 106
        CDR design, 105, 106
        reference design, 105

detuning
    cell-to-cell detuning, 39
    section-to-section detuning, 39
dispersion curve, 15
dispersion diagram, 15

emittance, 12
    multi-bunch, 14
    normalized emittance, 13
    rms emittance, 12
emittance growth, 114
equation of motion, 11

FODO cell, 13

group velocity, 15

higher order modes, 20
HOM, 20
    damping, 27
    in 9-cell cavity, 107
    in superstructure, 107
HOM couplers, 27

loss factor, 18
luminosity, 2

modes, 14
    dipole, 15
    monopole, 15
    TE, 14
    TE-like, 15
    TM, 14
    TM-like, 15
    transverse electric, 14
    transverse magnetic, 14
modulation frequency scan, 70
    step of, 70
multi-bunch emittance, 14

network analyzer, 29

offset amplitude, 60

Panofsky-Wenzel theorem, 19
passband, 15

phase space, 13
phase velocity, 15
pill box cavity, 14
polarization, 83

Q, 18
quality factor, 18
    external, 57, 94, 95
    loaded, 57
    total, 57

R/Q, 18
resonator, 14

S-band structure, 33
    HOM couplers, 40
S-Band Test Facility, 33
S-parameters, 29, 100
SBLC, 5
scattering matrix, 29
shunt impedance, 34
slice, 19
spectrum analyzer, 31
steady state, 60
superstructure, 105, 106
    higher order modes, 107
    required damping, 114

TESLA, 6
    higher order modes, 107
    main linac, 106
TESLA cavity, 56
    higher order modes, 57
    HOM couplers, 56
TESLA Test Facility, 53
transfer matrix, 12
TTF, 53
TTF modules, 135
Twiss parameters, 12

wake fields, 18
    long range, 20
    measurements, 29
    short range, 18
wake potential, 19
    delta wake, 19
    delta-function wake potential, 19
wave
    standing, 14
    traveling, 14
wire measurement, 31

Acknowledgments

Looking back at the work lying behind this PhD thesis, I feel indebted to many colleagues and friends who directly or indirectly contributed to it.

I would like to thank the Machine Group leader, Dr. Dieter Trines, for giving me the opportunity to make my PhD at DESY. I am indebted to Dr. Norbert Holtkamp for showing me the path to working on a very interesting subject in an exciting scientific atmosphere. I feel grateful to Dr. Reinhard Brinkmann for helping me understand various accelerator physics issues and orienting me with patience onto a good path. I am happy to have had as my supervisor Prof. Peter Schmüser, not only an excellent teacher of accelerator physics and related issues, but also a gentle man and very good adviser. I have also learned many things from Dr. Martin Dohlus, with whom I had a very fruitful and pleasant collaboration. I am grateful to Dr. Jörg Rossbach for agreeing to be my co-referee.

The work at the S-Band Test Facility was facilitated by my colleagues from the MIN group. Martin Nagl, Werner Herold and Rolf Jonas are the names of only a few of the people who helped me in my work. I would like to mention as well the collaborators from the Institute for Nuclear Research in Moscow, who were operating the linac, and also took part in experiments.

The results of the experimental work at the TESLA Test Facility is the fruit of the collaboration with CEA Saclay, in particular Dr. Olivier Napoly, Dr. Christian Magne, Dr. Marcel Jablonka, Dr. Alban Mosnier and Dr. Bernard Aune. The contributions of many other people were essential for this experiment, either with their preparatory work, or with their serious involvement in its course, including all operators. I would mention Dr. Siegfried Schreiber, Dr. Michiko Minty, Markus Hüning, Dr. Pedro Castro, Matthias Liepe, Manfred Wendt, Andre Gössel, Dr. Danielle Sertore, Dr. Bart Faatz and Dr. Armin Liero and Dr. Ingo Will from the Max-Born Institute in Berlin. Many others have helped me with microwave and mechanical measurements in the HF and Tuning laboratories.

I have profited from discussions and work with many other people as well. I would like to mention a few names, but I am aware that the list should be much longer: Dr. Jacek Sekutowicz, Dr. Hans Weise, Dr. Rainer Wanzenberg, Holger Schlarb, Dr. Stefan Simrock, Dr. Guennadi Kreps, Dr. Vladimir Puntus, Dr. Hans-Walter Glock from Institut für Allgemeine Elektrotechnik, Universität Rostock, Dr. Vassili Tsakanov from the Yerevan Institute of Physics, Dr. Bernd Krietenstein from TEMF, Technische Universität Darmstadt.

I am also grateful to Michaela Marx and Susan Wipf for their help with the MAFIA code and with issues related to the work in UNIX. The later, as a native English speaker,

has also shared the burden of correcting my language mistakes with Dr. Nicholas Walker and Dr. Marc Lomperski. Many thanks to Dr. Christopher Burnton for his help on many occasions.

I have had the great opportunity to work as part of the international team operating the TESLA Test Facility. People came from many groups inside DESY, especially from FDET, MPY and other machine groups and HASYLAB, but also from other institutes, to work together on these very promising projects, TESLA and the Free Electron Laser based on the Self-Amplified Spontaneous Emission principle. We have worked together, we have hoped together, we were happy together. I remember in particular two occasions of joy: the date of February 22nd, 2000, when the first FEL beam was observed at TTF and the DESY celebration of 40 years of existence in May 2000.

I appreciated the pleasant atmosphere created by my colleagues in building 30b, which helped me to concentrate on my work and also to relax. I enjoyed my stay in the Linac II building where the people welcomed me. I would like to mention in particular Jürgen Scholz, who helped me accommodate to the institute and to the German environment. Although DESY is quite an international institute, I enjoyed learning and speaking German with native and non-native speakers.

I would like to thank my colleagues from the Electron Accelerator Laboratory of the National Institute for Laser, Plasma and Radiation Physics in Bucharest for facilitating me to start this very interesting PhD work.

Last, but not least, I would like to express my gratitude to Dr. Sérgio S. Funari for his encouragement to come to DESY and for his constant moral support and practical advice all along the past few years. He also offered me, together with Dr. Gert Rapp, the first image about DESY.

I hope to have the opportunity to work again with you all and with DESY.